

UC Riverside

UC Riverside Electronic Theses and Dissertations

Title

Utilization of First-Principles Based Models in the Mechanistic Studies of Thermocatalytic and Photocatalytic Processes on Transition Metal Surfaces

Permalink

<https://escholarship.org/uc/item/3gk692vw>

Author

Avanesian, Talin

Publication Date

2016

Peer reviewed|Thesis/dissertation

UNIVERSITY OF CALIFORNIA
RIVERSIDE

Utilization of First-Principles Based Models in the Mechanistic Studies of
Thermocatalytic and Photocatalytic Processes on Transition Metal Surfaces

A Dissertation submitted in partial satisfaction
of the requirements for the degree of

Doctor of Philosophy

in

Chemical and Environmental Engineering

by

Talin Avanesian

December 2016

Dissertation Committee:

Dr. Phillip Christopher, Chairperson

Dr. Jianzhong Wu

Dr. Bryan Wong

Copyright by
Talin Avanesian
2016

The Dissertation of Talin Avanesian is approved:

Committee Chairperson

University of California, Riverside

ACKNOWLEDGEMENTS

I would like to express my sincere appreciation to my advisor Dr. Phillip Christopher for his continuous support, guidance, understanding and for his friendship throughout the course of my PhD. His immense knowledge, enthusiasm for research, strong work ethics and high expectations from me have inspired me to always aim for excellence in all areas of my research. Thanks to his positive influence I have learnt to push myself outside my comfort zone and become a better presenter and hopefully a better writer. I would also like to thank the members of my dissertation committee, Dr. Jianzhong Wu and Dr. Bryan Wong, for providing me with new perspectives in my research through their insightful comments and challenging questions.

A very special thanks to Dr. Hongliang Xin, who helped me with setting up and configuration of my computational system, guided me through learning all I know about DFT and parallel computing and always promptly responded to my endless questions. This work would not have been possible without his assistance. In addition, I would like to acknowledge Gabriel S. Gusmão for developing the microkinetic analysis code and providing his assistance in troubleshooting many technical issues. I would also like to thank Matt Kale and Jun Yan for collaborations.

The text of this dissertation, in part or in full, is a reprint of the material as it appears in the following publications: Journal of Physical Chemistry C, November 2014, under the title “Adsorbate Specificity in Hot Electron Driven Photochemistry on Catalytic Metal Surfaces”. ACS Catalysis, July 2016, under the title “Scaled Degree of Rate Control:

Identifying Elementary Steps That Control Differences in Performance of Transition-Metal Catalysts”. Journal of Catalysis, November 2016, under the title “Mechanism of CO₂ reduction by H₂ on Ru(0001) and general selectivity descriptors for late-transition metal catalysts”, Co-authored by Gabriel S. Gusmão who contributed with technical support. All the previously published work has been supervised and directed by co-author Phillip Christopher.

I would like to thank my coworkers in Christopher research group for their help and friendship, also for everything I know about experimental techniques and biochemistry. Particularly, thanks to John Matsubu and Matt Kale for the many stimulating discussions and their valuable ideas, and more importantly for always being there for me through the ups and downs of last five years and for providing a shoulder for me to cry on whenever I needed. Thanks to John Matsubu, Matt Kale, Leo DeRita, Sergei Hanukovich and Yibo Jiang for all the fascinating conversations and for the much-needed humor that turned the long hours spent in B365 to memorable experiences. Thanks to Chithra Asokan, Kun Li, Glen Svenningsen, Christian Alcaraz and Bhogeswararao Seemala for being great friends and for all the fun times we have had together.

I am grateful for all the friendships I have developed over the last five years at UCR and around Riverside. Thanks to all for making my graduate school years less stressful and full of enjoyable memories: John, Matt, Leo, Sergei, Wenyan, Heather, Andy, Noam, Sasha, Samarthya, Marzieh and Saba. I would also like to thank all my friends, near and far, who have inspired, supported and encouraged me throughout my life and specially during the challenging years of graduate school.

I would like to thank my parents for always being there for me, supporting my every decision in life and instilling in me to pursue excellence in everything I do. Special thanks to my brother and sister-in-law, Zareh and Melineh, for taking on some of the family responsibilities during the many times that I have been absent or busy with graduate school. I am thankful for my extended family, all the Avanesians and Andresians, for always making me feel loved and special with their affectionate and encouraging words.

DEDICATIONS

This disseration is dedicated to my parents, Arax Andresian and Vahe Avanesian, for
their endless support and devotion

ABSTRACT OF THE DISSERTATION

Utilization of First-Principles Based Models in the Mechanistic Studies of
Thermocatalytic and Photocatalytic Processes on Transition Metal Surfaces

by

Talin Avanesian

Doctor of Philosophy, Graduate Program in Chemical and Environmental Engineering
University of California, Riverside, December 2016
Dr. Phillip Christopher, Chairperson

In this work we utilized quantum chemical calculations coupled with numerical and analytical models to predict macroscopic observables associated with catalytic and photocatalytic processes on transition metal surfaces. All the predicted macroscopic observables were validated based on experimental measurements. The theoretical models developed here provide atomic scale insights into the mechanisms of catalytic and photocatalytic processes and suggest areas for future research in the design of novel catalysts.

In the first part of this dissertation, we focused on understanding characteristics that control performance of late transition metals for the catalytic reduction of CO₂ by H₂. By coupling Density Functional Theory (DFT) calculations with mean-field microkinetic models we found that on Ru-based catalysts CHO* dissociation to CH* and O* is the rate determining step (RDS) for CH₄ formation, while CO* desorption is the RDS for CO

production. The affinity of late transition metals for O* adsorption was identified as an effective predictor of selectivity between CO and CH₄ production on late transition metals, which matches well with previous experimental observations. We extended this study by developing an analytical approach, called the “scaled degree of rate control” (S-DoRC), to systematically identify rate and selectivity determining steps for reactions on late transition metals.

In the second part of this dissertation we coupled Δ SCF-DFT calculations with a Hamiltonian-based inelastic scattering model to understand the detailed mechanisms of photocatalysis on metal surfaces. We focused on understanding experimentally observed behaviors of photon-driven CO and NO desorption and O diffusion reactions on the Pt(111) surface. The developed models that accurately predicted previous wavelength-dependent and time-resolved measurements and suggested approaches to control selectivity in photon driven reactions on metal surfaces.

In the last part of this dissertation we coupled extensive DFT calculations with Wulff constructions to understand the process of CO-induced reconstruction of Pt nanoparticle catalysts, which is critical to catalytic converters. By correlating atom-resolved imaging via *in-situ* scanning transmission electron microscopy (STEM), with *in-situ* quantitative, site-specific infrared (IR) spectroscopy and DFT based Wulff-constructions we demonstrated that at high CO coverage, Pt nanoparticles undergo a facet selective reconstruction where (100) facets reconstruct to stepped vicinal surfaces, while (111) facets are stable. This is the first example of an atomic scale and quantitative view of adsorbate induced metal nanoparticle surface reconstruction at realistic conditions.

TABLE OF CONTENTS

Chapter 1 Introduction	1
1.1. Importance of Heterogeneous Catalysis	1
1.2. Fundamentals of Heterogeneous Catalysis	4
1.3. Future Directions: The role of analytical and computational methods.....	11
1.4. Dissertation Outline	14
1.5. References	17
Chapter 2 Introduction to Theoretical and Computational Methods	19
2.1. Summary	19
2.2. Reaction Rate Theories	20
2.2.1. Transition state theory (TST).....	21
2.2.2. Thermodynamic parameters.....	24
2.3. Trends in surface reactivity.....	26
2.3.1. Chemisorption.....	26
2.3.2. BEP relations	33
2.3.3. Linear Scaling Relations	35
2.4. Fundamentals of heterogeneous photocatalysis.....	37
2.5. Density Functional Theory	39
2.5.1. Fundamental Principles.....	40
2.5.2. Geometry optimization calculations	44
2.5.3. Climbing Image Nudged Elastic Band (CI-NEB) calculations	45
2.5.4. Vibrational frequencies and thermodynamic parameters	46
2.5.5. Linear-expansion delta self-consistent field (lr Δ SCF-DFT) method.....	47

2.6. Mean-field Microkinetic Modeling.....	48
2.6.1. Fundamentals of mean-field microkinetic modeling	48
2.6.2. Computational method.....	52
2.7. Wulff construction	52
2.8. References.....	54
Chapter 3 Mechanism of CO ₂ reduction by H ₂ on Ru(0001) and general selectivity descriptors for late-transition metal catalysts	58
3.1. Summary	58
3.2. Introduction.....	59
3.3. Methods.....	63
3.3.1. Elementary steps	63
3.3.2. DFT calculations	64
3.3.3. Enthalpy and Free energy calculations	68
3.3.4. Pre-exponential calculations	70
3.3.5. Microkinetic analysis	71
3.3.6. Rate and selectivity determining steps.....	72
3.3.7. DFT calculated energetics on transition metal 211 surfaces	73
3.4. Results and Discussion	74
3.4.1. CO ₂ methanation and rWGS mechanisms on Ru(0001).....	74
3.4.2. Microkinetic model	79
3.4.3. Sensitivity Analysis	87
3.4.4. Reaction rate expression	89
3.4.5. Selectivity descriptor on late-transition metals.....	93
3.5. Conclusions.....	99

3.6. References	101
Chapter 4 Scaled Degree of Rate Control: Identifying Elementary Steps that Control Differences in Performance of Transition Metal Catalysts	108
4.1. Summary	108
4.2. Introduction	109
4.3. Microkinetic model: CO ₂ reduction by H ₂	111
4.4. Scaled Degree of Rate Control	116
4.5. Conclusions	124
4.6. References	126
Chapter 5 Adsorbate Specificity in Hot Electron Driven Photochemistry on Catalytic Metal Surfaces	128
5.1. Summary	128
5.2. Introduction	129
5.3. Theoretical Methods	135
5.3.1. Extended Two Temperature Model	136
5.3.2. Inelastic Electron Scattering Model	141
5.3.3. Quantum Yield Calculations	148
5.4. Results and Discussions	150
5.4.1. Potential Energy Surfaces	150
5.4.2. Energetic Electron Induced Reaction Probabilities	153
5.4.3. Reaction Time Scales	155
5.4.4. Wavelength Dependent Quantum Yields	159
5.4.5. Impact of System Temperature	163
5.5. Discussion and Concluding Remarks	168

5.6. References.....	172
Chapter 6 An Atomic-Scale View of CO-Induced Pt Nanoparticle Surface Reconstruction	177
6.1. Summary	177
6.2. Introduction.....	178
6.3. Methods.....	181
6.3.1. Surface energy calculations	183
6.3.2. Coverage Dependent Surface Energies.....	186
6.3.3. Wulff Construction	190
6.3.4. In-situ scanning transmission electron microscopy (STEM).....	191
6.3.5. HAADF-STEM Intensity Simulation	192
6.3.6. In-situ diffuse reflectance Fourier transform infrared spectroscopy (DRIFTS)	192
6.3.7. Quantitative Site Fraction Analysis based on DRIFT measurements.....	194
6.3.8. Geometric Site Fraction Model.....	195
6.4. Results and Discussions	196
6.5. Conclusions.....	205
6.6. References.....	206
Chapter 7 Conclusions and Future Outlook.....	209
7.1. Summary	209
7.2. General Conclusions	210
7.3. Outlook on Future Research	213
7.4. References.....	218

LIST OF FIGURES

Figure 1.1. Fundamentals of heterogenous catalytic reactions.	5
Figure 1.2. Schematic representation of Sabatier Principle.....	7
Figure 1.3. A volcano plot of CH ₄ formation activity (log ₁₀ TOF) for CO ₂ reduction by H ₂ on transition metal catalysts.....	9
Figure 1.4. Surface structure of typical catalytic materials.	10
Figure 2.1: Potential energy diagram of an elementary reaction showing the formation of the transition state at the top of the energy barrier on the reaction pathway.	21
Figure 2.2. Electronic structure of a CO molecule illustrated based on a) molecular orbital theory b) Density of States.....	28
Figure 2.3. Schematic representation of band formation in metals, as a result of hybridization of a large number of molecular orbitals.....	28
Figure 2.4. Schematic representation of the energy levels of a typical 3d transition metal.	29
Figure 2.5. Schematic illustration of the interactions of a) atomic adsorbate states and b) molecular adsorbate states with transition metal sp and d-bands.	30
Figure 2.6. Interactions of adsorbate states with transition metal d-bands based on Newns-Anderson model with varying a) coupling strength b) d-band center.	32
Figure 2.7. The universal linear BEP relation between activation energies and dissociative adsorption energies of various diatomic molecules on a number of transition metals	34
Figure 2.8. Scaling relations for CH _x , OH _x , NH _x , and SH _x on close-packed, stepped, and fcc(100) surfaces.	36

Figure 2.9. Schematic representation of mechanisms associated with a) thermally driven and b) photon-induced chemical reactions on metal catalyst surfaces	38
Figure 2.10. Schematic illustration of Kohn-Sham implementation of DFT	43
Figure 2.11. Schematic of CI-NEB method to find minimum energy pathway on PES. .	46
Figure 2.12. Schematic of mean-field microkinetic model implementation for catalytic reactions	50
Figure 3.1: Potential energy diagram for competing initial hydrogenation steps in the $\text{CO}_2 + \text{H}_2$ reaction on Ru(0001).	75
Figure 3.2: Energy diagram of competing pathways for CHO^* dissociation and hydrogenation under low CO^* coverage calculated.	77
Figure 3.3: Potential energy diagram of competing pathways for CO_2 reduction by H_2 on Ru(0001).	79
Figure 3.4: Microkinetic model predictions of surface coverage for the most abundant surface species as a function of temperature and reactants partial pressures	81
Figure 3.5: Comparison of microkinetic model predictions of TOF for CH_4 production (1/s) and CO coverage with experimental measurements at similar reaction conditions	84
Figure 3.6: Microkinetic model prediction of CH_4 selectivity,	86
Figure 3.7: Sensitivity analysis results. a) Degree of rate control, X_{RC} , and b) Degree of selectivity control, X_{SC} , of elementary steps for CH_4 formation.	88
Figure 3.8: Comparison of free energies associated with CO^* desorption and CHO^* dissociation steps on Pt, Pd, Ni, Rh and Ru surfaces.	95

Figure 4.1. Volcano plots of a) CH ₄ formation activity, and b) CH ₄ selectivity for CO ₂ reduction by H ₂ on (211) surfaces of transition metals,.....	115
Figure 4.2. Linear correlation between the adsorption energies of O* and C* on (211) surfaces of late transition metals alloys of Pd, Pt, Ni, Co, Ir, Rh and Ru.	117
Figure 4.3. Potential energy surface for CO ₂ reduction by H ₂ on Ru (211) introducing the scaling factor ($\alpha_i=dH_{A,i}/dH_{O^*}$).....	120
Figure 4.4. Comparison of calculated X _{RC} and X _{S-RC} for a) CH ₄ formation and b) CO formation pathways and in c) X _{RC} and X _{S-RC} for CH ₄ formation are compared..	123
Figure 5.1: Schematic of substrate-mediated photochemistry on metal surfaces.	131
Figure 5.2: Schematic of the DIET mechanism.....	143
Figure 5.3: DFT calculated one-dimensional PES's of ground and TNI states.....	151
Figure 5.4: Reaction probabilities calculated with inelastic electron scattering model..	154
Figure 5.5: a-c) Temporal evolution of photo-excited electron distributions. d) Normalized instantaneous reaction rates as a function of time	156
Figure 5.6: Calculated quantum yields as a function of photon wavelength	161
Figure 5.7: Temperature dependence of quantum yields.....	164
Figure 6.1. Schematic diagram depicting the driving force for adsorbate induced reconstruction of surfaces through modification of competing facet surface energies ..	182
Figure 6.2. DFT-calculated CO coverage dependent surface energy of various Pt surface facets.	188
Figure 6.3. The configurations for identified saturation CO coverage of the investigated Pt surface facets.....	189

Figure 6.4. Visual comparison of a) DFT-based Wulff construction of a bare 3 nm Pt particle and b) HAADF-STEM image of a Pt nanoparticle, viewed along the <110> zone axis	196
Figure 6.5. Wulff constructions of a 7 nm Pt particle based on DFT calculated surface free energies for a) bare surfaces, and b) CO saturated surfaces.	198
Figure 6.6. Visual comparison of DFT-calculated and in-situ STEM measurements of facet-specific CO induced Pt nanoparticle surface reconstruction.	
Figure 6.7. Line scan intensity analysis of top layer of ~9 nm Pt particle based on a) Aberration-corrected STEM image and b) Simulated HAADF-STEM image.....	200
Figure 6.8. Demonstration of reversibility of surface reconstruction through <i>in-situ</i> STEM imaging of a 9 nm Pt particle under.....	201
Figure 6.9. STEM image of a ~6 nm Pt nanoparticle under identical conditions as Figure 6.8a, b and c, showing reversible reconstruction.....	202
Figure 6.10. Quantitative correlation between IR measurements and DFT predictions of CO-induced Pt nanoparticle surface reconstruction.	204
Figure 6.11. a) Results of <i>in-situ</i> quantitative IR analysis of UC and WC site fractions b) Quantitative analysis of clean and CO saturated DFT calculated Wulff constructions of various sizes. c) Geometric model of the change in UC and WC site fractions.	205

LIST OF TABLES

Table 3.1. Elementary steps included in the mechanism of CO ₂ hydrogenation, reaction free energies, forward activation barriers and forward/reverse pre-exponential factors on Ru(0001) surface at T=500K and P= 1 bar	64
Table 3.2. DFT calculated electronic energies, vibrational frequencies, zero-point energy and corrections to thermodynamic quantities for gas phase species involved in CO ₂ hydrogenation mechanism at T=500 K and P=1 bar	66
Table 3.3. DFT calculated electronic energies, vibrational frequencies, zero-point energy and corrections to thermodynamic quantities for surface species involved in CO ₂ hydrogenation mechanism at T=500 K and P=1 bar	67
Table 3.4. DFT calculated electronic energies, vibrational frequencies, zero-point energy and corrections to thermodynamic quantities for transition state configurations involved in CO ₂ hydrogenation mechanism at T=500 K and P=1 bar	68
Table 3.5. Elementary steps included in the derivation of rate expression.....	90
Table 4.1. The 13 elementary steps involved in the mechanism of CO ₂ reduction by H ₂ on Ru catalyst surface. Reaction enthalpies and activation barriers are derived LS relations, the forward and reverse pre-exponential factors are derived from DFT calculations. ...	113
Table 4.2. The scaling relations used in the microkinetic model of CO ₂ reduction mechanism, developed for adsorbed species and transition states on (211) surfaces of transition metals	114
Table 4.3. The calculated values of $\alpha_i=dH_{A,i}/dH_{O^*}$, X_{RC} , X_{SC} , X_{S-RC} and X_{S-SC} for the 13 elementary steps involved in the mechanism of CO ₂ reduction by H ₂	119
Table 5.1. List of Parameters Used in Extended Two Temperature Model	141

Table 5.2. List of Parameters Used in Inelastic Electron Scattering Model	145
Table 6.1. Surface energies of Pt {hkl} facets calculated as a function of slab thickness and number (thickness) of relaxed layers	185
Table 6.2. DFT calculated surface energies for different facets of Pt FCC crystal and their ratios with respect to (111) facet surface energy. The surface energies in third column are obtained by normalizing the most stable (111) surface to experimental surface energy of polycrystalline Pt and maintaining relative energies between facets.....	186
Table 6.3. Calculated CO adsorption energies in eV at different CO coverages on the investigated Pt {hkl} facets.....	187
Table 6.4. CO adsorption energies and interfacial energies of different Pt facets at saturation coverages.....	190

Chapter 1

Introduction

1.1. Importance of Heterogeneous Catalysis

Catalytic technologies play a major role in a wide variety of industrial processes ranging from pharmaceuticals to fuel and chemicals production and pollution mitigation processes. It is estimated that currently about 20% of the US and 30-40% of the global GDP depends on catalytic processes.¹ The use of innovative catalytic technologies has greatly impacted our quality of life in the past century. A few of the most noteworthy examples are: the development of Haber-Bosch ammonia synthesis and catalytic cracking processes and the invention of catalytic converters. The Haber-Bosch process is considered to be the major contributor to the industrialization of agriculture and steep population growth of 20th century.^{2,3} This technology provides affordable pathway to synthesize ammonia from atmospheric Nitrogen (N₂) and Hydrogen gas (H₂) on an Iron based catalyst and continues to play a major role in the production of fertilizers. The development of

catalytic cracking processes started in the early 1930s to upgrade the high molecular weight fractions of crude oil to lighter and higher value fuel products.⁴ The technology provided for the rapidly increasing demand of gasoline throughout the century. The modern fluidized catalytic cracking (FCC) units produce 5017 thousand barrels of gasoline per day using a specially designed zeolite catalyst.⁵ Catalytic converter technology, first implemented by American automobile industry in 1975, is an example of successful application of catalysis in pollution control which is now adopted by automobile industries all around the world. The technology reduces the toxic emissions from automobile exhaust gases by oxidation of CO and unburned hydrocarbons and reduction of NO_x over metal catalysts such as Pt, Pd and Rh.⁶

With the continuous growth of global demand of energy, food and chemicals and its accompanying environmental concerns, along with the declining supplies of energy and natural resources, it has become crucial for us to develop highly efficient and sustainable chemical conversion processes.^{7,8} Catalysis is going to play a central role in our endeavors to achieve clean and sustainable technologies, because it is the key technology that can accelerate and direct chemical transformations towards desired products. By rational design of new catalytic materials, we can enhance the efficiency of existing chemical processes in energy and raw material consumption, provide solutions for pollution mitigation and create new sustainable pathways for fuel and chemicals production from renewable sources (e.g. solar energy and biomass).

The vast majority of existing technologies in chemical industry are thermally driven processes. The efficiency of a thermal process is decided by its energy requirement to

achieve optimum reaction rates and its effective conversion of raw materials to products. In a heterogeneous catalytic process, these two factors can be adjusted by modifying the composition and structure of catalyst materials. Traditionally, the search for efficient catalytic processes have been achieved through a trial and error approach by probing large number of possible material compositions, synthesis methods and reaction conditions to optimize catalytic activity and selectivity. Although many economically successful technologies have been developed based on these strategies, most chemical processes still heavily rely on thermal energy provided by fossil fuel combustion. The limitations dictated by inherent thermodynamic properties (as discussed in section 1.2) and structure stability of catalytic materials, also a lack of atomistic level understanding of catalytic processes has made it difficult to design highly efficient catalyst materials that require little or no thermal energy input. The rapidly increasing need for energy efficient chemical processes and the inherent limitations of classical catalyst design approaches stress the necessity of new and enhanced sustainable catalytic technologies as well as improved rational strategies for catalyst design.

One of the more promising alternatives to current unsustainable processes is the utilization of solar energy to drive chemistry on catalyst surfaces.⁷ The possibility of targeted manipulation of molecules in photocatalytic processes on metal surfaces provides the potential advantage of enhanced control of selectivity and higher reaction efficiencies. Although scientific studies of light-induced chemistry have been carried out as early as 18th century,⁹ and the first successful photo-catalytic process was achieved more than 40 years ago in the laboratory of Fujishima and Honda,¹⁰ little advancement has been made towards

development of industrial-scale photocatalytic processes. It has been proven difficult to design versatile materials that hold all the desired properties of an effective photocatalyst; to efficiently adsorb light, channel the adsorbed energy to the desired chemical bonds and perform selective chemistry. To guide the design of efficient photo-catalysts, there is still a need for major advances in understanding of the fundamentals of these processes, ranging from the very short timescales of electron and atomic motion to those of elementary reaction processes.

The recent advancement in quantum chemical and computational methods has equipped us with strong set of tools that can be used to probe the reactions mechanisms and gain atomic level understanding which is paramount in the rational design of new catalyst materials. The continuously increasing computational power has facilitated the development of predictive theoretical models and has created the opportunity for rapid screening and fast discovery of novel catalyst materials. In this dissertation a variety of theoretical and computational techniques have been utilized to gain atomistic insight into underlying mechanism of heterogeneous catalytic and photocatalytic processes, predict behavior of catalyst-adsorbate systems and explore potential approaches for design of catalytic processes with higher selectivity towards desired products.¹¹⁻¹³

1.2. Fundamentals of Heterogeneous Catalysis

In a chemical reaction, the reactant molecules need to overcome energy barriers along their pathway to form products, as illustrated in potential energy diagram in Figure 1.1a. The energy to overcome these activation barriers are usually provided by thermal energy. The reaction rates are dependent on the temperature, T , and activation energy, E_a , through

the Arrhenius expression: $rate \propto A \exp(-E_a/k_B T)$, where A is a pre-exponential factor (accounts for the frequency at which the reaction is attempted) and k_B is the Boltzmann constant (A microscopic description of the Arrhenius rate expression is provided in section 2.2.1). Thus, the reaction rates can be enhanced by either increasing the temperature or lowering the activation barrier. Catalysts by interacting with the reactant molecules provide alternate energy pathways with lowered activation barriers and facilitate the chemical transformations (see Figure 1.1a).

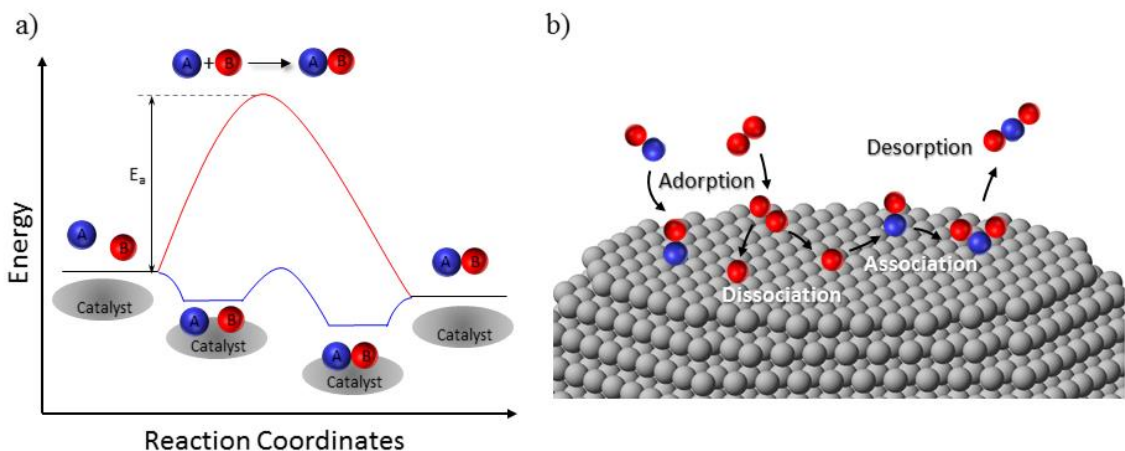


Figure 1.1. Heterogeneous catalytic reactions. **a)** Potential energy diagram of a model chemical reaction showing gas-phase and catalyzed pathways. Catalyst provides an alternate energy pathway with lower activation energy requirement. **b)** Schematic of surface reactions that happen during a catalytic reaction.

In heterogeneous catalysis, which is the main focus of this work, reactions happen on the surface of the solid catalyst material. The reactants first adsorb to the “active sites” on catalyst surface, either through dissociative or non-dissociative adsorption. The adsorbed species then move around and collide with one another, which results in bond breaking or formation of new bonds. The catalytic cycle is completed by the desorption of the new chemical species formed on the surface, leaving the surface intact. The elementary steps involved in a simple catalytic cycle are illustrated schematically in Figure 1.1b. However,

typical catalytic reactions consist of a complex network of elementary steps which occur simultaneously and with different rates. Identification of these elementary steps is the first step to understanding the reaction mechanism and determining the kinetics.

The two important factors that characterize the performance of a catalyst material are the activity and selectivity. The activity of a catalytic reaction, which is defined as the number of reaction events per catalytic active site per unit time, is dictated by the slowest of the elementary steps involved in the reaction network, known as the “rate limiting step” (RLS). The selectivity of a catalyst for a given reaction on the other hand is decided by the relative rates of competing elementary pathways. The ultimate objective in the design of highly efficient catalytic processes is to engineer materials that can attain high activities with minimal energy requirement and can selectively transform the reactants to the desired products. The key challenges to achieve this goal are the identification of the RLS and elementary pathways that control the selectivity, as well as devising methods to rationally manipulate these steps and optimize the catalytic performance, which require detailed knowledge of the reaction mechanism and an accurate account of kinetics of the elementary steps.

The rates of individual elementary reactions are governed by the associated energetics and the frequency with which each elementary step is attempted. For a given elementary reaction these parameters are determined by the electronic structure of the catalytic material. Therefore the catalytic properties can be tuned by modifying the electronic structure of the catalyst material, which in practice is achieved by changing the chemical composition and geometrical structure of catalytic active sites. The key to developing an

approach for rational design of catalyst material, is to gain an understanding of adsorbate surface interactions and access predictive theories of reactivity patterns of surfaces. Such predictive theories have been proposed by Sabatier (1911) and Brønsted (1928),¹⁴ Evans and Polanyi (1938).¹⁵ Based on Sabatier's principle, it is established that the highest catalytic rates can be achieved by finding the optimum reactant-surface binding energies, which is typically demonstrated by “volcano plots” schematically shown in Figure 1.2.¹⁶

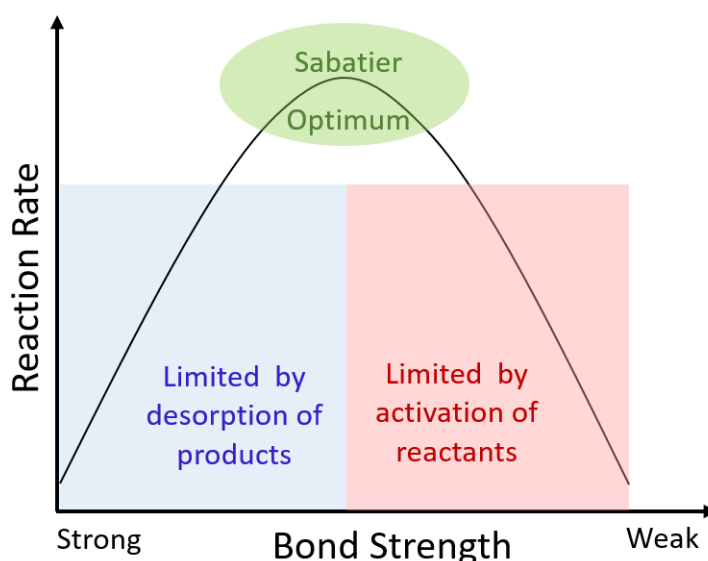


Figure 1.2. Schematic representation of Sabatier Principle shown as a volcano plot of reaction rate as a function of metal adsorbate bond strength. Adapted from reference 17, Copyright (2015), with permission from Elsevier

The models developed by Brønsted, Evans and Polanyi, known as BEP relations, explain the apparent linear relation between activation energies and heats of reactions of elementary steps. Based on BEP relations it can be demonstrated that strong binding of adsorbates to the surface, facilitates surface reactions by lowering the required activation barrier whereas reaction rates for weakly binding adsorbates are limited by large activation barriers. On the other hand, if the bond between catalyst and one of the reaction

intermediates is too strong, the catalyst surface will become poisoned by the strongly bound specie. Hence, an ideal catalyst is one that exhibits low activation barrier in addition to moderately binding reaction intermediates. This conclusion is in full agreement with Sabatier's principle and further elucidates the theory.

The advancements in computational chemistry methods have now enabled us to describe surface adsorbate interactions with reasonable accuracy and predict the reactivity trends of catalytic materials. The predictive theories have been further substantiated by DFT calculations. Libraries of binding energies and BEP correlations have been developed for elementary steps and catalyst materials associated with the most common industrially-relevant reactions. Furthermore, some recent theoretical and computational studies have developed new predictive correlations, known as linear scaling relations (LSR), which allow prediction of binding energies of many important surface species based on the binding energy of a single atom on the surface. The predictive power of these correlations comes from the fact that energy trends are proven to be universal; energies for adsorbates can be estimated based on energies calculated for other adsorbates with similar electronic structure. The implementation of BEP and LSR parametric correlations significantly reduces the required computational time and resources for the development of kinetic models and substantially accelerates the process of rational catalyst design. The studies of kinetic models that were developed based on the parametric correlations have also shed light on the inherent thermodynamic limitations of catalytic materials to achieve theoretically predicted maximum rates. As demonstrated in the 3D volcano plot in Figure 1.3 the maximum CH_4 production rates for CO_2 reduction by H_2 , correspond to O and C

binding energies that are not accessible by the late transition metals. As discussed in the introduction these thermodynamic limitations pose an additional challenge in the discovery of highly efficient catalytic materials.

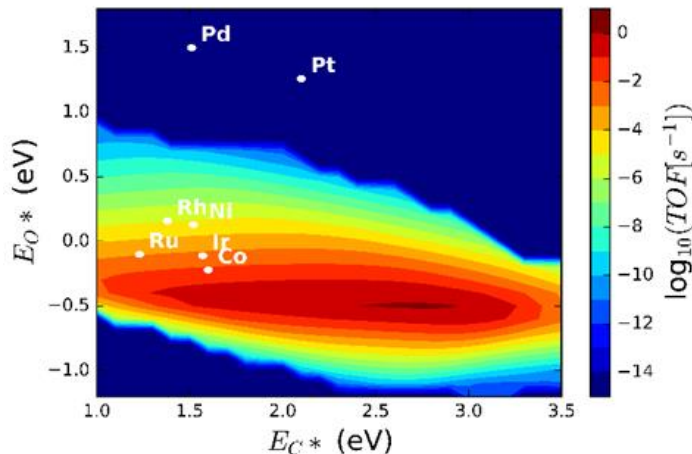


Figure 1.3. A volcano plot of CH_4 formation activity ($\log_{10} \text{TOF}$) for CO_2 reduction by H_2 , as a function of O and C adsorption energies on late transition metals at $T=500$ K and 1 bar. The plot shows that the maximum predicted activity is not accessible by the transition metals (the best known catalysts for the reaction) due to inherent thermodynamic limitations.¹³

The surface structure of catalyst particles is another factor that impacts the electronic structure and consequently the catalytic properties of the active sites. Most commonly used catalysts are made of finely dispersed metal particles on the surface of metal oxide supports (See Figure 1.4a). These metallic particles at thermodynamic equilibrium typically assume polyhedron shapes that minimize the particles total surface energy by predominantly exposing low surface energy facets (mostly (111) and (100) facets) (Figure 1.4b). Thus, the surface of a catalyst particle is comprised of a combination of active sites with different coordination numbers which have different electronic structures and reactivity. Despite many advancements in synthesis and characterization methods and our in-depth understanding of the correlations between geometry and reactivity of the active sites, it is

still difficult to engineer catalyst particles with targeted shapes and sizes and characterize the type and quantity of active sites on the surfaces. The instability of the catalyst particle surfaces under reaction conditions poses an additional challenge in the development of highly tailored catalysts and controlled catalytic processes. Strong interactions of adsorbate metal atoms have shown to influence the surface structures of the catalyst particles by modifying the equilibrium surface energies of exposed facets. The structure and reactivity of catalyst particles are also affected by various types of metal-support interactions. These interactions influence the reactivity of catalyst surface by modifying the concentration of active sites under reaction conditions. It is important to develop new theoretical and *in-situ* characterization approaches to obtain an accurate and quantitative analysis of catalyst surface reconstruction.

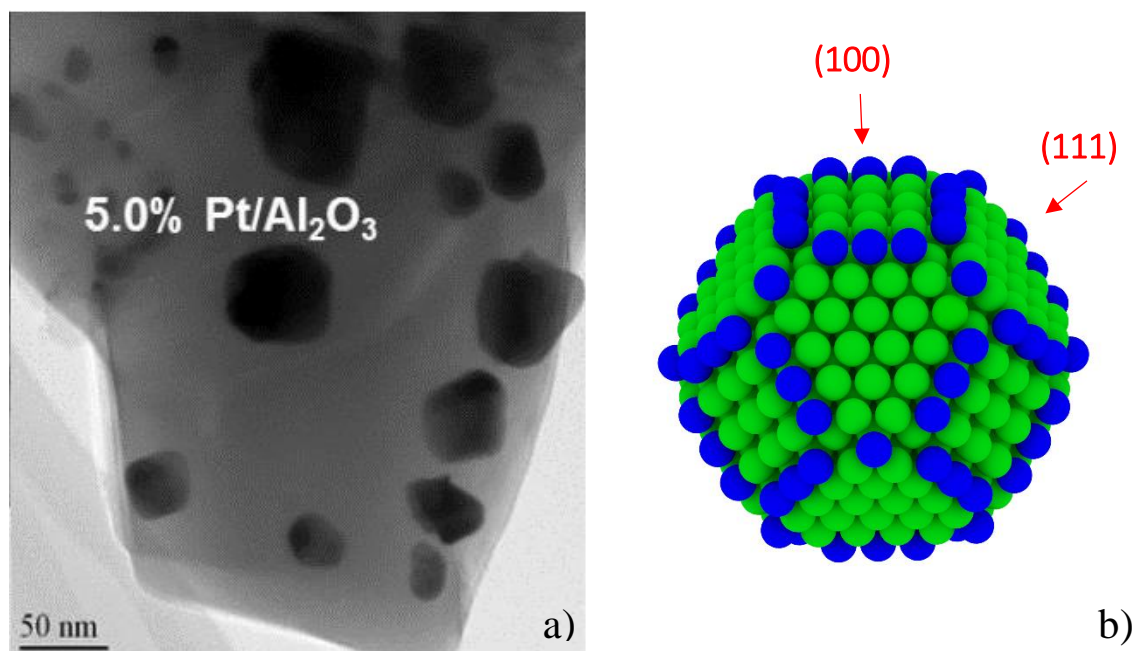


Figure 1.4. Surface structure of typical catalytic materials **a)** TEM image of an Alumina supported Pt nanoparticle catalyst sample. **b)** a typical truncated octahedron Pt nanoparticle (3 nm), the surface is made of (111) facets and (100) with a combination of well and under-coordinated sites, the under-coordinated sites are highlighted in blue.

1.3. Future Directions: The role of analytical and computational methods

As discussed in the previous sections, some of the main challenges in the approach to rational design of catalytic materials are obtaining detailed understanding of reactions mechanisms and dynamics of catalyzed reactions, identification of the elementary steps that control catalytic performance and development of predictive theories of adsorbate-surface interactions. Our main understanding of the catalytic processes in the early 20th century was based on theories developed by Langmuir and Hinshelwood in 1920s to describe the kinetics and mechanism of surface reactions, and transition state theory (TST) developed by Eyring, Polanyi and Evans in 1935.¹⁸ The development of surface science techniques since mid-20th century has opened the door to a new era of fundamental understanding of surface catalyzed reactions. A spectrum of analytical and characterization tools was developed such as spectroscopic and microscopic techniques that provided an accurate picture of geometric and electronic structures and adsorbate-surface interactions on the surfaces. The continuous advents in the atomic resolution techniques such as transmission electron microscopy (TEM) have now enabled us to observe the adsorbate-surface interactions *in-situ*, under reaction conditions.^{19,20}

The recent advances in quantum chemical theories, have further expanded our atomistic level knowledge of the catalytic processes and have accelerated the progress towards tailoring catalytic materials from first-principles. The density functional formalism was developed by Hohenberg, Kohn, and Sham in 1960s,^{21,22} but the major breakthrough in the applications of DFT in chemistry and material science came about in 1990s when the parallel computing resources became available. The Hohenberg-Kohn theorem

demonstrates that the ground state properties of a many-body system can be completely determined by the electron density of the system. Hence, by reducing the N -electron many-body problem of $3N$ dimensions to a 3-dimensional problem, it considerably reduces the computational efforts to calculate material properties. DFT has now become an indispensable part of research in the physics, chemistry and material sciences.

DFT methods are used in catalysis to provide detailed information on the adsorption energies, binding geometries, vibrational frequencies of adsorbates on the surfaces, stability of various surface structures, transition state geometries and activation energies associated with elementary steps. The information gained through these calculations can be used to map out entire mechanisms of catalytic reactions and predict steps that may control the overall reaction rate and selectivity.^{23–26} The geometric structure of catalytic particles can also be predicted based on the calculated surface free energies. The accuracy of the energies calculated with DFT methods are in the range of a few tenths of eV, which makes these methods particularly useful for investigating surface reactivity trends. By comparison of calculated energetics for different structures and compositions for a given reaction, reactivity trends can be developed which provide valuable predictive tools for the design of novel catalytic materials.

Furthermore, the information derived from DFT calculations can be used as an input into many other numerical methods to model a range of different time and length scale physical and chemical processes associated with (photo)catalysis. A few of more commonly used methods are mean-field kinetic models and statistical kinetic Monte Carlo (KMC) simulations. DFT-derived energies of surface species and transition states, and

corresponding vibrational frequencies can be used in kinetic models to predict reaction rates and selectivity and identify performance controlling elementary steps.

As a summary, the application of computational methods in the catalysis research can significantly contribute to the progress toward rational design of novel and efficient catalytic materials in several ways:

- By providing atomic level insight to the mechanisms of catalytic processes and allowing the identification of performance controlling elementary steps
- By facilitating the development of theoretical models to accurately describe adsorbate-surface interactions
- By enabling the development of predictive correlations and surface reactivity trends
- By complementing experimental studies to describe and validate macroscopic observables associated with surface catalyzed processes

In this dissertation, we demonstrated an example of application of DFT calculations coupled with mean-field microkinetic model to study the reaction mechanism of CO₂ reduction by H₂. In a second example, we coupled Δ SCF-DFT calculations with a Hamiltonian-based inelastic scattering model to understand the detailed mechanisms of photocatalysis on metal surfaces. In this example, we used DFT derived ground state and excited state potential energy surfaces and density of states (DOS) of investigated materials to calculate parameters used in the inelastic scattering model.

1.4. Dissertation Outline

The overall objective of this dissertation is to use the fundamental mechanistic insights gained through a combination of computational and analytical methods to predict macroscopic observables associated with catalytic and photocatalytic processes on transition metal surfaces. By utilizing combined numerical and experimental methods we were able to 1) Predict experimentally observed selectivity trends on transition metal catalysts for thermal reduction of CO₂ by H₂, 2) Predict previously observed adsorbate-specific trends in photocatalytic rates on metal catalysts and 3) Quantify the CO-induced reconstruction of Pt catalyst particles.

In Chapter 2 a brief description of fundamental theories used throughout the dissertation is provided, including theories describing reaction kinetics and rate laws, and the reactivity trends across transition metal catalysts. An introduction to the underlying mechanisms of heterogeneous photocatalytic processes is also provided. The computational methods used in the dissertation are discussed next, starting with an introduction to fundamentals of DFT calculations followed by specific DFT-based numerical methods that are applied to obtain different thermodynamic, kinetic and physical parameters used in our studies. A section is dedicated to the introduction of mean-field microkinetic modeling and the numerical methods used to solve the microkinetic systems. In the last section of the chapter, the theory of Wulff construction method is explained, which is employed in Chapter 6 to predict equilibrium shape of metal nanoparticles.

In Chapter 3 the mechanism of CO₂ reduction by H₂ at atmospheric pressure is investigated on Ru(0001) by coupling density functional theory (DFT) calculations with

mean-field microkinetic modeling. The initial CO₂ hydrogenation step leading to CH₄ production is shown to occur through CO₂ dissociation and subsequent hydrogenation of CO* to CHO*. The dissociation of CHO* to form CH* and O* is identified as the rate limiting step for CH₄ formation, while the rate limiting step for CO production through the reverse water gas shift reaction is identified as CO* desorption. Based on a scaling relations analysis of competing CHO* dissociation and CO* desorption, O* adsorption energy is found to be an effective descriptor of differences in selectivity between CO and CH₄ production previously observed on late-transition metal catalysts. These mechanistic insights provide critical information to guide the design of catalysts with tunable selectivity for CO₂ reduction by H₂ at atmospheric pressure.

In Chapter 4 we develop a computational approach for the identification of elementary steps that are responsible for the differences of catalytic behavior of transition metal catalysts, by implicitly incorporating inherent parametric correlations in sensitivity analysis of reaction systems. By extending the concept of “degree of rate control” (DoRC) through explicit incorporation of intrinsic parametric correlations relating chemistry on transition metal surfaces, we introduce the concept of “scaled degree of rate control” (S-DoRC). This approach identifies relevant rate or selectivity controlling steps that are tunable within the confines of parametric correlations on transition metal surfaces, by quantitatively modifying conclusions drawn from typical DoRC analysis using empirically derived scaling factors for each elementary step.

In Chapter 5 substrate mediated photochemistry on metal surfaces is analyzed by combining dynamical models associated with the metal substrate photo-excitation and

electron-mediated bond-activation processes. An extended version of two-temperature model is utilized to treat temporal evolution of photo-excited charge carriers in the metal substrate. The electron-induced adsorbate dynamics on the metal surface is modeled using a non-adiabatic, first-principles based inelastic electron scattering model. Photo-activation of three well studied reactions on Pt(111) surfaces, CO and NO desorption and O diffusion, are chosen as model systems. The unresolved issues associated with adsorbate specific reaction time scales and wavelength and temperature dependent behavior are addressed.

In Chapter 6 we investigate the CO-induced reconstruction of Pt nano-sized particles by correlating atom-resolved imaging via *in-situ* scanning transmission electron microscopy (STEM), with *in-situ* quantitative, site-specific infrared (IR) spectroscopy and DFT based Wulff-constructions. It is demonstrated that at high CO coverage, Pt nanoparticles undergo a facet selective reconstruction where (100) facets reconstruct to stepped vicinal surfaces, while (111) facets are stable. The importance of our results is discussed as a first example of a complete, atomic scale and quantitative picture of catalyst surface reconstruction under realistic condition.

In Chapter 7 we summarize the major conclusions drawn from this work and discuss their significance in the fields of heterogeneous catalysis and photocatalysis. The potential applications of this work in the future research directions is also discussed.

1.5. References

1. Adams, C. Applied catalysis: A predictive socioeconomic history. *Top. Catal.* **52**, 924–934 (2009).
2. Smil, V. Detonator of the population explosion. *Nature* **400**, 415–415 (1999).
3. Fryzuk, M. D. Ammonia Transformed. *Nature* **427**, 498–499 (2004).
4. Sadeghbeigi, R. *Fluid Catalytic Cracking Handbook*. (2012).
5. U.S. Downstream Processing of Fresh Feed Input. (2016). Available at: http://www.eia.gov/dnav/pet/pet_pnp_dwms_dc_nus_mbbldpd_m.htm.
6. Shelef, M. & McCabe, R. W. Twenty-five years after introduction of automotive catalysts: what next? *Catal. Today* **62**, 35–50 (2000).
7. Bell, A. T., Gates, B. C. & Ray, D. *Basic Research Needs: Catalysis for Energy*. U.S. Department of Energy (2008). doi:10.2172/927492
8. Somorjai, G. A. & Rioux, R. M. High technology catalysts towards 100% selectivity- Fabrication, characterization and reaction studies. *Catal. Today* **100**, 201–215 (2005).
9. Roth, H. D. The Beginnings of Organic Photochemistry. *Angew. Chemie Int. Ed.* **28**, 1193–1207 (1989).
10. Fujishima, A. & Honda, K. Electrochemical Photolysis of Water at a Semiconductor Electrode. *Nature* **238**, 37–38 (1972).
11. Avanesian, T. & Christopher, P. Adsorbate Specificity in Hot Electron Driven Photochemistry on Catalytic Metal Surfaces. *J. Phys. Chem. C* **118**, 28017–28031 (2014).
12. Avanesian, T., Gusmão, G. S. & Christopher, P. Mechanism of CO₂ reduction by H₂ on Ru(0001) and general selectivity descriptors for late-transition metal catalysts. *J. Catal.* **343**, 86–96 (2016).
13. Avanesian, T. & Christopher, P. Scaled Degree of Rate Control: Identifying Elementary Steps That Control Differences in Performance of Transition-Metal Catalysts. *ACS Catal.* **6**, 5268–5272 (2016).
14. Brønsted, J. N. Acid and Basic Catalysis. *Chem. Rev.* **5**, 231–338 (1928).
15. Evans, M. G. & Polanyi, M. Further Considerations on the thermodynamics of chemical equilibria and reaction rates. *J. Chem. Soc., Faraday Trans. 1* **32**, 1333–1359 (1936).
16. Sabatier, P. Hydrogenations et deshydrogenations par catalyse. *Berichte der Dtsch. Chem. Gesellschaft* **44**, 1984–2001 (1911).

17. Medford, A. J. *et al.* From the Sabatier principle to a predictive theory of transition-metal heterogeneous catalysis. *J. Catal.* **328**, 36–42 (2015).
18. Eyring, H. The Activated Complex in Chemical Reactions. *J. Chem. Phys.* **3**, 107–115 (1935).
19. Yoshida, H. *et al.* Visualizing Gas Molecules Interacting with Supported Nanoparticulate Catalysts at Reaction Conditions. *Science* **335**, 317–319 (2012).
20. Hansen, P. L. *et al.* Atom-resolved imaging of dynamic shape changes in supported copper nanocrystals. *Science* **295**, 2053–2055 (2002).
21. Hohenberg, P. & Kohn, W. Inhomogeneous Electron Gas. *Phys. Rev.* **136**, B 864–871 (1964).
22. Kohn, W. & Sham, L. J. Self-Consistent Equation Including Exchange and Correlation Effects. *Phys. Rev.* **140**, A 1133–1138 (1965).
23. Gokhale, A. A., Kandoi, S., Greeley, J. P., Mavrikakis, M. & Dumesic, J. A. Molecular-level descriptions of surface chemistry in kinetic models using density functional theory. *Chem. Eng. Sci.* **59**, 4679–4691 (2004).
24. Grabow, L. C. & Mavrikakis, M. Mechanism of Methanol Synthesis on Cu through CO₂ and CO Hydrogenation. *ACS Catal.* **1**, 365–384 (2011).
25. Andersson, M. P. *et al.* Structure sensitivity of the methanation reaction: H₂-induced CO dissociation on nickel surfaces. *J. Catal.* **255**, 6–19 (2008).
26. Andersson, M. P. *et al.* Toward computational screening in heterogeneous catalysis: Pareto-optimal methanation catalysts. *J. Catal.* **239**, 501–506 (2006).

Chapter 2

Introduction to Theoretical and Computational Methods

2.1. Summary

This chapter starts with a brief description of fundamental theories used throughout the dissertation, including theories describing reaction kinetics and rate laws and the reactivity trends across transition metal catalysts. An introduction to the underlying mechanisms of heterogeneous photocatalytic processes is also provided. The computational methods used in the dissertation are discussed next, starting with an introduction to fundamentals of DFT calculations followed by specific DFT-based numerical methods that are used to obtain different thermodynamic, kinetic and physical parameters utilized in our studies. A section is dedicated to the introduction of mean-field microkinetic modeling and the numerical methods used to solve the microkinetic systems. In the last section of this chapter the theory of Wulff construction method is explained, which is used in Chapter 6 to predict equilibrium shape of metal nanoparticles.

2.2. Reaction Rate Theories

The expression proposed by Arrhenius in 1889 for reaction rate constant (equation 2.1), was derived on experimental basis. In equation 2.1, k is the reaction rate constant, A is the pre-exponential factor, E_a is the activation energy, k_B is the Boltzmann constant and T is the absolute temperature.

$$k = A \exp\left(-\frac{E_a}{k_B T}\right) \quad (2.1)$$

Reaction rate theories developed in later years based on statistical thermodynamic formalism, collision theory (1921) and transition state theory (TST) (1935),^{1,2} show that the Arrhenius equation is in fact to a very good approximation correct. In this section the Arrhenius rate expression is explained based on the reaction rate theories to provide a molecular level understanding of the kinetics of catalytic reactions.

As described in Chapter 1, in a chemical reaction, the reactant molecules need to overcome energy barriers along their pathway to form products. The energetic pathway of reactants to products for an elementary surface reaction is shown in the potential energy surface (PES) diagram in Figure 2.1. Based on the reaction rate theories discussed here, the reacting molecules gain energy by collision with each other.³ In collision theory the molecules are assumed to be hard spheres and the required energy to cross activation barrier is provided by the kinetic energy of the combined molecules at the collision moment. The details about the structure, the vibrations and rotations of reacting molecules are not included in collision theory which play an important role in the energy exchange of the

colliding molecules. These limitations were addressed by TST which is discussed in the next section.

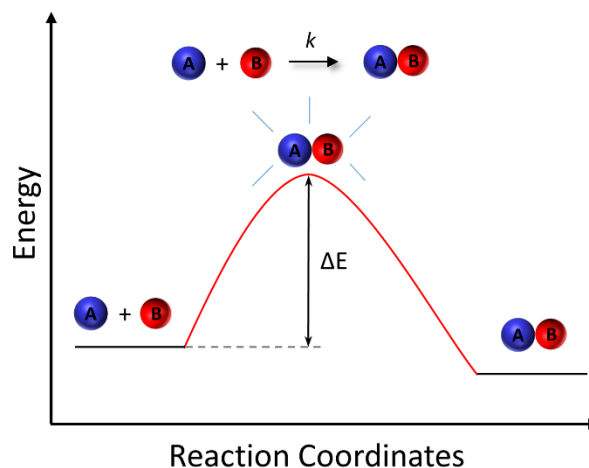


Figure 2.1: Potential energy diagram of an elementary reaction showing the formation of the activated complex, or transition state, at the top of the energy barrier on the reaction pathway. Adapted with permission from ref. 3, copyright (2003) WILEY-VCH

2.2.1. Transition state theory (TST)

The theory was developed around 1935 by Henry Eyring, and independently by M.G. Evans and Michael Polayni, on the basis of collision theory.^{2,4} According to TST, reactions proceed through formation of an activated complex, the transition state, located at the saddle point of energy pathway between reactants and molecule. The activate complex is formed when an efficient collision occurs between two reacting molecules. The energy pathway between reactant and products is defined by the reaction coordinate, which is usually a geometric parameter that changes during the conversion such as a stretching vibrational mode between two atoms of a dissociating molecule. The fundamental assumption is that once the transition state is formed reaction can only move forward

towards product formation. In other words, the transition states $[R^\ddagger]$ are fully equilibrated with the reactants $[R]$ with an equilibrium constant K^\ddagger , as shown in equation 2.2.³



The rate of products $[P]$ generation can be directly related to the concentration of transition states $[R^\ddagger]$ and the frequency at which each reaction event is attempted, defined by the vibrational frequency of the transition state in the reaction coordinate ν . Thus, the overall reaction rate can be written in the following form:

$$\frac{d[P]}{dt} = \nu [R^\ddagger] = \nu K^\ddagger [R] = \nu \frac{q^\ddagger}{q} [R] \quad (2.3)$$

In equation 2.3, the equilibrium constant K^\ddagger is written in terms of partition functions of reactants (q) and transition state (q^\ddagger). By separating the partition function of the reaction coordinate (q_ν), the equation can be written in the following form:³

$$\frac{d[P]}{dt} = \nu q_\nu \frac{q^\ddagger}{q} [R] = \nu \frac{e^{\frac{h\nu}{2k_B T}}}{1 - e^{\frac{h\nu}{k_B T}}} \frac{q^\ddagger}{q} [R] \quad (2.4)$$

The vibration frequency of the weakened reaction coordinate at transition state is small, therefore $k_B T \gg h\nu$, which simplifies equation 2.4 to:³

$$\frac{d[P]}{dt} = \frac{k_B T}{h} \frac{q^\ddagger}{q} [R] \quad (2.5)$$

The rate constant of the reaction according to equation 2.5 can be written in form of equation 2.6, in terms of partition functions of reactants and the transition state.

$$k = \frac{k_B T}{h} \frac{q^\ddagger}{q} \quad (2.6)$$

It should be noted that q^\ddagger is the partition function of the transition state which is defined by the same zero energy at the bottom of the PES well of reactants. To use a more convenient derivation, a new zero energy for transition state can be defined at the top of the saddle point with partition function q_0^\ddagger . The energy difference between the new and initial zero energy is the activation energy (E_a) of the reaction.³ By incorporating this new definition of partition function in the rate constant expression (equation 2.7) we can see its resemblance with Arrhenius expression:

$$k = \frac{k_B T}{h} \frac{q_0^\ddagger}{q} \exp\left(-\frac{E_a}{k_B T}\right) \quad (2.7)$$

To relate the rate constant derived from TST with the more familiar macroscopic formulation in terms of thermodynamic parameters, we can write the rate constant as shown in equation 2.8, which implies that the transition state is in full equilibrium with the reactants except for the degree of freedom representing the reaction coordinate.

$$k = \frac{k_B T}{h} K^\ddagger \quad (2.8)$$

By incorporating the relation between the equilibrium constant (K^\ddagger) and Gibbs free energy (ΔG^\ddagger), we can derive the familiar form of Arrhenius rate constant:

$$k = \frac{k_B T}{h} \exp\left(-\frac{\Delta G_0^\ddagger}{k_B T}\right) = \frac{k_B T}{h} \exp\left(\frac{\Delta S_0^\ddagger}{k_B}\right) \exp\left(-\frac{\Delta H_0^\ddagger}{k_B T}\right) \quad (2.9)$$

The comparison of equation 2.9 and Arrhenius expression defined with equation 2.1 gives us the microscopic definition of activation energy E_a , and pre-exponential factor A as follows:

$$E_a = \Delta H_0^\ddagger + k_B T \quad (2.10)$$

$$A = \frac{ek_B T}{h} \exp\left(\frac{\Delta S_0^\ddagger}{k_B}\right) \quad (2.11)$$

Rate expressions can be derived for surface reactions following the same principles in terms of adsorbed species partition functions. The resulting rate expressions are used in the development of microkinetic model for CO₂ reduction by H₂ in Chapter 3.

2.2.2. Thermodynamic parameters

The thermodynamic quantities used in rate expressions can be related to the vibrational degrees of freedom of reactant molecules and transition states, based on statistical thermodynamic formalisms. The vibrational frequencies of molecules in both in gas phase and adsorbed on surfaces can be calculated using DFT methods. The expressions relating the thermodynamic parameters to the vibrational modes of molecules are presented here.

Gas Phase: The thermodynamic properties of gas phase reactant and products are usually calculated in the ideal-gas limit. The enthalpy for an ideal gas at a given temperature T is given by:

$$H(T) = \int_0^T C_p dT \quad (2.12)$$

In equation 2.12, C_p is the constant pressure heat capacity which is correlated with constant volume heat capacity as $C_p = k_B + C_v$ (where k_B is the Boltzmann constant). The constant volume heat capacity can be broken down to the translational, rotational and vibrational parts (equation 2.13). For a 3D ideal gas, the translational constant volume heat capacity is $3/2k_B$ and the rotational heat capacities for monoatomic, linear and non-linear

molecules are 0, k_B , and $3/2k_B$ respectively.^{5,6} The contribution of vibrational heat capacity to the enthalpy at temperature T can be calculated by summing up vibrational energies ($\epsilon_i = h\omega_i$) of all the degrees of freedom (DoF), which are $3N-5$ for linear and $3N-6$ for non-linear molecules (equation 2.14).

$$C_p = k_B + C_{V,trans} + C_{V,rot} + C_{V,vib} \quad (2.13)$$

$$\int_0^T C_{V,vib} dT = \sum_i^{DoF} \frac{\epsilon_i}{e^{\epsilon_i/k_B T} - 1} \quad (2.14)$$

Similarly, the entropy for an ideal gas can be broken down into vibrational, translational and rotational components (equation 2.15). Equations 2.16-2.18 show the expressions for each entropy component:^{5,6}

$$S(T, P) = S_{trans} + S_{rot} + S_{vib} - k_B \ln \frac{P}{P^0} \quad (2.15)$$

$$S_{trans} = k_B \left\{ \ln \left[\left(\frac{2\pi M k_B T}{h^2} \right)^{3/2} \frac{k_B T}{P^0} \right] + \frac{5}{2} \right\} \quad (2.16)$$

$$S_{rot} = \begin{cases} 0 & , \text{ monoatomic} \\ k_B \left[\ln \left(\frac{8\pi^2 I k_B T}{\sigma h^2} \right) + 1 \right] & , \text{ linear} \\ k_B \left\{ \ln \left[\frac{\sqrt{\pi I_A I_B I_C}}{\sigma} \left(\frac{8\pi^2 k_B T}{h^2} \right)^{3/2} \right] + \frac{3}{2} \right\} & , \text{ non-linear} \end{cases} \quad (2.17)$$

$$S_{vib} = k_B \sum_i^{DoF} \left[\frac{\epsilon_i}{k_B T (e^{\epsilon_i/k_B T} - 1)} - \ln(1 - e^{-\epsilon_i/k_B T}) \right] \quad (2.18)$$

In equations 2.15-2.18, P^0 is the reference pressure, h is the Planck's constant, M is mass of the molecule, I is the moment of inertia and σ is the symmetry number. The Gibbs free energy of the gas molecules can then be calculated with $G(T,P) = H(T) - T S(T,P)$.

Adsorbates: The thermodynamic properties for surface species (including the transition states) are calculated in the harmonic limit where all $3N$ degrees of freedom of the adsorbates (with N atoms) are assumed to be harmonic vibrations (surface bound species don't have real translational or rotational degrees of freedom).⁵ The internal energy ($U(T)$) and entropy ($S(T)$) of the adsorbates are given by:

$$U(T) = \sum_i^{\text{harm DoF}} \frac{\epsilon_i}{e^{\epsilon_i/k_B T} - 1} \quad (2.19)$$

$$S(T) = k_B \sum_i^{\text{harm DoF}} \left[\frac{\epsilon_i}{k_B T (e^{\epsilon_i/k_B T} - 1)} - \ln(1 - e^{-\epsilon_i/k_B T}) \right] \quad (2.20)$$

Helmholtz free energy ($F(T)$) then can be calculated with $F(T) = U(T) - T S(T)$. Gibbs free energy is correlated with $F(T)$ through $G(T) = F(T) + pV$.⁵ In the study of isolated surface reactions, the pV (pressure-volume) term can be assumed negligible.

2.3. Trends in surface reactivity

2.3.1. Chemisorption

A detailed understanding of adsorbate-surface interactions is critical for explaining the underlying mechanisms of catalytic reactions, and for the rational design of catalyst surfaces to obtain desired catalytic properties. The strength of the bonds the reacting molecules make with the catalyst surface is the key descriptor for reactivity of a catalyst surface, as described by Sabatier's Principle (see section 1.2).⁷ To be able to accurately

analyze the chemical bonding between adsorbates and catalyst surfaces, it is necessary to have a thorough understanding of the electronic structures of metal-adsorbate systems.

The complex electronic structure of adsorbate-metal systems can be qualitatively explained using a simplified form of molecular orbital theory. A simple diatomic molecular bond formation is demonstrated in Figure 2.2a. The atomic orbitals of isolated C and O atoms are shown that have fully filled 2s orbitals and partially filled 2p orbitals. As these atoms approach each other, the electronic clouds of the *s* and *p* orbitals begin to overlap and form hybridized bonding (σ and π) and anti-bonding (σ^* and π^*) molecular orbitals. The bonding molecular orbitals have lower energy levels compared to corresponding atomic orbitals, and because based on Hund's rule these orbitals are filled before higher energy ones, the overall energy of the CO molecule is lower than isolated C and O atoms. In Figure 2.2b, these molecular orbitals (states) are shown in the form of density of states (DOS). DOS is the commonly used method in solid state physics to describe the number of states per interval of energy at each energy level.

The schematic in Figure 2.3 demonstrates that as the number of interacting atoms increases from a diatomic molecule to a linear chain, the number of resulting molecular orbitals increases, with smaller energy intervals between the orbitals. In a solid material with a large number of atoms and orbitals, the hybridized states are so close in energies that a continuous “band” of hybridized energy states is formed.

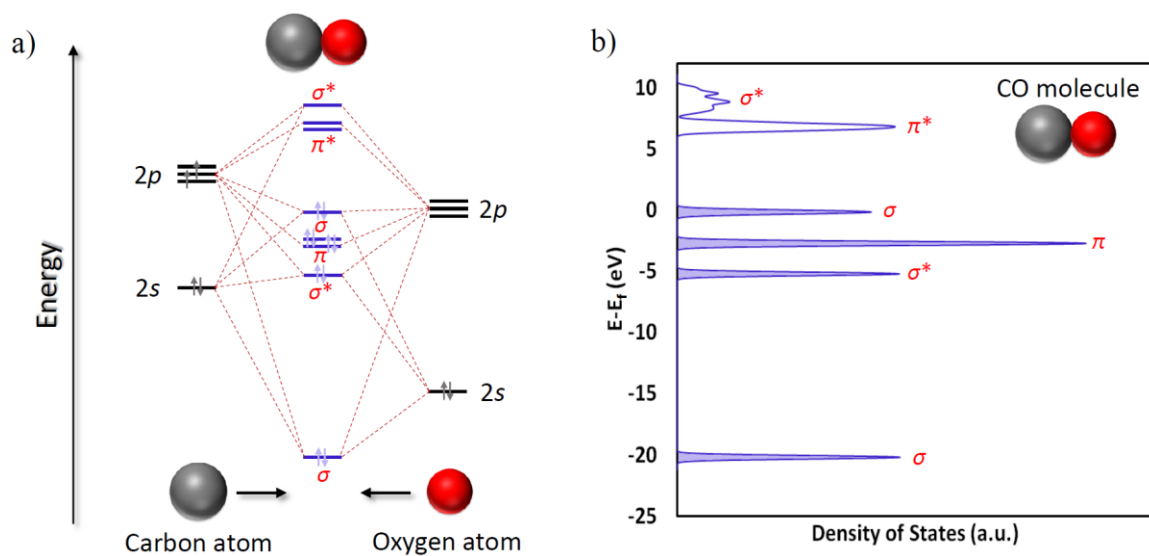


Figure 2.2. Electronic structure of a CO molecule illustrated based on **a)** molecular orbital theory **b)** Density of States

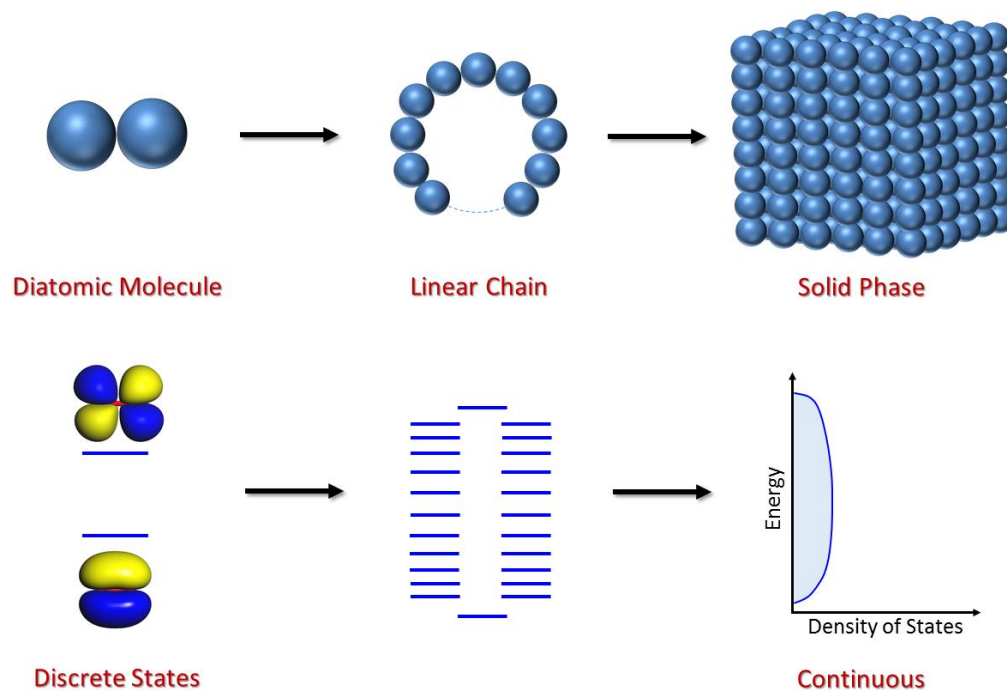


Figure 2.3. Schematic representation of band formation in metals, as a result of hybridization of a large number of molecular orbitals.

The electronic bands of transition metals consist of a broad, block-shaped sp -band and a localized d -band, because the overlap between highly localized atomic d states is small (Figure 2.4).³ The sp bands contribute to the free electron properties of metals and are very similar in features across the transition metals. The variation in properties of transition metals is associated with the extent of filling of d -bands.⁸

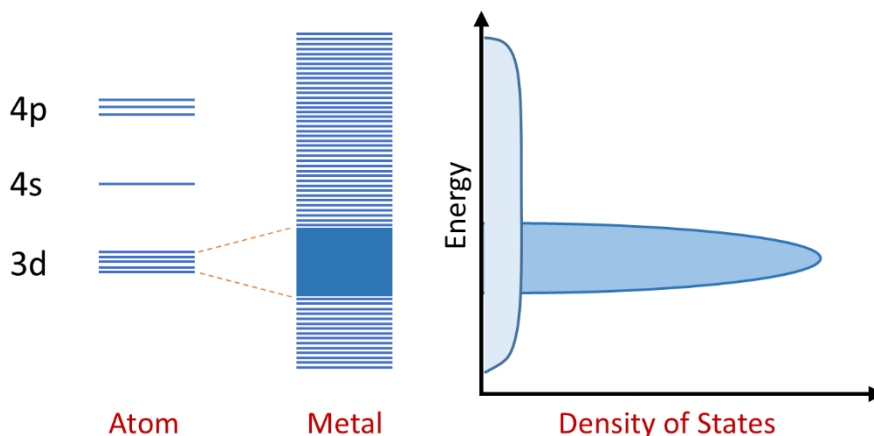


Figure 2.4. Schematic representation of the energy levels of a typical $3d$ transition metal. The extended s and p orbitals form a broad sp -band, whereas the highly localized d orbitals, form a narrow and dense d -band. Adapted with permission from ref. 3, copyright (2003) WILEY-VCH

The chemisorption of atoms and molecules on metallic surfaces is best described by the Newns-Anderson model.^{9,10} In this approach, the adsorption is modeled using only three parameters; (i) the energy-dependent DOS of the adsorbent $DOS(\epsilon)$, (ii) the discrete adsorbate state at an energy ϵ_a , and (iii) a coupling strength $|V|$.¹¹ In Figure 2.5a the schematic of an atomic adsorption on a transition metal surface is shown. As the atom approaches the surface, its discrete atomic orbital broadens and shifts down in energy through interaction with the metal sp -band. The broadened atomic state then interacts with the metal d -band. The interaction of the d -band, which can be considered as a broad orbital itself, with the adsorbate state lead to a pair of bonding and anti-bonding chemisorption

orbitals. A part of anti-bonding orbital that falls below the Fermi level is filled, which weakens the adsorbate-metal bond to some extent. Fermi level (ϵ_F), is the energy level of the highest occupied electronic states at 0 K.

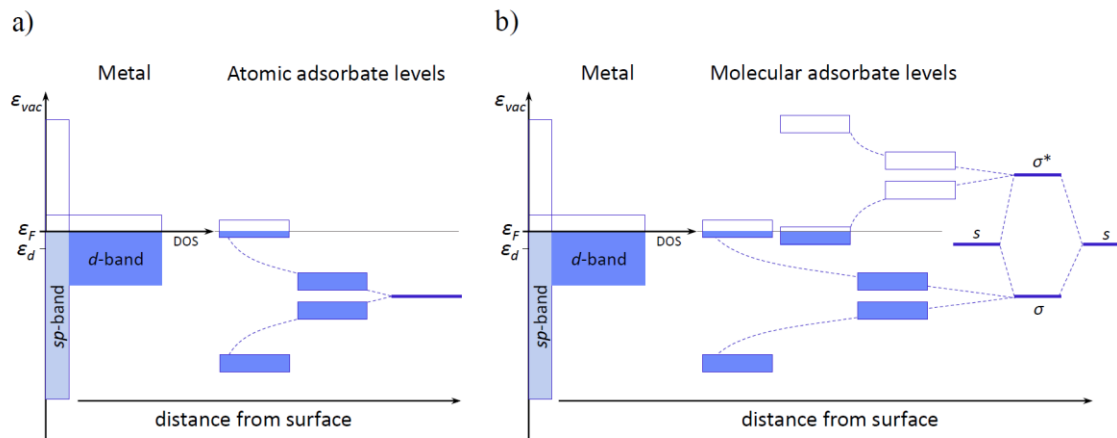


Figure 2.5. Schematic illustration of the interactions of **a)** atomic adsorbate states and **b)** molecular adsorbate states with transition metal sp and d -bands. Figure also shows the degree of filling of metal d -band impacts the chemisorption strength by partially filling adsorbate anti-bonding states. Adapted with permission from ref. 3, copyright (2003) WILEY-VCH

Same principles apply to the hybridized molecular orbitals when they interact with transition metal surface, as shown in Figure 2.5b for H_2 molecule. Both bonding and anti-bonding orbitals of the molecule interact with metal sp and d -bands, which results in fully filled bonding and partially filled anti-bonding metal-adsorbate hybridized orbitals. It is also possible that electrons fill the anti-bonding orbitals of the adsorbates. Such a filling, which is often called “back donation”, strengthens the adsorbate-surface bond but weakens the internal bonding of the molecule which may lead to dissociation of the molecular bond.

From this perspective of adsorbate-surface bond formation and with the knowledge that the variation in transition metals properties is associated with the d -band structure, it can be concluded that the extent of d -band and the filling are efficient descriptors for the surface

reactivity. Nørskov and Hammer have done extensive work on developing reactivity predictive models based on Newns-Anderson approximation and tight binding theories.^{8,11,12} Their *d*-band model uses three parameters to predict the reactivity of a transition metal surfaces: (i) the center of the *d*-bands (ϵ_d), (ii) the degree of filling (f_d) of the *d*-bands and (iii) the coupling matrix element V_{ad} between the adsorbate states and the metals *d*-states. The impact of two of these parameters are shown in Figure 2.6. In panel a, the impact of increasing coupling strength between adsorbate state and metal band is shown. The weak interaction causes the adsorbate orbital to broaden, which is characteristic of *sp*-bands. The resonance state continues to broaden with the increasing strength of the interaction to the point that splits to bonding and anti-bonding orbitals, which is characteristic of *d*-bands. In panel b, the center of *d*-band is continuously raised, as a result the anti-bonding orbital also moves up in energy and gets less occupied which means the adsorbate surface bonding are stronger. The *d*-band model has significantly contributed to our understanding of the surface interactions and has enabled us to explain surface reactivity trends on transition metals.

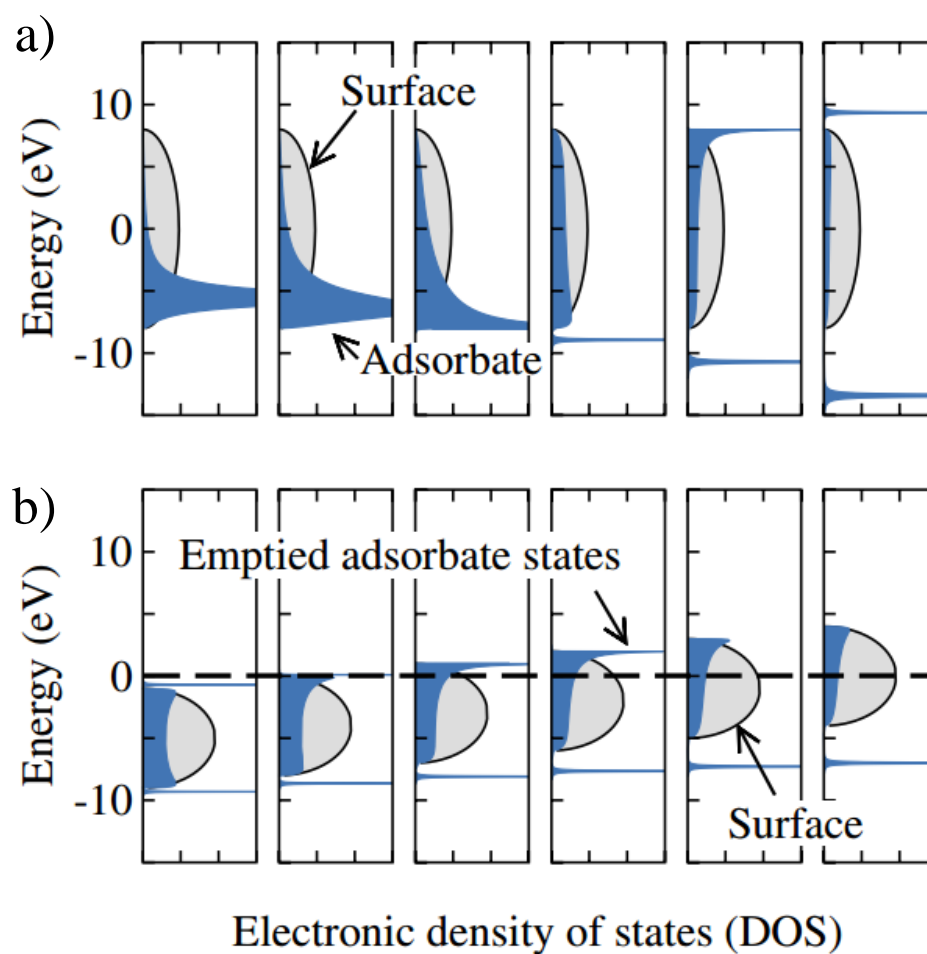


Figure 2.6. Interactions of adsorbate states with transition metal d -bands based on Newns-Anderson model with varying **a)** coupling strength **b)** d -band center. Adapted with permission from ref. 11, copyright (2006) Springer

2.3.2. BEP relations

As discussed in the previous sections, the binding energies of simple adsorbates are governed by electronic structure of the adsorbing site on catalyst surface. Same principles apply to the transition states of elementary chemical transformations on the same catalytic sites. Considering the similarity of transition state structures with either reactant or products, and the fact that the stability of different states of surface species are governed by the same underlying physics, it can be expected that there is correlation between energetics of various surface intermediates including transition states. In fact, linear relationships between activation barriers and reaction energies have been assumed to be valid for a long time. As introduced in Chapter 1 these correlations are called BEP relations after the Brønsted, Evans and Polanyi.^{4,13}

With the use of extensive DFT calculations, the BEP correlations were first proven to hold by Nørskov and coworkers in 2002, for dissociation reaction of a number of diatomic molecules (see Figure 2.7).¹⁴ In addition to validating the BEP relations, they also showed that these correlations are independent of the reactants and universal linear relations can be derived in the form of equations 2.21, with surface specific α , that hold for all the reactants.

$$E_a = \alpha \Delta E + \beta \quad (2.21)$$

In equation 2.21, E_a is the activation barrier and ΔE represents the dissociation reaction energy. These correlations have been shown to be reasonably accurate for the prediction of activation barriers of reactions, based on the adsorption energies of reaction intermediates. Extensive DFT calculations have since been used to develop many similar BEP

correlations for elementary steps and catalyst materials associated with the most common industrially-relevant reactions.^{15–17}

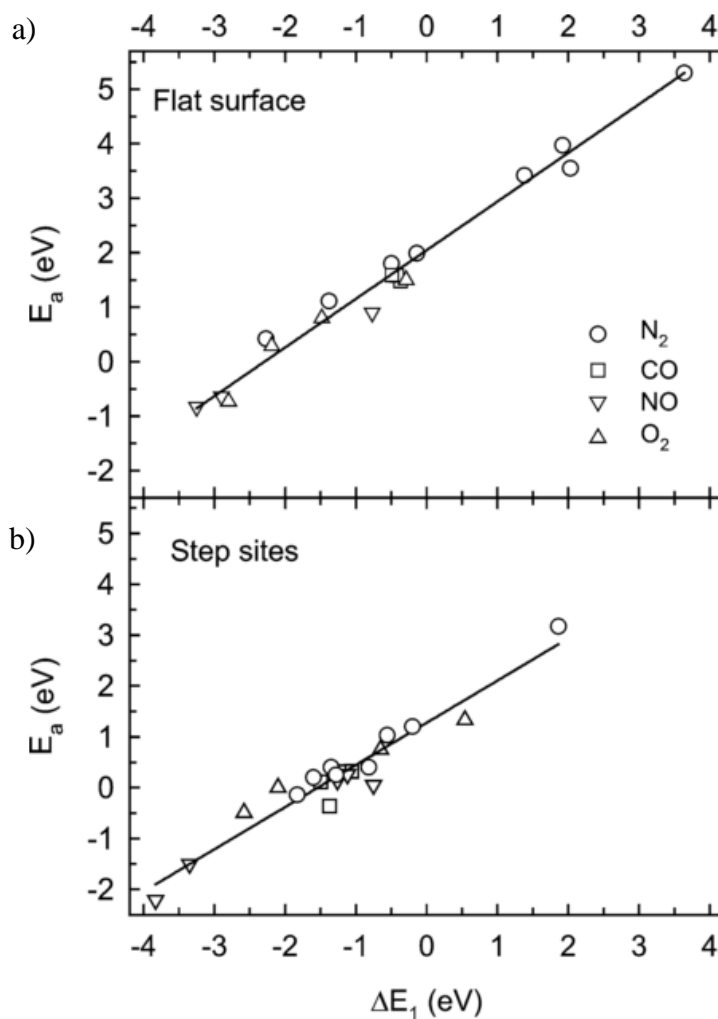


Figure 2.7. The universal linear BEP relation between activation energies (E_a) and dissociative adsorption energies (ΔE) of various diatomic molecules on a number of transition metals for **a)** flat surfaces and **b)** stepped surfaces. Reprinted from ref. 18, copyright (2004) with permission from Elsevier

2.3.3. Linear Scaling Relations

In the previous sections the importance of adsorption energy as a descriptor of surface-molecule interactions was discussed. It was also shown that the adsorption energies of reaction intermediates can be used in BEP relations to estimate the transition states energies. The adsorption energies can be measured with advanced surface science techniques.^{19,20} DFT methods also provide the possibility of calculating the energies. However, both these approaches to obtain the adsorption energies of molecules on the surfaces are feasible for only limited number of adsorbate-surface systems. Considering the importance of adsorption energies in the discovery of efficient catalytic materials, it is highly desirable to access predictive methods to facilitate calculations of the adsorption energies. Such a method was first initiated in 2007 by Nørskov and coworkers, which is commonly known as Linear Scaling Relations.²¹ They found that binding energies of hydrogen-containing adsorbates (OH_x , NH_x , CH_x and SH_x) on metal surfaces can be scaled approximately with the binding energy of the central, C, N, O, or S atom, and linear relationships can be derived in the form of equation 2.22, where γ is the scaling constant.

$$\Delta E^{AH_x} = \gamma \Delta E^A + \xi \quad (2.22)$$

The derived correlations for AH_x species (Figure 2.8) showed that the scaling factor γ only depends of value of x and independent of the species, since they are governed by the same underlying electronic structure. It was shown that γ can be approximated with a simple formulation, $(x_{\text{max}}-x)/x_{\text{max}}$, where x_{max} is the maximum number of H atoms that can stably bond to central atom A in the gas phase.

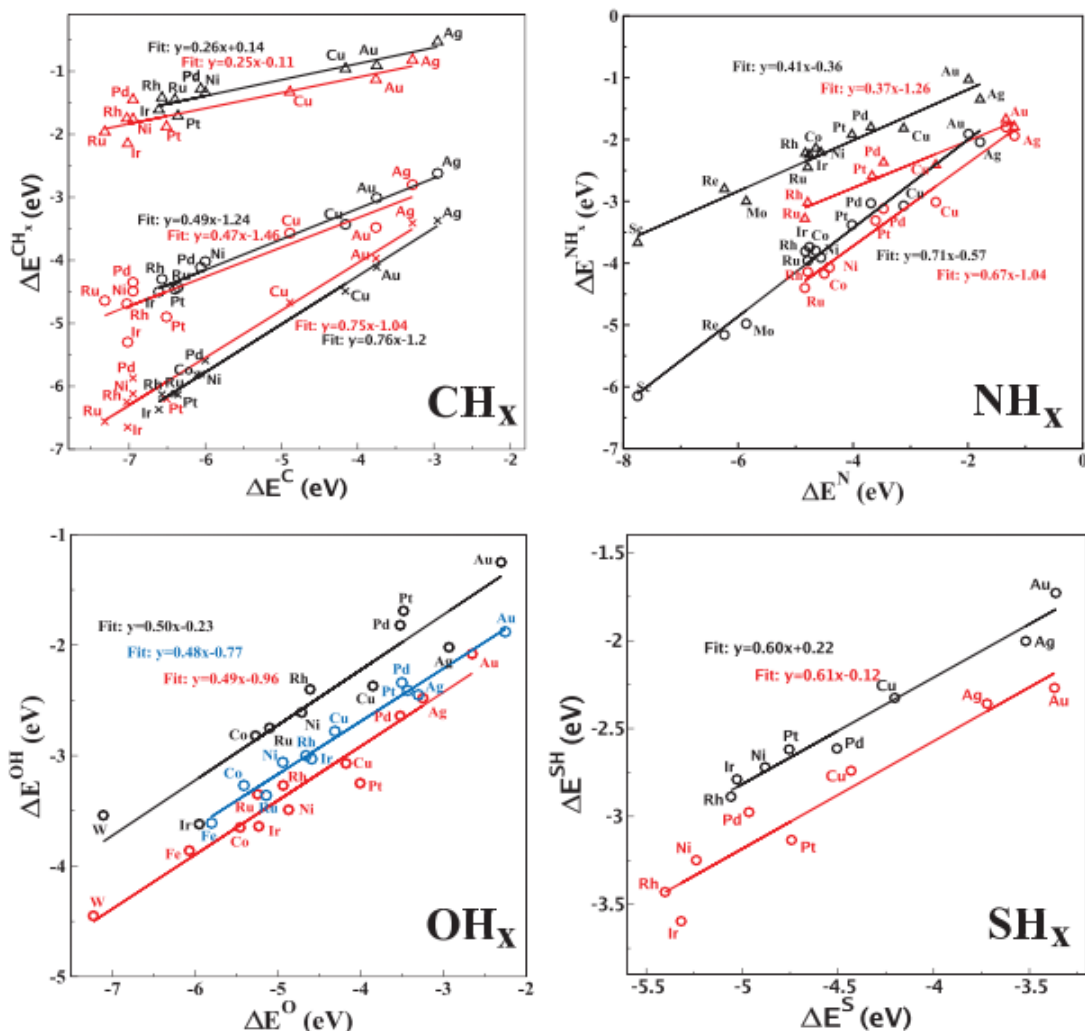


Figure 2.8. Scaling relations for CH_x , OH_x , NH_x , and SH_x on close-packed (black), stepped (red), and fcc(100) (blue) surfaces. Reprinted with permission from ref. 21, copyright (2007) American Physical Society

Similar relationships can be found for many other types of catalytic materials and adsorbates. The development of these correlations has significant impact in the field of catalysis, because they can be used to rapidly calculate the adsorption energies of many adsorbates based on a single adsorbate on a large number of catalyst surfaces. In addition, they provide fundamental insight into nature of chemical bonding and how molecular structure controls strength of adsorption and catalytic activity.²² In recent years significant

research has been dedicated to developing new scaling relations and refining the accuracy of the existing ones.^{22,23}

2.4. Fundamentals of heterogeneous photocatalysis

In the quantum-mechanical description of heterogeneous catalytic processes, reactions are driven by phonons (collective vibration of the metal lattice). Reactants adsorbed on a metal surface vibrate around their equilibrium bond distance on the ground state potential energy surface (PES). This is shown schematically in Figure 2.9a for a diatomic molecule where the internal bond of the molecule is assumed to be the reaction coordinate. When the vibrational degree of freedom (reaction coordinate) of the adsorbate couples with the surface phonon modes, the adsorbate gains vibrational energy and is driven across the ground state PES reaching higher vibrational modes.²⁴ If the vibrational energy gained by the adsorbate is sufficient to overcome the activation barrier, then the bond along the reaction coordinate breaks and reaction happens. Increasing the system temperature populates higher energy vibrational states along the ground state PES and thereby increases the reaction probability.

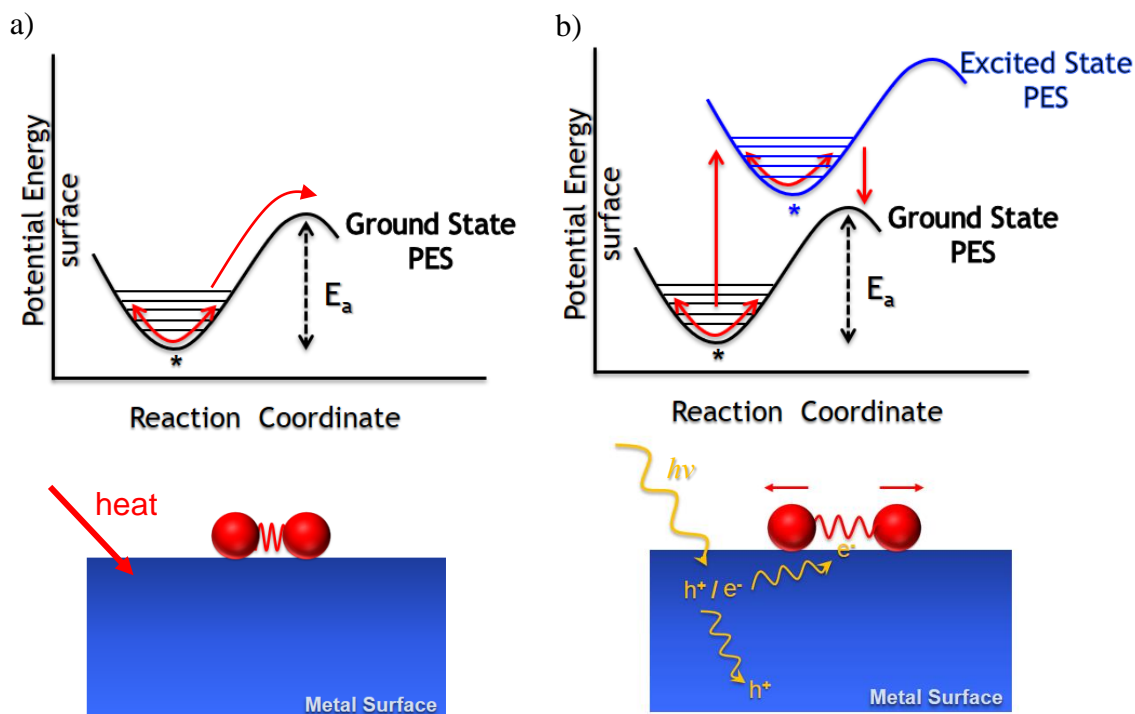


Figure 2.9. Schematic representation of mechanisms associated with **a)** thermally driven and **b)** photon-induced chemical reactions on metal catalyst surfaces

A photocatalytic reaction involves the same elementary steps as the thermally driven reaction, but in these reactions one or more of the elementary steps can proceed by coupling with photo-induced energetic electrons or holes. Multiple mechanisms have been explored to describe photon mediated, electron-driven chemistry on metal surfaces, including direct intramolecular photo-excitation of adsorbates, direct photo-excitation of adsorbate-metal bonds and substrate-mediated photo-excitation of adsorbates or adsorbate-metal bonds which is the focus of this study.^{25–28} In a substrate-mediated photocatalytic process, photons from a light source are absorbed by the metal photocatalyst which generates energetic electron-hole pairs in the metal bulk (Figure 2.9b). The energetic electron/hole pairs scatter through collisions with other charge carriers in the bulk of the catalyst

material. If the energetic charge carriers (electrons and holes) migrate to the metal surface, and are energetically aligned with the energy level of the adsorbate states, they can couple with the vibrational degree of freedom of the adsorbate and deposit vibrational energy into the bond, which can lead to dissociation of the bond and chemical conversion.

The vibrational energy transition from energetic charge carriers into adsorbate nuclear motion occurs via Franck-Condon transitions. According to the Franck-Condon principle molecular geometry or nuclear motions don't change during photon adsorption, since the frequency of the light inducing the electronic transition (10^{15} - 10^{16} Hz) is much larger than the frequency of molecular vibrations (10^2 - 10^{13} Hz).²⁷ Therefore, the excited state PES resulting from this energy transition (Figure 2.9b) is only vertically elevated to a higher energy level retaining its original shape. The resulting excited state adsorbate evolves on the elevated, repulsive PES for a short lifetime (~ 1 fs) and experiences acceleration towards the minimum of the excited state PES at a lengthened equilibrium bond distance, compared to the ground state PES minimum. The system returns to the ground state PES in a vibrationally excited state as the electron quenches back to the metal substrate. If the energy deposited from the electron into the PES plus the original vibrational energy of the system on the ground state PES is greater than the activation energy (E_a), the electron scattering process can induce bond breaking and surface reactions.

2.5. Density Functional Theory

DFT is utilized throughout this dissertation to calculate energies and vibrational frequencies of surfaces and molecular species involved in catalytic reactions. Detailed information on the adsorption energies, binding geometries, vibrational frequencies of

adsorbates on the surfaces, stability of various surface structures, transition state geometries and activation energies associated with elementary steps are obtained with DFT methods. The information gained through these calculations are used to map out entire mechanisms of catalytic reaction, predict steps that may control the overall reaction rate and selectivity (Chapters 3 and 4). Through these methods it is feasible to calculate energies of a collection of hundreds of atoms with high level of accuracy. The accuracy of the calculated energies is in the range of a few tenths of eV, which makes these methods particularly useful for investigating surface reactivity trends. In addition, by applying periodic boundary conditions, energies of extended surfaces can be calculated which are an excellent representation of real catalyst surfaces. In this section the fundamentals of DFT calculations are reviewed and the DFT methods that are used in this study are introduced.

2.5.1. Fundamental Principles

The density functional formalism was developed by Hohenberg, Kohn, and Sham in 1960s,^{29,30} but the major breakthrough in the applications of DFT in chemistry and material science came about in 1990s when the parallel computing resources became available. The Hohenberg-Kohn theorem demonstrates that the ground state properties of many-body system can be completely determined by the electron density of the system. Hence, by reducing the N-electron many-body problem of 3N dimensions to a 3-dimensional problem, it considerably reduces the computational efforts to calculate material properties. DFT has now become an indispensable part of research in the physics, chemistry and material sciences.

The main problem in determination of the electronic structures of material is to solve the Schrödinger's equation, $\hat{H}\Psi = E\Psi$, for the system of many electrons in the presence of nuclei. The solution to this problem is the wavefunction, Ψ , which contains all information about the system including the probability distribution of all the particles and energy associated with the particle configuration. The Hamiltonian for this many-body problem can be represented as:

$$\hat{H} = -\frac{\hbar^2}{2m} \sum_i \nabla_i^2 - \sum_{i,I} \frac{Z_I e^2}{|r_i - R_I|} + \frac{1}{2} \sum_{i,j} \frac{e^2}{|r_i - r_j|} - \frac{\hbar^2}{2M} \sum_I \nabla_I^2 + \frac{1}{2} \sum_{I,J} \frac{Z_I Z_J e^2}{|R_I - R_J|} \quad (2.23)$$

In equation 2.23, the first three terms represent the kinetic energy of the electrons, the interactions of electrons with nuclei and with other electrons respectively. The last two terms are the kinetic energy of nuclei and the interactions of nuclei with each other. According to Born-Oppenheimer approximation, the nuclei can be assumed fixed in the space in comparison to the fast movements of electrons, therefore the kinetic term of the nuclei can be neglected from the Hamiltonian and the nuclei repulsion energy can be approximated with a constant value.³¹ Even with this simplification, solving the Schrödinger equation still is a difficult task since many-body wavefunction relies on all the spatial coordination of the particles ($3N$, where N is the number of particles in the system). A significant breakthrough in the approaches for solving these many-body problems was the development of DFT formalism.

In 1964, Hohenberg and Kohn showed that the ground state total energy, E_0 , of a system of interacting electrons is a unique functional of the electron density in its ground state n_0 ,

$E_0[\rho(\mathbf{r})]=E[n_0(\mathbf{r})]$, and there exists a ground state electron density that minimizes the system energy.²⁹ Based on this theorem the N-electron many-body problem of 3N dimensions, $\psi(\mathbf{r}_1, \mathbf{r}_2, \dots, \mathbf{r}_N)$, reduces to a 3-dimensional problem $\psi(n(\mathbf{r}))$. The energy of such a system can be written in the following form:

$$E(n) = T(n) + \iint \frac{n(r)n(r')}{|r-r'|} dr dr' + \int n(r)v_{ext}(r)dr \quad (2.24)$$

In equation 2.24, $T(n)$ is the kinetic energy of the interacting electrons, the second term is the electron-electron interaction and the last term represents the external potential due to the positively charged nuclei given by:

$$v_{ext} = \sum_I \frac{-Z_I}{|R_I - r|} \quad (2.25)$$

The application of the formalism was not feasible by itself, because there was no accurate density functional for the kinetic term $T(n)$. It only became practical when in 1965, Kohn and Sham showed that the problem of many interacting electrons in an external potential can be mapped exactly to a set of non-interacting electrons in an effective external potential that has the same electron density as the real system.³⁰ The energy of such a system is given by:

$$E(n) = T_s(n) + \iint \frac{n(r)n(r')}{|r-r'|} dr dr' + \int n(r)v_{ext}(r)dr + E_{xc}(n) \quad (2.26)$$

where $T_s(n)$ is the kinetic energy of the non-interacting electrons and $E_{xc}(n)$, is the exchange and correlation energy. This led to a set of self-consistent, single particle Schrödinger-like equations known as Kohn-Sham (KS) equations:

$$\left(-\frac{\hbar^2}{2m} \nabla^2 + v_{eff}(\mathbf{r}) \right) \phi_i = \varepsilon_i \phi_i \quad (2.27)$$

where $v_{eff}(\mathbf{r})$ is given by:

$$v_{eff}(\mathbf{r}) = v(\mathbf{r}) + \int \frac{n(\mathbf{r}')}{|\mathbf{r} - \mathbf{r}'|} d\mathbf{r}' + v_{xc}(\mathbf{r}) \quad (2.28)$$

In equation 2.27, ϕ_i is the KS non-interacting particle orbital with energy ε_i , $v(\mathbf{r})$ is the external potential and $v_{xc}(\mathbf{r}) = \delta E_{xc} / \delta n$, is the exchange-correlation potential which includes all the energy contributions that are not accounted for by the Hamiltonian. The exchange-correlation potential depends on the entire density function, therefore the density $n(\mathbf{r})$ needs to be known to be able to solve equation 2.27. The ground state density, $n(\mathbf{r})$, is given by:

$$n(\mathbf{r}) = \sum_i |\phi_i(\mathbf{r})|^2 \quad (2.29)$$

These three equations 2.27-2.29 are then solved iteratively until self-consistency of electron density and energy is achieved, as shown schematically in Figure 2.10. Then ground state energy can be calculate using equation 2.26, provided that exchange-correlation energy, $E_{xc}(n)$, is known. However, the exact form of $E_{xc}(n)$ is not known and approximations are used. The quantitative success of DFT calculations depends on the accuracy of the exchange correlation functional used.

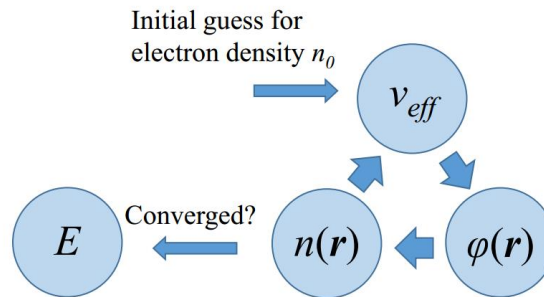


Figure 2.10. Schematic illustration of Kohn-Sham implementation of DFT

The two main types of exchange correlations that are used in DFT are local density approximation (LDA) and generalized gradient approximation (GGA). In LDA, which is the simplest approximation, it is assumed that charge density changes slowly and each small volume looks like a uniform electron gas of density.³⁰ Thus, the exchange-correlation potential can be calculated based on the exchange correlation energy per electron ($\epsilon_{xc}(n)$) of the uniform gas with density n as follows:

$$v_{xc}(n) = \int n(r) \epsilon_{xc}(n) dr \quad (2.30)$$

GGA approximations are developed to make corrections to the uniform electron density approximation of LDA, since in many actual problems, such as molecules in space and solids the electron density variations in space can be significant. In this approach ϵ_{xc} in addition to the electron density also depends on the gradient of the electron density in space, as shown in equation 2.31.

$$v_{xc}(n) = \int n(r) \epsilon_{xc}(n, \nabla n) dr \quad (2.31)$$

A number of different GGA methods have been developed, such as Perdew-Burke-Ernzerhof (PBE), revised PBE (RPBE) and revPBE, based on different forms of the applied corrective function.^{32,33} In this work, RPBE GGA exchange correlation functional is used, which has proven to generate accurate account of adsorption energies for atoms and molecules to surfaces.

2.5.2. Geometry optimization calculations

DFT calculations were carried out with the real space grid-based projector-augmented wave method (GPAW) code.³⁴ The Revised Perdew–Burke–Ernzerhof (RPBE) form of the generalized gradient approximation (GGA) was used to approximate exchange and

correlation effects.³³ The BEEF-vdW functional was also investigated for geometry optimization of larger adsorbed molecules in Chapter 3.³⁵ Transition metal catalyst surfaces were modeled by periodic semi-infinite slabs, by applying periodic boundary conditions in x and y directions and 15-20 Å of vacuum between consecutive metal slabs in z direction. A grid space of $h=0.2$ was used. Monkhorst–Pack method was used to sample k -points in Brillouin zone. All geometry configurations were allowed to relax using a quasi-Newton algorithm until the forces on all atoms converged to less than 0.1 eV/Å. In all calculations convergence was assured with respect to k -points, vacuum spacing between periodic slabs and the number of surface relaxed layers. For surface energy calculations the energies were also converged with respect to the thickness of the slabs (see details in Chapter 6).

2.5.3. *Climbing Image Nudged Elastic Band (CI-NEB) calculations*

The transition state configurations and activation barriers of the elementary surface reaction were found using the CI-NEB method,³⁶ which is a modified version of Nudged Elastic Band (NEB) method. In NEB method the minimum energy pathway (MEP) between an initial state (Reactant) and a final state (Product) of a chemical reaction is mapped out by first constructing a chain of images of the system as shown in Figure 2.11. This is typically done with a linear interpolation between initial and final states. The continuity of the chain is assured by adding a spring interaction between adjacent images which causes the chain to behave like an elastic band. Then the optimization of the band is performed by minimizing the force acting on the images, which brings the band to the MEP on the PES. In the CI-NEB method a feature is added to NEB to identify the highest energy image on the band (which is not necessary at the top of the MEP), and moves the image up

the PES along the elastic band and down the PES perpendicular to the band. By approaching the maxima of MEP, the closest geometry for transition state is identified.

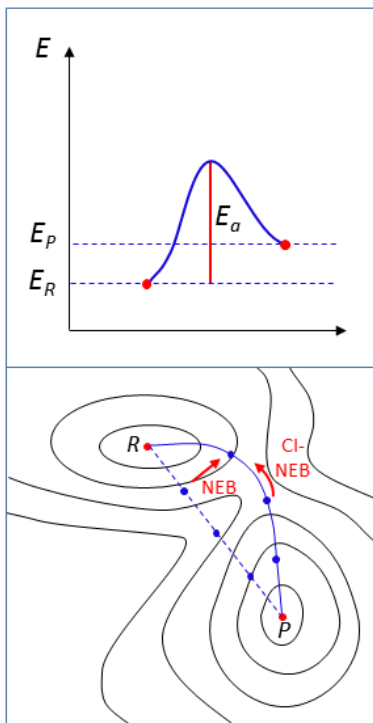


Figure 2.11. Schematic of CI-NEB method to find minimum energy pathway on PES.

2.5.4. Vibrational frequencies and thermodynamic parameters

Vibrational frequencies (ω_i) were calculated for gas phase, adsorbed species and transition states, using a finite-difference approximation of the Hessian matrix as implemented in Atomic Simulation Environment (ASE), a Python package used by GPAW to describe molecular configurations and run atomic simulations.⁶ The surface atoms were held fixed during the vibrational analysis of surfaces species. The thermochemical properties of reaction intermediates can be calculated using DFT derived vibrational

frequencies, as explained in section 2.2.2, using ideal-gas approximation for gas phase molecules and harmonic approximation for surface species.

The DFT calculated electronic energies need to be converted to thermodynamic quantities at operating conditions (T, P) of the catalytic reaction. First electronic energies are converted to ground state energy of the vibrating molecules/adsorbates at $T=0$ K and vacuum, by applying the zero-point-energy ($E_{ZPE}=0.5\sum\hbar\omega_i$) correction. Then T and P corrections are applied to calculate $H(T)$ and $S(T, P)$ of gas phase molecules, and $U(T)$ of adsorbed species using the following equations and the procedures described in 2.2.2:

$$H(T) = E_{elec} + E_{ZPE} + \int_0^T C_p dT \quad (2.32)$$

$$S(T, P) = S_{trans} + S_{rot} + S_{vib} - k_B \ln \frac{P}{P^0} \quad (2.33)$$

$$U(T) = E_{elec} + E_{ZPE} + \sum_i^{\text{harm DoF}} \frac{\epsilon_i}{e^{\epsilon_i/k_B T} - 1} \quad (2.34)$$

2.5.5. Linear-expansion delta self-consistent field (lr Δ SCF-DFT) method

lr- Δ SCF-DFT is a method implemented in GPAW that can be used to obtain the excited state potential energy surfaces.^{34,37} In the lr- Δ SCF approach the total energy of the system for the excited state is calculated by placing an electron from Fermi level in a targeted unoccupied molecular state, which is defined by a linear combination of empty Kohn Sham orbitals obtained in each SCF cycle. The density of the specified orbital is added to the total density in each step, and the electron density and energy of the system are calculated self-consistently. The computational cost of Δ SCF methods is comparable to ground state DFT calculation, which provides an advantage compared to other computationally more

expensive methods for excited state PES calculations, such as Time-dependent DFT, GW approximation and cluster configuration.³⁸ Furthermore, the Ir- Δ SCF method is designed for calculations with strongly hybridized orbitals such as molecules chemisorbed on transition metals, as are the studied cases in Chapter 5, and has been shown to produce results which are in reasonable agreement with inverse photoemission experimental measurement.³⁷

2.6. Mean-field Microkinetic Modeling

In Chapters 3 and 4, Mean-Field microkinetic modeling is used to investigate the mechanism of CO₂ reduction by H₂ on Ru(0001) surface and other late transition metal catalysts. The kinetic parameters used in the model were calculated with DFT methods as described in sections 2.4 and in detail the methods section of Chapter 3. In Chapter 4, previously developed linear scaling and BEP relations were incorporated into the microkinetic model to calculate the kinetic parameters for late transition metals.¹⁷ Here the framework of the microkinetic analysis is discussed and the computational method used to solve the model is introduced.

2.6.1. Fundamentals of mean-field microkinetic modeling

Controlling catalytic reactions at the molecular level depends critically on our understanding of the mechanism of reaction in terms of elementary surface reactions and our ability to determine kinetic parameters for each individual step. In the Microkinetic modelling the kinetics of the overall catalytic reaction is studied using the detailed mechanism and kinetics of individual elementary steps. The approach is used to predict activity and selectivity of complex catalytic reactions as a function of reaction operating

conditions. The approach was pioneered by Stoltze and Nørskov in 1985,³⁹ and its framework was further established in a book by Dumesic and Rudd in 1993.⁴⁰ The microkinetic models have become more relevant in recent years as the determination of kinetic and thermodynamic parameters are hugely facilitated by the advents of computational chemistry methods and development of predictive theories, as described in the previous sections. These models have been proven successful in describing reaction kinetics semi-quantitatively and have been repeatedly used in computational screening of catalyst materials.^{41–45}

The formalism used in mean-field microkinetic analysis, is developed based on the following reasonable assumptions: (i) Catalyst surfaces are modeled as a collection of adsorption sites which are all identical and the number of sites are constant under reaction conditions (ii) surface reactions follow Langmuir-Hinshelwood mechanism; reactants first adsorb on the surface, then adsorbed species on neighboring sites undergo surface reactions (iii) each reaction intermediate covers one site and no interactions exist between the intermediates (iv) elementary reactions are microscopically reversible.⁴⁶ Once the kinetic parameters are determined based on DFT calculations, the reaction rate expression for each of the individual elementary steps is written in the form of a first order reaction, using Arrhenius rate constants, as shown with an example in the schematic in Figure 2.12. The concentrations of surface species are specified by surface coverage θ (fraction of surface sites covered by a given species). A mass (/site) balance equation can be derived for each reaction intermediate based on the rate expressions of elementary steps. In Figure 2.12 an

example of balance equation is shown for adsorbed CO* in a mechanism where CO* is produced in steps 3 and 5 and consumed in steps 6, 7 and 18.

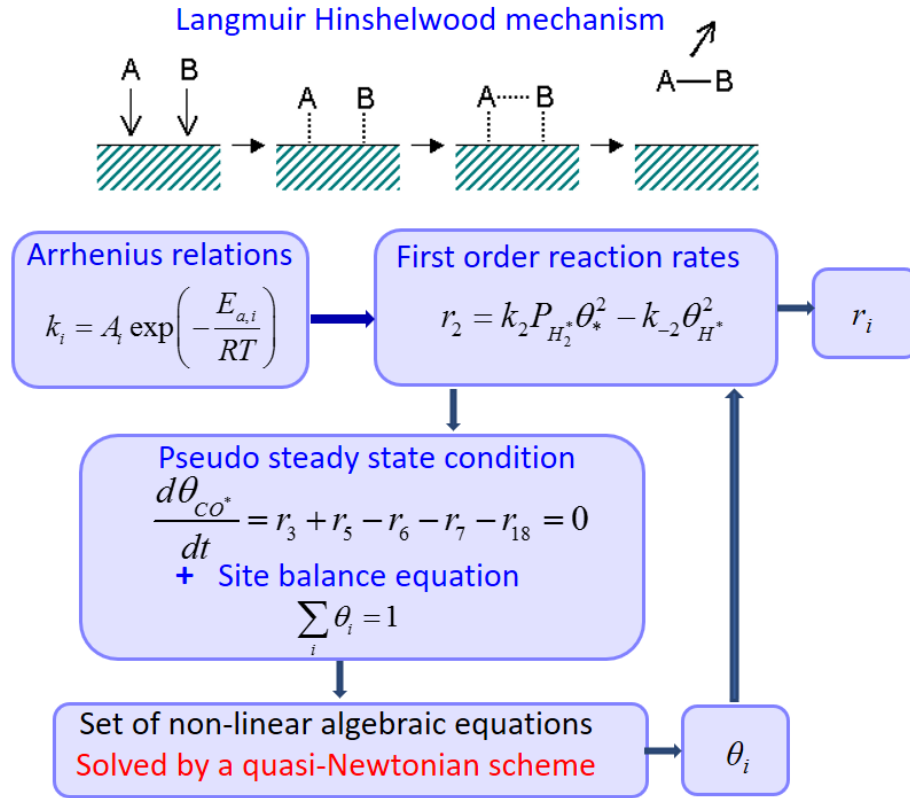


Figure 2.12. Schematic of mean-field microkinetic model implementation for catalytic reactions

An important advantage of microkinetic modeling is that it can provide realistic reaction rate and selectivity for complex catalytic reactions involving networks of elementary steps, with no *a priori* assumptions about the rate-limiting step. The reaction system can be considered under pseudo steady-state approximation, where the concentrations of the surface species are constant with respect to time. This approximation describes a snapshot picture of the system at any given moment with known concentration of reactants and operating conditions, which is a realistic depiction of a differential reactor

where initial reactant concentrations remain nearly unchanged in the small time and length scale of the reactor.

By applying the pseudo steady-state approximation, the mass balance equations of surface species result in a set of non-linear algebraic equations consisting of rate constants of the elementary steps (k) and the concentrations of adsorbed intermediates (θ) involved in the mechanism. An additional balance to complete the set of non-linear algebraic equations is the normalized overall site balance ($\sum \theta_i = 1$). The set of non-linear algebraic equations can be solved simultaneously, using numerical methods described below, to find the concentrations of all the involved surface species and the reaction rates of individual elementary reactions at the given operating conditions (pressure, temperature and reactant concentrations).

Another advantage provided by the microkinetic modeling is the possibility of predicting reaction kinetics over a large range of operating conditions, unlike the conventional analytical approaches where power law expressions are regressed to a specific range of experimental conditions.⁴⁷ These models can be used to find the concentration of all surface species, identify the most abundant surface intermediates and calculate reaction rates and selectivity with respect to any given product at a large range of operating conditions. Also, sensitivity analysis can be conducted using microkinetic models to identify the elementary steps that have the greatest impact on the overall reaction rates or selectivity, which helps identifying the rate limiting and selectivity determining steps (See chapters 3 and 4).

2.6.2. Computational method

A system of non-linear algebraic equation is typically solved using the trust-region methods and ordinary differential equation (ODE) solvers designed to solve differential algebraic equations (DAE).⁴⁸ Finding the solution for the system of mass balance equations associated with the microkinetic models is particularly difficult because the convergence to the solution is highly dependent on the initial guess of the adsorbate concentrations. A large number of iterations are required with varying convergence criteria to assure the convergence of often unstable systems to “the solution” with reasonable accuracy. Considering the large number of intermediates involved in the complex catalytic reactions, the computational cost of these numerical methods can be significant.

In this study an in-house numerical method was used which exhibited excellent robustness and efficiency with minimal dependence on initial conditions. In this method a general approach was introduced to define the microkinetic system only based on its stoichiometric matrix and kinetic parameters of elementary steps. The method is based on linearization of mass balance equations and uses a quasi-Newtonian approach to solve the linearized system.⁴⁹ The code was originally developed by Gabriel S. Gusmão in MATLAB,⁴⁹ the PYTHON version with refined convergence algorithms is now available via <https://github.com/gusmaogabriels/mkin4py>.

2.7. Wulff construction

The Wulff construction is a theoretical method proposed by George Wulff in 1901 to predict the shape of a crystalline structure at thermodynamic equilibrium.⁵⁰ The method is based on the concept of “equilibrium shape” proposed by J. W. Gibbs in 1878.⁵¹ According

to Gibb's theory a given quantity of matter will assume a shape that minimizes the total surface free energy of the system.⁵² The equilibrium shape of metal particles is typically a polyhedron enclosed mainly by lowest surface energy crystal orientations (hkl) which result in the minimum total surface energy as described in equation 2.35.

$$\gamma = \sum_{hkl} A_{hkl} \gamma_{hkl} \quad (2.35)$$

In equation 2.35 γ is total surface energy, A_{hkl} is the exposed surface area of the (hkl) crystal facet and γ_{hkl} is the surface free energy of the (hkl) crystal facet (the energy required to create a unit area of (hkl) facet).

Based on Gibb's theory, Wulff proposed that in the equilibrium shape that minimizes equation (2.35), the distance of each (hkl) facet from the center of the particle is proportional to the surface energy of the respective facet ($d_{hkl} \sim \gamma_{hkl}$). The Wulff constructions are built by drawing an (hkl) plane, for example the lowest surface energy facet (111), at distance d_{111} from origin. The other (hkl) facets are then drawn at distances $d_{hkl} = d_{111} \gamma_{hkl} / \gamma_{111}$ from origin. The polyhedron enclosed by these planes is the equilibrium shape.

2.8. References

1. Lindemann, F. A. *et al.* Discussion on ‘the radiation theory of chemical action’. *Trans. Faraday Soc.* **17**, 598–606 (1922).
2. Eyring, H. The Activated Complex in Chemical Reactions. *J. Chem. Phys.* **3**, 107–115 (1935).
3. Chorkendorff, I. & Niemantsverdriet, J. W. *Concepts of Modern Catalysis and Kinetics*. (WILEY-VCH, 2003).
4. Evans, M. G. & Polanyi, M. Further Considerations on the thermodynamics of chemical equilibria and reaction rates. *J. Chem. Soc., Faraday Trans. 1* **32**, 1333–1359 (1936).
5. Cramer, C. J. *Essentials of Computational Chemistry: Theories and Models Second Edition*. (John Wiley & Sons, Ltd, 2004).
6. Bahn, S. R. & Jacobsen, K. W. An object-oriented scripting interface to a legacy electronic structure code. *Comput. Sci. Eng.* **4**, 56–66 (2002).
7. Sabatier, P. Hydrogenations et deshydrogenations par catalyse. *Berichte der Dtsch. Chem. Gesellschaft* **44**, 1984–2001 (1911).
8. Hammer, B. & Nørskov, J. K. in *Chemisorption and Reactivity on Supported Clusters and Thin Films* (eds. Lambert, R. M. & Pacchioni, G.) 285–351 (Kluwer Academic Publishers, 1997).
9. Newns, D. M. Self-Consistent Model of Hydrogen Chemisorption. *Phys. Rev.* **178**, 1123–1135 (1969).
10. Anderson, P. W. Localized Magnetic States in Metals. *Phys. Rev.* **124**, 41–53 (1961).
11. Hammer, B. Special sites at noble and late transition metal catalysts. *Top. Catal.* **37**, 3–16 (2006).
12. Hammer, B. & Nørskov, J. K. Theoretical Surface Science and Catalysis — Calculations and Concepts. *Adv. Catal.* **45**, (2000).
13. Brønsted, J. N. Acid and Basic Catalysis. *Chem. Rev.* **5**, 231–338 (1928).
14. Nørskov, J. K. *et al.* Universality in Heterogeneous Catalysis. *J. Catal.* **209**, 275–278 (2002).
15. Wang, S. *et al.* Universal transition state scaling relations for (de)hydrogenation over transition metals. *Phys. Chem. Chem. Phys.* **13**, 20760 (2011).
16. Lausche, A. C., Falsig, H., Jensen, A. D. & Studt, F. Trends in the Hydrodeoxygenation Activity and Selectivity of Transition Metal Surfaces. *Catal.*

Letters **144**, 1968–1972 (2014).

17. Medford, A. J. *et al.* Activity and Selectivity Trends in Synthesis Gas Conversion to Higher Alcohols. *Top. Catal.* **57**, 135–142 (2014).
18. Bligaard, T. *et al.* The Brønsted-Evans-Polanyi relation and the volcano curve in heterogeneous catalysis. *J. Catal.* **224**, 206–217 (2004).
19. Brown, W. A., Kose, R. & King, D. A. Femtomole Adsorption Calorimetry on Single-Crystal Surfaces. *Chem. Rev.* **98**, 797–832 (1998).
20. Gross, H., Campbell, C. T. & King, D. A. Metal–carbon bond energies for adsorbed hydrocarbons from calorimetric data. *Surf. Sci.* **572**, 179–190 (2004).
21. Abild-Pedersen, F. *et al.* Scaling Properties of Adsorption Energies for Hydrogen-Containing Molecules on Transition-Metal Surfaces. *Phys. Rev. Lett.* **99**, 16105 (2007).
22. Montemore, M. M. & Medlin, J. W. Scaling relations between adsorption energies for computational screening and design of catalysts. *Catal. Sci. Technol.* **4**, 3748–3761 (2014).
23. Fernandez, E. M. *et al.* Scaling relationships for adsorption energies on transition metal oxide, sulfide, and nitride surfaces. *Angew. Chemie - Int. Ed.* **47**, 4683–4686 (2008).
24. Bonn, M. *et al.* Phonon-Versus Electron-Mediated Desorption and Oxidation of CO on Ru(0001). *Science* **285**, 1042–1045 (1999).
25. Kale, M. J., Avanesian, T., Xin, H., Yan, J. & Christopher, P. Controlling catalytic selectivity on metal nanoparticles by direct photoexcitation of adsorbate-metal bonds. *Nano Lett.* **14**, 5405–5412 (2014).
26. Watanabe, K., Sawabe, K. & Matsumoto, Y. Adsorbate-localized excitation in surface photochemistry: Methane on Pt(111). *Phys. Rev. Lett.* **76**, 1751–1754 (1996).
27. Zhou, X.-L., Zhu, X.-Y. & White, J. M. Photochemistry at adsorbate/metal interfaces. *Surf. Sci. Rep.* **13**, 73–220 (1991).
28. Petek, H. Photoexcitation of adsorbates on metal surfaces: one-step or three-step. *J. Chem. Phys.* **137**, 091704 1-11 (2012).
29. Hohenberg, P. & Kohn, W. Inhomogeneous Electron Gas. *Phys. Rev.* **136**, B 864–871 (1964).
30. Kohn, W. & Sham, L. J. Self-Consistent Equation Including Exchange and Correlation Effects. *Phys. Rev.* **140**, A 1133–1138 (1965).
31. Born, M. & Oppenheimer, R. Zur Quantentheorie der Molekeln. *Ann. Phys.* **389**,

457–484 (1927).

32. Perdew, J. P., Burke, K. & Ernzerhof, M. Generalized Gradient Approximation Made Simple. *Phys. Rev. Lett.* **77**, 3865–3868 (1996).
33. Hammer, B., Hansen, L. B. & Nørskov, J. K. Improved adsorption energetics within density-functional theory using revised Perdew-Burke-Ernzerhof functionals. *Phys. Rev. B* **59**, 7413–7421 (1999).
34. Enkovaara, J. *et al.* Electronic structure calculations with GPAW: a real-space implementation of the projector augmented-wave method. *J. Phys. Condens. Matter* **22**, 253202 (2010).
35. Wellendorff, J. *et al.* Density functionals for surface science: Exchange-correlation model development with Bayesian error estimation. *Phys. Rev. B* **85**, 235149 (2012).
36. Henkelman, G., Uberuaga, B. P. & Jónsson, H. A climbing image nudged elastic band method for finding saddle points and minimum energy paths. *J. Chem. Phys.* **113**, 9901–9904 (2000).
37. Gavnholt, J., Olsen, T., Englund, M. & Schiøtz, J. Δ Self-Consistent Field Method To Obtain Potential Energy Surfaces of Excited Molecules on Surfaces. *Phys. Rev. B* **78**, 75441 (2008).
38. González, L., Escudero, D. & Serrano-Andrés, L. Progress and challenges in the calculation of electronic excited states. *ChemPhysChem* **13**, 28–51 (2012).
39. Stoltze, P. & Nørskov, J. K. Bridging the ‘pressure gap’ between ultrahigh-vacuum surface physics and high-pressure catalysis. *Phys. Rev. Lett.* **55**, 2502–2505 (1985).
40. Dumesic, J. a., Rudd, D. F., Aparicio, L. M., Rekoske, J. E. & Trevino, A. A. *The Microkinetics of Heterogeneous Catalysis*. (American Chemical Society, 1993).
41. Studt, F. *et al.* Discovery of a Ni-Ga catalyst for carbon dioxide reduction to methanol. *Nat. Chem.* **6**, 320–324 (2014).
42. Abild-Pedersen, F. Computational catalyst screening: Scaling, bond-order and catalysis. *Catal. Today* **272**, 6–13 (2016).
43. Grabow, L. C. & Mavrikakis, M. Mechanism of Methanol Synthesis on Cu through CO₂ and CO Hydrogenation. *ACS Catal.* **1**, 365–384 (2011).
44. Nørskov, J. K., Abild-Pedersen, F., Studt, F. & Bligaard, T. Density functional theory in surface chemistry and catalysis. *Proc. Natl. Acad. Sci. U. S. A.* **108**, 937–43 (2011).
45. Stegelmann, C., Schiødt, N. C., Campbell, C. T. & Stoltze, P. Microkinetic modeling of ethylene oxidation over silver. *J. Catal.* **221**, 630–649 (2004).

46. Lynggaard, H., Andreasen, A., Stegelmann, C. & Stoltze, P. Analysis of simple kinetic models in heterogeneous catalysis. *Prog. Surf. Sci.* **77**, 71–137 (2004).
47. Saliccioli, M., Stamatakis, M., Caratzoulas, S. & Vlachos, D. G. A review of multiscale modeling of metal-catalyzed reactions: Mechanism development for complexity and emergent behavior. *Chem. Eng. Sci.* **66**, 4319–4355 (2011).
48. Conn, A. R., Gould, N. I. M. & Toint, P. L. *Trust Region Methods*. (Society for Industrial and Applied Mathematics, 2000).
49. Gusmão, G. S. & Christopher, P. A General and Robust Approach for Defining and Solving Microkinetic Catalytic Systems. *AIChE J.* **61**, 188–199 (2015).
50. Wulff, G. On the Question of Speed of Growth and Dissolution of Crystal Surfaces. *Zeitschrift für Krist.* **34**, 449–530 (1901).
51. Gibbs, J. W. On the equilibrium of heterogeneous substances. *Am. J. Sci.* **16**, 441–458 (1878).
52. Barmparis, G. D. & Remediakis, I. N. Dependence on CO adsorption of the shapes of multifaceted gold nanoparticles: A density functional theory. *Phys. Rev. B* **86**, 085457 1-7 (2012).

Chapter 3

Mechanism of CO₂ reduction by H₂ on Ru(0001) and general selectivity descriptors for late-transition metal catalysts

3.1. Summary

The mechanism of CO₂ reduction by H₂ at atmospheric pressure was investigated on Ru(0001) by coupling density functional theory (DFT) calculations with mean-field microkinetic modeling. The initial CO₂ hydrogenation step leading to CH₄ production was shown to occur through CO₂ dissociation and subsequent hydrogenation of CO* to CHO*. The dissociation of CHO* to form CH* and O* was identified as the rate limiting step for CH₄ formation, while the rate limiting step for CO production through the reverse water gas shift reaction was identified as CO* desorption. Based on a scaling relations analysis of competing CHO* dissociation and CO* desorption, O* adsorption energy was found to be an effective descriptor of differences in selectivity between CO and CH₄ production previously observed on late-transition metal catalysts. These mechanistic insights provide

critical information to guide the design of catalysts with tunable selectivity for CO₂ reduction by H₂ at atmospheric pressure.

3.2. Introduction

More than 85% of the current global energy need is provided by combustion of fossil fuels, which is accountable for continuously increasing atmospheric concentrations of CO₂ and accompanying climate change effects.¹ The search for approaches to reduce atmospheric CO₂ concentration has become a high priority research area. Recent efforts show the potential promise of directly sequestering CO₂ from the atmosphere using amine based sorbent materials, among other methods.²⁻⁶ If approaches to directly sequester CO₂ from the atmosphere prove successful, it will be important to develop efficient, low temperature and pressure processes for converting CO₂ to higher value hydrocarbon feedstocks for chemical and fuel production. The coupling of CO₂ sorption technologies with solar-based H₂ production through catalytic reduction processes would provide an energy efficient, environmentally friendly and carbon neutral approach for chemical and fuel production. This approach relies, in part, on the development of materials that facilitate catalytic conversion of CO₂ and H₂ into desired products with high selectivity.

Because of high energy requirements, C-C coupling reactions are rare at low temperature and pressure and it is expected that C1 molecules (CO, CH₃OH and CH₄) will be the dominant products of environmentally friendly CO₂ reduction processes. CH₃OH synthesis from CO₂ and H₂ on Cu and “Cu-like” catalysts has received significant attention, due the extensive use of CH₃OH as a precursor for production of chemicals and liquid fuels. However, CH₃OH is a minimal side product under low pressure CO₂ hydrogenation

conditions.⁷⁻⁹ On the other hand, highly selective catalytic CH₄ and CO production has been demonstrated at low temperature (as low as 150 °C) and atmospheric pressure over a range of supported transition metal catalysts (eg. Ni, Ru, Rh, Pd, Pt).¹⁰⁻¹⁵ Supported Ru and Rh catalysts are consistently observed to exhibit high activity and selectivity for CO₂ methanation ($\text{CO}_2 + 4\text{H}_2 \rightarrow \text{CH}_4 + 2\text{H}_2\text{O}$) at moderate temperatures and atmospheric pressure. Pt and Pd have been shown to facilitate CO production through the reverse Water Gas Shift reaction (rWGS, $\text{CO}_2 + \text{H}_2 \rightarrow \text{CO} + \text{H}_2\text{O}$) and Ni has exhibited a combination of CO and CH₄ selectivity.^{10-14,16-23} In spite of extensive theoretical and experimental studies of catalytic reduction of CO₂ by H₂ on late transition metal catalysts, outstanding mechanistic questions remain, including most importantly the elementary steps and factors that control catalytic performance and selectivity.^{10-14,16-22,24-33}

Based on the excellent reactivity of Ru for CO₂ methanation and extensive experimental evidence, we use this system as a base case to develop mechanistic insights. Three main initial CO₂ hydrogenation mechanisms have been proposed in literature on late transition metal catalysts: (1) direct hydrogenation of CO₂ to HCOO* or COOH* (adsorbed species are denoted by a star), (2) CO₂ dissociation followed by hydrogenation of CO*,^{18,21,29,34,35} and (3) dissociation of CO₂, followed by direct dissociation of CO* and hydrogenation of surface bound C*.^{14,36} Surface formates (HCOO*) have been observed by *in-situ* Fourier Transform Infrared (FTIR) spectroscopy, however results have shown that these species are most likely spectators on the support.³⁷⁻³⁹ Further, the relatively low barrier for CO₂ dissociation on Ru indicates that direct CO₂ hydrogenation to form COOH* is not a primary reaction pathway on Ru.^{31,40,41} *In-situ* FTIR studies of CO₂ hydrogenation

on Ru have repeatedly shown adsorbed CO* to be the dominant surface species, ^{11-13,17,25,35-37,42,43} suggesting that hydrogenation following CO₂ dissociation is more feasible than direct hydrogenation of CO₂. Therefore it is likely that the main reaction pathway involves hydrogenation of CO*, which has led to the suggestion that CO₂ hydrogenation follows similar mechanism to CO hydrogenation after CO₂ is dissociated on the surface. However experiments have shown that CO and CO₂ hydrogenation kinetics differ considerably in terms of partial pressure dependences and activation barriers, suggesting important mechanistic differences.^{17,22} As discussed in the Results and Discussion sections, this can be attributed to differences in the surface coverage of CO* on Ru under CO and CO₂ hydrogenation reaction conditions. CO* hydrogenation can evolve through formation of COH* or CHO* intermediates. Theoretical studies based on density functional theory (DFT) calculations favor CHO* route over COH* formation.^{31,32,44-46} A few studies report traces of elemental carbon (C*), which can be a result of direct CO* dissociation, however both theoretical and experimental studies have agreed that the H-assisted CO* dissociation is the more energetically favorable route.^{21,32,33,44,46-48}

Although there has been significant experimental analysis of the mechanism of CO₂ reduction by H₂ on late transition metal catalysts, there is no consensus on the initial hydrogenation pathway, or the rate-limiting step (RLS) of the reaction. The most commonly proposed RLS's are direct CO* bond breaking, or in more recent studies H-assisted CO* dissociation through formation of CH_xO*.^{26,37,46} Importantly, there is also no consensus on what properties of late transition metals dictate selective CO production through rWGS (Pt, Pd) versus CH₄ production through methanation (Ru and Rh). A recent

study showed that the catalytic metal d-band center energy trends with competing selectivity for CO and CH₄ production. However, significant variations in the trends observed in this study suggest that d-band center correlation cannot completely describe previously observed variations in selectivity among late transition metal catalysts.¹⁹

In this work we utilize DFT calculations coupled with mean-field microkinetic modeling to develop molecular level insights into the mechanisms that control performance and selectivity of Ru catalysts in CO₂ reduction by H₂ at atmospheric pressure. Mean-field microkinetic models have been proven successful in describing reaction kinetics semi-quantitatively and have been repeatedly used in computational screening of catalyst materials.^{7,49–51} To investigate the mechanism of CO₂ hydrogenation reaction at realistic operating conditions, without a known rate expression and a priori assumption of RLS, it is essential to conduct a detailed microkinetic analysis using temperature and pressure corrected free energies and entropies. In this study the thermodynamic and kinetic parameters are obtained from DFT calculations and used to build a microkinetic model of competing rWGS and methanation pathways on Ru(0001). The microkinetic model captures experimentally observed trends in reaction selectivity and the impact of reactant partial pressures on catalytic rate and surface coverage of reaction intermediates, validating mechanistic insights gained from the model. The initial CO₂ hydrogenation pathway on Ru catalysts was shown to occur through CO₂ dissociation on the catalyst surface and subsequent hydrogenation of CO* to CHO*, in-line with recent FTIR results.^{11–13,17,25,35–37,42,43} Using Campbell’s degree of rate control analysis it was identified that the RLS for CH₄ formation on Ru(0001) is the dissociation of CHO* to form CH* and O*, while the

RLS for the competing CO production through rWGS is CO* desorption.^{52,53} Insights into competing RLS's for CO and CH₄ production on Ru, coupled with linear scaling and Brønsted–Evans–Polanyi (BEP) relationships that extend insights on Ru to Rh, Ni, Pt and Pd catalysts,^{54–57} establish that the O* adsorption energy is an effective descriptor of competing selectivity between CO and CH₄ production on late-transition metal catalysts. That is, more exothermic oxygen adsorption energy is associated with higher selectivity towards CH₄ production. This relationship derives from the impact of the O* adsorption energy on the exothermicity of CHO* dissociation, the resulting influence on the CHO* dissociation barrier (the RLS for CH₄ formation), and the lack of significant variation in CO* binding energy on late transition metal surfaces. The use of oxygen adsorption energy as a selectivity descriptor for CH₄ versus CO production in CO₂ reduction by H₂ accurately explains experimentally observed variations in selectivity on late transition metal catalysts.

3.3. Methods

3.3.1. Elementary steps

The most relevant elementary steps in the reaction mechanism of CO₂, listed in Table 3.1, were identified by a thorough analysis of possible reaction pathways based on DFT calculated energetics and previously postulated mechanisms in literature.^{31–33,37,44,46–48,58,59} Further discussion on competing pathways is provided in the Results and Discussion section (see section 3.4.1). To analyze the reaction mechanism under realistic experimental operating conditions, the reaction free energies, activation barriers and pre-exponential factors were calculated for a temperature of 500 K and atmospheric pressure (shown in Table 3.1), using DFT-derived electronic energies and vibrational frequencies in

conjunction with statistical thermodynamic methods. The details of calculation methods for the thermodynamic and kinetic parameter are provided in the following sections.

Table 3.1. Elementary steps included in the mechanism of CO₂ hydrogenation, reaction free energies, forward activation barriers and forward/reverse pre-exponential factors on Ru(0001) surface at T=500K and P= 1 bar

	Elementary steps	ΔH (eV)	ΔH_f^\ddagger (eV)	A_f (s ⁻¹)	A_r (s ⁻¹)
1	CO ₂ + * → CO ₂ *	-0.11	0.00	2 × 10 ⁸	2 × 10 ¹³
2	H ₂ + 2* → 2H*	-0.91	0.00	8 × 10 ⁸	1 × 10 ^{10 a}
3	CO ₂ * + * → CO* + O*	-0.99	0.07	1 × 10 ¹²	4 × 10 ¹³
4	CO ₂ * + H* → COOH* + *	-0.04	1.00	2 × 10 ¹²	4 × 10 ¹²
5	COOH* + * → CO* + OH*	-0.71	0.71	4 × 10 ¹²	2 × 10 ¹³
6	CO* + H* → COH* + *	0.87	1.77	4 × 10 ¹³	9 × 10 ¹²
7	CO* + H* → CHO* + *	1.10	1.31	3 × 10 ¹³	1 × 10 ^{10 b}
8	O* + H* → OH* + *	0.23	1.15	2 × 10 ¹³	6 × 10 ¹²
9	OH* + H* → H ₂ O* + *	0.28	1.03	2 × 10 ¹³	2 × 10 ¹²
10	COH* + * → C* + OH*	0.23	1.32	5 × 10 ¹²	2 × 10 ¹³
11	CHO* + * → CH* + O*	-0.83 ^c	0.83 ^c	1 × 10 ^{13 b}	1 × 10 ¹³
12	C* + H* → CH* + *	-0.14	0.71	2 × 10 ¹³	6 × 10 ¹²
13	CH* + H* → CH ₂ * + *	0.43	0.58	1 × 10 ¹³	6 × 10 ¹²
14	CH ₂ * + H* → CH ₃ * + *	0.09	0.52	1 × 10 ¹³	5 × 10 ¹²
15	CH ₃ * + H* → CH ₄ * + *	-0.14	0.37	4 × 10 ¹²	2 × 10 ¹²
16	CH ₄ * → CH ₄ + *	0.04	0.04	2 × 10 ¹³	3 × 10 ⁸
17	H ₂ O* → H ₂ O + *	0.21	0.21	5 × 10 ¹⁰	3 × 10 ⁸
18	CO* → CO + *	1.30 ^d	1.30 ^d	6 × 10 ⁷	2 × 10 ⁸

^a Calculated using reverse reaction activation energy as $A_r = k_B T / h \exp(-\Delta S_r^\ddagger / k_B T)$

^b Revised based on previously calculated values on Rh from reference⁶⁰

^c Revised based on previously calculated values on Ru(0001) from reference³²

^d Adjusted by 0.25 eV from DFT calculated values based on known correction factors⁵⁶

3.3.2. DFT calculations

DFT calculations were carried out with the real space grid-based projector-augmented wave method (GPAW) code.⁶¹ The Revised Perdew–Burke–Ernzerhof (RPBE) form of

the generalized gradient approximation (GGA) was used to approximate exchange and correlation effects.⁶² The BEEF-vdW functional was also investigated for geometry optimization of larger intermediate molecules.⁶³ Comparisons between RPBE and BEEF-vdW calculated results are provided in the Results and Discussion section (see section 3.4.1). The Ru(0001) termination was selected to represent the catalyst surface, because it has been demonstrated that larger catalyst particles (>5 nm diameter) have higher activity and selectivity towards CH₄ production, indicating that CO₂ hydrogenation occurs preferably on well-coordinated surfaces of metal catalyst particles.^{64–66} It is important to note that, the support materials such as TiO₂ can have important effects on catalytic behavior of transition metals catalysts, by participating in the reaction mechanism or inducing the well-known metal-support interactions, which are not considered in our model. However the results derived with our model are expected to be comparable with the experiments conducted on support materials such as Al₂O₃, which have shown negligible influence on catalyst activity.⁶⁷

The Ru(0001) surface was modeled as a 3×3×4 periodically repeated unit cells in *x* and *y* directions with 15 Å vacuum space between consecutive metal slabs in *z* direction. A grid space of *h*=0.2 was used. The Brillouin zone was sampled with a 4×4×1 Monkhorst–Pack *k*-point set.⁶⁸ Geometry optimization calculations were performed for single adsorbed species by adding 1/9 Mono Layer (ML) of adsorbate molecules to the top surface of the slab and fixing the lower two layers. The optimized configurations of co-adsorbed reactant and products of the elementary steps were also obtained using similar slab geometry and addition of 2/9 ML of adsorbates on the top surface. The transition state geometries and

energy barriers for reaction elementary steps were obtained using the climbing image nudged elastic band method (CI-NEB).⁶⁹ All geometry configurations were allowed to relax using a quasi-Newton algorithm until the forces on all atoms converged to less than 0.1 eV/Å. The calculated energies of optimized geometries for considered species are provided in Table 3.2-3.4.

Table 3.2. DFT calculated electronic energies, vibrational frequencies, zero-point energy and corrections to thermodynamic quantities for gas phase species involved in CO₂ hydrogenation mechanism at $T=500\text{ K}$ and $P=1\text{ bar}$

Gas phase species	E_{elec}	Vibrational frequencies (meV)	E_{ZPE}	$\Delta H(0 \rightarrow T)$	$T \cdot S$	dG
H ₂	-6.72	542.4	0.271	0.151	0.754	-0.331
CO ₂	-22.64 ^a	77.6, 78.1, 162.5, 289.8	0.305	0.185	1.221	-0.731
CH ₄	-23.52	158.5, 159, 159.3, 187.8, 188.8, 367.1, 380.6, 380.7, 380.9	1.182	0.190	1.075	0.168
H ₂ O	-14.10	200.7, 461.6, 472.1	0.565	0.175	1.071	-0.332
CO	-14.66	262.9	0.131	0.152	1.104	-0.821

^a Corrected by 0.29 eV to minimize DFT errors in reaction enthalpy calculations

Table 3.3. DFT calculated electronic energies, vibrational frequencies, zero-point energy and corrections to thermodynamic quantities for surface species involved in CO₂ hydrogenation mechanism at $T=500\text{ K}$ and $P=1\text{ bar}$

Adsorbed species	E_{elec}	Vibrational frequencies (meV)	E_{ZPE}	U	T^*S	dG
H*	-288.34	117.1	0.152	0.181	0.054	0.127
C*	-292.83	72.1	0.097	0.152	0.091	0.061
CO*	-300.84	43.1, 49.5, 50.7, 241.1	0.196	0.355	0.281	0.074
CO ₂ *	-306.96	12.9, 27.9, 42.4, 52.9, 81.6, 139.5, 210.3	0.284	0.418	0.293	-0.246 ^a
COH*	-303.64	21.7, 48.9, 50.7, 61, 140.7, 159.1, 446.9	0.473	0.610	0.270	0.340
CH*	-296.81	47.3, 49.7, 65.5, 77.7, 84.5, 360.7	0.343	0.432	0.174	0.258
CH ₂ *	-300.17	29.8, 36.6, 43, 61.9, 82.7, 95, 185.6, 266.5, 369.6	0.585	0.714	0.225	0.489
CH ₃ *	-303.98	23.1, 43.9, 50.1, 92.4, 134.7, 160.6, 169.2, 340.8, 349.2, 351.2	0.868	1.013	0.233	0.780
CH ₄ *	-307.96	9.8, 25.7, 46.8, 136.6, 159.4, 162.8, 175.7, 189.9, 368.3, 380.8, 381.8, 382.5	1.210	1.336	0.216	0.766 ^a
H ₂ O*	-298.80	16.2, 21.3, 34.5, 109.6, 193.7, 451, 461.6	0.644	0.743	0.206	0.191 ^a
OH*	-295.19	10.1, 26.2, 49, 66.2, 78.2, 458.7	0.344	0.424	0.172	0.252
CHO*	-303.44	26.5, 42.7, 71.8, 92.1, 155.6, 169.5, 357.1	0.472	0.632	0.371	0.261
COOH*	-310.80	13.3, 18.3, 42.2, 56.1, 59.6, 56.8, 121, 140.5, 175.2, 451.3	0.617	0.811	0.354	0.457
O*	-291.85	55.9	0.031	0.145	0.111	0.034

^a Free energies of weakly adsorbed species were estimated as an average of gas phase and chemisorbed species Gibbs free energies

Table 3.4. DFT calculated electronic energies, vibrational frequencies, zero-point energy and corrections to thermodynamic quantities for transition state configurations involved in CO₂ hydrogenation mechanism at $T=500\text{ K}$ and $P=1\text{ bar}$

Transition States	E _{elec}	Vibrational frequencies (meV)	E _{ZPE}	U	T*S	dG
CO-O	-306.83	16.6, 36.7, 52.2, 82.3, 126.5, 201.5	0.27	0.409	0.281	0.128
COO-H	-309.63	19.9, 30.9, 36.6, 57.6, 81.2, 111.6, 131.5, 154.4, 207.7	0.453	0.618	0.293	0.325
CO-OH	-310.41	8.6, 17.5, 38.2, 72.5, 73.9, 121.6, 147.6, 190.1, 427.9	0.583	0.712	0.228	0.484
CO-H	-302.54	30.9, 39, 51, 54.4, 163, 174.7	0.263	0.404	0.272	0.132
H-CO	-303.07	32.9, 38.5, 74.1, 101, 206.3, 299.8	0.386	0.506	0.235	0.271
O-H	-294.11	55.8, 57.3, 124.9	0.162	0.265	0.187	0.078
H-OH	-297.86	41.7, 53.7, 75.3, 101.1, 113, 461.5	0.435	0.55	0.207	0.343
C-OH	-302.28	46, 54.5, 62.2, 67.5, 96.6, 455.7	0.411	0.573	0.311	0.263
O-CH	-302.26	50.6, 54.4, 70.5, 79.7, 123.7, 379.9	0.409	0.555	0.277	0.279
C-H	-295.84	59.8, 67.3, 217.5	0.226	0.31	0.138	0.172
H-CH	-300.02	48.7, 63.5, 83.9, 122.1, 233.5, 363.7	0.513	0.625	0.184	0.441
H-CH ₂	-303.40	42.3, 44.6, 73.8, 93.5, 113.8, 165.7, 221.1, 307.1, 370.6	0.749	0.864	0.188	0.676
H-CH ₃	-307.37	53.5, 80, 88.8, 90.8, 106.6, 143.5, 151.9, 171.8, 173.6, 362.8, 374, 374.9	1.094	1.257	0.310	0.947

3.3.3. Enthalpy and Free energy calculations

Enthalpies and Gibbs free energies were calculated for gas phase and adsorbed species (including transition states) by applying zero-point energy, thermal energy and entropic corrections using DFT calculated vibrational frequencies and statistical mechanics correlations. Vibrational frequencies (ω_i) were calculated for gas phase, adsorbed species

and transition states, using a finite-difference approximation of the Hessian matrix as implemented in Atomic Simulation Environment (ASE), a Python package used by GPAW to describe molecular configurations and run atomic simulations.⁷⁰ The Ru slab atoms were held fixed during the vibrational analysis of surfaces species. The calculated vibrational frequencies for gas phase, adsorbed species and the transition state configurations are listed in Table 3.2-3.4. The thermodynamic quantities of gas phase species were calculated at $T=500$ K and $P=1$ bar, using equations 3.1 and 3.2.

$$H_g(T) = E_{elec} + E_{ZPE} + \int_0^T C_P dT \quad (3.1)$$

$$G_g(T, P) = H_g(T) - TS(T, P) \quad (3.2)$$

In equations 3.1 and 3.2, $H_g(T)$ is the enthalpy, $G_g(T, P)$ is the free energy of gas phase species, E_{elec} is the DFT calculated electronic energy at 0 K and $E_{ZPE}=0.5\sum\hbar\omega_i$ is the zero-point energy. C_P and $S(T, P)$ are the constant pressure heat capacity and entropy of the gas phase species calculated in the ideal gas limit.⁷¹

The internal energy ($U(T)$) and entropy for the adsorbed species and transition state configurations at $T=500$ K, were calculated in the harmonic limit where all degrees of freedom are treated harmonically. Adsorbed species enthalpy and Gibbs free energy, $H_{A^*}(T)$ and $G_{A^*}(T)$, were calculated using equations 3.3 and 3.4.

$$H_{A^*}(T) = U_{A^*}(T) = E_{elec} + E_{ZPE} + \int_0^T C_{V,vib} dT \quad (3.3)$$

$$G_{A^*}(T) = H_{A^*}(T) - TS(T) \quad (3.4)$$

The species enthalpies were used to calculate reaction energies and activation barriers for all elementary steps using equations 3.5 and 3.6 respectively.

$$\Delta H_{rxn,i} = \sum_{j \in products} H_{j,i} - \sum_{j \in reactants} H_{j,i} \quad (3.5)$$

$$\Delta H_i^{\ddagger} = H_i^{\ddagger} - \sum_{j \in reactants} H_{j,i} \quad (3.6)$$

Activation barriers of all molecular adsorption steps were assumed to be zero. Enthalpies of weakly adsorbed species (H₂O, CO₂ and CH₄) were estimated as an average of gas phase and chemisorbed species enthalpies. It should be also noted that the enthalpies were assumed to be independent of temperature in the narrow temperature range investigated in this study (T=480-520K) and enthalpies were held constant at values calculated at 500 K in the microkinetic analysis of the system in this temperature range.

3.3.4. Pre-exponential calculations

Pre-exponential factors for adsorption steps at T=500 K were obtained using collision theory and a sticking coefficient of 1 for all the adsorbing species based on equation 3.7⁵⁰. In this equation, σ is the sticking coefficient, m_A is the molecular mass of the adsorbing species, k_B is the Boltzmann constant and T is temperature. The reverse (desorption) reaction pre-exponential factors were then calculated based on the equilibrium constant and calculated forward (adsorption) pre-exponential factors ($A_r = A_f / K_{eq}$).

$$A_{f/r} = \frac{\sigma}{\sqrt{2\pi m_A k_B T}} \quad (3.7)$$

The pre-exponential factors for forward (reverse) surface reactions were calculated based on DFT-derived entropies of transition state and reactants (products) at T=500 K,

per equation 3.8, where k_B and h are the Boltzmann and Planck constants, T is temperature, S^\ddagger is the entropy of the transition state and $\Delta S_{f/r}^\ddagger$ is defined as $\Delta S_{f/r}^\ddagger = S^\ddagger - \sum S(\text{reactants/products})$

$$A_{f/r} = \frac{k_B T}{h} \exp \left(\frac{\Delta S_{f/r}^\ddagger}{k_B} \right) \quad (3.8)$$

The calculated pre-exponential factors of all elementary steps are provided in Table 3.1. The variations of pre-exponential factors with temperature in the narrow temperature range of 480-520 K are assumed to be negligible and calculated values at $T=500$ K are used for the entire range.

3.3.5. Microkinetic analysis

A mean-field microkinetic model was constructed based on 18 elementary steps (See Table 3.1 for details on all considered elementary steps). It was assumed that all elementary reactions are microscopically reversible and follow Langmuir-Hinshelwood type mechanisms. No assumptions of RLS were made. Rate expressions for each elementary step in the mean-field microkinetic model were written in the form of equation 3.9 where $k_{f,i}$ and $k_{r,i}$ are the forward and reverse rate constants defined by Arrhenius expressions (equation 3.10 and 3.11) using DFT calculated pre-exponential factors $A_{f/r,i}$ (equation 3.7 and 3.8), P_j is the partial pressure of gas phase reactants/products (Initial State (IS_g)/Final State (FS_g)) and θ_j is the surface coverage of adsorbed reactants/products (IS_{A^*}/FS_{A^*}).^{72,73} All values used in the microkinetic analysis were enthalpies.

$$r_i = k_{f,i} \prod_{j \in IS_g} P_j \prod_{j \in IS_{A^*}} \theta_j - k_{r,i} \prod_{j \in FS_g} P_j \prod_{j \in FS_{A^*}} \theta_j \quad (3.9)$$

$$k_{f,i} = A_{f,i} \exp\left(-\frac{\Delta H_i^{\ddagger}}{k_B T}\right) \quad (3.10)$$

$$k_{r,i} = A_{r,i} \exp\left(-\frac{(\Delta H_i^{\ddagger} - \Delta H_{rxn,i})}{k_B T}\right) \quad (3.11)$$

A pseudo steady state hypothesis was used in the microkinetic model, where the accumulation of surface species as a function of time was considered to be zero. This is comparable to the steady state condition of a differential reactor. The rate of accumulation for each surface species, in the limit of pseudo steady state, was written in the form of equation 3.12, where $\nu_{j,i}$ is the stoichiometry of species j in the reaction i (a negative value if j is a reactant, and positive value if it is a product).

$$\frac{d\theta_j}{dt} = \sum_i \nu_{j,i} r_i = 0 \quad (3.12)$$

Mole balances on adsorbed intermediate species and vacant catalyst sites provide a set of non-linear algebraic equations. An in house MATLAB code based on a quasi-Newtonian scheme was used to solve a linearized set of the mole balances.⁷⁴ At any given temperature, pressure and set of reactant concentrations the surface coverage of the adsorbed species were obtained and used in rate expressions to calculate the instantaneous reaction rates.

3.3.6. Rate and selectivity determining steps

The RLS's were identified using Campbell's degree of rate control ($X_{RC,i}$) as shown in equation 3.13.^{52,53} In this approach, the impact of small variations in elementary step activation barriers on the overall reaction rate is analyzed to identify elementary steps that have the most impact on the overall mechanism. In equation 3.13, k_i is the rate constant of

an elementary step and r is the overall reaction rate. Degree of Selectivity control ($X_{SC,i}$) for all elementary steps was also calculated in a similar manner to $X_{RC,i}$ using equation 3.14. In our definition of $X_{SC,i}$, the impact of small variations in elementary step activation barriers on the difference in apparent activation barriers for CH₄ and CO production is analyzed. It should be noted that $X_{RC,i}$ and $X_{SC,i}$ are calculated at instantaneous reaction conditions.

$$X_{RC,i} = \frac{k_i}{r} \left(\frac{\partial r}{\partial k_i} \right)_{K_i, k_{j \neq i}} \quad K_i = \text{const} \quad (3.13)$$

$$X_{SC,i} = \frac{k_i}{S} \left(\frac{\partial S}{\partial k_i} \right)_{K_i, k_{j \neq i}} \quad K_i = \text{const} \quad (3.14)$$

3.3.7. DFT calculated energetics on transition metal 211 surfaces

The formation energies of C* and O* on (211) surface terminations of late transition metals (Pd, Pt, Ni, Rh and Ru) were taken from Medford et al.,⁵⁶ where DFT calculated raw electronic energies are converted to formation energy by defining gas phase CH₄, H₂O, and H₂ as common references. The formation energies of C* and O* were used in scaling relations to calculate formation energies of CH* and CHO*, and CH-O* transition state.⁵⁶ The electronic formation energies were converted to free energies, then activation barrier and reaction energies of CHO* dissociation and CO* desorption were calculated following approaches described in section 3.3.3.

3.4. Results and Discussion

3.4.1. CO₂ methanation and rWGS mechanisms on Ru(0001)

First we address an un-resolved question of the initial hydrogenation step in the mechanism of CO₂ methanation on Ru catalysts. The potential energy diagram shown in Figure 3.1 compares three competing free energy pathways; direct hydrogenation of physisorbed CO₂*, hydrogenation of CO* after dissociation of adsorbed CO₂* to CO* and O*,^{18,21,34,35} and hydrogenation following complete dissociation of CO₂* to C* and 2O*.^{14,36} Our calculated electronic energies are in good agreement with similarly calculated energies on Ru(0001) surfaces.^{31–33,40,41} A comparison between direct and hydrogen assisted CO₂* dissociation paths in Figure 3.1 (blue and red lines, respectively) shows that the first hydrogenation step for CO₂ methanation is more favorable through the dissociation of CO₂* to CO* and O* and subsequent hydrogenation of CO* to CHO*. This is due to the considerably lower activation barrier for CO₂* dissociation, compared to CO₂* hydrogenation to COOH* ($\Delta G^\ddagger=0.45$ eV compared to $\Delta G^\ddagger=1.42$ eV), and more stable products (1.1 eV more stable). However, the elementary steps involving COOH* species were also included in our microkinetic model and their impact on the overall reaction mechanism will be discussed in the sensitivity analysis section (see section 3.4.3). It is important to note that CO₂ hydrogenation through HCOO* formation was excluded from our analysis based on ample experimental data proving that formates (HCOO*) are spectator species and don't impact the mechanism of the CO₂ hydrogenation on Ru.^{37–39}

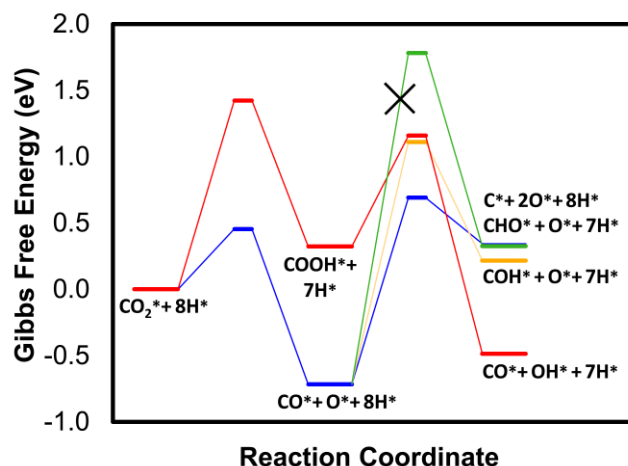


Figure 3.1: Potential energy diagram for competing initial hydrogenation steps in the $\text{CO}_2 + \text{H}_2$ reaction on Ru(0001). All energies are reported relative to the free energy of $\text{CO}_2^* + 8 \text{H}^*$ on Ru(0001). Free energies were calculated at 500 K and atmospheric pressure.

As discussed in the introduction, the initial hydrogenation mechanism following CO_2^* dissociation, has been proposed to proceed by two main pathways: (1) direct CO^* dissociation, and (2) H-assisted CO^* dissociation. CO^* activation on Ru and other transition metal surfaces has been studied extensively in the context of CO hydrogenation (Fischer Tropsch) reaction. While a majority of theoretical calculations show CO^* hydrogenation to form COH^* or CHO^* are energetically more favorable compared to direct CO^* dissociation on terrace sites, direct CO^* dissociation has been shown to have a lower activation barrier on under-coordinated sites such as step sites of (211) and corrugated sites of (1121) facets on Ru catalysts.^{75–77} However, as mentioned previously, CO_2 hydrogenation is known to occur primarily at terraces on Ru nanoparticles.^{64–66} The significant CO^* dissociation barrier on Ru terrace sites ($\Delta G^\ddagger = 2.5 \text{ eV}$), relatively low barrier for CO_2^* dissociation and CO^* hydrogenation to CHO^* , and strong CO^* signals observed by in-situ FTIR studies,^{11–13,17,25,35–37,42,43} suggest that CO^* is the main intermediate in

both the methanation and rWGS reaction pathways and that it is reasonable to exclude the CO* dissociation step from our kinetic studies.

Although CO and CO₂ hydrogenation mechanisms are hypothesized to both evolve through the common pathway of CO* hydrogenation, we suggest differences in CO* coverage during these reactions, as observed via in-situ FTIR measurements, leads to different minimum energy pathways for CO* hydrogenation to form CH₄. Comparison of CHO* and COH* formation pathways under both high and low CO* coverage have shown CHO* formation to be the more favorable route.^{31,44} Comparison of CHO* hydrogenation and dissociation pathways in Figure 3.2a, based on electronic energies calculated under low CO* coverage, shows CHOH* to have higher energy compared to CHO* dissociation products (by 1.2 eV) and larger activation barrier compared to CHO* dissociation pathway (1.16 vs 0.91 eV). Therefore, CHO* dissociation pathway is proposed to be the main pathway towards CH₄ formation in CO₂ hydrogenation mechanism. However, under high CO* coverage (conditions more relevant for CO hydrogenation on Ru), CHOH* formation has been identified to be the most relevant (rate limiting) step in the mechanism of CO hydrogenation.⁴⁴ It is suggested that under CO hydrogenation reaction condition, where the Ru surface is saturated with CO*, repulsive forces increase CHO* dissociation barrier by weakening the final state O*-Ru bond. Similarly, H*-Ru bonds are weakened due to high CO* coverage, which facilitate H*-Ru bond breaking and CHO*-H* bond formation. Thus, it seems that the differences in the CO* coverage under CO and CO₂ hydrogenation reaction conditions on Ru, drive the hydrogenation of CO* to CH₄ to occur through different reaction pathways.⁴⁴

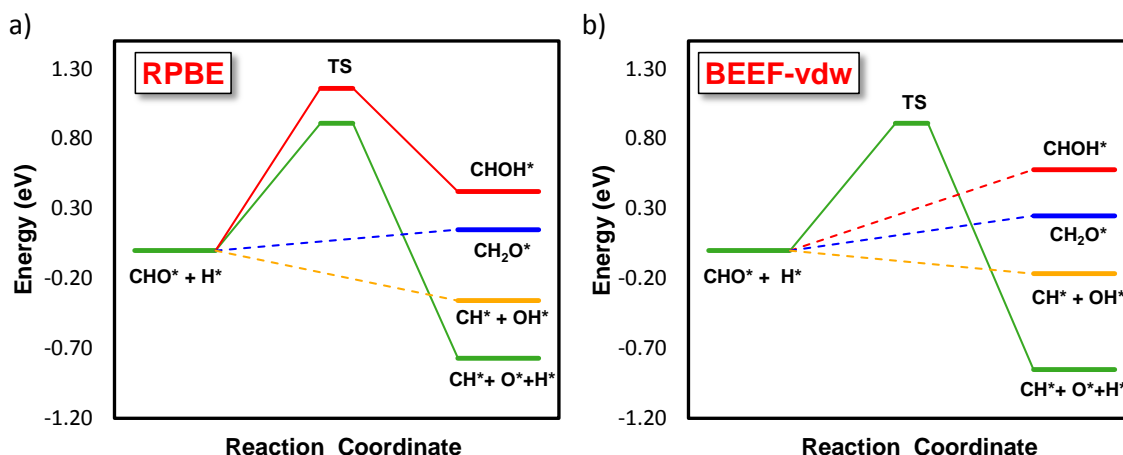


Figure 3.2: Energy diagram of competing pathways for CHO^* dissociation and hydrogenation under low CO^* coverage calculated using a) RPBE functional and, b) BEEF-vdW functional.

The inclusion of van der Waals forces in DFT calculations has shown to stabilize larger molecules on catalytic surfaces and have little effect on the adsorption energies of smaller molecules.⁷⁸ To analyze the effect of van der Waals forces in the CO_2 conversion pathways on Ru(0001), the BEEF-vdW functional was used in the calculation of possible CHO^* hydrogenation pathways that included larger intermediate molecules. The results, provided in Figure 3.2b, agree well with calculations performed using the RPBE functional (Figure 3.2a). Both functionals predict that pathways involving larger intermediates (such as CHOH^* and CH_2O^*) are thermodynamically less favorable, in comparison to the routes with smaller molecules (CH^* and OH^*) and can be excluded from kinetic studies of reaction mechanism. Based on this comparison, the RPBE calculated values were used in the microkinetic modeling. It should be noted that energies presented in Figure 3.2 are based on DFT derived electronic energies while all other plots in this chapter use free energies.

The parallel pathways of CO* hydrogenation through COH* and CHO* formation are compared in the potential energy diagram plotted in Figure 3.3. In this figure the complete energetic pathways of CO₂ methanation, and the competing rWGS reaction are mapped out at 500 K and atmospheric pressure. The calculated free energy pathways are in good agreement with similarly calculated free energy pathways for CO₂ conversion on Ru and other metal surfaces.^{30–33,45,46} Based purely on the thermodynamics of competing COH* and CHO* pathways, the more favorable route toward CH₄ formation after CO₂* dissociation is the formation of CHO* and its dissociation to CH* and O* (green line in Figure 3.3). Although energetically, CO* desorption (i.e. rWGS pathway) is more favorable than either COH* and CHO* formation, the larger pre-exponential factors for the latter create a competition between methanation and rWGS that cannot be predicted based purely on the free energy landscapes in Figure 3.3, and will be discussed below in the results of the microkinetic model. The overall energy diagram identifies CO* and CH* as the most stable free energy states in the mechanism. It would be expected that CO* is the most abundant surface species under reaction conditions due to the lower energy barrier of CO₂* dissociation to form CO* ($\Delta G^\ddagger=0.45$ eV), compared to barriers of CO* hydrogenation (CO*+H*→CHO* $\Delta G^\ddagger=1.42$ eV) and CH* formation (CHO*+*→CH*+O* $\Delta G^\ddagger=0.93$ eV). Also, CH* can easily overcome the small barrier of 0.63 eV to form CH₂*. Based on a simple examination of the calculated competing free energy surfaces for rWGS and CO₂ methanation on Ru(0001), it would be expected that the most abundant surface intermediate would be CO*, although the favored reaction

pathway (CO vs. CH₄ production) and rate and selectivity controlling steps cannot be predicted based on the shape of the free energy landscapes alone.

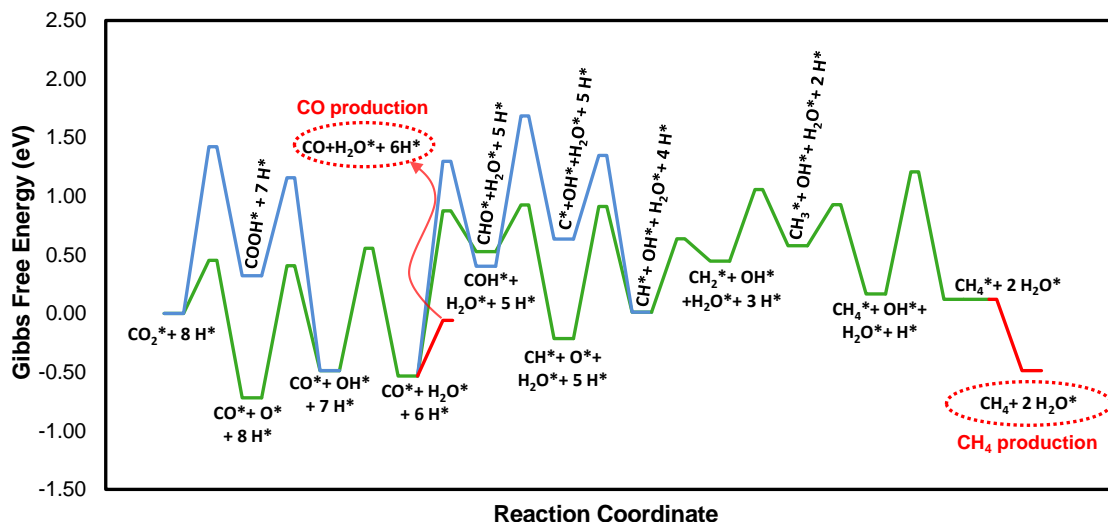


Figure 3.3: Potential energy diagram of competing pathways for CO₂ reduction by H₂ on Ru(0001). The rWGS (CO formation) and methanation (CH₄ formation) pathways are shown. The most favorable pathways for CO₂ methanation and rWGS are shown in green. The elementary steps in red are associated with product evolution from the catalyst. The pathways shown in light blue are competing potential pathways for the initial hydrogenation of CO₂ and conversion of CO* to CH*. All energies are reported relative to CO₂* + 8H*. Gibbs free energies were calculated at 500 K and atmospheric pressure.

3.4.2. Microkinetic model

A steady state microkinetic model of the 18 elementary step reaction system (listed in Table 3.1) was solved for the surface coverage of all reaction intermediates. Figure 3.4a shows the surface coverage of the most abundant (>0.1% coverage) surface species as a function of temperature (480-520 K) at atmospheric pressure and stoichiometric methanation reactant concentrations (CO₂:4H₂, no inert is included). Figure 3.4a shows that in the temperature range of 480-520 K, the Ru(0001) surface is predominantly covered by CO* (46%-68%) and H* (31%-53%). CO* and H* are the two main species competing for the surface adsorption sites under atmospheric conditions explored here. Because CO₂*

dissociation ($\Delta H_{rxn} = -1.0$ eV) is slightly more exothermic than H₂ dissociative adsorption ($\Delta H_{rxn} = -0.91$ eV), the forward energy barrier of CO* hydrogenation steps are relatively high ($\Delta H_{H-CO^*}^\ddagger = 1.31$ eV and $\Delta H_{CO-H^*}^\ddagger = 1.77$ eV) and H* and O* are easily consumed by elementary steps with lower activation energies (O*+H*→OH*+*, $\Delta H^\ddagger = 1.15$ eV and OH*+H*→H₂O*+*, $\Delta H^\ddagger = 1.03$ eV), CO* is the dominant surface species at temperature below 510 K and $P_{H_2} < 0.7$ bar. These results agree with *in-situ* FTIR spectroscopic measurements that consistently show strong signals of CO* compared to smaller intensities of other surface species.^{11-13,17,25,35-37,42,43} It is also important to point out that H* vibrational modes cannot be detected in FTIR measurements. Although it was postulated earlier that CH* may be a significant surface species based on an inspection of the free energy pathway, the formation of CH₄ from CH* apparently occurs with low enough energy barriers to minimize CH* coverage under reaction conditions. The low surface concentrations of other key intermediates in the methanation pathway, such as CHO* and CH_x* species, indicate that these species are highly reactive and it can be expected that their identification in spectroscopic experiments would be difficult. Figure 3.4a also shows that with increasing temperature the concentration of CO* decreases while H* coverage increases, which can be attributed to the increased number of adsorbed CO* crossing the hydrogenation reaction barrier to form CHO* and eventually CH₄. The lower CO* concentration provides more adsorption sites available for H* species to bind.

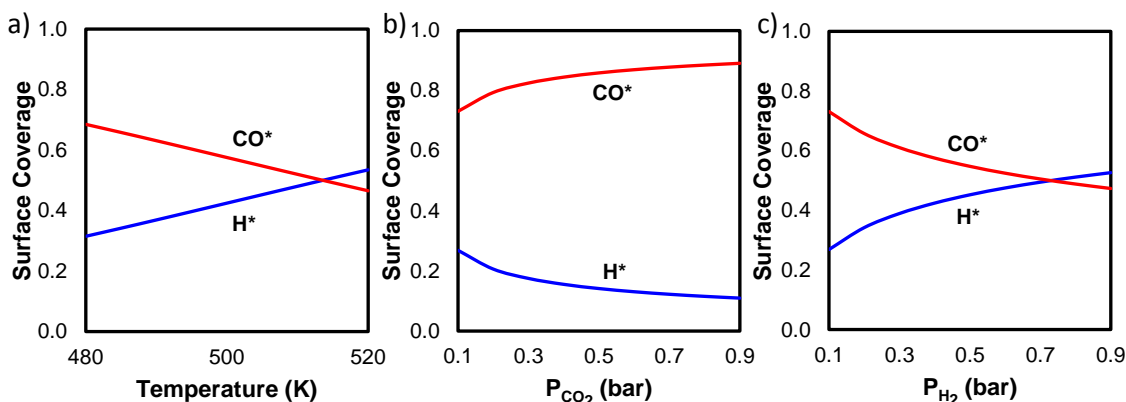


Figure 3.4: Microkinetic model predictions of surface coverage for the most abundant surface species (> 0.01 fractional coverage), **a)** as a function of temperature at 1 bar total pressure and stoichiometric methanation feed composition ($CO_2:4H_2$), **b)** as a function of CO_2 partial pressure at 500K and constant H_2 partial pressure ($P_{H_2}=0.1$ bar), and **c)** as a function of H_2 partial pressure at 500 K and constant CO_2 partial pressure ($P_{CO_2}=0.1$ bar).

Figure 3.4b and c show the most abundant surface species coverage as a function of CO_2 and H_2 partial pressures, respectively. The surface coverages were calculated at a temperature of 500 K and total pressure of 1 bar. The partial pressure of CO_2 (H_2) was varied in the range of 0.1-0.9 bar while the partial pressure of the other reactant was kept constant at 0.1 bar (varying amount of inert gas is assumed to balance the total pressure). The results show that under atmospheric reaction conditions, regardless of the feed composition explored, CO^* and H^* are the most abundant surface species. It can be seen in Figure 3.4b that as CO_2 partial pressure is increased from 0.1 to 0.9 bar, CO^* coverage increases slightly by replacing surface H^* ($\Delta\theta=0.16$). Conversely, Figure 3.4c shows that a higher concentration of H_2 in the reactant mixture results in an increase in H^* coverage and decrease in CO^* coverage ($\Delta\theta=0.26$). While the absolute magnitude of the coverage changes was small, the relative change in H^* coverage with varying reactant partial pressure is significant, which is expected to have an impact on the reactivity of the surface.

Experimental FTIR studies have shown the surface coverage of CO*, the most abundant FTIR-detectable species, is about 20%-40% of saturation coverage. Therefore it is expected that there should be a considerable number of vacant sites present on the surface under reaction condition, which is not captured by our model. We believe this is because the destabilizing effects of increasing surface coverage on CO* and H* binding energies was not considered in our microkinetic model. It has been shown that at high CO* coverages, >50%, repulsive interactions of surface species can have a significant effect on binding energies.⁷⁹ As the CO* coverage during CO₂ reduction reaction is not expected to exceed 40%, this is not expected to significantly impact mechanistic insights gained from the study. However, we believe including an accurate account of surface coverage effects in the calculation of binding energies would improve the calculated free site concentrations. A rigorous study to include the correct coverage dependent surface kinetic would require kinetic Monte Carlo (kMC) simulations which involves numerous DFT calculations to account for various adsorbate configurations and is computationally expensive and outside the scope of this work.⁸⁰

To investigate the effect of feed composition on the CH₄ production rate, the turn over frequency (TOF) for CH₄ formation was calculated as a function of H₂ partial pressure at 500 K, 1 bar total pressure, constant CO₂ partial pressure of 0.1 bar and varying amounts of inert gas depending on H₂ partial pressure. Variations in the calculated TOF and CO* coverage as a function of H₂ partial pressure in the feed stream are shown in Figure 3.5a. CH₄ TOF is positively correlated with the variation in H₂ partial pressure, where a change in H₂ partial pressure from 0.1 to 0.6 bar causes a 27% increase in the TOF for CH₄

formation (from 1.67×10^{-4} to $2.12 \times 10^{-4} \text{ s}^{-1}$). The coupled inverse correlation of CO* coverage and positive correlation of CH₄ TOF with the H₂ partial pressure in the feed stream observed in Figure 3.5a was also observed experimentally by Prairie et al.³⁶ In this study, CO₂ reduction by H₂ on Ru catalysts was investigated under similar reaction conditions as Figure 3.5a (H₂ partial pressure varying in the range of 0.1-0.6 bar at temperature of 463 K, atmospheric pressure and CO₂ partial pressure of 0.13 bar), using *in situ* diffuse reflectance FTIR spectroscopy (DRIFTS). CO* coverage was quantified by normalizing the band integrals associated with CO* during the hydrogenation reaction to the value for the CO* saturated catalyst.³⁶ A 70% increase in the CH₄ production rate (from 7.4 to 12.6 $\mu\text{mol/g.s}$) and 7% decrease in relative CO* coverage was measured with a change in H₂ partial pressure from 0.1-0.6 bar, as shown in Figure 3.5b.³⁶ The agreement between trends in theoretical and experimentally derived changes in CH₄ TOF (30% versus 70% increase) and relative CO* coverage (7% versus 28%) as a function of H₂ partial pressure provide confidence in the microkinetic model for qualitatively describing experimental systems.

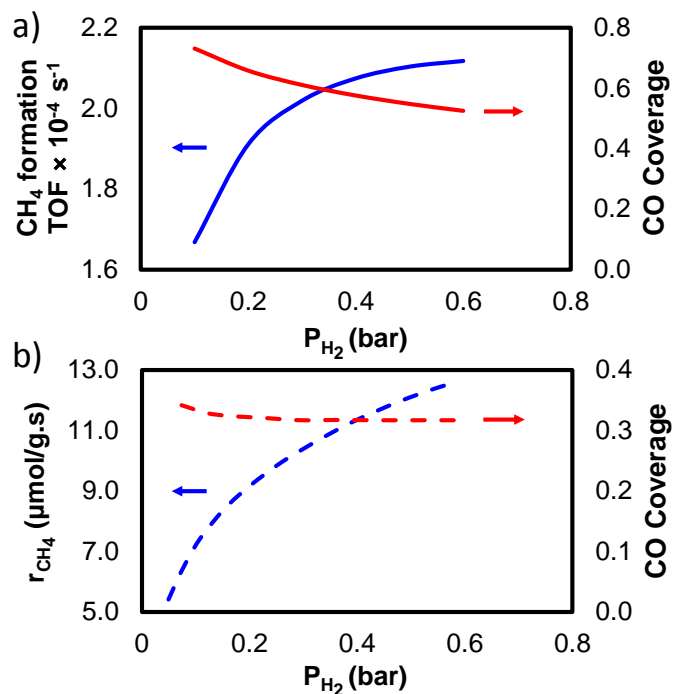


Figure 3.5: **a)** Microkinetic model predictions of TOF for CH₄ production (1/s) and CO coverage as a function of H₂ partial pressure in the reactant mixture at 1 bar total pressure, 500 K, and fixed CO₂ partial pressure (P_{CO_2} = 0.1 bar). **b)** Experimentally measured CH₄ production rate ($\mu\text{mol/g.s}$) and CO coverage as a function of H₂ partial pressure at 1 bar total pressure, 463 K, and fixed CO₂ partial pressure (P_{CO_2} = 0.13 bar), adapted from Prarie et al.³⁶

Experimentally measured reaction orders with respect to H₂ partial pressure are in the range of 0.5-1.0,^{17,27,81} which are larger than the value calculated based on the data in Figure 3.5a (about 0.13). The dependence of CH₄ production on CO₂ partial pressure was also investigated through its variation in the range of 0.1- 0.9 bar at temperature of 500 K, total pressure of 1 bar and constant H₂ partial pressure of 0.1 bar (data not shown here). The reaction order with respect to CO₂ partial pressure for CH₄ formation was found to be - 0.32, which is lower than reported values in the range of 0.1-0.5. The apparent activation energy calculated with our model is about 47 Kcal/mol which is larger than experimentally measured apparent barriers in the range of 19-25 Kcal/mol.^{17,27} We believe the discrepancies observed between the calculated and experimentally measured partial

pressure dependence and apparent activation barriers are mainly related to the underestimation of vacant sites, which will be discussed more in detail in section 3.4.4.

It is important to note that the absolute values of TOF obtained from DFT-based microkinetic modeling are known to have uncertainties of several orders of magnitudes.⁸² In addition, as discussed above, the exclusion of coverage dependence of adsorption energies for surface species is believed to cause an underestimation of vacant site concentration by the microkinetic model. Furthermore, the magnitude of adsorbate coverage is also difficult to quantify through *in-situ*, spectroscopy. While calculated rates, reaction orders and coverages are difficult to quantitatively relate to experimental values, it is possible to quantitatively compare the trends of the calculated rates and coverage with experimental measurements under similar reaction conditions due to a cancellation of errors in DFT calculations. Thus, we believe that the reasonable agreement between experimental observed trends and our model predictions in Figure 3.5 and the justifiable differences between measured and predicted reaction orders and activation enthalpies (see more discussion below) provide evidence that the microkinetic model is a reasonable representation of experimental systems.

As mentioned in the Introduction, Ru catalysts are known to be highly selective towards CH₄ production, rather than catalyzing rWGS. To ensure that the microkinetic model accurately captures this behavior, catalytic selectivity toward CH₄ production ($S_{CH_4} = r_{CH_4} / (r_{CH_4} + r_{CO})$) was calculated as a function of temperature and CO₂ partial pressure. Under stoichiometric feed composition (CO₂:4H₂) and 1 bar total pressure, in the temperature range of 480-520 K, Ru(0001) exhibits a high CH₄ selectivity in the range of

97% to >99%, increasing with temperature, Figure 3.6a. These results are in agreement with experimentally measured selectivity of Ru catalyst particles towards CH₄ formation and observed temperature dependence of the selectivity.^{10,14,17,35,36} Figure 3.6b shows the dependence of CH₄ selectivity on CO₂ partial pressure, calculated at a temperature of 500 K, atmospheric pressure and H₂ partial pressure of 0.1 bar. Ru(0001) is calculated to be selective for CH₄ production in the entire range of explored CO₂ partial pressures, but shows a negative correlation with the increasing CO₂ partial pressure. The calculated CH₄ selectivity drops from 98% to 95% as CO₂ partial pressure increases from 0.1 to 0.9 bar. This is consistent with the conclusions drawn in the previous sections regarding the correlation of CH₄ production rate with H* surface coverage and its inverse correlation with CO* surface coverage and CO₂ partial pressure.

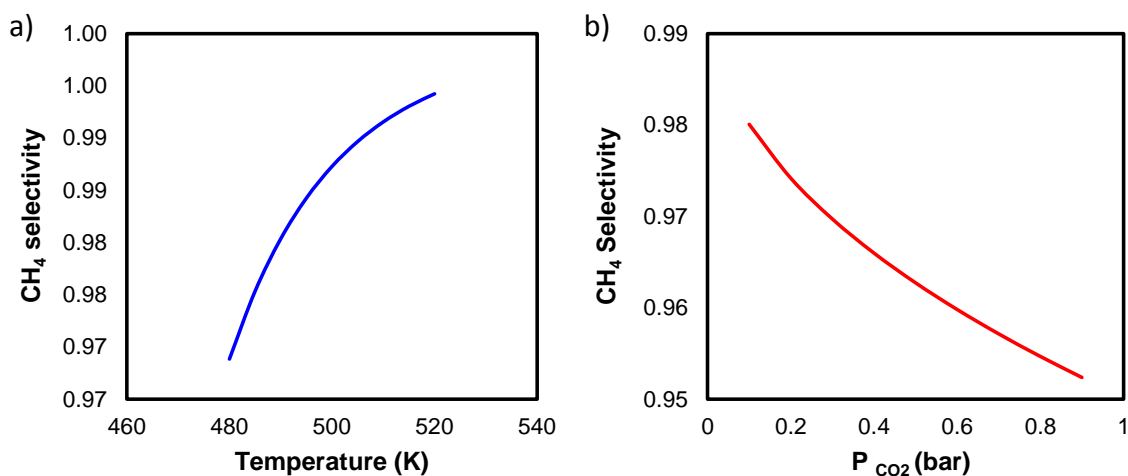


Figure 3.6: Microkinetic model prediction of CH₄ selectivity, **a**) as a function of temperature at 1 bar total pressure and stoichiometric methanation feed composition (CO₂:4H₂) and, **b**) as a function of CO₂ partial pressure at 1 bar total pressure, 500 K and constant H₂ partial pressure (P_{H2}=0.1 bar).

To summarize, the calculated microkinetic model predicted high selectivity (>95%) to CH₄ for CO₂ reduction by H₂ on Ru(0001) at atmospheric pressure for a wide range of

reactant partial pressures and temperatures of 480-520 K. Over the range of considered conditions, the surface was covered predominantly by CO* and H*. It was found that there is a positive correlation between H* coverage and CH₄ production rate. The observed trends were in good agreement with various experimental reports, providing confidence in mechanistic conclusions drawn from the calculated microkinetic model.

3.4.3. Sensitivity Analysis

To determine the RLS for CH₄ production in the microkinetic model, $X_{RC,i}$ was calculated for all elementary steps in a temperature range of 480-520 K, at 1 bar total pressure and stoichiometric feed composition (CO₂:4H₂), Figure 3.7a. Under these reaction conditions CHO* dissociation was identified as the primary RLS for CH₄ formation. This is consistent with previous experimental and theoretical studies that have suggested H-assisted CO bond cleavage is the slowest step in CO₂ hydrogenation towards CH₄ production.^{26,37,46} The results from the degree of rate control analysis, coupled with previous studies, provide strong evidence that CO₂ methanation on Ru occurs through CHO* formation and has a RLS of CHO* dissociation.

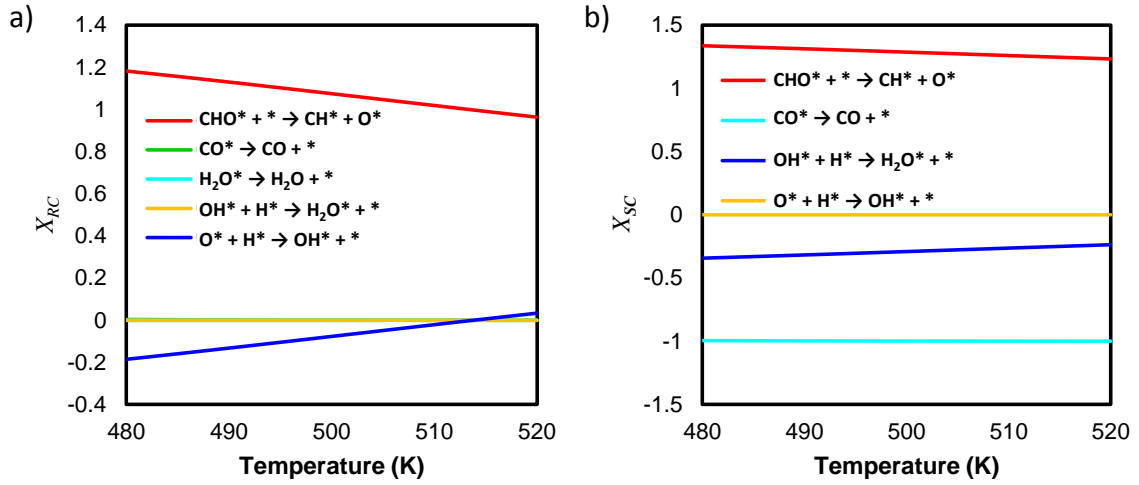


Figure 3.7: **a)** Degree of rate control, X_{RC} , for elementary steps that exhibit significant control ($|X_{RC,i}| > 0.01$) for the CH_4 formation rate. **b)** Degree of selectivity control, X_{SC} , for elementary steps that exhibit significant control ($|X_{SC,i}| > 0.01$) of selectivity for CH_4 formation. $X_{RC,i}$ and $X_{SC,i}$ were calculated at a total pressure of 1 bar and stoichiometric methanation feed composition ($\text{CO}_2:\text{4H}_2$) in the temperature range of 480-520 K.

The elementary step, $\text{O}^* + \text{H}^* \rightarrow \text{OH}^*$, has slight negative $X_{RC,i}$ at lower temperatures. This indicates that an increase in the rate of this step will have an impeding effect on the CH_4 formation rate. All other elementary steps have $X_{RC,i}$ values close to zero ($< 10^{-3}$), indicating that they have little or no effect on the overall CH_4 formation rate. The negligible impact of COOH^* formation and dissociation steps on the overall reaction rate ($X_{RC,4,5} < 10^{-3}$) further substantiates the assertion made in previous section that CO_2 dissociation followed by hydrogenation is the more feasible CO_2 activation route compared to the direct CO_2 hydrogenation pathway on Ru.

The degree of selectivity control, $X_{SC,i}$, for CH_4 formation was calculated for all elementary steps using equation 3.14. It should be noted that a modified selectivity definition ($S_{\text{CH}_4} = r_{\text{CH}_4}/r_{\text{CO}}$) was used in the $X_{SC,i}$ calculations, compared to how selectivity was calculated in Figure 3.6. Defining selectivity as the ratio of CH_4 and CO formation rates, makes it possible to directly analyze the impact of a change in the activation barrier

of a single elementary step on the difference of apparent activation barriers for competing CO and CH₄ formation, ($X_{SC,i} = \ln(r_{CH_4}/r_{CO})/\ln(k_i) \approx (\Delta H_{CH_4}^\ddagger - \Delta H_{CO}^\ddagger)/\Delta H_i^\ddagger$). Figure 3.7b shows the calculated $X_{SC,i}$ values of the elementary steps that have the largest impact on selectivity for CH₄ formation in the temperature range of 480-520 K and 1 bar total pressure with a feed composition of CO₂:4H₂. The degree of selectivity control for CH₄ formation has primarily a strong positive correlation with the CHO* dissociation step, consistent with the degree of rate control analysis in Figure 3.7a. The CO* desorption step has a large negative degree of selectivity control for CH₄ formation indicating that CO* desorption is the primary RLS for CO production in the rWGS pathway. From these results it can be concluded that the two main elementary steps determining selectivity of late transition metal catalysts (those with similar electronic structure to Ru) for methanation versus the rWGS reaction are CHO* dissociation and CO* desorption.

3.4.4. Reaction rate expression

A simplified reaction rate expression was derived for CH₄ formation based on the identified rate limiting step, CHO* → CH* + O*, and other important elementary steps leading to CHO* dissociation, as listed in Table 3.5. Steps 1-7 are assumed to be quasi equilibrated ($r_i=0$) which result to the following expressions for the surface concentrations of predominant species CO* and H*:

$$\theta_{CO^*} = \alpha \frac{P_{CO_2} P_{H_2}}{P_{H_2O}} \theta_* \quad (3.15)$$

$$\theta_{H^*} = \gamma P_{H_2}^{0.5} \theta_* \quad (3.16)$$

And the vacant site concentration can be derived from $\theta_* + \theta_{CO*} + \theta_{H*} = 1$, as shown in equation 3.17:

$$\theta_* = \frac{1}{\left(1 + \alpha \frac{P_{CO_2} P_{H_2}}{P_{H_2O}} + \gamma P_{H_2}^{0.5}\right)} \quad (3.17)$$

In equations 3.15-3.17 α , β and γ are kinetic parameters defined as follows:

$$\begin{aligned} \alpha &= K_1 K_2 K_3^{1.5} K_4 K_5 K_6 K_7 k_8 \\ \beta &= K_1 K_2 K_3 K_5 K_6 K_7 \\ \gamma &= K_3^{0.5} \end{aligned}$$

The rate expression is then derived in the form presented in equation 3.18.

$$-r_{CH_4} = \frac{\alpha P_{CO_2} P_{H_2}^{1.5}}{P_{H_2O} \left(1 + \beta \frac{P_{CO_2} P_{H_2}}{P_{H_2O}} + \gamma P_{H_2}^{0.5}\right)^2} \quad (3.18)$$

In equation 3.18 r_{CH_4} is the CH_4 production rate, P_{CO_2} , P_{H_2} and P_{H_2O} are partial pressures of CO_2 , H_2 and H_2O , respectively.

Table 3.5. Elementary steps included in the derivation of rate expression

		ΔH (eV)	H_{af} (eV)
1	$CO_2 + * \rightarrow CO_2^*$	-0.10	0.00
2	$CO_2^* + * \rightarrow CO^* + O^*$	-1.00	0.06
3	$H_2 + 2* \rightarrow 2H^*$	-0.91	0.00
4	$CO^* + H^* \rightarrow CHO^* + *$	1.10	1.31
5	$O^* + H^* \rightarrow OH^* + *$	0.23	1.15
6	$OH^* + H^* \rightarrow H_2O^* + *$	0.28	1.03
7	$H_2O^* \rightarrow H_2O + *$	0.21	0.21
8	$CHO^* + * \rightarrow CH^* + O^*$	-1.14	0.84

It is important to note that equation 3.18 is derived for CH₄ formation pathway only with the assumption of a single RLS, CHO* dissociation. The contributions of other elementary steps that have a smaller impact on the kinetics of the reaction system and CO production route are not captured with this rate expression. However, the derived rate expression can be used to explain the wide range of reaction orders and activation barriers reported in the literature for CH₄ formation reaction on Ru, which will strongly depend on the experimental conditions and relative concentration of dominant surface species.^{17,27,81} The discrepancies observed between the calculated and experimentally measured partial pressure dependences and activation barriers, as well as among the experimental measurements alone, can be explained based on the following analysis of the rate expression in equation 3.18. The three terms inside the parentheses in the denominator of equation 3.18 represent surface concentration of vacant sites (*), CO* and H* respectively, which are expected to be present at similar concentrations during reaction conditions. The underestimation of surface vacant site concentration in our model, $\theta^* \sim 0$, increases CO* and H* concentrations and the contribution of the second and third terms inside the parentheses to the reaction rate. The increased negative contribution of these two terms will reduce the order of reaction with respect to P_{CO_2} and P_{H_2} , hence the microkinetic model predicts reaction orders that are smaller than experimentally measured values ($n_{CO_2} = -0.32$ and $n_{H_2} = 0.13$, compared to experimental values of $n_{CO_2} = 0.1-0.5$ and $n_{H_2} = 0.5-1$).

In a similar analysis it is shown that variations in the contribution of the CO* and H* concentration terms in the rate expression can significantly influence the calculated apparent activation barrier, which we believe is the main reason for the overestimated

activation barrier obtained from the microkinetic model. This can be explained more clearly through the analysis of the following two hypothetical cases. In the first hypothetical case where θ_* is significantly larger than θ_{CO^*} and θ_{H^*} , the rate equation can be simplified to:

$$-r_{CH_4} = \frac{\alpha P_{CO_2} P_{H_2}^{1.5}}{P_{H_2O}} \quad (3.19)$$

The rate constant in this case becomes $\alpha = K_1 K_2 K_3^{1.5} K_4 K_5 K_6 K_7 k_8$. Using an Arrhenius expression and reaction energies listed in Table 3.5 the apparent activation barrier can be calculated as shown in equation 3.20, which results in an apparent activation barrier of 0.195 eV (4.5 Kcal/mol).

$$\begin{aligned} \alpha &= A \exp\left(\frac{-\Delta H_{app}}{RT}\right) \\ &= A \exp\left(\frac{-\left(\Delta H_1 + \Delta H_2 + 1.5 * \Delta H_3 + \Delta H_4 + \Delta H_5 + \Delta H_6 + \Delta H_7 + H_8^{\ddagger}\right)}{RT}\right) \end{aligned} \quad (3.20)$$

A different scenario where surface is entirely covered with CO^* , yields the rate expression shown in equation 3.21, where the rate constant is α/β^2 and the apparent activation barrier is 2.8 eV (64.6 Kcal/mol).

$$-r_{CH_4} = \frac{\alpha P_{H_2O}}{\beta^2 P_{CO_2} P_{H_2}^{0.5}} \quad (3.21)$$

These two hypothetical cases show that, increasing CO^* (and similarly H^*) concentration will increase the positive contribution of the second (and third) term inside the parentheses in the denominator of rate expression to the calculated apparent activation

energy, which results in an increase in the activation barrier. As discussed above, we believe that the underestimation of vacant sites (due to not including coverage effects in the microkinetic model) and the resulting overestimation of CO* and H* concentrations, is the main reason the apparent activation barrier calculated from the microkinetic model (47 Kcal/mol) is larger than experimentally measured barriers (in the range of 19-25 Kcal/mol). This simple analysis shows that as the vacant site concentration increases it would be expected that the apparent barrier predicted by the model would decrease closer to the experimentally measured value. We expect that a model, where surface coverage effects are incorporated accurately, will predict more accurate vacant site concentrations and improved reaction orders and apparent activation barriers.

3.4.5. Selectivity descriptor on late-transition metals

To understand how the competition between CHO* dissociation and CO* desorption can be used to explain the trend in selectivity for late transition metals (CO production on Pt and Pd and CH₄ production on Rh and Ru), reaction free energies and barriers of the two steps were calculated for Pt, Pd, Ni, Rh and Ru. The free energies in Figure 3.8 were calculated using DFT-derived formation energies of C* and O* elements on (211) surface terminations by Medford et al.⁵⁶ Formation energies for surface species are equivalent to adsorption energies calculated relative to common gas phase reference molecules H₂, H₂O and CH₄. These energies were coupled with scaling relations to calculate adsorption energies of CH* and CHO*, and the HC-O* transition state energy. It is critical to mention that while scaling relations applied here were developed using calculations on stepped (211) surfaces and our calculations were done on a flat (0001) surface, there is strong

evidence that the coordination number of the active site only impacts the y-intercept of the scaling relations, rather than the slope.⁸³ Thus the trend in the adsorption energies and activation barriers of the selectivity controlling steps predicted by (211) or flat surface scaling relations should be identical (within error of the scaling relations themselves) and simply offset by a constant value. As a result, because we are looking only to identify a trend in the energetics of the two competing elementary steps that correlates with the experimentally observed trend in selectivity, we believe our use of (211) scaling relations to perform this analysis is fully justified and would provide identical conclusions compared to scaling relations developed on flat surfaces. It can be seen in Figure 3.8a that CO* desorption free energies (red bars in Figure 3.8a) for the five metals are similar and vary in the range of 0.27-0.71 eV. Furthermore, the CO* desorption free energy is essentially identical (0.57, 0.56 and 0.63 eV) for Pd, Ni and Rh, which have been shown to exhibit very different selectivity in CO₂ reduction by H₂ at atmospheric conditions, as mentioned previously. Thus, CO* desorption energy alone cannot be used as a descriptor to predict the tendency of a metal to promote CO₂ methanation or rWGS. Conversely, CHO* dissociation activation energies (blue bars in Figure 3.8a) are significantly different for the investigated metals. There is a difference greater than 1 eV in the energy barriers of CHO* dissociation on Pt ($\Delta G^\ddagger=2.51$ eV) and Pd ($\Delta G^\ddagger=2.55$ eV) with the barriers on Ni ($\Delta G^\ddagger=1.44$ eV), Rh ($\Delta G^\ddagger=1.43$ eV) and a difference of 1.4 eV with that of Ru ($\Delta G^\ddagger=1.18$ eV). The CHO* dissociation free energies (orange bars in Figure 3.8a), which are linearly correlated with activation energies based on BEP relationships,^{54,55} show the same trend. Comparison of the CHO* dissociation free energies shows that the dissociation step switches from

endothermic on Pd ($\Delta G=0.64$ eV) and Pt ($\Delta G=0.64$ eV) to exothermic on Ni ($\Delta G=-0.72$ eV), Rh ($\Delta G=-0.75$ eV) and Ru ($\Delta G=-1.07$ eV).

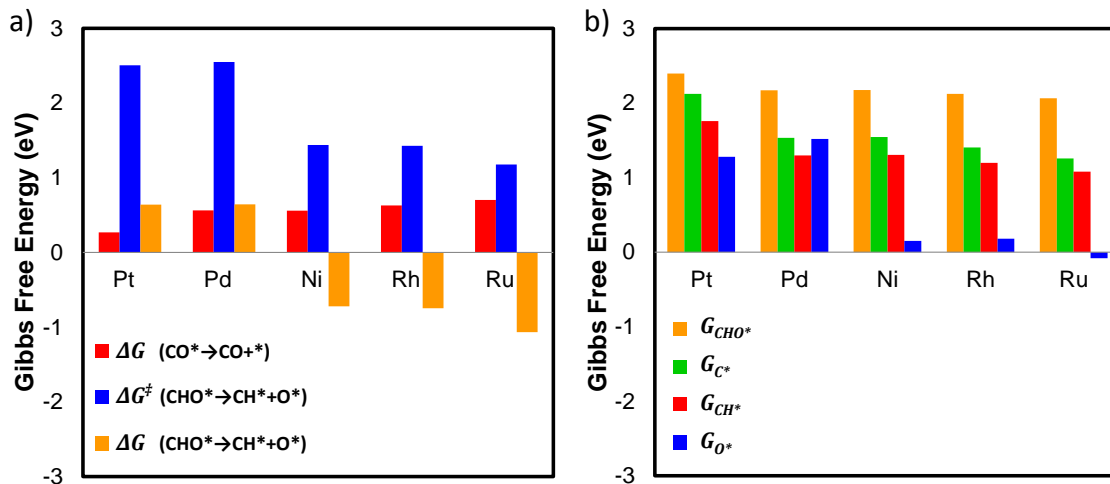


Figure 3.8: **a)** Comparison of free energy for CO* desorption, CHO* dissociation activation barrier, and free energy for the CHO* dissociation reaction on Pt, Pd, Ni, Rh and Ru surfaces. **b)** Comparison of free energy of formation for CHO*, C*, CH* and O* on Pt, Pd, Ni, Rh and Ru (211) surfaces. Values were derived from previously developed scaling relations and DFT calculated formation energies of C* and O*. See Supplementary Material for details on the calculations.⁵⁶

The switch from endothermic to exothermic CHO* dissociation free energies agrees well with experimentally observed selectivity trends. CHO* dissociation is difficult on Pd and Pt surfaces due to its endothermic reaction energy and high activation barrier; hence these are superior rWGs catalysts. Whereas on Ni, Rh and Ru surfaces, CHO* dissociation is exothermic, the barrier for CHO* dissociation is comparable to CO* desorption (an endothermic step) and thus CH₄ is the dominant CO₂ hydrogenation product. Furthermore, Ru exhibits the most exothermic CHO* dissociation free energy of the compared metals and is consistently shown to be the best monometallic methanation catalyst. It is worth mentioning that the mechanism of rWGS on late transition metals was recently shown to occur through COOH* formation and dissociation on Pt and Pd and via direct CO₂

dissociation on Rh and Ru.³⁰ These mechanistic differences are consistent with our results and do not impact our analysis, because regardless of the mechanism, CO* desorption remained the RLS for rWGS on all metals.

Differences in free energies of the CHO* dissociation elementary step among the compared metals can be decomposed into the impacts of constitutive species. The free energy of CHO* formation, remember this is essentially the adsorption energy of this species, for the considered late transition metals is shown in Figure 3.8b. Minimal differences exist between the CHO* formation energies on the compared metals due to a direct correlation of the free energy of CHO* formation to the free energy of C* formation (shown in green color bars on Figure 3.8b), which also varies little on the compared metals. The story is similar for the formation free energy of CH*, due again to direct correlation to C* formation energy, where minimal variation across the compared metals cannot account for the switch from endothermic to exothermic free energy of the CHO* dissociation step. Finally, Figure 3.8b shows that variations in the O* formation free energy exhibit a significant, ~1 eV, difference comparing Pt and Pt to Ni, Ru and Rh. Clearly the change in O* formation free energy across the late transition metals is primarily responsible for the trends in CHO* dissociation free energy (and as a result CHO* dissociation activation barrier) and thus dictates the switch in CO₂ reduction selectivity from CO to CH₄ observed in this series of late transition metal catalysts. The competition between CO and CH₄ production in CO₂ reduction by H₂ seems to be controlled by the strength of the atomic oxygen-metal surface interaction, which induces a thermodynamic bias towards CH*

formation thereby facilitating the kinetics for CH₄ production, without significantly impacting the CO production kinetics.

It is interesting to consider our results in light of previous studies that implicate the role of atomic oxygen adsorption energy for understanding CO₂ reduction on metal surfaces. As mentioned above, it was recently shown that the mechanism of rWGS differs on late transition metals switching from a COOH* mediated CO₂ dissociation on Pt, Pd and Ag to direct CO₂ dissociation on Ni, Rh and Cu.³⁰ It was observed that the increased oxygen adsorption energy on more reactive metals facilitated the direct CO₂ dissociation pathway through the relationship between the oxygen adsorption energy and the CO₂ dissociation barrier. Further, a recent report of descriptor based design of catalysts for CO₂ hydrogenation to CH₃OH found that an optimum oxygen adsorption energy exists to maximize CH₃OH selectivity that is similar to the oxygen adsorption energy on Cu.⁷ This occurs due to the relationship between most intermediates in the CH₃OH synthesis pathway and oxygen adsorption energy through scaling relations. Coupling these results with ours, we observe that increasing oxygen adsorption energy among late-transition and noble metal catalysts is related to increasing levels of CO₂ reduction by H₂. For example, the weakest oxygen adsorption occurs on Ag, Pt and Pd where CO (a 2e⁻ reduction from CO₂) is the dominant product. Cu is the next weakest O* adsorbing metal and produces a combination of CO and CH₃OH (a 6e⁻ reduction from CO₂). Finally the stronger O* adsorbing metals (Ni, Rh and Ru) produce predominantly CH₄ (8e⁻ reduction from CO₂). The higher exothermicity of the CO_x hydrogenation steps induced by increasing O* adsorption energy and the resulting impact on the kinetics of the reaction, determines the level of CO₂

reduction past the mildest reduction product, CO. Fundamentally this can be understood by considering that reduction of CO₂ occurs effectively via the breaking of C-O bonds, whereby strong interactions between the metal surface and O* coupled with reasonable H* coverage, facilitates the breaking of C-O bonds and the hydrogenation of intermediates. It is worth noting that even if the primary reaction pathway towards CH₄ formation on less reactive metals (Pd and Pt) does not proceed through CHO* formation and dissociation, it must always involve a dissociation step resulting in an adsorbed O* or OH* species on the catalyst surface. Thus, the strength of the metal-O* interaction will always dictate the relative thermodynamic favorability of CH₄ formation pathway and the kinetics of the reaction.

Summarizing these findings, the C* formation free energy varies little across late transition metals and as a result, the CO*, CH* and CHO* formation free energies also vary by only a small amount due to correlations between the formation free energy of C* and these species. Because of these minimal variations, the energetics of the RLS for rWGS, CO* desorption, are similar for late transition metals. However, the O* formation free energy varies with a step function like behavior moving from Pt and Pd to Ni, Rh and Ru and due to existing scaling relations a similar step-function change in the free energy and activation energy for CHO* dissociation exists. This causes a switch in selectivity among late transition metals when CHO* dissociation kinetics become more favorable than CO* desorption. The difference in trends associated with the adsorption energy of species binding through C* and O* was recently associated with a difference in the dominant forces controlling the strength of adsorbate metal binding (attraction for C* based species

adsorption and repulsion for O* based species adsorption)^{56,84–87} It was shown that while the adsorption energy of species binding through C* and O* both trend with the d-band energy of metal surfaces to a varying degree, the p-band characteristics also are important in controlling adsorption energies. Variations in the relative contribution of d-band and p-band interactions account for variations in the trends of adsorption energies of species binding through O* and C* across late transition metals and therefore selectivity in CO₂ reduction by H₂. Our mechanistic conclusions agree with a recent assertion that selectivity in CO₂ reduction can be correlated with the d-band center.¹⁹ However, we point to the importance of differentiation between adsorbates binding through C* and O* on the kinetics of competing rWGS and methanation steps and the role that both d-band and p-band characteristics play in dictating this differentiation.

3.5. Conclusions

The mechanism of CO₂ reduction was investigated over Ru(0001) using DFT calculations and mean field microkinetic modeling. A reaction mechanism consisting of 18 elementary steps was proposed. Energetic pathways of competing reactions were explored and direct CO₂ dissociation followed by hydrogenation of CO* to CHO* was identified as the prominent pathway for CH₄ production. The microkinetic model successfully predicted experimentally observed trends of surface coverage variations with temperature and reactant partial pressures, as well as CH₄ selectivity and rate dependence on feed composition. It was demonstrated through sensitivity analysis that CHO*→CH*+O* is the RLS in CH₄ formation, whereas CO* desorption is the RLS for CO production via rWGS. Although CHO* dissociation and CO* desorption steps control selectivity, comparison of

these species binding energies among late transition metal catalysts does not explain experimentally observed differences in selectivity. On the other hand, the tendency of the late transition metals for CH₄ formation was found to correlate well with the affinity of the metals for O* binding. It is shown that depth of catalytic CO₂ reduction by H₂ on late transition metal catalysts is directly related to the catalysts' oxygen adsorption strength, where weaker oxygen binding metals can only reduce CO₂ mildly to CO, whereas stronger oxygen binding metals reduce CO₂ more deeply to CH₄.

3.6. References

1. Bell, A. T., Gates, B. C. & Ray, D. *Basic Research Needs: Catalysis for Energy*. U.S. Department of Energy (2008). doi:10.2172/927492
2. Khatri, R. A., Chuang, S. S. C., Soong, Y. & Gray, M. Thermal and chemical stability of regenerable solid amine sorbent for CO₂ capture. *Energy and Fuels* **20**, 1514–1520 (2006).
3. Hicks, J. C. *et al.* Designing adsorbents for CO₂ capture from flue gas-hyperbranched aminosilicas capable of capturing CO₂ reversibly. *J. Am. Chem. Soc.* **130**, 2902–2903 (2008).
4. Jones, C. W. CO₂ Capture from Dilute Gases as a Component of Modern Global Carbon Management. *Annu. Rev. Chem. Biomol. Eng.* **2**, 31–52 (2011).
5. Yu, C. H., Huang, C. H. & Tan, C. S. A review of CO₂ capture by absorption and adsorption. *Aerosol Air Qual. Res.* **12**, 745–769 (2012).
6. Yu, K. M. K., Curcic, I., Gabriel, J. & Tsang, S. C. E. Recent advances in CO₂ capture and utilization. *ChemSusChem* **1**, 893–899 (2008).
7. Studt, F. *et al.* Discovery of a Ni-Ga catalyst for carbon dioxide reduction to methanol. *Nat. Chem.* **6**, 320–324 (2014).
8. Liu, C. *et al.* Carbon Dioxide Conversion to Methanol over Size-selected Cu₄ Clusters at Low Pressures. *J. Am. Chem. Soc.* **137**, 8676–8679 (2015).
9. Behrens, M. *et al.* The Active Site of Methanol Synthesis over Cu/ZnO/Al₂O₃ Industrial Catalysts. *Science* **336**, 893–897 (2012).
10. Abe, T., Tanizawa, M., Watanabe, K. & Taguchi, A. CO₂ methanation property of Ru nanoparticle-loaded TiO₂ prepared by a polygonal barrel-sputtering method. *Energy Environ. Sci.* **2**, 315–321 (2009).
11. Jacquemin, M., Beuls, A. & Ruiz, P. Catalytic production of methane from CO₂ and H₂ at low temperature: Insight on the reaction mechanism. *Catal. Today* **157**, 462–466 (2010).
12. Beuls, A. *et al.* Methanation of CO₂: Further insight into the mechanism over Rh/ γ -Al₂O₃ catalyst. *Appl. Catal. B Environ.* **113–114**, 2–10 (2012).
13. Karelavic, A. & Ruiz, P. Mechanistic study of low temperature CO₂ methanation over Rh/TiO₂ catalysts. *J. Catal.* **301**, 141–153 (2013).
14. Solymosi, F. & Erdöhelyi, A. Hydrogenation of CO₂ to CH₄ over alumina-supported noble metals. *J. Mol. Catal.* **8**, 471–474 (1980).
15. Ravindranathan Thampi, K., Kiwi, J. & Grätzel, M. Methanation and photo-methanation of carbon dioxide at room temperature and atmospheric pressure.

Nature **327**, 506–508 (1987).

16. Solymosi, F., Erdöhelyi, A. & Bánsági, T. Methanation of CO₂ on Supported Rhodium Catalysts. *J. Catal.* **68**, 371–382 (1981).
17. Solymosi, F., Erdöhelyi, A. & Kocsis, M. Methanation of CO₂ on Supported Ru Catalysts. *J. Chem. Soc., Faraday Trans. 1* **77**, 1003–1012 (1981).
18. Peebles, D. E., Goodman, D. W. & White, J. M. Methanation of carbon dioxide on Ni(100) and the effects of surface modifiers. *J. Phys. Chem.* **87**, 4378–4387 (1983).
19. Porosoff, M. D. & Chen, J. G. Trends in the catalytic reduction of CO₂ by hydrogen over supported monometallic and bimetallic catalysts. *J. Catal.* **301**, 30–37 (2013).
20. Yaccato, K. *et al.* Competitive CO and CO₂ methanation over supported noble metal catalysts in high throughput scanning mass spectrometer. *Appl. Catal. A Gen.* **296**, 30–48 (2005).
21. Weatherbee, G. D. & Bartholomew, C. H. Hydrogenation of CO₂ on Group VIII Metals, II. Kinetics and Mechanism of CO₂ Hydrogenation on Nickel. *J. Catal.* **77**, 460–472 (1982).
22. Panagiotopoulou, P., Kondarides, D. I. & Verykios, X. E. Selective methanation of CO over supported noble metal catalysts: Effects of the nature of the metallic phase on catalytic performance. *Appl. Catal. A Gen.* **344**, 45–54 (2008).
23. Matsubu, J. C., Yang, V. N. & Christopher, P. Isolated Metal Active Site Concentration and Stability Control Catalytic CO₂ Reduction Selectivity. *J. Am. Chem. Soc.* **137**, 3076–3084 (2015).
24. Wang, W., Wang, S., Ma, X. & Gong, J. Recent advances in catalytic hydrogenation of carbon dioxide. *Chem. Soc. Rev.* **40**, 3703–3727 (2011).
25. Panagiotopoulou, P., Kondarides, D. I. & Verykios, X. E. Mechanistic aspects of the selective methanation of CO over Ru/TiO₂ catalyst. *Catal. Today* **181**, 138–147 (2012).
26. Wang, W. & Gong, J. Methanation of carbon dioxide: an overview. *Front. Chem. Sci. Eng.* **5**, 2–10 (2011).
27. Kuśmierz, M. Kinetic study on carbon dioxide hydrogenation over Ru/ γ -Al₂O₃ catalysts. *Catal. Today* **137**, 429–432 (2008).
28. Gogate, M. R. & Davis, R. J. Comparative study of CO and CO₂ hydrogenation over supported Rh-Fe catalysts. *Catal. Commun.* **11**, 901–906 (2010).
29. Trovarelli, A., Mustazza, C., Dolcetti, G., Kašpar, J. & Graziani, M. Carbon dioxide hydrogenation on rhodium supported on transition metal oxides. *Appl.*

- Catal.* **65**, 129–142 (1990).
30. Dietz, L., Piccinin, S. & Maestri, M. Mechanistic Insights Into CO₂ Activation via Reverse Water-Gas Shift On Metal Surfaces. *J. Phys. Chem. C* **119**, 4959–4966 (2015).
 31. Akamaru, S., Shimazaki, T., Kubo, M. & Abe, T. Density functional theory analysis of methanation reaction of CO₂ on Ru nanoparticle supported on TiO₂ (101). *Appl. Catal. A Gen.* **470**, 405–411 (2014).
 32. Zhang, S.-T., Yan, H., Wei, M., Evans, D. G. & Duan, X. Hydrogenation mechanism of carbon dioxide and carbon monoxide on Ru(0001) surface: a density functional theory study. *RSC Adv.* **4**, 30241–30249 (2014).
 33. Alfonso, D. R. Further Theoretical Evidence for Hydrogen-Assisted CO Dissociation on Ru(0001). *J. Phys. Chem. C* **117**, 20562–20571 (2013).
 34. Falconer, J. L. & Zağli, E. Adsorption and Methanation of Carbon Dioxide on a Nickel/Silica Catalyst. *J. Catal.* **62**, 280–285 (1980).
 35. Marwood, M., Doepper, R. & Renken, A. In-situ surface and gas phase analysis for kinetic studies under transient conditions The catalytic hydrogenation of CO₂. *Appl. Catal. A Gen.* **151**, 223–246 (1997).
 36. Prairie, M. R., Renken, A., Highfield, J. G., Ravindranathan Thampi, K. & Grätzel, M. A fourier transform infrared spectroscopic study of CO₂ methanation on supported Ruthenium. *J. Catal.* **129**, 130–144 (1991).
 37. Eckle, S., Anfang, H.-G. & Behm, R. J. Reaction Intermediates and Side Products in the Methanation of CO and CO₂ over Supported Ru Catalysts in H₂-Rich Reformate Gases. *J. Phys. Chem. C* **115**, 1361–1367 (2011).
 38. Cheng, D., Negreiros, F. R., Aprà, E. & Fortunelli, A. Computational Approaches to the Chemical Conversion of Carbon Dioxide. *ChemSusChem* **6**, 944–965 (2013).
 39. Vesselli, E. *et al.* Hydrogen-Assisted Transformation of CO₂ on Nickel: The Role of Formate and Carbon Monoxide. *J. Phys. Chem. Lett.* **1**, 402–406 (2010).
 40. Falsig, H. *et al.* Trends in the catalytic CO oxidation activity of nanoparticles. *Angew. Chemie - Int. Ed.* **47**, 4835–4839 (2008).
 41. Zhang, C. J., Hu, P. & Alavi, A. A density functional theory study of CO oxidation on Ru(0001) at low coverage. *J. Chem. Phys.* **112**, 10564–10570 (2000).
 42. Henderson, M. A. & Worely, S. D. An infrared study of the hydrogenation of carbon dioxide on supported rhodium catalysts. *J. Phys. Chem.* **89**, 1417–1423 (1985).
 43. Gupta, N. M. *et al.* FTIR Spectroscopic Study of the Interaction of CO₂ and

- CO₂+H₂ over Partially Oxidized Ru/TiO₂ Catalyst. *J. Catal.* **146**, 173–184 (1994).
44. Loveless, B. T., Buda, C., Neurock, M. & Iglesia, E. CO chemisorption and dissociation at high coverages during CO hydrogenation on Ru catalysts. *J. Am. Chem. Soc.* **135**, 6107–6121 (2013).
 45. Fajín, J. L. C., Gomes, J. R. B. & D. S. Cordeiro, M. N. Mechanistic Study of Carbon Monoxide Methanation over Pure and Rhodium- or Ruthenium-Doped Nickel Catalysts. *J. Phys. Chem. C* 150710111820004 (2015). doi:10.1021/acs.jpcc.5b01837
 46. Inderwildi, O. R., Jenkins, S. J. & King, D. A. Fischer-Tropsch Mechanism Revisited: Alternative Pathways for the Production of Higher Hydrocarbons from Synthesis Gas. *J. Phys. Chem. C* **112**, 1305–1307 (2008).
 47. Andersson, M. P. *et al.* Structure sensitivity of the methanation reaction: H₂-induced CO dissociation on nickel surfaces. *J. Catal.* **255**, 6–19 (2008).
 48. Ojeda, M. *et al.* CO activation pathways and the mechanism of Fischer–Tropsch synthesis. *J. Catal.* **272**, 287–297 (2010).
 49. Abild-Pedersen, F. Computational catalyst screening: Scaling, bond-order and catalysis. *Catal. Today* **272**, 6–13 (2016).
 50. Grabow, L. C. & Mavrikakis, M. Mechanism of Methanol Synthesis on Cu through CO₂ and CO Hydrogenation. *ACS Catal.* **1**, 365–384 (2011).
 51. Nørskov, J. K., Abild-Pedersen, F., Studt, F. & Bligaard, T. Density functional theory in surface chemistry and catalysis. *Proc. Natl. Acad. Sci. U. S. A.* **108**, 937–43 (2011).
 52. Campbell, C. T. Micro- and macro-kinetics: their relationship in heterogeneous catalysis. *Top. Catal.* **1**, 353–366 (1994).
 53. Campbell, C. T. Finding the Rate-Determining Step in a Mechanism. *J. Catal.* **204**, 520–524 (2001).
 54. Brønsted, J. N. Acid and Basic Catalysis. *Chem. Rev.* **5**, 231–338 (1928).
 55. Evans, M. G. & Polanyi, M. Further Considerations on the thermodynamics of chemical equilibria and reaction rates. *J. Chem. Soc., Faraday Trans. 1* **32**, 1333–1359 (1936).
 56. Medford, A. J. *et al.* Activity and Selectivity Trends in Synthesis Gas Conversion to Higher Alcohols. *Top. Catal.* **57**, 135–142 (2014).
 57. Medford, A. J. *et al.* From the Sabatier principle to a predictive theory of transition-metal heterogeneous catalysis. *J. Catal.* **328**, 36–42 (2015).

58. Zhu, Y.-A., Chen, D., Zhou, X.-G. & Yuan, W.-K. DFT studies of dry reforming of methane on Ni catalyst. *Catal. Today* **148**, 260–267 (2009).
59. Peterson, A. a., Abild-Pedersen, F., Studt, F., Rossmeisl, J. & Nørskov, J. K. How copper catalyzes the electroreduction of carbon dioxide into hydrocarbon fuels. *Energy Environ. Sci.* **3**, 1311–1315 (2010).
60. Mhadeshwar, A. B. & Vlachos, D. G. Hierarchical, multiscale surface reaction mechanism development: CO and H₂ oxidation, water–gas shift, and preferential oxidation of CO on Rh. *J. Catal.* **234**, 48–63 (2005).
61. Enkovaara, J. *et al.* Electronic structure calculations with GPAW: a real-space implementation of the projector augmented-wave method. *J. Phys. Condens. Matter* **22**, 253202 (2010).
62. Hammer, B., Hansen, L. B. & Nørskov, J. K. Improved adsorption energetics within density-functional theory using revised Perdew-Burke-Ernzerhof functionals. *Phys. Rev. B* **59**, 7413–7421 (1999).
63. Wellendorff, J. *et al.* Density functionals for surface science: Exchange-correlation model development with Bayesian error estimation. *Phys. Rev. B* **85**, 235149 (2012).
64. Panagiotopoulou, P., Kondarides, D. I. & Verykios, X. E. Selective methanation of CO over supported Ru catalysts. *Appl. Catal. B Environ.* **88**, 470–478 (2009).
65. Abrevaya, H., Cohn, M. J., Targos, W. M. & Robota, H. J. Structure Sensative Reactions Over Supported Ruthenium Catalysts during Fischer Tropsch Synthesis. *Catal. Letters* **7**, 183–189 (1990).
66. Abdel-Mageed, A. M., Eckle, S. & Behm, R. J. High selectivity of supported Ru catalysts in the Selective CO Methanation - Water makes the difference. *J. Am. Chem. Soc.* 150626152444002 (2015). doi:10.1021/jacs.5b03689
67. Panagiotopoulou, P. & Kondarides, D. I. Effect of the nature of the support on the catalytic performance of noble metal catalysts for the water–gas shift reaction. *Catal. Today* **112**, 49–52 (2006).
68. Monkhorst, H. J. & Pack, J. D. Special points for Brillouin-zone integrations. *Phys. Rev. B* **13**, 5188–5192 (1976).
69. Henkelman, G., Uberuaga, B. P. & Jónsson, H. A climbing image nudged elastic band method for finding saddle points and minimum energy paths. *J. Chem. Phys.* **113**, 9901–9904 (2000).
70. Bahn, S. R. & Jacobsen, K. W. An object-oriented scripting interface to a legacy electronic structure code. *Comput. Sci. Eng.* **4**, 56–66 (2002).
71. Cramer, C. J. *Essentials of computational chemistry*. (Wiley, 2004).

72. Gokhale, A. A., Kandoi, S., Greeley, J. P., Mavrikakis, M. & Dumesic, J. A. Molecular-level descriptions of surface chemistry in kinetic models using density functional theory. *Chem. Eng. Sci.* **59**, 4679–4691 (2004).
73. Dumesic, J. a., Rudd, D. F., Aparicio, L. M., Rekoske, J. E. & Trevino, A. A. *The Microkinetics of Heterogeneous Catalysis*. (American Chemical Society, 1993).
74. Gusmão, G. S. & Christopher, P. A General and Robust Approach for Defining and Solving Microkinetic Catalytic Systems. *AIChE J.* **61**, 188–199 (2015).
75. Ciobîcă, I. M. & Santen, V. Carbon monoxide dissociation on planar and stepped Ru(0001) surfaces. *J. Phys. Chem. B* **107**, 3808–3812 (2003).
76. Shetty, S., Jansen, A. P. J. & van Santen, R. A. Direct versus hydrogen-assisted CO dissociation. *J. Am. Chem. Soc.* **131**, 12874–12875 (2009).
77. Li, H., Fu, G. & Xu, X. A new insight into the initial step in the Fischer-Tropsch synthesis: CO dissociation on Ru surfaces. *Phys. Chem. Chem. Phys.* 16686–16694 (2012). doi:10.1039/c2cp43176a
78. Studt, F., Abild-Pedersen, F., Varley, J. B. & Nørskov, J. K. CO and CO₂ Hydrogenation to Methanol Calculated Using the BEEF-vdW Functional. *Catal. Letters* **143**, 71–73 (2013).
79. Grabow, L. C., Gokhale, A. a., Evans, S. T., Dumesic, J. a. & Mavrikakis, M. Mechanism of the Water Gas Shift Reaction on Pt: First Principles, Experiments, and Microkinetic Modeling. *J. Phys. Chem. C* **112**, 4608–4617 (2008).
80. Grabow, L. C., Hvolbæk, B. & Nørskov, J. K. Understanding Trends in Catalytic Activity: The Effect of Adsorbate–Adsorbate Interactions for CO Oxidation Over Transition Metals. *Top. Catal.* **53**, 298–310 (2010).
81. Duyar, M. S., Ramachandran, A., Wang, C. & Farrauto, R. J. Kinetics of CO₂ methanation over Ru/ γ -Al₂O₃ and implications for renewable energy storage applications. *J. CO₂ Util.* **12**, 27–33 (2015).
82. Medford, A. J. *et al.* Assessing the reliability of calculated catalytic ammonia synthesis rates. *Science* **345**, 197–200 (2014).
83. Calle-Vallejo, F., Loffreda, D., Koper, M. T. M. & Sautet, P. Introducing structural sensitivity into adsorption – energy scaling relations by means of coordination numbers. *Nat. Chem.* **7**, 403–410 (2015).
84. Montemore, M. M. & Medlin, J. W. A Unified Picture of Adsorption on Transition Metals through Different Atoms. *J. Am. Chem. Soc.* **136**, 9272–9275 (2014).
85. Montemore, M. M. & Medlin, J. W. Predicting and comparing C-M and O-M bond strengths for adsorption on transition metal surfaces. *J. Phys. Chem. C* **118**, 2666–2672 (2014).

86. Greeley, J., Nørskov, J. K. & Mavrikakis, M. Electronic structure and catalysis on metal surfaces. *Annu. Rev. Phys. Chem.* **53**, 319–348 (2002).
87. Xin, H. & Linic, S. Exceptions to the d-band model of chemisorption on metal surfaces: The dominant role of repulsion between adsorbate states and metal d-states. *J. Chem. Phys.* **132**, 221101 (2010).

Chapter 4

Scaled Degree of Rate Control: Identifying Elementary Steps that Control Differences in Performance of Transition Metal Catalysts

4.1. Summary

Degree of rate control (DoRC) analysis is a valuable method for identifying influential elementary steps in heterogeneous catalytic processes. By extending the concept of DoRC through explicit incorporation of intrinsic parametric correlations relating chemistry on transition metal surfaces, we introduce the concept of “scaled degree of rate control” (S-DoRC). This approach identifies relevant rate or selectivity controlling steps that are tunable within the confines of parametric correlations on transition metal surfaces, by quantitatively modifying conclusions drawn from typical DoRC analysis through the use of empirically derived scaling factors for each elementary step.

4.2. Introduction

Heterogeneous catalytic reactions on metal surfaces involve complex networks of elementary step surface processes. Critical to the design of catalytic metals that maximize rates or selectivity is identifying elementary surface reactions involved in the minimum energy pathway from reactants to products and the rate limiting steps (RLS). This has become possible with advancements in parallel computing coupled with Density Functional Theory (DFT) and statistical mechanics based approaches used to calculate the energetic landscapes. DFT-derived thermochemical parameters and activation energies of elementary catalytic steps implemented in mean field microkinetic models have been shown to predict the kinetic behavior of catalysts with reasonable accuracy.¹⁻⁶

To identify influential elementary steps that control the behavior of catalytic reactions, sensitivity analyses are implemented that probe correlations between perturbations in the kinetics of single elementary steps and the overall rate or selectivity of a microkinetic system. A commonly used method, proposed by Campbell et al.⁷, is a sensitivity analysis based on the RLS concept. Having a fully defined microkinetic model of a reaction system on a given catalyst (typically a known good catalyst), the “degree of rate control” (DoRC or X_{RC}) of each elementary step is calculated as the ratio of the change in apparent activation free energy of the overall reaction system over the change in activation free energy of a single elementary step while holding constant the kinetics of all other elementary steps, as described in equation 4.1.

$$X_{RC,i} = \left(\frac{\partial \ln r}{\partial \left(-G_i^\ddagger / RT \right)} \right)_{G_{j \neq i}^\ddagger, \Delta G_i} \quad (4.1)$$

In equation 4.1, r is the overall reaction rate, G_i^\ddagger is the free energy of transition state i (∂G_i^\ddagger is equivalent to a change in the activation free energy ($\partial G_{A,i}$), while the initial state energy is kept constant), ΔG_i is the reaction energy of step i , R is the gas constant and T is the temperature. DoRC is an extremely useful approach that provides valuable insights into kinetics of complex reactions and has been used successfully to identify kinetically important elementary steps, thereby facilitating the identification of novel catalysts.^{6,8-10}

In the DoRC analysis, reaction energies are treated as independent. However, adsorption and transition state energies on metal surfaces are related through parametric correlations, such as linear scaling (LS)¹¹ and Brønsted-Evans-Polanyi (BEP)^{12,13} relations, which limit the possibility of modifying the energy of an individual state without affecting energies of other states. Thus, while the DoRC approach identifies kinetic bottlenecks in reaction pathways, by not including parametric correlations, DoRC does not necessarily distinguish the steps whose energies can be effectively modified by changing catalyst compositions.

In an important recent publication, Sutton et al. showed that the inclusion of parametric correlations in a DoRC analysis has a significant influence on the identified rate and selectivity controlling steps.¹⁴ The results suggest that parametric correlations between the energies of all elementary steps should be included within sensitivity analyses on microkinetic systems to correctly identify the steps which could be tuned to control reaction

rate or selectivity. However, in the work by Sutton et al., parametric correlations were derived from a statistical error analysis of a huge number of DFT calculations on a single metal. Because parametric correlations between all species were only derived from a single metal, this approach does not allow the identification of which steps control differences in catalytic performance between different materials, i.e. those that can be used as descriptors to identify new catalysts.

Here we propose an analytical approach for the identification of elementary steps that are responsible for differences in catalytic behavior of transition metal catalysts by explicitly incorporating BEP and LS parametric correlations in X_{RC} calculations. We introduce the concept of “scaled degree of rate control” (S-DoRC or X_{S-RC}), an easily implemented extension of DoRC method. Because LS and BEP parametric correlations were developed based on trends in energetics for a range of transition metals, the S-DoRC approach identifies only rate or selectivity controlling steps that are tunable within the confines of LS and BEP relations, rather than identifying all steps that could influence rate or selectivity, but cannot be independently modified as in the typical DoRC analysis.

4.3. Microkinetic model: CO₂ reduction by H₂

To demonstrate the S-DoRC approach, we focus on the reaction of CO₂ reduction by H₂ on a Ru catalyst surface, which we previously studied using a full DFT microkinetic model with 18 elementary steps.^{15,16} The mechanism includes competing pathways of CO₂ methanation to form CH₄ and reverse water gas shift to form CO. We use a simplified model including 13 elementary steps shown in Table 4.1, which reproduces the same reaction orders, rates and selectivity as the 18-step model. The 5 removed steps were

previously determined to have no influence on calculated rates and selectivity. Rather than using our DFT calculated reaction energies, we derived the reaction enthalpies (ΔH) and activation barriers (H_{Af}) of the elementary steps using O* and C* binding energies on Ru and previously developed LS and BEP relations, so-called transition state scaling relations listed in Table 4.2. The correlations are developed for (211) transition metal surfaces using DFT calculated raw electronic energies, which are converted to formation energy by defining gas phase CH₄, H₂O, and H₂ as common references.¹⁷ Vibrational frequencies of the intermediate and transition states are assumed constant on transition metals and the values calculated for Ru(111) surface were used to convert the electronic energies to enthalpies.¹⁵ The forward and reverse pre-exponential factors (A_f , A_r) are also obtained from DFT calculated vibrational frequencies on Ru(111) surface (see Section 3.3.4). An in house Python code based on a quasi-Newtonian scheme was used to solve a linearized set of mole balance equations at pseudo steady state.¹⁶

Table 4.1. The 13 elementary steps involved in the mechanism of CO₂ reduction by H₂ on Ru catalyst surface. Reaction enthalpies and activation barriers are derived LS relations, the forward and reverse pre-exponential factors are derived from DFT calculations.

		ΔH (eV)	H_{Af} (eV)	A_f (s ⁻¹)	A_r (s ⁻¹)
1	CO ₂ +*→CO ₂ *	0.00	0.00	2 × 10 ⁸	2 × 10 ¹³
2	H ₂ +2*→2H*	-0.69	0.00	8 × 10 ⁸	1 × 10 ¹⁰
3	CO ₂ *+*→CO*+O*	-0.88	0.21	1 × 10 ¹²	4 × 10 ¹³
4	CO*+H*→CHO*+*	0.90	0.79	3 × 10 ¹³	1 × 10 ¹⁰
5	O*+H*→OH*+*	0.33	1.15	2 × 10 ¹³	6 × 10 ¹²
6	OH*+H*→H ₂ O*+*	0.31	0.87	2 × 10 ¹³	2 × 10 ¹²
7	CHO*+*→CH*+O*	-0.68	1.03	1 × 10 ¹³	1 × 10 ¹³
8	CH*+H*→CH ₂ *+*	0.60	0.91	1 × 10 ¹³	6 × 10 ¹²
9	CH ₂ *+H*→CH ₃ *+*	-0.18	0.56	1 × 10 ¹³	5 × 10 ¹²
10	CH ₃ *+H*→CH ₄ *+*	-0.35	0.69	4 × 10 ¹²	2 × 10 ¹²
11	CH ₄ *→CH ₄ +*	0.00	0.00	2 × 10 ¹³	3 × 10 ⁸
12	H ₂ O*→H ₂ O+*	0.21	0.21	5 × 10 ¹⁰	3 × 10 ⁸
13	CO*→CO+*	1.23	1.23	6 × 10 ⁷	2 × 10 ⁸

Table 4.2. The scaling relations used in the microkinetic model of CO₂ reduction mechanism, developed for adsorbed species and transition states on (211) surfaces of transition metals¹⁷

Adsorbed Species Scaling		Transition State Scaling	
Relations		Relations	
1	$E_{H^{*h}} = 0.16E_{C^{*f}} - 0.604$	8	$E_{CO-O^{*s}} = 0.687(E_{CO^{*s}} + E_{O^{*s}}) + 0.313E_{CO_2^*} + 0.95$
2	$E_{CO^{*s}} = 0.56E_{C^{*f}} + 0.52$	9	$E_{H-CO^{*s}} = 0.77(E_{CO^{*s}} + E_{H^{*h}}) + 1.12$
3	$E_{OH^{*s}} = 0.552E_{O^{*s}} - 0.494$	10	$E_{O-H^{*s}} = 0.867(E_{O^{*s}} + E_{H^{*h}}) + 0.841$
4	$E_{CH^{*f}} = 0.777E_{C^{*f}} - 0.13$	11	$E_{H-OH^{*s}} = 0.756(E_{OH^{*s}} + E_{H^{*h}}) + 0.874$
5	$E_{CH_2^{*t}} = 0.447E_{C^{*f}} + 0.469$	12	$E_{O-CH^{*s}} = 0.814(E_{O^{*s}} + E_{CH^{*f}}) + 2.312$
6	$E_{CH_3^{*t}} = 0.205E_{C^{*f}} + 0.469$	13	$E_{H-CH^{*f}} = 0.904(E_{CH^{*f}} + E_{H^{*h}}) + 1.085$
7	$E_{HCO^{*s}} = 0.378E_{C^{*f}} + 1.227$	14	$E_{H-CH_2^{*t}} = 1.012(E_{CH_2^{*t}} + E_{H^{*h}}) + 0.622$
		15	$E_{H-CH_3^{*t}} = 0.957(E_{CH_3^{*t}} + E_{H^{*h}}) + 0.737$

(a) Derived using a BEP correlation¹⁸ and gas phase CO₂ formation energy for E_{CO2*}

(b) Step, fourfold, terrace and h reservoir sites are denoted by s, f, t and h respectively.

The use of energies derived from scaling relations in the microkinetic model allows us to generate volcano plots of CH₄ and CO formation turn over frequency (TOF) and CH₄ selectivity as a function of two simple descriptors, the adsorption energies of C* (E_{C^*}) and O* (E_{O^*}) (Figure 4.1a, b). The 13-step model with energies derived from scaling relations predicts CH₄ formation TOF (about 10⁻⁴ s⁻¹) and selectivity (about 1) on Ru, which are in excellent agreement with the results obtained from the full DFT model on Ru. The formation energies of C* and O* on (211) surface terminations of late transition metals (Pd, Pt, Ni, Co, Ir, Rh and Ru) were obtained from reference¹⁷. The results in Figure 4.1b capture the experimentally observed trends of CO₂ reduction selectivity on transition

metals; Ru, Rh, Co, Ir and Ni are known to mainly produce CH₄, whereas Pd and Pt are good CO producing catalysts.¹⁵

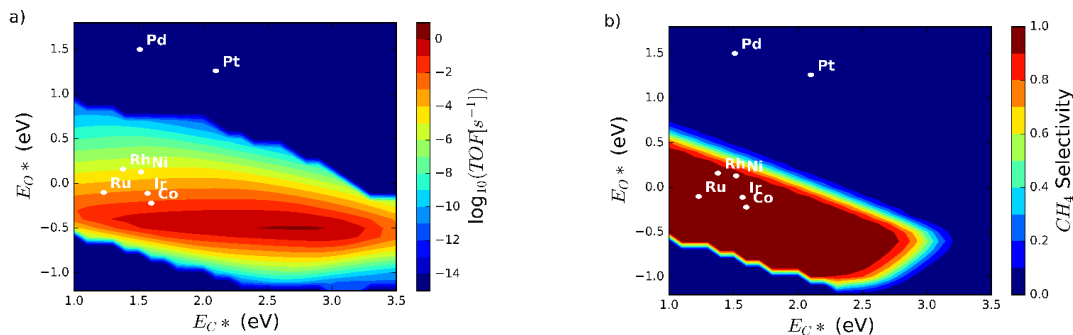


Figure 4.1. Volcano plots of **a)** CH₄ formation activity ($\log_{10}\text{TOF}$), and **b)** CH₄ selectivity for CO₂ reduction by H₂ on (211) surfaces of transition metals, plotted as a function of adsorption energies of O* and C* at T=500 K, P=1 atm and stoichiometric reactant concentrations.

In Figure 4.1b it is seen that the trend in CH₄ selectivity, comparing the late transition metals, is predominantly related to variations in E_{O^*} . CO selective catalysts (Pt and Pd) consistently exhibit a ~1.5 eV weaker O* binding energy than CH₄ selective catalysts, whereas Pd exhibits a similar E_{C^*} compared to the CH₄ selective catalysts and Pt has a much weaker E_{C^*} than the CH₄ selective catalysts. In our previous analysis of this system, we used the DoRC analysis to identify two elementary steps, CHO* dissociation to CH* and O*, and CO* desorption, to be equally important in controlling CO₂ reduction selectivity on Ru. To analyze this conclusion more deeply, inspection of Figure 4.1b shows that the CO* adsorption energy, which is directly correlated with E_{C^*} through the LS relations (See equation 2 in Table 4.2), varies little across the investigated metals and cannot account for differences in selectivity. On the other hand, the CHO* dissociation barrier is directly correlated with E_{O^*} (See equation 9 in Table 4.2),¹⁷ because this elementary step has a late transition state and thus the activation energy is correlated to the

energy of the final state ($E_{O^*} + E_{CH^*}$). Based on the observed trend in selectivity correlating with strong variations in E_{O^*} , Figure 4.1b, it can be concluded that CHO^* dissociation is the elementary step predominantly controlling differences in CO_2 reduction selectivity among late transition metals. While our qualitative analysis using information from parametric correlations (the volcano plot) coupled with DoRC analysis allow us to identify the critical step controlling differences in catalytic performance, it would be preferred to develop an analytical approach that directly differentiates the elementary steps that could control performance from those that control differences between catalyst performances.

4.4. Scaled Degree of Rate Control

The first approach to explicitly include parametric correlations in the DoRC analysis, proposed by Nørskov et al.¹⁹, is the Degree of catalyst control (X_{CC}). In this approach, the sensitivity of the overall reaction rate is analyzed in response to a perturbation in one descriptor energy, (E_{C^*}) using parametric correlations to relate this perturbation to changes in energetics of all related reaction intermediates. This analysis tells us how good the catalyst is, with X_{CC} close to 1 being a bad catalyst and X_{CC} close to 0 being a good catalyst. However, because this approach treats the descriptors (E_{C^*} and E_{O^*}) independently, and because the perturbation is applied simultaneously to all elementary steps that relate to each descriptor, X_{CC} does not allow us to identify elementary steps that control differences in catalytic performance of transition metals.

To expand on the X_{CC} concept and allow us to analytically include LS and BEP correlations in DoRC analysis, we apply perturbations to each elementary step separately and introduce a scaling relationship between all transition states and a single descriptor.

Although E_{O^*} and E_{C^*} are typically treated as independent descriptors,²⁰ we introduce a linear scaling correlation between E_{O^*} and E_{C^*} on late transition metals, based on previously calculated energies on (211) surfaces of late transition metals (Pd, Pt, Ni, Co, Ir, Rh and Ru) and their alloys, as shown in Figure 4.2.^{21,22} The mean absolute error of the correlation, MAE=0.34, is only slightly larger than typical MAE for DFT-derived LS and BEP correlations (~ 0.2), and this we believe is accurate enough for the purpose of predicting catalytic behavior trends and relative importance of key kinetic parameters. Deviations from this correlation are expected for a wider range of metals (coinage metals for example). However, given the importance of late transition metals for a broad set of catalytic reactions involving organic molecules, this approach can be applied for many important systems such as reactions involving oxygenation or reduction of hydrocarbons or oxygenated hydrocarbons and selective conversion of biomass-based molecules on late transition metal surfaces.

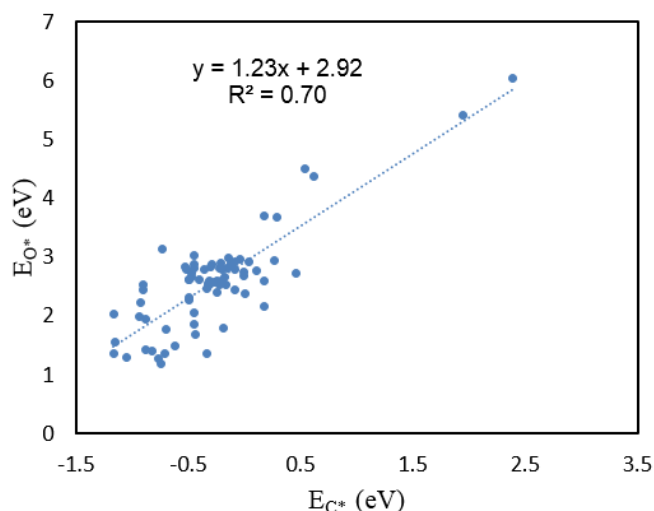


Figure 4.2. Linear correlation between the adsorption energies of O^* and C^* on (211) surfaces of late transition metals alloys of Pd, Pt, Ni, Co, Ir, Rh and Ru. Data obtained from reference 21 and 22

This simplification allows us to linearly relate all transition state energies to E_{O^*} as the single descriptor. To incorporate these correlations in the DoRC analysis (see below), energies are converted to enthalpies. The derivatives of activation barriers with respect to H_{O^*} , are then defined as a constant scaling factor $\alpha_i = dH_{A,i}/dH_{O^*}$ (where $H_{A,i} = H_{TS} - H_{IS}$), because they are linearly related through the transition state scaling relations. The calculated values of α are shown in Table 4.3 for the 13 elementary steps. These are calculated using the LS and BEP relations from Table 4.2 and H_{C^*} and H_{O^*} correlations from Figure 4.2 for each elementary step. For example, α_{10} calculation is shown below:

$$\alpha_{10} = \frac{dH_{A,10}}{dH_{O^*}} = \frac{d}{dH_{O^*}}(H_{H-CH_3^*} - H_{CH_3^*} - H_{H^*}) \quad (4.2)$$

Incorporating scaling relations 15, 4 and 1 from Table 4.2 in equation 4.2 (enthalpy corrections are constant values that results in zero when differentiated), α_{10} is determined to be -0.01.

$$\alpha_{10} = \frac{d}{dH_{O^*}}(-0.043(0.205H_{C^*})) - \frac{d}{dH_{O^*}}(0.043(0.16H_{C^*})) \quad (4.3)$$

$$\alpha_{10} = -0.009 \frac{dH_{C^*}}{dH_{O^*}} - 0.007 \frac{dH_{C^*}}{dH_{O^*}} = -0.016 \times \frac{1}{1.23} = -0.01 \quad (4.4)$$

Table 4.3. The calculated values of $\alpha_i=dH_{A,i}/dH_{O^*}$, X_{RC} , X_{SC} , X_{S-RC} and X_{S-SC} for the 13 elementary steps involved in the mechanism of CO₂ reduction by H₂.

	X_{RC,CH_4}	$X_{RC,CO}$	X_{SC,CH_4}	α_i	X_{S-RC,CH_4}	$X_{S-RC,CO}$	X_{S-SC,CH_4}
1 CO ₂ +*→CO ₂ *	0.00	0.00	0.00	0.00	0.00	0.00	0.00
2 H ₂ +2*→2H*	0.00	0.00	0.00	0.00	0.00	0.00	0.00
3 CO ₂ *+*→CO*+O*	0.00	0.01	-0.02	0.97	0.00	0.01	-0.01
4 CO*+H*→CHO*+*	0.00	0.00	0.00	-0.12	0.00	0.00	0.00
5 O*+H*→OH*+*	-0.05	0.22	-0.26	-0.15	0.01	-0.03	0.04
6 OH*+H*→H ₂ O*+*	-0.11	0.00	0.00	-0.17	0.02	0.00	0.00
7 CHO*+*→CH*+O*	1.05	-0.22	1.28	1.02	1.07	-0.23	1.30
8 CH*+H*→CH ₂ *+*	0.00	0.00	0.00	-0.07	0.00	0.00	0.00
9 CH ₂ *+H*→CH ₃ *+*	0.00	0.00	0.00	0.01	0.00	0.00	0.00
10 CH ₃ *+H*→CH ₄ *+*	0.00	0.00	0.00	-0.01	0.00	0.00	0.00
11 CH ₄ *→CH ₄ +*	0.00	0.00	0.00	0.00	0.00	0.00	0.00
12 H ₂ O*→H ₂ O+*	0.00	0.00	0.00	0.00	0.00	0.00	0.00
13 CO*→CO+*	0.00	0.99	-0.98	-0.41	0.00	-0.40	0.40

The scaling factor (α_i) is a measure of how significantly each activation barrier is perturbed due to a small change in H_{O^*} . This is graphically depicted in Figure 4.3 for a few steps in the CO₂ reduction reaction being perturbed from the potential energy surface on Ru.

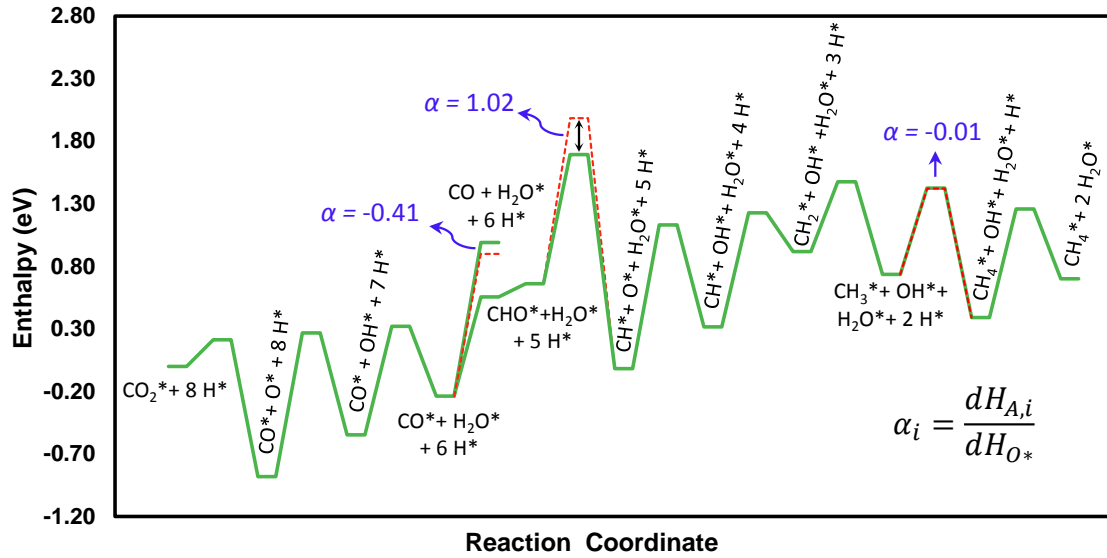


Figure 4.3. Potential energy surface for CO₂ reduction by H₂ on Ru (211). The perturbation of transition state enthalpies with the descriptor enthalpy ($\alpha_i = dH_{A,i}/dH_{O^*}$) is shown for a few steps relative to energy pathway on Ru. In this case H_O* was perturbed by 0.3 eV, to enable visual comparison of α for different elementary steps. The α values were calculated using scaling relation for (211) transition metal surfaces (for details see supporting information section S.5).

For the small perturbations applied here, entropies can be assumed constant across transition metals, thus X_{RC} can be written in terms of enthalpies, as shown in equation 4.5.

$$X_{RC,i} = \left(\frac{\partial \ln r}{\partial \left(-H_{A,i} / RT \right)} \right)_{H_{A,j \neq i}, \Delta H_i} \quad (4.5)$$

We then explicitly include the correlations between $H_{A,i}$ and H_{O^*} by applying the chain rule to equation 4.5, thus the S-DoRC of an elementary step ($X_{S-RC,i}$) is defined as follows:

$$X_{S-RC,i} = \left(\frac{\partial \ln r}{\partial \left(-H_{A,i} / RT \right)} \right)_{H_{A,j \neq i}, \Delta H_i} \times \frac{dH_{A,i}}{dH_{O^*}} = \alpha_i X_{RC,i} \quad (4.6)$$

As equation 4.6 shows, given the previously developed parametric correlations, the S-DoRC can be easily calculated as the product of the $X_{RC,i}$ and the scaling factor α_i . Similarly a scaled degree of selectivity control can be defined as $X_{S-SC,i} = \alpha_i X_{SC,i}$ (equation 4.7), where $X_{SC,i}$ is the degree of selectivity control (equation 4.8). Selectivity, S , was calculated as the ratio of CH_4 formation to CO formation rates, $S = \text{TOF}(\text{CH}_4)/\text{TOF}(\text{CO})$.

$$X_{S-SC,i} = \left(\frac{\partial \ln S}{\partial \left(-H_{A,i} / RT \right)} \right)_{H_{A,j \neq i}, \Delta H_i} \times \frac{dH_{A,i}}{dH_{O^*}} = \alpha_i X_{SC,i} \quad (4.7)$$

$$X_{SC,i} = \left(\frac{\partial \ln S}{\partial \left(-H_{A,i} / RT \right)} \right)_{H_{A,j \neq i}, \Delta H_i} \quad (4.8)$$

The calculated values of α_i for transition states of surface reactions and desorption elementary steps in the 13-step mechanism range from -0.41 for CO^* desorption to 1.02 for CHO^* dissociation, Table 4.3. The negative value of α indicates a change in the activation barrier of the corresponding elementary step in the opposite direction of the change in H_{O^*} . For example, the CO^* desorption energy (activation barrier of step 13) is increased when a negative perturbation is applied to H_{O^*} . Variations in α values clearly show that transition state energies are correlated with H_{O^*} very differently; activation enthalpies of only a few elementary steps change significantly with changes in H_{O^*} ($\alpha \sim$

0.9-1.0), while the majority of steps show little or no change with variations in H_O^* ($\alpha \sim 0$). The largest change is observed for CO_2^* and CHO^* dissociation steps ($\alpha = 0.97$ and 1.02 respectively), where a new metal-O* bond is formed in the reaction, followed by CO^* desorption ($\alpha = -0.41$) where a metal-C* bond is broken. This tells us that the transition states of elementary steps involving a gain or loss of metal-C* or metal-O* bond are affected the most by a change in catalyst material and likely are the steps that contribute to the differences in the catalytic behavior of transition metals. Conversely, activation energies of steps with similar primary metal-adsorbate bonding motifs for reactants and products exhibit small α , and thus are not likely to be related to differences in catalytic performance among transition metals.

The calculated X_{RC} and X_{S-RC} values for the CH_4 and CO formation pathways in the 13-step model are presented in Table 4.3. The X_{S-RC} and X_{RC} values of important elementary steps (steps 3-7 and 13 from Table 4.1) are compared for CH_4 and CO formation reactions in Figures 4.4a and b, respectively. The DoRC analysis, as shown in Figure 4.4a, identified CHO^* dissociation to be the primary RLS for CH_4 formation ($X_{RC} = 1.05$), with OH^* and H_2O^* formation steps also having small and negative values ($X_{RC} = -0.05$ and -0.11 respectively). However, the X_{S-RC} for the latter two steps are reduced to negligible values (0.01 and 0.02 respectively), while CHO^* dissociation ($\alpha = 1$) is the only step that controls the CH_4 formation rate on late transition metals ($X_{S-RC} = 1.07$), Figure 4.4a. Comparison of X_{RC} and X_{S-RC} for the CO^* desorption step in the CO formation reaction (0.99 and -0.4, respectively) shows that the CO^* desorption step plays a less significant role in controlling the rate if parametric correlations are taken into consideration. It should be noted that the

negative value of X_{S-RC} for CO* desorption step is a result of a positive perturbation in the CO* desorption enthalpy in response to a negative perturbation in H_{O^*} ($\alpha = -0.4$).

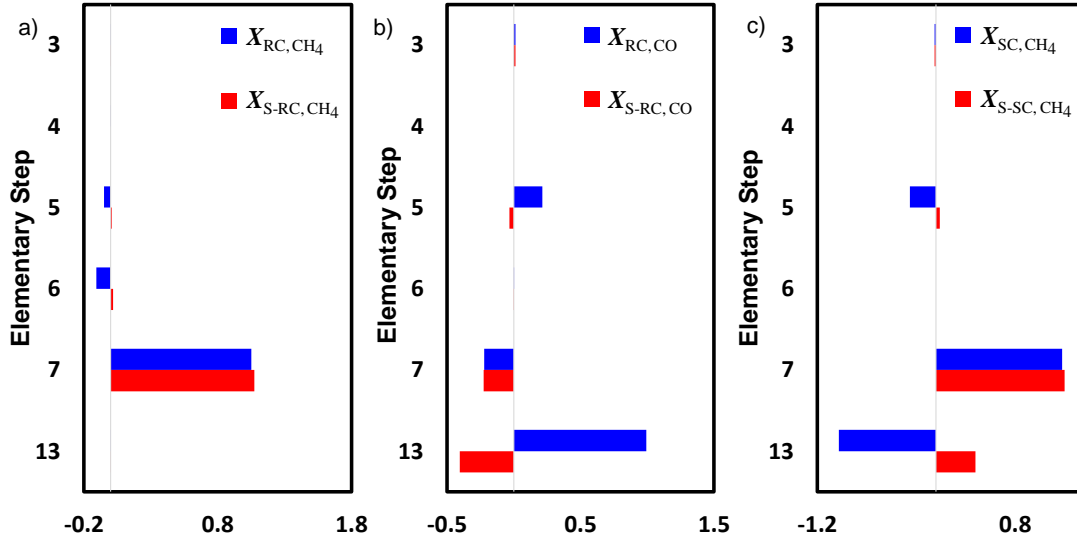


Figure 4.4. Calculated X_{RC} and X_{S-RC} are compared for the pathways of **a)** CH₄ formation and **b)** CO formation for the important elementary steps involved in the mechanism of CO₂ reduction by H₂. The calculated X_{SC} and X_{S-SC} of the CH₄ formation pathway for the important elementary steps are compared in **c)**.

Comparison of X_{SC} and X_{S-SC} in Table 4.3 and Figure 4.4c shows a profound result that incorporating parametric correlations in the sensitivity analysis influences the identified selectivity controlling steps significantly. The X_{SC} analysis identified CHO* dissociation ($X_{SC, 7} = 1.28$) and CO* desorption ($X_{SC, 13} = -0.98$) as the main selectivity controlling steps, Figure 4.4c. The OH* formation step also had a small influence on CH₄ formation selectivity with $X_{SC, 5} = -0.26$. X_{S-SC} data presented with red bars in Figure 4.4c shows that the impact of CO* desorption ($X_{S-SC, 13} = 0.4$) and OH* formation ($X_{S-SC, 5} = 0.04$) steps on selectivity are reduced significantly when parametric correlations are incorporated in the sensitivity analysis, whereas CHO* dissociation remains the dominant selectivity controlling step ($X_{S-SC, 7} = 1.3$).

4.5. Conclusions

The results discussed in the previous sections demonstrate that the S-DoRC approach allows us to analytically obtain identical conclusions to the qualitative conclusions derived from using the volcano plot in Figure 4.1b to interpret our previous DoRC analysis. Simply, while DoRC analysis demonstrates that CHO* dissociation and CO* desorption could both influence CO₂ reduction selectivity, S-DoRC demonstrates that CHO* dissociation is much more important than CO* desorption for controlling differences in catalytic performance of different metals. By including intrinsic parametric correlations of the late transition metals in the $X_{S,SC}$ calculations, we are able to guide the sensitivity analysis in the specific direction that is relevant for transition metals and directly identify the parameters that are most influential and tunable across these surfaces.

It is important to discuss the limitations of the proposed approach, specifically related to the scaling relationship between E_{C^*} and E_{O^*} . This relationship, as developed here, is only reasonable for the series of late transition metals we considered. While these materials are broadly applicable for a huge number of important catalytic reactions, a similar approach to what we proposed could be used where the influence of parametric correlations relating to E_{C^*} and E_{O^*} are treated independently.¹⁹ This likely would be required for analysis of catalytic materials composed of more noble metals (Ag, Au, Cu).

We use a simple reaction to demonstrate the S-DoRC method. However, it is expected that this analysis will have an even more significant influence on more complex reactions where multiple elementary steps control the kinetics. It is also important to note that, although in our analysis we rely on a linear correlation between E_{C^*} and E_{O^*} which is

applicable only for the late transition metals explored here, considering the importance of these metals in a wide range of selective hydrogenation and oxygenation reactions, the S-DoRC approach as proposed here is applicable to many important reaction systems. In addition, by using recently developed LS relations for active site coordination numbers, the S-DoRC framework could be implemented (using different parametric correlations) to identify elementary steps that control differences of catalytic performance on active sites of surfaces with similar composition, but different geometries.²³ Another important conclusion that arises from our study is that elementary steps involving a gain or loss of metal-C* or metal-O* bond when moving from reactant to product are likely the steps that contribute to the differences in the catalytic behavior of late transition metals.

4.6. References

1. Dumesic, J. a., Rudd, D. F., Aparicio, L. M., Rekoske, J. E. & Trevino, A. A. *The Microkinetics of Heterogeneous Catalysis*. (American Chemical Society, 1993).
2. Studt, F. *et al.* Discovery of a Ni-Ga catalyst for carbon dioxide reduction to methanol. *Nat. Chem.* **6**, 320–324 (2014).
3. Grabow, L. C. & Mavrikakis, M. Mechanism of Methanol Synthesis on Cu through CO₂ and CO Hydrogenation. *ACS Catal.* **1**, 365–384 (2011).
4. Stegelmann, C., Schiødt, N. C., Campbell, C. T. & Stoltze, P. Microkinetic modeling of ethylene oxidation over silver. *J. Catal.* **221**, 630–649 (2004).
5. Nørskov, J. K., Abild-Pedersen, F., Studt, F. & Bligaard, T. Density functional theory in surface chemistry and catalysis. *Proc. Natl. Acad. Sci. U. S. A.* **108**, 937–43 (2011).
6. Meskine, H., Matera, S., Scheffler, M., Reuter, K. & Metiu, H. Examination of the concept of degree of rate control by first-principles kinetic Monte Carlo simulations. *Surf. Sci.* **603**, 1724–1730 (2009).
7. Campbell, C. T. Micro- and macro-kinetics: their relationship in heterogeneous catalysis. *Top. Catal.* **1**, 353–366 (1994).
8. Linic, S., Jankowiak, J. & Barteau, M. A. Selectivity driven design of bimetallic ethylene epoxidation catalysts from first principles. *J. Catal.* **224**, 489–493 (2004).
9. Kandoi, S. *et al.* Prediction of Experimental Methanol Decomposition Rates on Platinum from First Principles. *Top. Catal.* **37**, 17–28 (2006).
10. Wolcott, C. a., Medford, A. J., Studt, F. & Campbell, C. T. Degree of rate control approach to computational catalyst screening. *J. Catal.* **330**, 197–207 (2015).
11. Abild-Pedersen, F. *et al.* Scaling Properties of Adsorption Energies for Hydrogen-Containing Molecules on Transition-Metal Surfaces. *Phys. Rev. Lett.* **99**, 16105 (2007).
12. Brønsted, J. N. Acid and Basic Catalysis. *Chem. Rev.* **5**, 231–338 (1928).
13. Evans, M. G. & Polanyi, M. Further Considerations on the thermodynamics of chemical equilibria and reaction rates. *J. Chem. Soc., Faraday Trans. 1* **32**, 1333–1359 (1936).
14. Sutton, J. E., Guo, W., Katsoulakis, M. A. & Vlachos, D. G. Effects of correlated parameters and uncertainty in electronic-structure-based chemical kinetic modelling. *Nat. Chem.* **8**, 331–337 (2016).
15. Avanesian, T., Gusmão, G. S. & Christopher, P. Mechanism of CO₂ reduction by H₂ on Ru(0001) and general selectivity descriptors for late-transition metal

- catalysts. *J. Catal.* **343**, 86–96 (2016).
16. Gusmão, G. S. & Christopher, P. A General and Robust Approach for Defining and Solving Microkinetic Catalytic Systems. *AIChE J.* **61**, 188–199 (2015).
 17. Medford, A. J. *et al.* Activity and Selectivity Trends in Synthesis Gas Conversion to Higher Alcohols. *Top. Catal.* **57**, 135–142 (2014).
 18. Dietz, L., Piccinin, S. & Maestri, M. Mechanistic Insights Into CO₂ Activation via Reverse Water-Gas Shift On Metal Surfaces. *J. Phys. Chem. C* **119**, 4959–4966 (2015).
 19. Nørskov, J. K., Bligaard, T. & Kleis, J. Rate control and reaction engineering. *Science* **324**, 1655–6 (2009).
 20. Montemore, M. M. & Medlin, J. W. Predicting and comparing C-M and O-M bond strengths for adsorption on transition metal surfaces. *J. Phys. Chem. C* **118**, 2666–2672 (2014).
 21. Hummelshøj, J. S., Abild-Pedersen, F., Studt, F., Bligaard, T. & Nørskov, J. K. CatApp: a web application for surface chemistry and heterogeneous catalysis. *Angew. Chem. Int. Ed. Engl.* **124**, 278–280 (2012).
 22. Studt, F. *et al.* CO hydrogenation to methanol on Cu–Ni catalysts: Theory and experiment. *J. Catal.* **293**, 51–60 (2012).
 23. Calle-Vallejo, F., Loffreda, D., Koper, M. T. M. & Sautet, P. Introducing structural sensitivity into adsorption – energy scaling relations by means of coordination numbers. *Nat. Chem.* **7**, 403–410 (2015).

Chapter 5

Adsorbate Specificity in Hot Electron Driven Photochemistry on Catalytic Metal Surfaces

5.1. Summary

Visible light driven catalysis on metal surfaces and nanoparticles has attracted significant attention in recent years as a potential route for driving selective chemical reactions that are difficult to achieve with thermal energy. It is most often assumed that photochemistry on metal surfaces occurs through a substrate-mediated process of adsorbate-metal bond photo-excitation, although crucial underlying phenomena controlling the efficiency of this process are still poorly understood. In this work, substrate mediated photochemistry on metal surfaces was analyzed by combining dynamical models associated with the metal substrate photo-excitation and electron-mediated bond-activation processes. An extended version of two-temperature model was utilized to treat temporal evolution of photo-excited charge carriers in the metal substrate. The electron-induced

adsorbate dynamics on the metal surface was modeled using a non-adiabatic, first-principles based inelastic electron scattering model. Photo-activation of three well studied reactions on Pt(111) surfaces, CO and NO desorption and O diffusion, were chosen as model systems. Through our approach, we addressed unresolved issues associated with adsorbate specific reaction time scales and wavelength and temperature dependent behavior. The results suggest that activating adsorbate-metal bonds with targeted photon wavelengths and at optimal system temperatures could provide an approach to control selectivity in photon driven reactions on metal surfaces.

5.2. Introduction

A long-standing goal in the field of surface chemistry is demonstrating that UV or visible photon excitation of catalytically active transition and noble metal surfaces can be used to drive selective chemical reactions that cannot be achieved purely by thermal excitation. The catalytic functionality of metal surfaces (manifested through small activation barriers for chemical reactions) suggests that photo-excitation of catalytic metals could drive chemistry through non-thermal, electron mediated, processes even though the lifetimes of excited charge carriers in metals and adsorbates on metal surfaces are very short. Indeed chemistry induced by non-thermal processes via photon excitation of metal surfaces has been demonstrated, spanning a wide range of systems from desorption or diffusion of adsorbates on single crystals driven by femtosecond laser illumination to complete catalytic reactions driven by low intensity continuous wave (CW) excitation on metal nanoparticle surfaces.¹⁻⁹ Importantly, there have been unique demonstrations of photons driving catalytic chemistry at metal surfaces that cannot be achieved by thermal

excitation of the same systems, garnering significant interest in the physical processes governing these chemical transformations.^{10–13}

Multiple mechanisms have been explored to describe photon mediated, electron-driven chemistry on metal surfaces, including direct intramolecular photo-excitation of adsorbates, direct photo-excitation of adsorbate-metal bonds and substrate-mediated photo-excitation of adsorbates or adsorbate-metal bonds.^{12,14–16} The latter mechanism has received the most attention, although underlying mechanistic details of this process still remain unaddressed.^{17–20} In the substrate mediated photo-excitation mechanism, photons are absorbed by bulk metal states forming uncorrelated electron-hole pairs. The continuous density of electronic states (DOS) in metals allows the photo-excitation process to induce electronic transitions between any states separated by the metal Fermi Level (ε_F) and an energy equal to the energy of impinging photons, thus creating a distribution of possible electronic excitations (Figure 5.1a). The primary, non-thermalized, excited electrons and holes inelastically scatter off excited or ground state charge carriers in the metal on the time scale of 10-100 fs after photon absorption, spreading their energy into the sea of metal states near ε_F . 100-1000 fs after photon absorption, redistribution of the primary charge carrier energy evolves into a charge carrier distribution that resembles a Fermi-Dirac (FD) thermal distribution, albeit at a higher temperature than phonons in the metal lattice. Finally, electrons couple to the metal lattice phonons to thermally heat the system towards equilibrium between the metal electrons and phonons on a time scale of 1 to 10s of ps. Concurrently with these processes, energetic, or “hot” charge carriers that scatter to the adsorbate-metal interface can transiently transfer into adsorbate states and induce

chemistry through the deposition of vibrational energy into adsorbate nuclear motion via Franck Condon transitions. These processes are all highly dynamic, occurring on ultrafast time scales and must be treated simultaneously to accurately depict these non-equilibrium systems (Figure 5.1b).

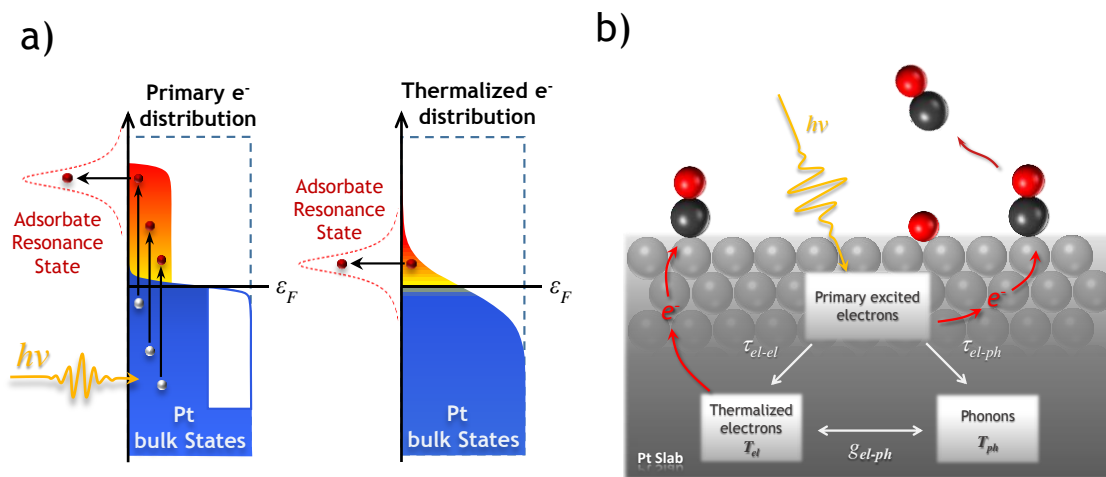


Figure 5.1: Schematic of substrate-mediated photochemistry on metal surfaces. **a)** Primary electron-hole distribution in a metal upon photon excitation at the instant of photon absorption (Left panel). The continuous metal DOS, allowing transitions between any states across ε_F and separated by incident photon energy with equal probability, creates a uniform primary electron-hole distribution, which evolves into a thermalized (FD) electron distribution 100-1000 fs after the photon absorption (Right panel). Photo-excited “hot” electrons can scatter through adsorbate resonance states inducing chemistry. **b)** Schematic of the energy exchange processes among primary excited electrons, thermalized electrons and phonons with different time scales.

Although hole mediated chemistry has been identified and could play an important role in photon driven chemical processes on metal surfaces,^{21,22} a majority of studies have focused on chemistry driven by transient scattering of energetic, hot electrons through normally unpopulated adsorbate states. The process of energy deposition from a photon induced energetic electron distribution in the metal into adsorbate nuclear motion has been theoretically treated using two primary approaches, frictional coupling and explicit treatment of adsorbate movement along electronically excited state potential energy

surfaces (PES).^{16,23–25} In the frictional model it is assumed that the photo-excited metal system reaches a FD type electronic distribution instantaneously and that the temporally evolving electron energy distribution can be described using an effective electronic temperature. The temporal evolution of the electronic temperature following the absorption of a laser pulse by the metal is then treated through coupling of the electron temperature bath to the vibrational temperature of the adsorbate (defined by a Bose-Einstein distribution) and the metal lattice temperature. In this approach, energy transfer from the metal to the adsorbate is considered an adiabatic process. Coupled heat transfer equations, with empirically derived coefficients defining the rate of energy transfer between each temperature bath, describe the temporal evolution of the different temperatures after a laser pulse. Photon induced chemical reactivity is calculated by integrating over the fraction of molecules that gain sufficient energy to traverse an activation barrier. This approach is a simple extension of the well-known two-temperature model (TTM) to include the adsorbate vibrational temperature and has had success in predicting behaviors of systems under very high fluence (where the thermalization process is fast due to high scattering rates) and addressing the temporally evolving system from the point of view of the metal substrate.^{19, 25–27} However, the applicability toward modeling the behavior of systems under low intensity CW illumination is limited due to the explicit assumption that non-thermalized charge carriers (those that do not follow a FD behavior) do not participate in driving chemistry.²⁸ In addition, the empirical nature of defining adsorbate dependent frictional coefficients limits the potential for predicting unique selective behavior of photon driven reactions at metal surfaces.

Modeling photon driven reactions at metal surfaces through explicit treatment of adsorbate nuclear motion on excited state PES has also received significant attention and is generally called dynamics induced by electronic transitions (DIET).^{17,23,29–32} In this model it is assumed that inelastic scattering of an electron through an adsorbate resonance state shifts the system onto a PES associated with a transiently formed negative ion (TNI), where equilibrium bond distances are different than on the ground state PES. The differing equilibrium bond distances on the TNI PES, compared to the ground state PES, induce transient forces on the adsorbate or adsorbate-metal bonds thereby depositing vibrational energy in the system through a non-adiabatic process. At the core of modeling this mechanism is the calculation of transition matrices to define the probability that a molecule will gain vibrational energy due to transient localization of an energetic electron in a normally unpopulated adsorbate resonant state. This probability is dependent primarily on the TNI lifetime and shapes of the TNI and ground state PES. Once probabilities have been calculated for all possible vibrational transitions, the probability that an inelastic electron scattering event induces chemistry is calculated by a summation of the transition probabilities that cross the activation barrier on the ground state PES. The DIET mechanism has been shown to properly treat the known transition of reaction rate dependence on photon intensity from the linear to super-linear power law regime.^{33,34} In addition, advances in quantum chemical calculation methods for obtaining ground and excited PES of adsorbates on metal surfaces are beginning to allow relatively accurate description of adsorbate dependent behavior in electron driven processes at metal surfaces.³⁵ However, unlike the friction approach, the DIET modeling only describes the

inelastic scattering of energetic electrons through adsorbate resonance state and it does not treat the temporally evolving electronic structure in the metal following photon absorption.

In this work, we couple a first principles based treatment of the DIET mechanism with an extended version of the TTM to simultaneously treat the dynamics of the photo-excited metal and inelastic electron-adsorbate scattering processes, which allows us to address several unanswered questions about the substrate-mediated photo-excitation mechanism. Coupling the dynamics of the temporally evolving electronic structure of the metal with the dynamics of the transient hot electron transfer to the adsorbate are requisite for exploring the temporal and photon energy dependent phenomenon.³ Specifically we focus on adsorbate dependent behavior in three well studied model processes, CO and NO desorption from Pt surfaces and O diffusion on Pt surfaces under low photo-excitation densities ($<10^{-3}$ e⁻/atom), which are characteristic of the linear regime of rate dependence on intensity. We address how the shape of the adsorbate PES and unpopulated resonance states impact the time scale of photon driven reactivity, importance of non-thermalized electrons, wavelength dependent reaction cross-sections and the impact of temperature. It is shown that the potential for controlling selectivity in catalysis on metal surfaces by the substrate mediated photo-excitation mechanism is dictated by the role that non-thermalized electrons and initial system temperature play in driving chemistry. We expect these results and our general approach will provide a theoretical underpinning for understanding low intensity photo-excitation driven chemical processes at the surface of transition and plasmonic metal nanoparticles, which have received significant recent attention.³⁶⁻⁴²

5.3. Theoretical Methods

In this section, we outline our approach to model photon driven reactions at metal surfaces within the substrate mediated photo-excitation mechanism. A model system consisting of a spatially isolated 5-nanometer diameter Pt particle illuminated by a single photon of a given energy, between 1.5-4 eV, is analyzed. By comparing chemical reactivity driven by single photon absorption events at different wavelengths, reaction cross-section, or quantum yield, as a function of photon energy can be calculated. The excitation density is consistent with a single ultrafast laser pulse with 10 fs width and 1-4 $\mu\text{J}/\text{cm}^2$ energy flux, or a CW source with flux $< \sim 1 \text{ W}/\text{cm}^2$. It is assumed that the electron distribution and temperature are homogeneous within the nanoparticles, that the metal electronic DOS is constant within the energy window $-4 \text{ eV} < \epsilon_F < 4 \text{ eV}$, and that primary energetic electrons “cool” into a thermalized FD distribution following the Fermi-liquid theory. All of these assumptions could be relaxed within the framework of the proposed model.

An approach developed by Carpena, the extended two-temperature model (ETTM), is used to describe the temporally evolving electronic structure of the metal particle after photon absorption.⁴³ Surface chemistry driven by inelastic electron scattering is modeled using the first principles-based approach developed by Olsen et al., an extension of a model previously developed by Gadzuk, where PES's for the adsorbate systems are calculated using Density Functional Theory (DFT).^{30,44,45} This approach provides a quantitative value for the probability that an energetic electron with a given energy can induce a reaction. We couple the electron energy dependent reaction probability with the temporally evolving electron energy distribution from the ETTM to provide a time dependent instantaneous

reaction rate induced by a single photon absorption event, effectively allowing comparison of photon energy dependent quantum yields. We assumed that the amount of energy that a photo-excited electron deposits into the vibrational motion of an adsorbate system is small enough to ignore in the overall photon energy balance in the ETM, which is justified by the relatively small calculated quantum yields. The low quantum yields and our focus on a single photon absorption event allow us to also exclude the adsorbate coverage dependent phenomenon in our treatment. We start by explaining the fundamentals of the ETM, followed by a description of the DIET modeling approach and finally the time dependent reaction rates, and photon wavelength and adsorbate dependent quantum yield calculations.

5.3.1. Extended Two Temperature Model

The first necessary component to an effective approach that models the substrate mediated photo-excitation mechanism is having a reasonable description of the temporally evolving metal electronic structure following a photon absorption event. We are interested in understanding photon driven reactions on metal surfaces (more specifically on nanoparticle surfaces) in the limit of the linear rate dependence on source intensity. Effectively this means that each photon absorption event is significantly separated from the next, such that sequential photon absorption events are discrete (greater than ~ 100 ps between sequential photon absorption events). We define a photon source power, $P(t')$, that has a Gaussian temporal profile with a full-width half maximum (FWHM) of 10 fs and is equal to 1 quantum of photon energy when integrated over time. Most metals exhibit a photon energy dependent absorption cross section in the visible and UV regime, α , and

thus the time dependent power density absorbed by the metal ($W_a(t')$) is defined by the metal absorption cross-section multiplied by the pulse power, equation 5.1.

$$W_a(t') = \alpha P(t') \quad (5.1)$$

The photon power absorbed by the metal initially drives primary electron-hole pair excitations. Based on the assumed flat metal DOS near ε_F and identical probability for all excitations in this energetic window, the infinitesimal charge carrier excitation generated in the time interval dt' can be described by δ_i in equation 5.2, which is symmetric about ε_F .

$$\delta_i(t') = \frac{W_a(t') dt'}{g(\varepsilon_F)(h\nu)^2} \quad (5.2)$$

Here t' is the time scale of energy input into the system and is separated from the overall time, t , used to follow the temporal evolution of charge carrier distribution and the chemical reactivity. In this expression, integration of $W_a(t')dt'$ over the laser pulse duration gives the total absorbed energy by the metal, $g(\varepsilon_F)$ is the density of metal states at ε_F and $h\nu$ is the energy of the incident photon. The initial distribution of primary electron-hole pair excitations has a constant magnitude for all energies, $\varepsilon_F \pm h\nu$. The time dependent distribution of primary excitations, which is our definition of the non-thermalized electron distribution, acts as the dynamic source of energy in the metal that spreads into a FD thermal electronic distribution and heats up the lattice. The source of primary electron-hole pair excitations, δ_i , is multiplied by decay terms in equation 5.3 to produce the infinitesimal change in the distribution of primary charge carriers (not simply the excitations as shown in equation 5.2), which is a function of time and charge carrier energy.

$$\delta_p(\varepsilon, t-t') = \delta_i(t') \exp \left[-\frac{t-t'}{\tau_0} \left(\frac{\varepsilon - \varepsilon_F}{\varepsilon_F} \right)^2 - \frac{t-t'}{\tau_{el-ph}} \right] \quad (5.3)$$

It is assumed that energy transfer from primary holes into a FD charge carrier distribution and into the lattice is identical to that of electrons and thus we focus on the electron processes.

The decay rate of primary electron energy into a thermalized FD electron distribution is defined by Fermi Liquid theory, which exhibits an inverse quadratic relationship of characteristic decay time on electron energy. This is defined in the first exponential decay term in equation 5.3, as a function of pulse time (t'), the overall time in the system (t), the primary charge carrier energy (ε), Fermi energy (ε_F), and τ_0 , which is the proportionality constant in the formulation of electron-electron relaxation time per Fermi Liquid theory, $\tau_{el-el} = \tau_0 (\varepsilon_F / (\varepsilon - \varepsilon_F))^2$. The primary electron excitations are also directly coupled to the phonon bath (describing the lattice temperature) using a characteristic time constant for electron-phonon coupling, which is independent of electron energy. Coupling of primary electron excitations to the phonon bath is captured in the second exponential decay term in equation 5.3, where τ_{el-ph} is the electron-phonon relaxation time. δ_p is a measure of how the infinitesimal primary charge carrier excitations created at t' , ($\delta_i(t')$), decay with time t following t' , relaxing into each scattering channel. Integration of these infinitesimal changes in the primary carrier distribution (δ_p) over time prior to t , as it is shown later, gives the primary electron distribution at a given time, t .

Equation 5.3 can be used to define the energy density exchange rate from primary electron-hole pair excitations into populating the thermalized FD distribution and heating

up the lattice. This approach involves separating δ_p into expressions for each decay channel, performing energy-weighted integration over electron-hole energies and a temporal integration. The energy density exchange rates from primary excitations into FD distribution ($\partial U_{el-el}/\partial t$) and lattice ($\partial U_{el-ph}/\partial t$) can be defined in terms of the infinitesimal changes of primary carrier distribution and DOS of Pt metal particles, see ref⁴³ for more details. The energy density exchange rates serve as the sources for coupling primary electronic excitations to the electronic and lattice temperatures; no direct coupling of the photon source to the electronic and lattice temperatures, as done in the standard TTM, is included.

Using the energy density exchange rates as input, a modified version of the TTM can be defined with the following pair of equations:

$$C_{el} \frac{\partial T_{el}}{\partial t} = -g_{el-ph} (T_{el} - T_{ph}) + \frac{\partial U_{el-el}}{\partial t} \quad (5.4)$$

$$C_{ph} \frac{\partial T_{ph}}{\partial t} = g_{el-ph} (T_{el} - T_{ph}) + \frac{\partial U_{el-ph}}{\partial t} \quad (5.5)$$

The time dependent energy balance between the thermalized electron and phonon baths is modeled by two differential equations where an electron-phonon coupling constant (g_{el-ph}) and the heat capacities of electrons (C_{el}) and lattice (C_{ph}) are used to describe the energy exchange between electronic temperature (T_{el}) and lattice temperature (T_{ph}) baths as a function of time. Because we have assumed a homogeneous model system in all spatial directions, there are no spatial energy conduction terms in the differential equations. The

solution of these differential equations provides T_{el} and T_{ph} as a function of time, which can be used to define the temporal evolution of the photo-excited metal electronic structure.

The temporally evolving thermalized electron distribution, due to photo-excitation of the metal, can be calculated using the temporally evolving electronic temperature (T_{el}) in a FD distribution (equation 5.6). This expression calculates how the thermalized electron energy distribution changes from the FD distribution at the initial system temperature (T_0), due to photo-excitation.

$$\Delta f_{FD}(\varepsilon, t) = \frac{1}{1 + \exp\left[\frac{(\varepsilon - \varepsilon_F)}{k_B T_{el}(t)}\right]} - \frac{1}{1 + \exp\left[\frac{(\varepsilon - \varepsilon_F)}{k_B T_0}\right]} \quad (5.6)$$

The primarily excited electron distribution at a given time t after the start of irradiation ($\Delta f_p(\varepsilon, t)$), is calculated by integrating the infinitesimal excitations and relaxations (from equation 5.3) over all previous infinitesimal time steps, equation 5.7.

$$\Delta f_p(\varepsilon, t) = \int_{-\infty}^t \delta_i(\varepsilon, t') \times \exp\left[-\frac{t-t'}{\tau_0} \left(\frac{\varepsilon - \varepsilon_F}{\varepsilon_F}\right)^2 - \frac{t-t'}{\tau_{el-ph}}\right] dt' \quad (5.7)$$

By summing the primarily excited electron distribution and the change in the thermalized electron distribution, we can define temporal evolution of the total change in the electronic structure of the metal due to photon absorption as $\Delta h_f(\varepsilon, t) = \Delta f_p(\varepsilon, t) + \Delta f_{FD}(\varepsilon, t)$. These temporally evolving descriptors of the metal electronic structure provide a measure of the density of photo-excited electrons as a function of energy and time following absorption of a single photon, which will be used in the time dependent instantaneous

reaction rate and QY calculations. All the relevant parameters used in the model are listed in Table 5.1.

Table 5.1. List of Parameters Used in Extended Two Temperature Model

Parameter		Units	ref
α	0.77-0.91	10^6 cm^{-1}	46
$g(\varepsilon_F)$	1.69	$10^{22} \text{ eV}^{-1} \text{ cm}^{-3}$	
γ^a	0.75	$10^{-3} \text{ J cm}^{-3} \text{ K}^{-2}$	47
C_{ph}	2.8	$\text{J cm}^{-3} \text{ K}$	48
g_{el-ph}	3.8-8.8	$10^{11} \text{ W cm}^{-3} \text{ K}$	47
τ_f^b	10	fs	49
θ_D	240	K	50
τ_0	1	fs	43

^a Used in the calculation of $C_{el} = \gamma T_{el}$

^b Used in the calculation of $\tau_{el-ph} = \tau_f \hbar \omega / k_B \theta_D$

5.3.2. Inelastic Electron Scattering Model

It is now necessary to define the coupling of energetic electrons to the adsorbate nuclear motion along a particular PES. Our approach follows the Menzel-Gomer-Redhead (MGR) desorption model (Figure 5.2).^{51,52} We highlight this model because our calculated PES's (see results section) exhibit repulsive TNI states that are characteristic of the MGR mechanism. In this model a photo-excited electron with initial energy ε_i (in the inelastic scattering model we use $\varepsilon_F = 0$ as reference for the energy of ε_i) inelastically scattering through an adsorbate resonance state induces a Franck-Condon excitation in the adsorbate-metal complex. The resulting TNI evolves on an elevated, repulsive PES for a short lifetime ($\tau_R \sim 1 \text{ fs}$) and experiences acceleration towards the minimum of the TNI PES at a

lengthened equilibrium bond distance, compared to the ground state PES minimum. The system returns to the ground state PES in a vibrationally excited state as the electron quenches back to the metal with energy, $\varepsilon_f < \varepsilon_i$. If the energy deposited from the electron into the PES ($\Delta\varepsilon = \varepsilon_i - \varepsilon_f$) plus the original vibrational energy of the system on the ground state PES is greater than the activation energy (E_a), the electron scattering process can induce bond breaking and surface reactions. The energy gained through the electron scattering process can also be envisioned based on the transition in vibrational energy levels (for example from m to n in Figure 5.2) of the system on the ground state PES. The dynamics of electron-adsorbate energy exchange and surface reaction probabilities strongly depend on the TNI lifetime (τ_R) and the PES shapes. The TNI lifetime is governed by the energy width of the resonant state $\tau_R = \hbar/\Gamma$, which can be measured by inverse photoemission experiments. The values of Γ used in the model for the three adsorbates and their corresponding TNI lifetimes are listed in Table 5.2 and were derived from experimental results.⁵³ The impact of the magnitude of Γ on our results will be discussed in the results section.

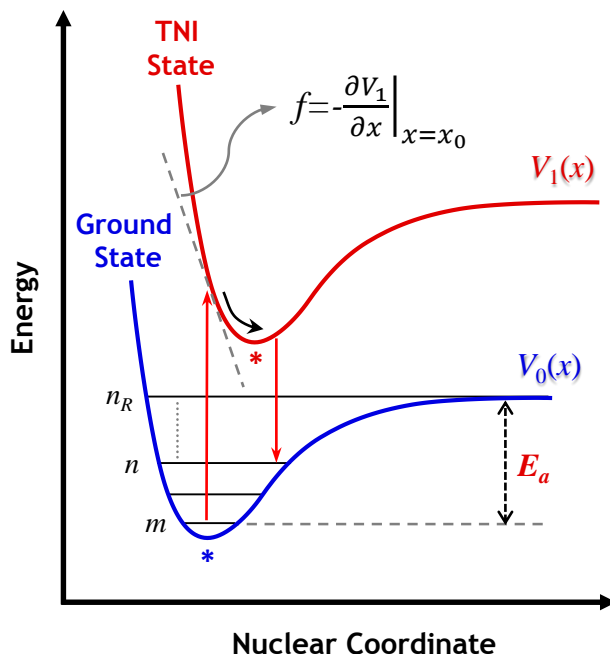


Figure 5.2: Schematic of the DIET mechanism. Energy deposition into an adsorbate-metal system during an inelastic electron scattering event occurs due to an exerted repulsive force (f) that accelerates the system along an elevated TNI PES towards a longer equilibrium bond distance. The adsorbate-metal system returns to the ground state PES in a vibrationally excited state. If sufficient vibrational energy is gained by the system to overcome an activation barrier, reactions occur. See main text for description of the variables.

Until recently, model PES's were used in theoretical treatments of photon driven reactions at metal surfaces. Advances in DFT computational methods have made it possible to calculate the excitation energies and construct TNI PES's based on first-principles calculations.^{35,54,55} The ground state and TNI PES can be obtained by calculating the energy of an adsorbate-metal system, as a function of an assumed reaction coordinate (adsorbate translational mode that dominates the reaction process). The ground state PES's used in this work were obtained using standard DFT calculations, while the Linear-Expansion Delta Self-consistent field (Δ SCF) method was used to calculate the TNI PES's. In the Δ SCF approach the total energy of the system for the TNI is calculated by placing an electron in a targeted unoccupied adsorbate state, which is defined by a linear combination

of empty Kohn Sham orbitals. The resonance energy, the energy required to excite an electron from Fermi level to the empty orbital of the adsorbate, is the difference between the total energies of the system calculated in ground and TNI states at the ground state minimum ($\varepsilon_a^0 = V_1(x_0) - V_0(x_0)$), see Figures 5.2 and 5.3. This approach has been shown to accurately calculate resonance energies for adsorbates on transition metal surfaces, when compared to experimental inverse photoemission measurements.³⁵

The PES of the O/Pt(111) system, with an O atom adsorbed on an fcc hollow site, was obtained by calculating the energy of the system as a function of the O vertical distance to Pt(111) surface. TNI formation in the O/Pt(111) system was assumed to involve the excitation of an electron from the metal ε_F to the 2p orbital of the O atom.¹² The PES of CO on atop sites and NO on hcp hollow sites on Pt(111) surfaces were obtained as a function of their internal bond lengths based on previously calculated parameters in ref ⁴⁵. The center of mass vibrational modes of the diatomic molecules were found to have minor effect in the desorption probabilities of CO and NO.⁴⁵ The presented resonant energies for both molecules were calculated by exciting an electron from the metal ε_F into $2\pi^*$ antibonding orbitals. The electron coupling with the translational modes of adsorbates in the plane parallel to the surface are neglected in this study. The vibrational frequencies of adsorbates were obtained by normal mode analysis. All relevant parameters obtained from ground state DFT and Δ SCF-DFT calculations for O, CO and NO on Pt(111) are tabulated in Table 5.2. All systems were calculated assumed a $\frac{1}{4}$ monolayer of adsorbates on the Pt(111) surface.

Table 5.2. List of Parameters Used in Inelastic Electron Scattering Model

Parameter	Units	CO	NO	O
Γ	eV	0.66 ^a	0.80 ^a	1.32 ^a
τ_R	fs	1.0	0.8	0.5
E_a	eV	1.37 ^b	1.29 ^b	0.8 ^c
\mathcal{E}_a^0	eV	3.89 ^b	1.71 ^b	1.37 ^d
$\hbar\omega$	meV	255 ^b	196 ^b	55.3 ^d
λ	meV	-145 ^b	-53 ^b	-32.4 ^d

^a ref⁵³, ^b ref⁴⁵, ^c ref²⁶, ^d ref¹²

The probabilities of photo-excited electron induced reactions are calculated using an inelastic scattering model, originally developed by Gadzuk for photo-desorption on a one-dimensional PES induced by single electrons (DIET).^{30,44} The model was recently extended by Olsen *et al.* to utilize first principles based PES's and allow for inclusion of multiple vibrational degrees of freedom and multiple electronic transitions.⁴⁵ We have employed a modified version of the one-dimensional model and strictly focus on the single excitation regime (linear rate dependence on intensity that is characteristic of low intensity photon excitation). The original model was modified to incorporate finite temperature effects through the use of an initial thermal distribution of adsorbate vibrational states (Bose-Einstein distribution) in the reaction probability calculations.³⁴

The essential function of this model is to calculate the probability that an electron with energy \mathcal{E}_i , scattering through a normally unpopulated adsorbate resonance, will deposit $\Delta\mathcal{E}$ into the ground state system PES. The interaction between the adsorbate and the metal surface is described using a Newns-Anderson type Hamiltonian shown in equations 5.8-5.11.

$$H = H_{el} + H_{ph} + H_{int} \quad (5.8)$$

$$H_{el} = \varepsilon_a^0 c_a^\dagger c_a + \sum_k \varepsilon_k c_k^\dagger c_k + \sum_k (V_{ak} c_a^\dagger c_k + V_{ak}^* c_k^\dagger c_a) \quad (5.9)$$

$$H_{ph} = \hbar\omega \left(a^\dagger a + \frac{1}{2} \right) \quad (5.10)$$

$$H_{int} = \lambda c_a^\dagger c_a (a^\dagger + a) \quad (5.11)$$

The Hamiltonian consists of an electron term (H_{el}), a phonon term (H_{ph}) and an electron-phonon interaction term (H_{int}). In the electron Hamiltonian, a localized adsorbate electronic state $|a\rangle$ with energy ε_a is coupled with the metal electronic states $|k\rangle$ with eigenvalues ε_k , through substrate-adsorbate coupling coefficients V_{ak} (Hopping matrix elements) where c, c^\dagger are the Fermion operators. The adsorbate-metal system phonon is described as a one-dimensional harmonic oscillator, with vibrational frequency ω . In a multidimensional PES this term would be a summation of the harmonic oscillators. When the adsorbate resonant state is occupied with an electron, the transient perturbation in the system results in a linear displacement of the oscillator. The interaction Hamiltonian is written in terms of the force acting on the adsorbate over the linear displacement in the reaction coordinate x . λ in equation 5.11 is the linear coupling constant, which corresponds to the force exerted on the adsorbate-metal oscillator, with reduced mass m , during the acceleration of the adsorbate on the TNI PES, as calculated by equation 5.12 (See Figure 5.2).

$$\lambda = \frac{l}{\sqrt{2}} \frac{\partial}{\partial x} V_1 \Big|_{x=x_0} \quad , \quad l = \sqrt{\frac{\hbar}{m\omega}} \quad (5.12)$$

The probability that an incident electron from the metal, with energy ε_i , scatters through the adsorbate resonance and returns to the metal with final state of energy ε_f can be obtained by calculating the reflection matrix of the Hamiltonian in equation 5.8. This has been calculated exactly in the wideband limit where the coupling coefficients V_{ak} can be assumed constant and the adsorbate resonant states are of a Lorentzian shape and centered at the resonant energy ε_a^0 .^{30,44}

The probabilities can be expressed as a function of the number of vibrational quanta gained by the adsorbate-metal complex during the scattering event ($\Delta\varepsilon = \varepsilon_i - \varepsilon_f = \Delta n \hbar \omega$). The vibrational transition probabilities, $P(m \rightarrow n)$, are calculated for any given initial vibrational state m gaining Δn ($\Delta n = m - n$) vibrational quanta. The probability of the adsorbate-metal system being in the n th vibrational state after an electron scattering event, $Q(n)$, is calculated as the sum of all the possible transitions that end up at state n as shown in equation 5.13.

$$Q(n) = \sum_{m=0}^{n_R-1} p(m) P(m \rightarrow n) \quad (5.13)$$

In equation 5.13, $p_0(m)$ is the Bose-Einstein distribution of the adsorbate-metal system at the original, equilibrium, system temperature, which defines the probability of the adsorbate-metal system initially being at vibrational state m , and n_R is the vibrational quantum number representing the reaction activation barrier, $(n_R + 1/2) \hbar \omega \geq E_a$. Adsorbates with energies above the activation barrier are assumed to react instantaneously. Adsorbates with vibrational energy less than n_R can decay back towards the initial

distribution before the next scattering event. Because we are operating in the linear regime, where the decay of vibrationally excited molecules occurs on a faster time scale compared to sequential electron excitations, multiple excitations of a system are not considered here. The model can be expanded to include sequential electron excitation and decays in a DIMET regime.^{34,45} It should be noted that $Q(n)$, for all $n > n_R$, is strictly the probability of molecules above E_a induced by the electron excitation and thus contains none of the original thermal reactivity. Temperature effects on $Q(n)$ are easily incorporated with the temperature dependent Bose-Einstein $p_0(m)$ term in equation 5.13.

The reaction probability, P_R , for an excitation process by an electron with a given energy, ε_i , is then calculated as the sum of probabilities of all vibrational states above the activation barrier as shown in equation 5.14.

$$P_R(\varepsilon_i) = \sum_{n=n_R}^{\infty} Q(n) \quad (5.14)$$

The probability of inducing the reactions (CO and NO desorption and O diffusion) was calculated for all electron energies in the range of the maximum considered photon excitation energy ($0 < \varepsilon_i < 4$ eV), to give a reaction probability distribution as a function of scattering electron energy.

5.3.3. Quantum Yield Calculations

The temporally evolving metal electronic structure following photon absorption and the electron energy dependent reaction probability are then coupled to calculate the relative reaction rate as a function of time after the peak of the photon pulse. The instantaneous

reaction rate ($R(t)$) at any time t after the start of a laser pulse is calculated as a product of the total change in the metal electron structure, Δh_f as evaluated by ETM, and energy dependent reaction probability distribution obtained from the inelastic scattering model, P_R , integrated over all available electron energies (in the range of ε_F and $\varepsilon_F + h\nu$).

$$R(t) = \int_{\varepsilon_F}^{\varepsilon_F + h\nu} \Delta h_f(\varepsilon, t) \times P_D(\varepsilon) d\varepsilon \quad (5.15)$$

We note that the ETM uses an absolute electron energy scale in reference to vacuum, whereas the inelastic scattering model considers electron energies in reference to $\varepsilon_F = 0$. Because of this, it is important to shift the inelastic scattering results to the absolute vacuum reference (by adding ε_F to all ε_i) for reaction rate calculation in equation 5.15. In equation 5.15, $\Delta h_f(\varepsilon, t)$ is the temporally evolving change in the metal electronic structure following the metal photo-excitation. The individual contributions of FD thermalized and primary electron excitations in the calculated instantaneous reaction rates can be independently obtained by substitution of $\Delta h_f(\varepsilon, t)$ with the corresponding electron distributions by those defined in the ETM description. The overall QYs for each considered reaction are calculated by integration of the time dependent instantaneous reaction rate over the time required for the system to reach equilibrium (3 ps), (equation 5.16). Once again, calculation of the quantum yield is enabled by defining the laser pulse impinging on the metal such that integration over $P(t')dt'$ is equal to 1 quantum of photon energy

$$QY(h\nu) = \int_0^3 \int_{\varepsilon_F}^{\varepsilon_F + h\nu} \Delta h_f(\varepsilon, t) \times P_R(\varepsilon) d\varepsilon dt \quad (5.16)$$

5.4. Results and Discussions

5.4.1. Potential Energy Surfaces

Figure 5.3a, b and c show the ground and TNI state one-dimensional PES's associated with the adsorbate (CO, NO, O) reactions on a Pt(111) surface, as derived from the DFT and DFT- Δ SCF calculated parameters listed in Table 5.2. The PESs are plotted in terms of internal bond lengths for CO and NO molecules (Figures 5.3a and b) and vertical O distance from the Pt surface plane for atomic O (Figure 5.3c). As discussed above, it has been shown that excitation of the internal molecular vibrations of CO and NO play a larger role in governing the photo-desorption process than the molecule-surface vibrational modes.⁴⁵ Furthermore, it is assumed in this work that the Pt-O vertical stretching mode controls the diffusion process. The resonance energies for the calculated electronic transitions (excitation from the metal ε_F into the unpopulated adsorbate state, $\varepsilon_a^0 = V_1(x_0) - V_0(x_0)$) are 3.89, 1.71 and 1.37 eV for Pt-CO, Pt-NO and Pt-O, respectively. The adsorbate-derived resonant states involved in the calculated electronic transitions are depicted in the insets of Figure 5.3a, b and c. The width of each resonant state, Γ , is inversely proportional to the lifetime that the electron spends in the resonant state during the electron scattering (TNI formation and decay) process, such that $\tau_R = \hbar/\Gamma$. The assumed FWHM associated with unpopulated adsorbate states are 0.66 (Pt-CO), 0.8 (Pt-NO) and 1.32 eV (Pt-O), which give TNI lifetimes of 1, 0.8 and 0.5 fs, respectively. The resonance energies and widths for the identified electronic transitions are in good agreement with measurements using inverse photoemission spectroscopy.⁵³

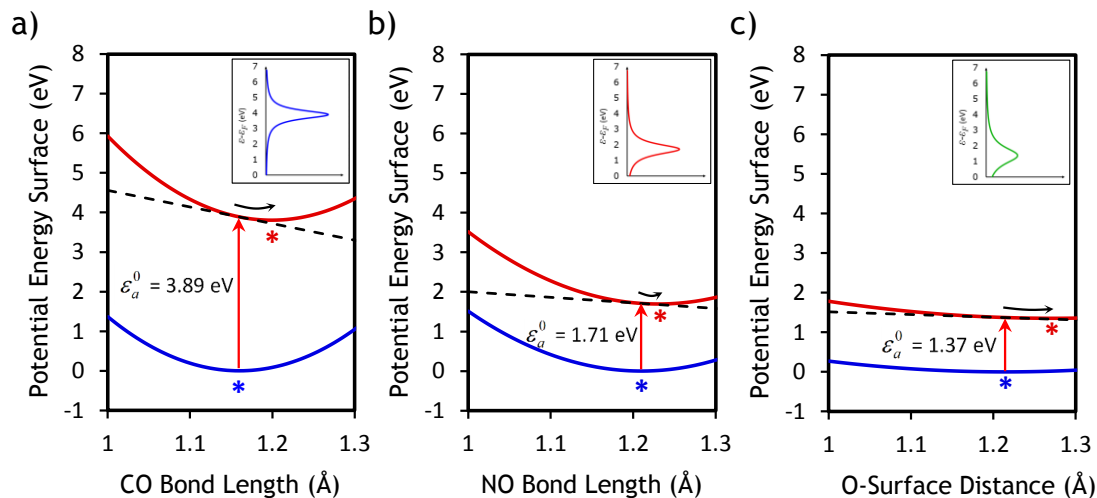


Figure 5.3: DFT calculated one-dimensional PES's of ground and TNI states associated with the **a)** internal vibrational mode of CO on a Pt(111) surface, **b)** internal vibrational mode of NO on a Pt(111) surface, and **c)** O atom - Pt(111) surface bond vibrational mode. The insets are the adsorbate resonance states (Lorentzian shape) involved in the inelastic electron scattering. Parameters used in the PES calculations are listed in Table 5.2.

The trend in the magnitude of the resonance energies can be explained in terms of the gas-phase population of the adsorbate states. In the gas phase CO species the $2\pi^*$ orbital is fully unoccupied, whereas the $2\pi^*$ orbital of NO is 50% populated and the $2p$ state associated with atomic O is 67% populated. When each of these states hybridizes with Pt d -states, the energy and filling of the antibonding orbital formed due to this hybridization trends with the original energy and filling of the adsorbate state in the gas phase species. For CO on Pt(111) it would be expected that the antibonding $2\pi^*$ should be situated well above the system ϵ_F and completely unpopulated in the system ground state, which is consistent with the calculated picture in the inset of Figure 5.3a. On the other hand, for O on Pt(111), the antibonding state derived from the O $2p$ state is expected to lie just above ϵ_F and be partially populated, as depicted in the inset of Figure 5.3c. In addition to the resonance energy and population of the antibonding state in the adsorbed species, the

population of adsorbate states in the gas phase species also dictates the efficiency of inelastic electron scattering (TNI formation) for activation of the adsorbate-metal bonds.

The transient addition of an electron to the antibonding orbitals associated with the adsorbate-metal bonds disturbs the configuration of electrons in the bonds and creates a repulsive force, driving the TNI systems towards longer equilibrium bond distances along the 1-D PES's. The magnitude of the repulsive force felt during a transition from the ground to TNI state PES is quantified using the derivative of the TNI PES at the equilibrium bond distance of the ground state system, $f = -\partial V_1 / \partial x|_{x=x_0}$. The magnitudes of these forces are shown graphically in Figure 5.3 as the slope of the black dashed lines running tangent to the TNI PESs at the equilibrium bond distance of the ground state PESs. A larger slope is related to a larger repulsive force felt by the system during TNI formation. For example, the force felt by Pt-CO, Pt-NO and Pt-O systems due to TNI formation are 42 eV/nm, 14 eV/nm and 6.7 eV/nm, respectively. The trend in the forces felt due to TNI formation are inversely related to the initial population of the gas phase adsorbate orbital involved in the electron scattering process.

The frequency of vibration along the PES also impacts the coupling efficiency associated with the conversion of the electronic excitation (TNI formation) into the vibrational energy of the system (the activation of adsorbate-metal bonds). The linear coupling constant, λ , defined in equation 5.12 exhibits a proportional relationship to the initial force felt by the system upon TNI formation and an inverse square-root relationship on the vibrational frequency of the considered PES. Based on the calculated values from Figure 5.3, all tabulated in Table 5.2, the linear coupling constants for the activation of Pt-

CO, Pt-NO and Pt-O bonds are -145, -53 and -32.4 meV, respectively. The stronger linear coupling constant for the Pt-CO system compared to the others suggests that upon TNI formation due to resonant electron excitation, CO desorption will exhibit the highest quantum efficiency.

5.4.2. Energetic Electron Induced Reaction Probabilities

The calculated ε_a^0 , λ , $\hbar\omega$ and estimated Γ associated with the three adsorbate systems were used as inputs into the inelastic scattering model to calculate the probability that an energetic electron of a given energy, scattering through the normally unpopulated antibonding state, will induce a reaction (based on equation 5.14). The results, shown in Figure 5.4a, were obtained using the parameters listed in Table 5.2 and consider an initial system temperature of 300K. The reaction probabilities associated with NO desorption and O diffusion on Pt(111) were multiplied by 10^5 and 10^8 in Figure 5.4a to allow their comparison to the Pt-CO case. All three reactions exhibit a maximum probability centered at energies about $E_a/2$ larger than the resonance energy, ε_a^0 , for each considered adsorbate state. The shifts in maximum reaction probability in Figure 5.4a by $E_a/2$ from the resonance energies depicted in Figure 5.3 exist because this is the condition where the incoming and outgoing electrons with energy difference due to inelastic scattering process, $\Delta\varepsilon = \varepsilon_i - \varepsilon_f = E_a$, have the minimum collective difference from the resonant state energy, ε_a^0 .

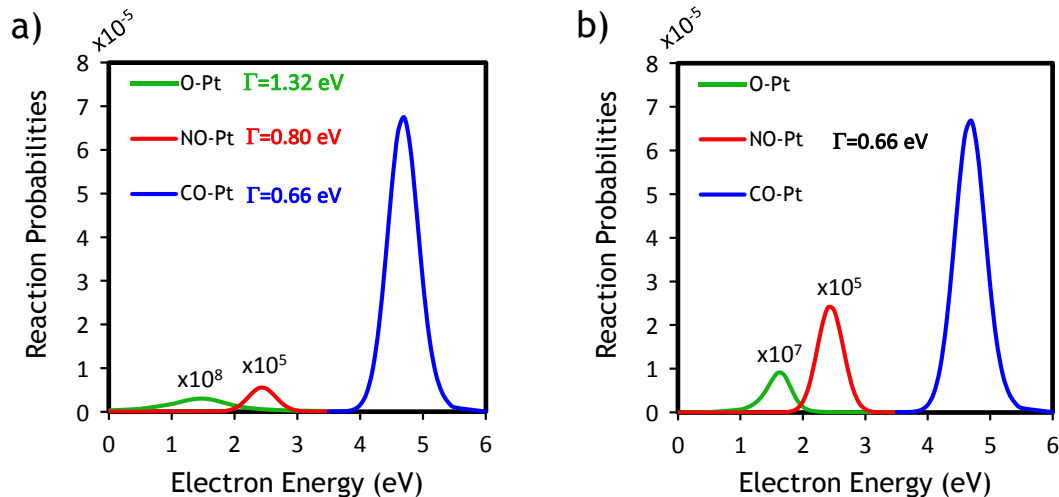


Figure 5.4: Reaction probabilities calculated with the inelastic electron scattering model for CO and NO desorption from Pt(111) surface and O diffusion on Pt(111) surface as a function of incident electron energy. Reaction probabilities are calculated **a)** based on estimated values of resonance energy width (Γ) for each adsorbate **b)** with $\Gamma=0.66$ eV for all three adsorbates

Based on significant differences in the reaction probability for CO compared with the NO and O systems, and uncertainty in the values of Γ , reaction probabilities were also calculated for identical ε_a^0 , λ , and $\hbar\omega$ as Figure 5.4a, but with $\Gamma=0.66$ eV for all adsorbates, see Figure 5.4b. Comparison of Figure 5.4a and b show that reduction of Γ for the NO and O cases increased their reaction probabilities, but the probability for the reaction of CO was still greater than the other adsorbates by at least 5 orders of magnitude. The greater magnitude of the CO reaction probabilities compared to NO and O, regardless of Γ , is due to a significantly larger linear coupling constant for the Pt-CO system. These results show that an electron with energy near the reaction probability maximum of each adsorbate can more efficiently couple with the activation of Pt-CO than Pt-NO and Pt-O bonds. This fact will be important in understanding how each adsorbate system interacts with the continuous distribution of energetic electrons produced in a metal substrate following

photon absorption. In the remainder of the paper we will use the original estimated values of Γ for all calculations, i.e. the results in Figure 5.4a.

5.4.3. Reaction Time Scales

Before focusing on how an energetic electron distribution in a photo-excited metal induces chemistry, we will discuss characteristics of the temporally evolving electronic structure in the metal following photon absorption. An example of the dynamics of photo-generated energetic electron distributions is highlighted for the model 5 nm Pt nanoparticle, during and following the absorption of a single photon with energy of 3.5 eV (remember that this is absorbed by the system following a temporal Gaussian pulse shape with FWHM of 10 fs). The temporal evolution of primary, thermalized and total (primary + thermalized) electron distributions are shown in Figure 5.5a, b and c, respectively. The distributions are plotted in terms of the change in the probability of an electron occupying a given energy level, due to photon absorption by the metal. By comparing the magnitude of the change in occupation probability for primary (Figure 5.5a) and thermalized electrons (Figure 5.5b), or by inspection of the total distribution in Figure 5.5c, it is seen that at all times the relative magnitude of the thermalized electron impact on occupation probability is greater than the primary electrons. However, the primarily excited electrons are responsible for the majority of change in occupation probability for electrons with energy $> 1\text{eV}$ above ε_F at all times. In addition, the primary electron distribution decays with a faster time scale defined predominantly by Fermi liquid theory, whereas the thermalized electron distribution decays with a slower time scale defined by the electron-phonon coupling constant. The unique temporal and energetic characteristics of primary and thermalized charge carriers

play a significant role in governing the efficiency of photon driven chemical processes at metal surfaces.

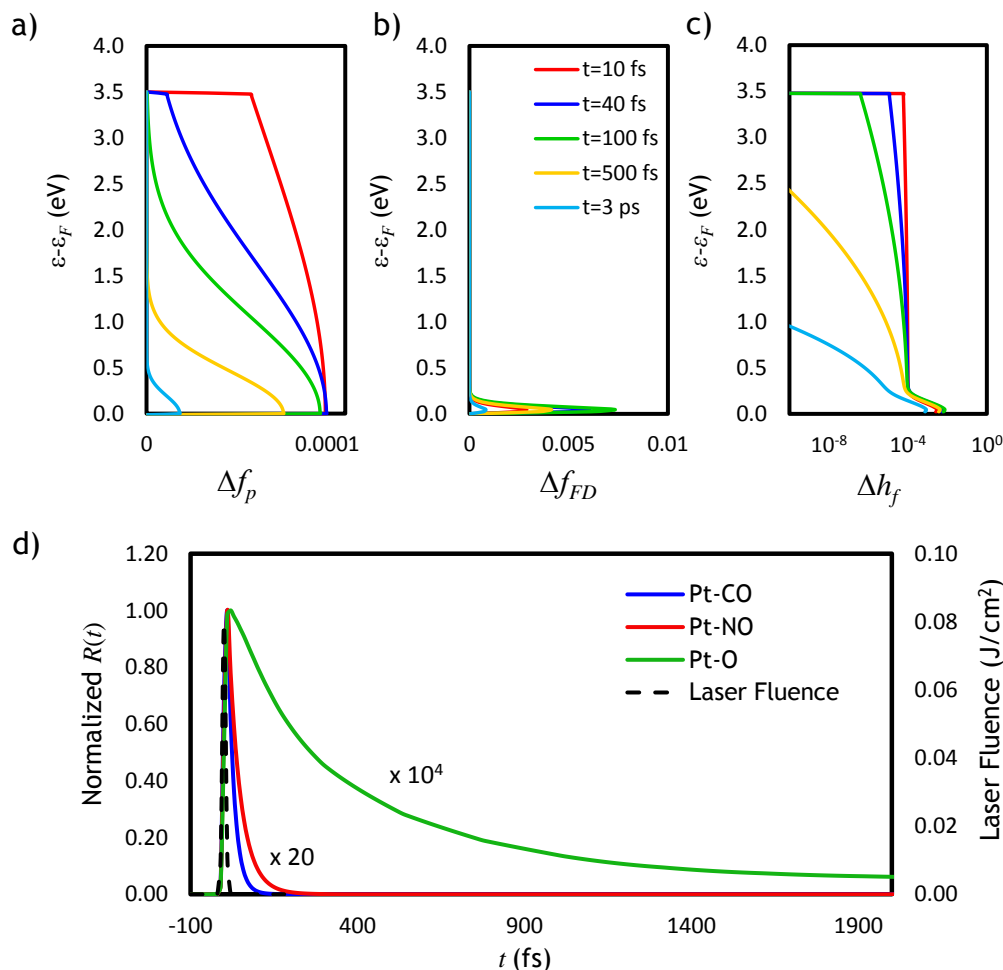


Figure 5.5: **a-c)** Temporal evolution of photo-excited electron distributions in a 5 nm Pt particle induced by a 10 fs laser pulse of 3.5 eV energy photon (total pulse energy is equal to 1 photon). **a)** Primary non-thermalized electron distribution, **b)** Thermalized (FD) electron distribution and **c)** Total (primary + thermalized) electron distribution. **d)** Normalized instantaneous reaction rates as a function of time, calculated for the three reactions induced by a 10 fs laser pulse of 3.5 eV energy photon (total pulse energy is equal to 1 photon). The relative magnitudes of NO desorption and O diffusion rates in reference to the CO desorption instantaneous rate are shown to facilitate comparison. The right axis shows the laser pulse fluence (dashed black line in the plot).

The temporally evolving energetic electron distribution in the metal was coupled with the electron energy dependent reaction probabilities for each reaction (described above) to

give temporally evolving instantaneous photon driven reaction rates, using equation 5.15. To compare the time scales and characteristics of photon driven activation of Pt-CO, Pt-NO and Pt-O bond activation under similar excitation conditions, the instantaneous reaction rates were plotted as a function of time in response to the absorption of a 3.5 eV photon by the metal at 300 K, see Figure 5.5d. In these plots, the maximum instantaneous reaction rates for all three adsorbates were normalized to 1 to allow comparison of the time dependent nature of the processes. The values of relative magnitudes of CO desorption rates compared to NO desorption and O diffusion rates are indicated in Figure 5.5d. The results show that when driven by 3.5 eV photons at 300 K, the maximum instantaneous rate of CO desorption is ~ 20 times greater than NO desorption and $\sim 10^4$ times greater than O diffusion. The relative magnitudes of NO desorption and O diffusion rates, in comparison to CO desorption, are significantly larger than the calculated electron energy dependent reaction probabilities shown in Figure 5.4. This can be understood by the larger population of lower energy electrons (in resonance with the maximum reaction probabilities for O and NO) as compared to higher energy electrons (in resonance with the maximum probabilities for CO) following the absorption of the 3.5eV photon by the Pt nanostructure.

Figure 5.5d provides insight into the role of the primary electron versus thermalized electron distribution in driving chemistry. The temporally evolving instantaneous reaction rate for CO and NO desorption both decay very rapidly in the time scale of 100 and 200 fs after initiation of the photon pulse, respectively. On the other hand, the instantaneous reaction rate for O diffusion has measurable and impactful rate at much longer time scales,

> 1ps after initiation of the photon pulse. These values are in a reasonably good agreement with time scales measured experimentally for these reactions with two-pulse correlation methods. It has been shown that the electrons in a Pt(111) slab, excited with a 800 nm laser pulse of 130 fs duration, couple with adsorbed CO in a time scale of 200 fs.⁵⁶ It is expected that shorter time scales would be observed with lower wavelength photons (closer to the CO resonance state energy) and shorter pulse durations. The measured time scales of NO photo-desorption induced by 80 fs laser pulses at 680 nm, are smaller than 1 ps, as limited by the resolution of the experimental systems.⁵⁷ A time constant of 1.5 ps was reported for O diffusion on Pt(111) surface induced by 800 nm light course with a 50 fs pulse.²⁶ Comparison of the experimental and theoretical results show that our model was able to qualitatively capture the trend in the time scales associated with these reactions. This provides confidence in the theoretical results and the analysis of the underlying physical mechanism controlling the different time scales of these reactions.

The trend in the time scales of these photo-induced reactions can be understood by realizing that the electron energies most efficient for driving CO and NO desorption, > 1.5 eV above ε_F , can only come from the primarily excited electron distribution in the photo-excited metal. However, relatively efficient O diffusion can be driven by lower energy electrons, < 1.5 eV above ε_F , which fall predominantly in the range of electron energy dominated by the thermalized distribution, see Figure 5.5c. Thus, it can be suggested that the rates of CO and NO desorption are governed predominantly by the interaction of unpopulated adsorbate resonance states with the primary electron distribution, whereas the

rate of O diffusion is governed predominantly by the interaction of unpopulated adsorbate resonance states with the thermalized electron distribution.

5.4.4. Wavelength Dependent Quantum Yields

The involvement of primary or non-thermalized electrons in driving photochemistry on metal surfaces has been established in several studies, based on observed wavelength dependent quantum yields and kinetic energy distributions.^{1,5,58} A characteristic of photocatalytic reactions on metal surfaces driven by primary or non-thermalized electrons is a dependence of quantum yield (sometimes referred to as reaction cross section) on excitation wavelength that does not follow the absorption spectrum of the metal substrate.^{3,5,24} It has been shown in two similar experimental studies for photo-induced CO desorption from Pt(111), due to low intensity photo-excitation, that the cross section for CO desorption increased by ~20 fold as the photon excitation wavelength was decreased from 400 to 266 nm and from 440 to 340 nm; the absorption coefficient of the bulk Pt substrate only changes by a few percent over this range.^{5,9,46} Wavelength dependent measurements for NO photo-desorption from Pt(111) have shown constant reaction cross sections in the wavelength range 355-532 nm with a 10-fold decrease in cross section by 1032 nm, displaying a markedly different trend than the bulk Pt absorption spectrum.¹ These sets of experimental observations show that there is an adsorbate specificity in wavelength dependent photoreaction cross sections driven by a low intensity photon flux and suggest that this phenomenon is controlled by the role that non-thermalized (or primary) electrons play in governing reactivity.

To explore the cause of the discrepancy between the observed wavelength dependent CO and NO desorption cross sections and bulk Pt absorption cross section we calculated the wavelength dependent QYs considering the thermalized electron distribution alone and the total (thermalized + primary) electron distribution. As described in the methods section, the QYs were calculated by integrating the instantaneous rates (Figure 5.5d) over time. Separating the temporally evolving thermalized electron distribution from the total electron distribution and using each of these as inputs into the QY calculations (equation 5.16), we are able to analyze the importance of these distributions in controlling the overall calculated reactions rates. The results of these calculations for the three model reactions are shown in Figure 5.6 together with the experimental data discussed above. The calculated wavelength dependent trends for the total electron distribution agree very well with the experimental data of NO desorption. Although the CO desorption results show an overestimation of QY dependence on wavelength at higher energy photons. We will discuss potential origins of this over estimation below. However there is a reasonably well qualitative agreement of the wavelength dependent trends of total electron induced rates with experimentally measured data, which further proves the role of non-thermalized electron distribution in activating CO desorption reaction.

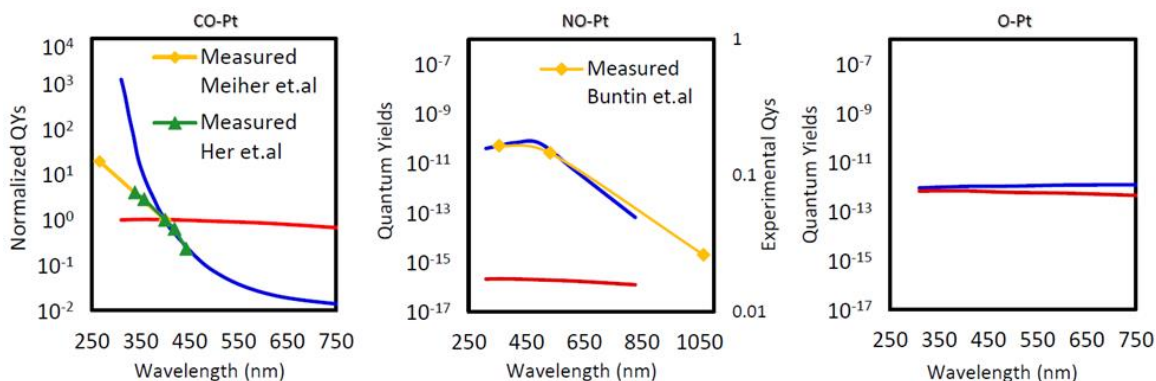


Figure 5.6: Calculated QYs as a function of photon wavelength for **a)** CO desorption, **b)** NO desorption and **c)** O diffusion on a Pt(111) surface. The QYs are calculated using the total (primary + thermalized) electron distribution (depicted with blue line), and thermalized electron (FD) distribution only (shown with red line). All calculations were performed at 300K. Experimentally measured wavelength-dependent QYs from literature are shown in yellow and green lines for CO and NO desorption.^{1,5,9}

Comparison of the thermalized electron induced rates for all three cases (Figure 5.6) shows identical wavelength dependent trends that quantitatively follow the bulk Pt absorption spectrum. By comparing O diffusion QYs for the chemistry driven by the thermalized and total electron distributions, it is seen that the thermalized electron distribution is predominantly responsible for chemistry (Figure 5.6c). This is consistent with the longer time scale of the instantaneous O diffusion rate observed in Figure 5.5d. In opposition to the O diffusion case, the impact of the thermalized distribution on the calculated QY for CO and NO desorption using the total electron distribution is minimal at most wavelengths (Figure 5.6a and b). The predominant role of the non-thermalized or primary electron distribution in controlling desorption of NO and CO from Pt(111) is consistent with the short time scale of the temporal profile of instantaneous rate for these two cases seen in Figure 5.5. Differences in the observed wavelength dependent trends of total electron distribution induced QYs for the reactions can be explained by the energy of the adsorbate resonance state. Because our approach to modeling the dynamic electronic

structure in the metal involves directly coupling primary excitations to the thermalized FD electronic distribution, the energy of the adsorbate resonance state significantly impacts the wavelength dependent QY driven by the primary electron distribution. For example, due to considerably greater probabilities of electrons with energy greater than 4 eV to induce CO desorption (Figure 5.4), the wavelength dependent QYs, driven by primary electrons, continuously increase at higher photon energies. However, in the NO desorption case a plateau in the wavelength dependent QY around 500 nm wavelength (2.5 eV) is caused by the primary electrons being in resonance with the NO unoccupied state. It is expected that these effects would be diminished if a more sophisticated model for the temporally evolving metal electronic structure were utilized, where the entire thermalization process (rather than immediate conversion of primary excitations into an FD distribution) is considered. Furthermore, recently measured QYs for catalytic reactions involving CO desorption from nano-sized Pt particle surfaces (particle diameter of 35 nm), displayed a wavelength dependence that follows Pt particles absorption spectra closely, indicating very little impact of non-thermal electrons on QYs.¹² The disagreement between these results, our calculations and the previous experimental measurements on Pt(111) surfaces mentioned above are due to potential differences in the systems thermalization rates and spatially dependent electron conduction, which will be discussed below.

It can also be noted that the magnitude of total electron derived QYs are similar for all three reactions in the photon wavelength range of 400-650 nm, despite the significantly greater reaction probability for CO desorption due to resonant electron scattering (Figure 5.4). This highlights the required compromise between the magnitudes of the linear

coupling constant and the excitation energy of an adsorbate resonance state to achieve high rates in visible photon driven reactions on metal surfaces. Specifically, even though O diffusion has a very low reaction probability under resonant electron scattering (Figure 5.4), the larger number of electrons with energy in resonance with the excitation energy following visible photon absorption by the metal causes the QY to be on the same magnitude as CO desorption.

It is worth discussing the important implications of the adsorbate specific wavelength dependences. The wavelength dependent results suggest that different elementary chemical processes involving different adsorbates will exhibit unique wavelength dependences that are controlled by the strength of their interaction with the primary or non-thermalized energetic electron distribution. In the context of controlling selectivity on metal surfaces, this means that by varying photon excitation wavelength it would be expected that competing elementary steps in a catalytic cycle should couple to the energetic electrons with different efficiencies and thereby wavelength dependent photo-excitation of metal catalysts may provide a unique knob to control catalytic reaction selectivity.

5.4.5. Impact of System Temperature

Another potential lever for controlling selectivity in photon driven reactions on metal surfaces is through variation of the process operating temperature. It has been experimentally demonstrated that photocatalytic QYs for reactions on metal surfaces increase with operating temperature, and that the magnitude of the increase is dependent on the reaction.^{12,34,59} To explore this phenomenon we calculated the temperature dependent ($T = 100\text{--}500\text{ K}$) QYs for the three adsorbate systems in response to photo-

excitation of the metal by a 3.5 eV photon. The results are shown in Figure 5.7a where it is seen that the QY for all three reactions depend positively on initial system temperature, but that the increase in the O diffusion QY with temperature is significantly larger than the increase for CO and NO desorption. Specifically, increasing temperature from 100-500 K raises the QYs by 5-fold, 30-fold and 15 orders of magnitude for CO desorption, NO desorption and O diffusion, respectively. At lower temperatures the O diffusion QY is significantly lower than for CO and NO desorption, however in the temperature range of 350-500K the QYs for all three reactions are comparable. The unique temperature dependence of the three reactions strongly suggests that the operating temperature could be used to induce unique selective behavior in photon driven catalytic processes.

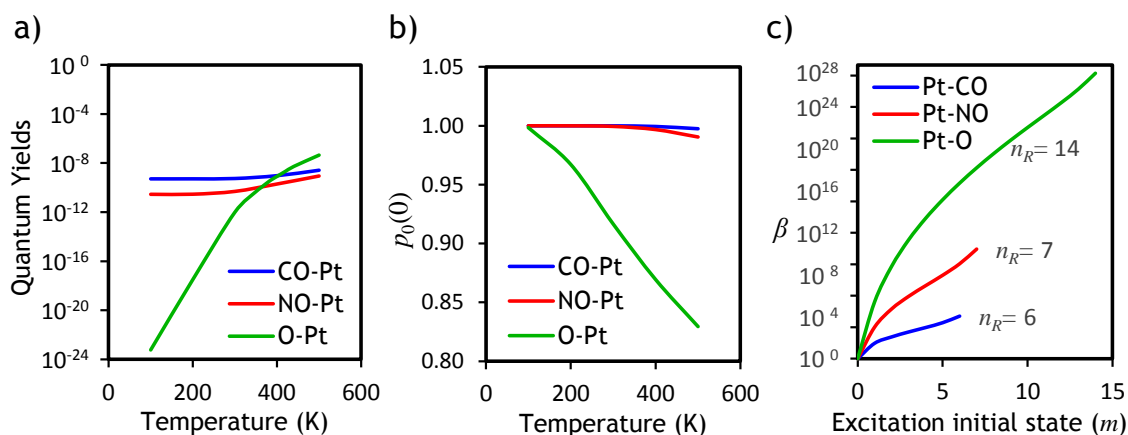


Figure 5.7: **a)** Temperature dependent QYs calculated for the three adsorbate systems in the temperature range, 100-500 K. **b)** Initial occupation probability of vibrational ground state of each adsorbate-metal PES as a function of temperature. **c)** Comparison of the ratio of the probability of exciting an adsorbate system from a vibrationally excited state into a state above the activation barrier to the probability of exciting from the system ground state into a state above the activation barrier, β , for the three reaction systems. Values of β are calculated as a function of initial vibrational state.

In order to understand the underlying physical phenomena controlling the significant difference in temperature dependent QYs in the three systems, it is important to consider

how system temperature could affect the substrate-mediated photon driven chemical reactions. The charge carrier distribution in the photo-excited metal substrate depends very weakly on system temperature due to the small change in Fermi Dirac statistics in electron energy levels $> 1\text{eV}$ above ε_F in the temperature range 100-500 K. Thus, the mechanism of the observed adsorbate dependent impact of temperature on QY must be caused by variations in the efficiency of energetic electron coupling with the vibrational modes along reaction PESs. The system temperature defines the initial population of vibrational states in a given reaction PES, as dictated by the Bose-Einstein distribution. Increasing system temperature results in an increase in the population of higher energy vibrational states closer to the activation barrier energy. The larger fraction of molecules in vibrational states closer to the activation barrier has two primary impacts on the efficiency of the photon driven process, which explain the adsorbate dependent nature of the impact of temperature on QY.

The two factors defining the efficiency of energy transfer during the inelastic scattering event are the initial population of the vibrational states, $p_0(m)$, and the vibrational transition probabilities, $P(m \rightarrow n)$, as described in the calculation of electron induced reaction probabilities from equations 5.15 and 5.16. We explore the role of each of these factors in describing the adsorbate specific temperature dependence of the photocatalytic QYs. Bose-Einstein statistics predict a ground state occupation probability of above 99% ($p_0(0) > 99\%$) at low temperatures (around 100 K) for all three adsorbate systems, which means that more than 99% of molecules available for reaction are residing in their ground state vibrational state. As the molecules in the ground state gain vibrational energy with

increasing temperature and redistribute to the higher vibrational energy states, the occupation probability of the ground state drops.

The variation of $p_0(0)$ with temperature for the adsorbate PES's is depicted in Figure 5.7b, and provides a measure of the collective change in population of higher (above ground) vibrational states. PES's with larger vibrational energy (steeper well) and thus higher ground state energies, have a higher probability of ground state occupation that varies slower with temperature, as compared to an adsorbate PES with smaller vibrational frequency. For example, with temperature varying from 100-500 K, $p_0(0)$ is almost constant for CO (99.99% to 99.7%) and NO (99.9% to 99%) internal vibrational modes with energies 0.255 and 0.196 eV respectively, whereas $p_0(0)$ varies from 99.8% to 89.2% over the same temperature range for the O-Pt vibrational mode with energy 0.055 eV. Although the decline in the ground state occupation probability (and the increase in the higher vibrational state occupation probability) is relatively small, it has a significant impact on the reaction probability due to the significantly higher transition probabilities of excited vibrational states to vibrational states with energies above the activation barrier.

To explore the impact of an adsorbate system initially being in an excited vibrational state on the reaction probability, we calculated the ratio of the probability of exciting an adsorbate system from a vibrationally excited state into a state above the activation barrier to the probability of exciting from the system ground state into a state above the activation barrier, $\beta(m, n) = P(m \rightarrow n) / P(0 \rightarrow n)$. In Figure 5.7c, β is plotted as a function of the initial state m for the final state just above the activation barrier (n_R) (corresponding to the

largest value of $Q(n)$ contributing to the reaction probability in equation 5.14) for each of the three systems. The values presented in Figure 5.7c are calculated based on transitions induced by inelastic scattering of energetic electrons corresponding to the maximum reaction probabilities in Figure 5.4a for each adsorbate ($\varepsilon_i = 4.7, 2.5$ and 1.7 eV for CO, NO and O, respectively). Figure 5.7c shows that for systems with larger linear coupling constants, the impact of starting from excited vibrational states is smaller on the reaction probability (smaller β), as compared to systems with smaller linear coupling constants. For example in the case of O-Pt(111) with smallest coupling constant (0.032 eV) of the considered reactions, the probability of transition from the 1st excited vibrational state ($m=1$) to final state n_R is 5 orders of magnitude greater than exciting from the system ground state to n_R . This impact is larger for the O case than NO (3 orders of magnitude) and CO (30 fold), which have larger coupling constants 0.053 and 0.145 eV, respectively. This means that the same population increase in the 1st excited vibrational state, will impact the photo-induced reaction probability of O diffusion far more greatly than NO and CO desorption. Furthermore, it was shown in Figure 5.7b that the O diffusion case also exhibits the larger temperature dependence of excited vibrational state population probability. The strong dependence of O diffusion QY on temperature can be explained by compounding effects of a large change in the population of excited vibrational states at increasing temperature, due to the small vibrational frequency, and greater impact of excited vibrational states on inelastic scattering induced reaction probability, due to the small coupling constant.

Our analysis shows that both vibrational frequency (controlling the temperature dependence of the initial distribution of adsorbate vibrational modes, $p_0(m)$) and linear coupling constants of adsorbates (through the impact on the transition probability of higher vibrational states into states above the activation barrier) play roles in controlling the adsorbate-specific QY dependence on temperature. The predicted adsorbate specific dependence of QYs on temperature, in addition to the wavelength dependent behavior described above, suggests that photo-excitation of metal catalysts with targeted wavelength and at optimal temperatures may provide a unique approach to control selectivity in heterogeneous catalysis. These results provide physical intuition for the temperature dependent behavior of photon driven reactions on metal surfaces, but quantitatively the huge magnitudes of the differences in temperature dependent behavior of the examined systems have not previously been observed. Potential issues bringing about the magnification or minimization of thermal impacts on the chosen reaction systems, in particular the over or under estimation of linear coupling constants, will be discussed in the following section.

5.5. Discussion and Concluding Remarks

In the previous sections we have shown how our relatively simple, first-principles based, modeling approach predicts the time, wavelength and temperature dependent nature of photon driven reactions on metal surfaces in the context of the substrate mediated photo-excitation mechanism. We have also shown that the predicted behavior of the three reaction systems qualitatively agrees with trends in previous experimental measurements, wherever possible, providing confidence in the framework of our approach. However we have also

seen that the model predictions falls short of quantitative predictive power, and that significant magnification in adsorbate specific effects were found, particularly in the temperature dependence.

The primary shortcoming of our approach is the simplicity of the DFT calculated 1-D PES's associated with the adsorbate reactions. For example, it is well established in the case of photo-induced CO desorption from Pt surfaces that PES's associated with frustrated rotational motion of CO play a major role in controlling the desorption process.^{56,60} The framework we utilized is well suited for handling multi-dimensional ground and TNI state PES's and thus could handle the inclusion of multiple PES's associated with different electron scattering processes (i.e. different orbitals involved). It is also important to emphasize that the Δ SCF-DFT method only allows us to calculate the TNI PES using a static approach. To capture the dynamics of the excitation process and estimate TNI lifetimes, accurate Time Dependent DFT calculations are required, which are still computationally expensive and cumbersome to employ.³⁵ Therefore the TNI lifetime values used in our model are taken from experimental measurements. It is expected that with increasing computational power of calculating excited states of adsorbates on metal surfaces, more advanced potential energy landscapes and accurately calculated TNI lifetimes will provide more quantitative results within the framework of our model.

In addition to the simplicity of the adsorbate PES model, the employed model for treating the temporally evolving electronic structure of the metal following photon absorption is relatively simple. For example, Pt exhibits DOS near ε_F that is not flat (as considered here) and also exhibits time dependent electron cooling behavior that deviates

from Fermi-Liquid theory.⁶¹ Both of these complexities could easily be included in our modeling approach and require electronic structure calculations at varying levels of complexity, for example the G_0W_0 approximation could be used to predict the non-Fermi Liquid behavior.⁶¹ The effect of nanometer size confinement of the Pt metal on the photo-induced processes is only included in our model through the assumption of a spatially homogenous charge carrier distribution in the system and the spatial isolation of photon absorption events. However, it has been demonstrated that the particle size reduction enhances the electron-electron interaction and scattering rates.⁶² These effects can be incorporated into the model by use of size dependent characteristic times of electron-electron and electron-phonon scattering processes and would be expected to impact intricacies of the resulting wavelength dependent QY's and potentially reaction time scales. Lastly, the model considered here assumes the direct conversion of primary excitations into thermalized charge carrier distributions. In reality, multiple new excitations typically occur during this conversion process, which could be included more rigorously through the use of Boltzmann Transport equations.⁶² Inclusion of these effects are expected to minimize the strong agreement between the shapes of wavelength dependent QY for primary electron driven reactions (Figure 5.6) and the electron energy dependent inelastic scattering probabilities (Figure 5.4).

The power of our approach is that in its simplest form, shown here with many assumptions, we can still explain unique adsorbate dependent behaviors that have been observed previously. Furthermore, the approach is flexible enough to include much future advancement in theoretical treatments of various mechanisms. It is expected that this

approach will be very useful in explaining many of the unique observations surrounding the recent excitement in the field of photochemistry on metal nanoparticles.

In conclusion, we investigated adsorbate specific behavior of photo-activated processes on metal surfaces with a focus on three well-studied model reactions on Pt(111) surfaces, CO and NO desorption and O diffusion. We proposed a theoretical approach to model the dynamics of substrate-mediated photochemistry on metal surfaces by coupling a first-principles based treatment of DIET mechanism with an extended version of the TTM. The model calculations provided predictions of the time scales, wavelength dependent and temperature dependent behavior of photon induced reactions on metal surfaces in qualitatively good agreement with experimentally observed trends. The calculated probabilities of photo-induced reactions show significant dissimilarities in the efficiency of electron coupling with the resonant states of the three reaction systems, which is related to differences in the shape of unpopulated resonance states and PESs of the associated reactions. It was found that dissimilarities in the PES and resonance shapes of the three reaction systems caused unique temperature and wavelength dependent behavior in the systems, displaying significant adsorbate specificity. It is suggested that driving photocatalytic reactions on metal surfaces with a targeted wavelength and at an optimal temperature may provide increased control of reaction selectivity on metal catalyst surfaces.

5.6. References

1. Buntin, S. A., Richter, L. J., King, D. S. & Cavanagh, R. R. State-resolved evidence for hot carrier driven surface reactions: Laser-induced desorption of NO from Pt(111). *J. Chem. Phys.* **91**, 6429–6446 (1989).
2. Prybyla, J. A., Heinz, T. F., Misewich, J. A., Loy, M. M. T. & Glownia, J. H. Desorption Induced by Femtosecond Laser Pulses. *Phys. Rev. Lett.* **64**, 1537–1540 (1990).
3. Weik, F., Meijere, A. de & Hasselbrink, E. Wavelength dependence of the photochemistry of O₂ on Pd(111) and the role of hot electron cascades. *J. Chem. Phys.* **99**, 682–694 (1993).
4. *Laser Spectroscopy and Photochemistry on Metal Surfaces*. (World Scientific, 1995).
5. Her, T.-H., Finlay, R. J., Wu, C. & Mazur, E. Surface femtochemistry of CO/O₂/Pt(111): The importance of nonthermalized substrate electrons. *J. Chem. Phys.* **108**, 8595–8598 (1998).
6. Ravindranathan Thampi, K., Kiwi, J. & Grätzel, M. Methanation and photo-methanation of carbon dioxide at room temperature and atmospheric pressure. *Nature* **327**, 506–508 (1987).
7. Christopher, P., Xin, H. & Linic, S. Visible-light-enhanced catalytic oxidation reactions on plasmonic silver nanostructures. *Nat. Chem.* **3**, 467–472 (2011).
8. Kao, F.-J., Busch, D. G., Gomes da Costa, D. & Ho, W. Femtosecond versus Nanosecond surface Photochemistry: O₂+CO on Pt(111) at 80 K. *Phys. Rev. Lett.* **70**, 4098–4101 (1993).
9. Mieher, W. D. & Ho, W. Photochemistry of oriented molecules coadsorbed on solid surfaces: The formation of CO₂+O from photodissociation of O₂ coadsorbed with CO on Pt(111). *J. Chem. Phys.* **91**, 2755–2756 (1989).
10. Bonn, M. *et al.* Phonon-Versus Electron-Mediated Desorption and Oxidation of CO on Ru(0001). *Science* **285**, 1042–1045 (1999).
11. Misewich, J. A., Nakabayashi, S., Weigand, P., Wolf, M. & Heinz, T. F. Anomalous branching ratio in the femtosecond surface chemistry of O₂/Pd(111). *Surf. Sci.* **363**, 204–213 (1996).
12. Kale, M. J., Avanesian, T., Xin, H., Yan, J. & Christopher, P. Controlling catalytic selectivity on metal nanoparticles by direct photoexcitation of adsorbate-metal bonds. *Nano Lett.* **14**, 5405–5412 (2014).
13. Marimuthu, A., Zhang, J. & Linic, S. Tuning Selectivity in Propylene Epoxidation by Plasmon Mediated Photo-Switching of Cu Oxidation State. *Science* **339**, 1590–

1593 (2013).

14. Watanabe, K., Sawabe, K. & Matsumoto, Y. Adsorbate-localized excitation in surface photochemistry: Methane on Pt(111). *Phys. Rev. Lett.* **76**, 1751–1754 (1996).
15. Zhou, X.-L., Zhu, X.-Y. & White, J. M. Photochemistry at adsorbate/metal interfaces. *Surf. Sci. Rep.* **13**, 73–220 (1991).
16. Petek, H. Photoexcitation of adsorbates on metal surfaces: one-step or three-step. *J. Chem. Phys.* **137**, 91704 (2012).
17. Gadzuk, J. W. Resonance-assisted, hot-electron-induced desorption. *Surf. Sci.* **342**, 345–358 (1995).
18. Lisowski, M. *et al.* Ultra-fast dynamics of electron thermalization, cooling and transport effects in Ru(001). *Appl. Phys. A Mater. Sci. Process.* **78**, 165–176 (2004).
19. Funk, S. *et al.* Desorption of CO from Ru(001) induced by near-infrared femtosecond laser pulses. *J. Chem. Phys.* **112**, 9888–9897 (2000).
20. Saalfrank, P. Quantum dynamical approach to ultrafast molecular desorption from surfaces. *Chem. Rev.* **106**, 4116–4159 (2006).
21. Thrall, E. S., Steinberg, A. P., Wu, X. & Brus, L. E. The Role of Photon Energy and Semiconductor Substrate in the Plasmon-Mediated Photooxidation of Citrate by Silver Nanoparticles. *J. Phys. Chem. C* **117**, 26238–26247 (2013).
22. Mulugeta, D., Watanabe, K., Menzel, D. & Freund, H.-J. State-resolved investigation of the photodesorption dynamics of NO from (NO)₂ on Ag nanoparticles of various sizes in comparison with Ag(111). *J. Chem. Phys.* **134**, 164702 (2011).
23. Misewich, J. A., Heinz, T. F. & Newns, D. M. Desorption Induced by Multiple Electronic Transitions. *Phys. Rev. Lett.* **68**, 3737–3740 (1992).
24. Frischkorn, C. & Wolf, M. Femtochemistry at metal surfaces: nonadiabatic reaction dynamics. *Chem. Rev.* **106**, 4207–4233 (2006).
25. Brandbyge, M., Hedegard, P., Heinz, T. F., Misewich, J. A. & Newns, D. M. Electronically driven adsorbate excitation mechanism in femtosecond-pulse laser desorption. *Phys. Rev. B* **52**, 6042–6056 (1995).
26. Stépán, K., Gütde, J. & Höfer, U. Time-Resolved Measurement of Surface Diffusion Induced by Femtosecond Laser Pulses. *Phys. Rev. Lett.* **94**, 236103 (2005).
27. Budde, F., Heinz, T. F., Kalamarides, A., Loy, M. M. T. & Misewich, J. A. Vibrational distributions in desorption induced by femtosecond laser pulses:

- coupling of adsorbate vibration to substrate electronic excitation. *Surf. Sci.* **283**, 143–157 (1993).
28. Busch, D. G. & Ho, W. Direct Observation of the Crossover from Single to Multiple Excitations in Femtosecond Surface Photochemistry. *Phys. Rev. Lett.* **77**, 1338–1341 (1996).
 29. Gadzuk, J. W., Richter, L. J., Buntin, S. A., King, D. S. & Cavanagh, R. R. Laser-excited hot-electron induced desorption: a theoretical model applied to NO/Pt(111). *Surf. Sci.* **235**, 317–333 (1990).
 30. Gadzuk, J. W. Inelastic resonance scattering, tunneling, and desorption. *Phys. Rev. B* **44**, 13466–13477 (1991).
 31. Palmer, R. E. & Rous, P. J. Resonances in electron scattering by molecules on surfaces. *Rev. Mod. Phys.* **64**, 383–440 (1992).
 32. Zhu, X.-Y. Surface Photochemistry. *Annu. Rev. Phys. Chem.* **45**, 113–144 (1994).
 33. Olsen, T. & Schiøtz, J. Origin of Power Laws for Reactions at Metal Surfaces Mediated by Hot Electrons. *Phys. Rev. Lett.* **103**, 238301 (2009).
 34. Christopher, P., Xin, H., Marimuthu, A. & Linic, S. Singular characteristics and unique chemical bond activation mechanisms of photocatalytic reactions on plasmonic nanostructures. *Nat. Mater.* **11**, 1044–1050 (2012).
 35. Gavnholt, J., Olsen, T., Engelund, M. & Schiøtz, J. Δ Self-Consistent Field Method To Obtain Potential Energy Surfaces of Excited Molecules on Surfaces. *Phys. Rev. B* **78**, 75441 (2008).
 36. Linic, S., Christopher, P. & Ingram, D. B. Plasmonic-metal nanostructures for efficient conversion of solar to chemical energy. *Nat. Mater.* **10**, 911–921 (2011).
 37. Zhang, H. & Govorov, A. O. Optical Generation of Hot Plasmonic Carriers in Metal Nanocrystals : The Effects of Shape and Field Enhancement. *J. Phys. Chem. C* **118**, 7606–7614 (2014).
 38. Mukherjee, S. *et al.* Hot Electrons Do the Impossible: Plasmon-Induced Dissociation of H₂ on Au. *Nano Lett.* **13**, 240–247 (2013).
 39. Kale, M. J., Avanesian, T. & Christopher, P. Direct Photocatalysis by Plasmonic Nanostructures. *ACS Catal.* **4**, 116–128 (2014).
 40. Linic, S., Christopher, P., Xin, H. & Marimuthu, A. Catalytic and Photocatalytic Transformations on Metal Nanoparticles with Targeted Geometric and Plasmonic Properties. *Acc. Chem. Res.* **46**, 1890–1899 (2013).
 41. Kim, K. H., Watanabe, K., Mulugeta, D., Freund, H.-J. & Menzel, D. Enhanced Photoinduced Desorption from Metal Nanoparticles by Photoexcitation of Confined Hot Electrons Using Femtosecond Laser Pulses. *Phys. Rev. Lett.* **107**,

- 47401 (2011).
42. Mulugeta, D., Kim, K. H., Watanabe, K., Menzel, D. & Freund, H.-J. Size Effects in Thermal and Photochemistry of (NO)₂ on Ag Nanoparticles. *Phys. Rev. Lett.* **101**, 146103 (2008).
 43. Carpenne, E. Ultrafast laser irradiation of metals: Beyond the two-temperature model. *Phys. Rev. B* **74**, 24301 (2006).
 44. Wingreen, N. S., Jacobsen, K. W. & Wilkins, J. W. Inelastic scattering in resonant tunneling. *Phys. Rev. B* **40**, 11834–11850 (1989).
 45. Olsen, T., Gavnholt, J. & Schiøtz, J. Hot-electron-mediated desorption rates calculated from excited-state potential energy surfaces. *Phys. Rev. B* **79**, 35403 (2009).
 46. *Handbook of Optical Constants of Solids*. (Academic Press, 1985).
 47. Lin, Z., Zhigilei, L. V. & Celli, V. Electron-phonon coupling and electron heat capacity of metals under conditions of strong electron-phonon nonequilibrium. *Phys. Rev. B* **77**, 75133 (2008).
 48. *CRC Handbook of Chemistry & Physics*. (2014).
 49. Ashcroft, N. M. & Mermin, N. D. *Solid State Physics*. (Holt, Rinehart and Winston, 1976).
 50. Kittel, C. *Introduction to Solid State Physics*. (Wiley, 1996).
 51. Menzel, D. & Gomer, R. Desorption from Metal Surfaces by Low-Energy Electrons. *J. Chem. Phys.* **41**, 3311–3328 (1964).
 52. Redhead, P. A. Interaction of slow electrons with chemisorbed oxygen*. *Can. J. Phys.* **42**, 886–905 (1964).
 53. Dose, V. Momentum-resolved inverse photoemission. *Surf. Sci. Rep.* **5**, 337–378 (1985).
 54. Libisch, F., Cheng, J. & Carter, E. A. Electron-Transfer-Induced Dissociation of H₂ on Gold Nanoparticles: Excited-State Potential Energy Surfaces via Embedded Correlated Wavefunction Theory. *Zeitschrift für Phys. Chemie* **227**, 1455–1466 (2013).
 55. Gavnholt, J., Rubio, A., Olsen, T., Thygesen, K. S. & Schiøtz, J. Hot-electron-assisted femtochemistry at surfaces: A time-dependent density functional theory approach. *Phys. Rev. B* **79**, 195405 (2009).
 56. Fournier, F., Zheng, W., Carrez, S., Dubost, H. & Bourguignon, B. Vibrational dynamics of adsorbed molecules under conditions of photodesorption: pump-probe SFG spectra of CO/Pt(111). *J. Chem. Phys.* **121**, 4839–4847 (2004).

- 57. Yamanaka, T., Hellman, A., Gao, S. & Ho, W. State-resolved femtosecond two-pulse correlation measurements of NO photodesorption from Pt(111). *Surf. Sci.* **514**, 404–408 (2002).
- 58. Fukutani, K., Murata, Y., Schwarzwald, R. & Chuang, T. J. UV-laser-induced desorption of NO from Pt(111). *Surf. Sci.* **311**, 247–256 (1994).
- 59. Xiao, Q. *et al.* Visible Light-Driven Cross-Coupling Reactions at Lower Temperatures Using a Photocatalyst of Palladium and Gold Alloy Nanoparticles. *ACS Catal.* **4**, 1725–1734 (2014).
- 60. Fournier, F., Zheng, W., Carrez, S., Dubost, H. & Bourguignon, B. Ultrafast Laser Excitation of CO/Pt(111) Probed by Sum Frequency Generation: Coverage Dependent Desorption Efficiency. *Phys. Rev. Lett.* **92**, 216102 (2004).
- 61. Ladstädter, F., Hohenester, U., Puschnig, P. & Ambrosch-Draxl, C. First-principles calculation of hot-electron scattering in metals. *Phys. Rev. B* **70**, 235125 (2004).
- 62. Voisin, C. *et al.* Ultrafast electron-electron scattering and energy exchanges in noble-metal nanoparticles. *Phys. Rev. B* **69**, 195416 (2004).

Chapter 6

An Atomic-Scale View of CO-Induced Pt Nanoparticle Surface Reconstruction

6.1. Summary

A detailed understanding of the correlations that govern catalyst surface structure and catalytic performance is critical for the design and optimization of chemical processes. Gaining such an understanding for industrially relevant, high surface area supported metal catalysts has been hindered due to less than atomic resolutions of typical environmental transmission electron microscopy (TEM) techniques at atmospheric pressures and lack of quantitative information regarding active site distribution at different operating conditions. We introduce an approach to overcome these limitations, by correlating atom-resolved imaging via *in-situ* scanning transmission electron microscopy (STEM) at atmospheric pressure, quantitative sample-averaged measurements of surface site distribution via *in-situ* infrared (IR) spectroscopy and DFT based Wulff-constructions. The approach is used

here to gain a complete atomic scale insight into CO-induced surface reconstruction of Pt nanoparticles. It is demonstrated that the truncated octahedron shape adopted by bare Pt nanoparticles undergoes a reversible, facet-selective reconstruction due to CO adsorption, where {100} facets roughen into vicinal stepped high Miller-index facets, while {111} facets remain intact.

6.2. Introduction

The most commonly used heterogeneous catalysts are made of finely dispersed metal particles on the surface of metal oxide supports. These metal nanoparticles at equilibrium typically assume a polyhedron shape that minimizes the total surface free energy of the particle by predominantly exposing low surface energy facets. The surface structure of these particles has been observed to reconstruct under reaction conditions, upon interaction with reactant species. Due to the structure-sensitive adsorption energy of reactive species on different metal surface facets, the formation of adsorbate-metal bonds under reaction conditions can significantly modify the surface free energy of metal facets and drive metal nanoparticle surface reconstruction. The catalyst surface reconstruction affects the geometry and concentration of different active sites (with different coordination numbers) and hence the reactivity of the catalyst particles under reaction conditions can be significantly different compared to freshly prepared catalysts. Therefore, characterization of metal surface structure under reaction conditions at an atomic scale is critical for developing a complete understanding of structure-reactivity relationships that will be ultimately used to design better catalysts.

Several analytical approaches have been developed to examine various characteristics of catalytic metal nanoparticles under reaction conditions. Most commonly used are spectroscopic approaches that provide sample-averaged measurements of the metal electronic structure, local geometric environment, and vibrational fingerprints of adsorbed species. Although these techniques provide valuable information, without direct imaging of the catalysts under reaction conditions it is difficult to conclude the geometric structures and composition of exposed active sites that are responsible for driving catalysis. Due to recent advances in direct imaging techniques such as *in-situ* scanning transmission electron microscopy (STEM), it is now possible to examine the structures of catalytic particles under reaction conditions and obtain atomic scale information associated with structural transformations. However, currently *in-situ* STEM can only provide direct imaging through 2-dimensional projections and don't provide a complete picture of the catalyst structure changes. In addition, the information provided by these techniques represent very small sample sizes and iterative measurement methods are required to obtain atomic resolution sample-averaged data. The *in-situ* TEM techniques have previously either been performed at pressures well below atmospheric pressure,^{1,2} or been limited by atomic resolution when performed at atmospheric pressure.³⁻⁵ These limitations suggest that to obtain atomic scale and quantitative insights into the surface structure of supported metal catalysts during catalytic reactions, *in-situ* STEM should be coupled with alternative *in-situ* techniques that provide sample-averaged and quantitative information about the distribution and nature of active catalytic sites under reaction conditions.

One of the most studied examples of adsorbate induced catalyst surface reconstruction is the reconstruction of Pt surfaces due to the adsorption of CO, which is the first step in the CO oxidation reaction occurring in automotive catalytic converters. Atomic scale and quantitative descriptions of CO-induced Pt surface reconstruction have been achieved for model Pt single crystal surfaces, mainly through coupling direct imaging via scanning tunneling microscopy (STM) with quantitative surface characterization by X-Ray photoelectron spectroscopy (XPS) at close to ambient pressures. All the previous studies on Pt single crystals show evidence of Pt surface reconstruction at high CO coverage, except for the most stable surface facet, {111}, which is characterized by the formation of increased concentrations of under-coordinated (UC) Pt surface atoms.⁶⁻¹⁰ However, a complete picture of CO-induced surface reconstruction of industrially relevant, high surface area oxide-supported Pt nanoparticles has not been achieved yet. This is due to the limited spatial resolution of scanning probe techniques on nanoparticle surfaces at relevant pressures, as discussed above, and the high degree of structural complexity associated with supported metal nanoparticle surfaces. Although direct imaging techniques and *in-situ* spectroscopic investigation of these systems have shown signatures of CO-induced reconstruction that are consistent with increased concentrations of UC Pt atoms, a complete atomic scale picture of surface structure of Pt nanoparticles at saturation CO coverage has not yet been elucidated.

In this study, we successfully characterize the atomic scale surface structure of Pt nanoparticles at high CO coverage by correlating atom-resolved direct imaging via *in-situ* scanning transmission electron microscopy (STEM), with *in-situ* quantitative, site-specific

infrared (IR) spectroscopy and Density Functional Theory (DFT) based Wulff-construction modeling. It is observed that the truncated octahedron shape adopted by clean Pt nanoparticles undergoes a reversible, facet specific reconstruction due to CO adsorption, where flat (100) facets roughen into stepped higher miller index facets, while flat (111) facets remain intact. The approach introduced here allows for analysis of adsorbate-induced reconstruction on high surface area metal nanoparticle catalysts at an atomic scale, which is expected to be useful for other catalytic systems where there exists high adsorbate coverage under reaction conditions.

6.3. Methods

As described in the previous section, the equilibrium shapes of adsorbate-free metal nanoparticles are determined by the free energies of competing surface facets in vacuum. The low Miller-index, close-packed metal facets have the lowest surface energies therefore metal nanoparticles are typically found in the shape of truncated octahedrons that mainly expose {111} and {100} facets. Upon the interaction of metal nanoparticles with gas phase reactants, due to structure-sensitive adsorption energy of reactants on different facets, the surface energies of the competing facets can modify to different extent, which provides the thermodynamic driving force for surface reconstruction of these metal nanoparticles. The adsorbates bind more strongly to higher Miller-index, stepped facets compared to more stable, low Miller-index facets, and have greater impact on the surface energies of these facets.⁸ For example, Figure 6.1 shows an energy diagram of arbitrary surface facets {abc} and {xyz}. While {abc} is more stable than {xyz} in vacuum environment, the structure

sensitivity of molecular adsorption can stabilize the surface energy of {xyz} to become the lowest energy facet, thereby driving surface reconstruction.

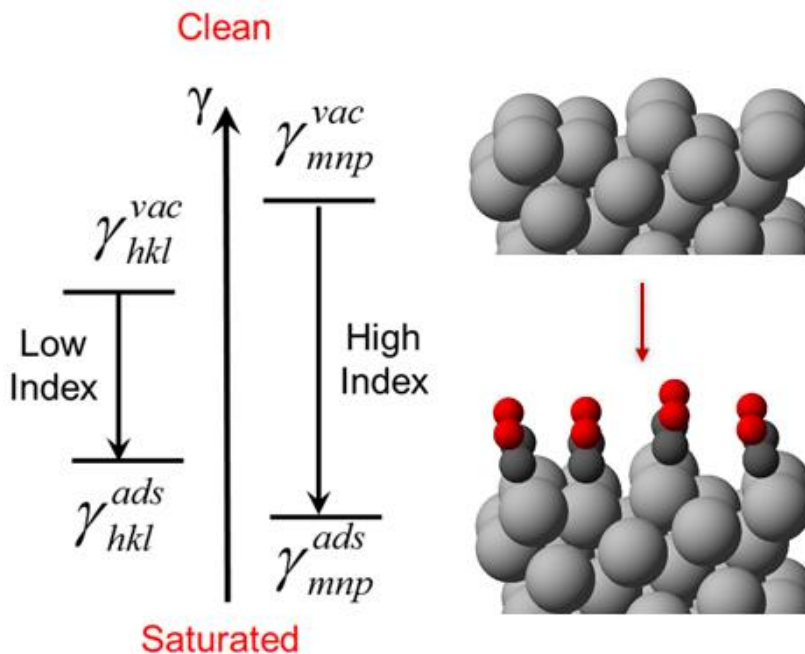


Figure 6.1. Schematic diagram depicting the driving force for adsorbate induced reconstruction of surfaces through modification of competing facet surface energies

The shape of the metal nanoparticles can be predicted by Wulff construction method given the free energies of bare and adsorbate covered surface facets. We used DFT-derived surface free energies of bare and CO covered Pt facets as inputs to Wulff construction method to predict the shape of Pt nanoparticles at two equilibrium conditions, vacuum and saturation coverage. The two equilibrium shapes were then used to calculate the amount of surface reconstruction as a function of particle size. The details of calculation methods are provided in the sections 6.3.1 through 6.3.3.

The DFT predicted CO induced Pt surface reconstruction were validated by comparison with direct imaging of Pt nanoparticles under low and high CO coverage conditions using

in-situ STEM experiments. Furthermore, quantitative IR spectroscopy techniques were used to provide a sample-averaged measurement of the CO induced reconstruction of Pt nanoparticles. The details of the experimental methods used in this study are described in sections 6.3.4 through 6.3.7.

6.3.1. Surface energy calculations

The surface energy calculations were performed within DFT framework using the real space grid-based projector-augmented wave method (GPAW) open source code.¹¹ The Revised Perdew–Burke–Ernzerhof (RPBE) form of the generalized gradient approximation (GGA) was used to approximate exchange and correlation effects.¹² The surface energies for exposed Pt nanoparticle facets were calculated using periodic slabs of low Miller-index {100}, {110}, and {111} and higher index facets, {210}, {211}, {310}, and {311}, which have been shown to well represent the behavior of catalytic particles with diameters greater than ~1.6 nanometers.¹³ The low index facets were chosen because they represent the most common facets found on bare Pt particles and the higher index facets are vicinal, stepped surfaces that are most likely to form upon reconstruction of the low index facets. The consecutive metal slabs were separated by 15 Å vacuum space in *z* direction in periodically repeated unit cells in *x* and *y* directions. Orthogonal unit-cells were used for all the facets except for {111}, {211} and {311} facets which were constructed using hexagonal unit-cell. A grid space of $h = 0.2$ was used. The Brillouin zone sampling for all the unit cells was performed with a $8 \times 8 \times 1$ Monkhorst–Pack *k*-point set, which was assured to be sufficient for the convergence of the smallest unit cells.¹⁴ The calculated slab

energies were used in equation 6.1 to obtain the surface energies (γ_{hkl}^{vac}) of hkl facets in vacuum.

$$\gamma_{hkl}^{vac} = \frac{E_{slab} - NE_{bulk}}{2A_{cell}} \quad (6.1)$$

In equation 6.1, E_{slab} is the total energy of the slab, N is the number of atoms in the slab, E_{bulk} is the energy of each atom in bulk and A_{cell} is the surface area of unit cell. Two different values of E_{bulk} were used for hexagonal and orthogonal unit cells.¹⁵ For each unit cell type, E_{bulk} was calculated as the slope of an N -Layer slab energy as a function of slab thickness (N). The calculated bulk energies were -5.83 eV and -5.79 eV for hexagonal and orthogonal unit cells respectively. The calculated surface energies for individual facets were converged with respect to slab thickness and number of relaxed layers within 0.01 J/m². In addition, it was assured the thickness of the slabs and relaxed layers are consistent among all the facets within 1 and 1.7 Å respectively, as shown in Table 6.1. The converged surface energies are highlighted with asterisk in Table 6.1.

Table 6.1. Surface energies of Pt $\{hkl\}$ facets calculated as a function of slab thickness and number (thickness) of relaxed layers

Surface	Atomic Layer	Slab thickness	γ_{hkl}	Relaxed layers	γ_{hkl}	Relaxed layers	γ_{hkl}	Relaxed layers
	N	Å	(J/m ²)	Å	(J/m ²)	Å	(J/m ²)	Å
(111)	6	11.6	1.35					
	7	13.9	1.37	2.3	1.37*	4.7		
	8	16.2	1.38					
	9	18.5	1.39					
(100)	6	10.0	1.56					
	7	12.0	1.55					
	8	14.0	1.55	2.0	1.55*	4.0		
(110)	10	12.6			1.65			
	11	14.0	1.65	2.7	1.66*	4.1		
	12	15.4			1.63			
(211)	9	12.9	1.56					
	10	14.5	1.57	2.3	1.57*	3.9		
	11	16.2	1.57					
(210)	6	9.8	1.69					
	7	11.4	1.66					
	8	13.0	1.68					
	9	14.6	1.66	2.5	1.66	3.4	1.66*	4.3
(311)	10	10.7	1.62					
	11	11.9	1.64					
	12	13.1	1.62					
	13	14.5	1.63	2.9	1.64	3.4	1.63*	4.7
(310)	8	9.3	1.68					
	10	11.8	1.65					
	11	13.3	1.67					
	12	14.3	1.66	2.4	1.65	3.6	1.65*	4.2

* Converged surface energy for each facet

The calculated surface energies were then normalized to the experimental surface energy for polycrystalline Pt (2.49 J/m²). The results are shown in Table 6.2. The calculated relative surface energies (the ratios of calculated surface energies to the surface energy of (111) facet), are in good agreement with values reported in literature.^{15–17}

Table 6.2. DFT calculated surface energies for different facets of Pt FCC crystal and their ratios with respect to (111) facet surface energy. The surface energies in third column are obtained by normalizing the most stable (111) surface to experimental surface energy of polycrystalline Pt and maintaining relative energies between facets.

Surface	DFT Calculated γ_{hkl} (J/m ²)	Ratio to γ_{111}	Normalized to γ_{exp} . (J/m ²)
(111)	1.37	1.00	2.49
(100)	1.55	1.14	2.83
(110)	1.66	1.21	3.02
(211)	1.57	1.15	2.85
(210)	1.66	1.21	3.02
(311)	1.63	1.19	2.97
(310)	1.65	1.21	3.01

6.3.2. Coverage Dependent Surface Energies

To investigate the impact of carbon monoxide (CO) adsorption on the reconstruction of Pt nanoparticle, the interfacial energies of Pt facets were calculated at different CO coverages on the slabs used for vacuum surface energy calculations in the previous section. First, the CO adsorption energies were calculated as a function of coverage for each facet using equation 6.2.

$$E_{ads} = \frac{E_{slab+X} - N_{ads} E_X - E_{slab}}{N_{ads}} \quad (6.1)$$

In equation 6.2 E_{slab+X} is the energy of the covered slab, N_{ads} is the number of the adsorbed CO on the slab, E_X is the gas phase CO energy and E_{slab} is the energy of the bare slab. Our calculated coverage dependent and facet dependent adsorption energies, shown in Table 6.3, are in very good agreement with experimental and theoretical reports.^{18–20}

Table 6.3. Calculated CO adsorption energies in eV at different CO coverages on the investigated Pt $\{hkl\}$ facets

Surface	Coverage (ML)								
	0.25	0.5	0.75	1	1.25	1.5	2	2.5	3
{111}	-1.60	-1.28	-1.01	-0.74					
{100}	-1.69	-1.69	-1.25	-1.02					
{110}	-1.87	-1.84	-1.68	-1.58	-1.15				
{211} ^a		-1.76		-1.47		-1.39	-1.25	-0.89	-0.57
{210}	-1.98	-1.94		-1.95		-1.61	-1.09		
{311} ^a		-1.81		-1.48	-1.41	-1.10			
{310}				-1.96		-1.82	-1.71	-1.31	-1.00

^a E_{ads} were calculated using orthogonal unit cells since the E_{ads} calculated with hexagonal unit cell showed ~0.2 eV overestimation compared to reported values in literature.¹⁸

The calculated adsorption energies from equation 6.2 were then used to obtain the interfacial energies of the facets at different CO coverages as shown in equation 6.3.²¹

$$\gamma_{hkl}^{ads} = \gamma_{hkl}^{vac} + \theta \frac{E_{ads}}{A} \quad (6.2)$$

In equation 6.3 γ_{hkl}^{ads} is the interfacial energy of the adsorbate-covered facet $\{hkl\}$, γ_{hkl}^{vac} is the surface energy of $\{hkl\}$ in vacuum, θ is the fractional adsorbate coverage, E_{ads} is the coverage dependent molecular adsorption energy (equation 6.2), and A is the surface area per adsorbate at 1 monolayer (ML) coverage. 1 ML coverage was defined as the surface where all the atoms with lowest coordination number are covered by CO molecules. At low coverage, exothermic CO adsorption stabilizes the interfacial energy of all Pt facets. With increasing coverage, CO adsorption energies decrease due to intermolecular interactions, and ultimately increasing coverage causes increased interfacial free energy (as shown in Figure 6.2). The lowest interfacial free energy for each surface facet was

considered representative of the interfacial free energy at saturation CO coverage. The saturation CO coverage configuration for the seven surface facets investigated here are shown in Figure 6.3. The calculated adsorption energies and interfacial energies of different Pt facets at saturation coverages are provided in Table 6.4.

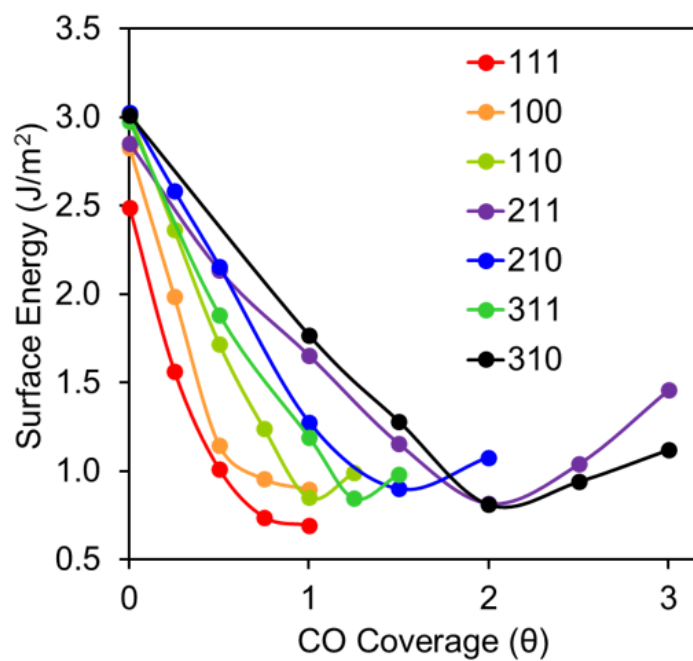


Figure 6.2. DFT-calculated CO coverage dependent surface energy of various Pt surface facets, based on equation 6.3

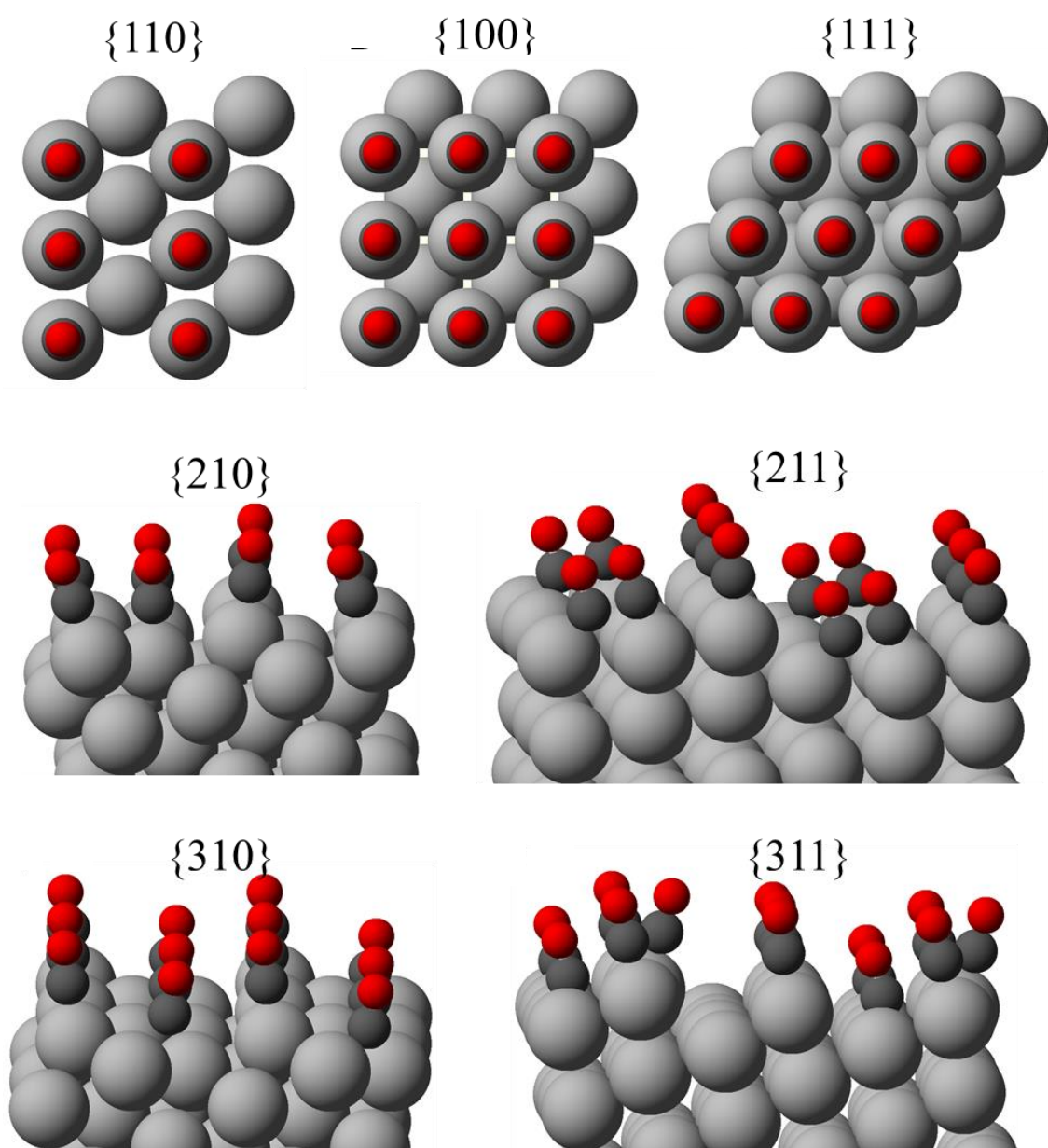


Figure 6.3. The configurations for identified saturation CO coverage of the investigated Pt surface facets. The corresponding adsorption energies are used to calculate surface energies at CO covered equilibrium condition

Table 6.4. CO adsorption energies and interfacial energies of different Pt facets at saturation coverages

Surface	E_{ads} (eV)	γ_{hkl} (J/m ²)	Ratio to γ_{111}
{111}	-0.78	0.69	1.00
{100}	-0.97	0.90	1.29
{110}	-1.54	0.85	1.23
{211}	-1.25	0.82	1.18
{210}	-1.58	0.90	1.30
{311}	-1.41	0.85	1.22
{310}	-1.69	0.87	1.25

6.3.3. Wulff Construction

The Wulff construction method was used to predict the shape of Pt nanoparticles in vacuum and at saturation CO coverage, based on DFT calculated surface energies.^{21,22} In this method the equilibrium shape (the shape that minimizes the total surface energy) of a given size of the nanoparticle is determined based on relative energies of $\{hkl\}$ facets. The distance of each $\{hkl\}$ facet from the center of the particle is proportional to the surface energy of the respective facet ($d_{hkl} \sim \gamma_{hkl}$). We used the module provided in Atomic Simulation Environment (ASE)²³ to construct the Wulff constructions using our calculated lattice constant, surface energies and approximate particle sizes as inputs. The equilibrium shapes of similar particle dimeters, Wulff constructions made with surface energies of Pt facets in vacuum ($\gamma_{hkl}^{\text{vac}}$) and at saturation CO coverage ($\gamma_{hkl}^{\text{ads}}$), were used to quantify the extent of particle surface reconstruction. The relative site fractions of under-coordinated (UC, atoms with a metal-metal coordination number of 6 or 7) and well-coordinated (WC, atoms with a metal-metal coordination number greater than 7) Pt surface atoms were

calculated for different nanoparticle sizes and the extent of the reconstruction was defined as the difference in the UC (or WC) site fraction at the two equilibrium conditions (bare and CO covered).

6.3.4. *In-situ scanning transmission electron microscopy (STEM)*

In-situ STEM experiments were used to directly image the Pt nanoparticles under low and high CO coverage conditions and validate the DFT predicted CO-induced Pt surface reconstruction. *In-situ* STEM experiments were performed using a gas cell system which allows for dynamic, atomic-resolution observation of nanomaterials heated in reactive gas environment at atmospheric pressure.^{24,25} A carbon-supported Pt catalyst (containing 4.8 ± 0.6 nm Pt particles) was used to maximize contrast between the metal and support in STEM images, and minimize metal-support interactions that may influence metal facet interfacial energies and the particle shape. The Pt/C samples were first dispersed in a solvent, and the suspension was deposited directly onto a thermal E-chip, which is equipped with a thin ceramic controlled heating membrane system. A second E-chip window was then placed on top of the thermal chip in the holder, creating a thin gas cavity sealed from the high vacuum of the TEM column. The Pt nanoparticles were situated between two SiN membranes, each 30-50 nm in thickness, with a 5-micron gap in between.

High-angle annular dark field (HAADF) STEM images of adsorbate-free Pt nanoparticles were taken at 423 K in an inert environment consisting of 500 Torr N₂. For details of *in-situ* STEM imaging methods see previous publications.^{24,25} Saturation CO coverages were achieved by pumping the N₂ out of the cell and introducing 500 Torr of a 5% CO environment (25 Torr CO and 475 Torr Ar) into the gas cell while the temperature

was maintained at 423 K. It has been demonstrated that under these conditions the Pt nanoparticle surface is saturated in CO.²⁶ The system was allowed ~10 minutes of exposure to CO, as it was demonstrated previously based on time resolved IR measurements that the surface reconstruction process is fast at this temperature in analogous conditions.²⁷ To minimize beam effects, the electron beam was only turned on during image collection.

6.3.5. HAADF-STEM Intensity Simulation

The HAADF-STEM images were used to perform intensity simulations. In this approach the relative intensity of the atomic columns in the 2-dimensional STEM images are analyzed to infer information regarding the number of atoms in each atomic column. To compare the results with DFT-predicted CO-induced Pt particle reconstruction, similar intensity analysis was performed on simulated HAADF-STEM images derived from the clean and CO-covered Wulff construction models. {100} surface slabs (where reconstruction is observed) along the [110] zone axis was used in both analysis. HAADF-STEM image simulation was performed using the QSTEM simulation package.²⁸ The simulation was carried out using a 512×512 pixel area and a single slice thickness of 1.96 Å. The microscopy parameters used for the simulations were the same as those for imaging.

6.3.6. In-situ diffuse reflectance Fourier transform infrared spectroscopy (DRIFTS)

The DRIFT experiments were used to quantify the fraction of total exposed Pt atoms existing as either WC or UC Pt sites. In this approach the IR spectra of CO saturated Pt nanoparticles were measured, the peaks associated with CO vibrational modes on WC and UC were identified and integrated. The peak areas were normalized by mode-specific

attenuation coefficients.^{25,27} The fraction of each type of surface sites were then calculated as a ratio of corresponding normalized peak area to the total peak area.

To measure site distribution in adsorbate-free condition, CO-covered Pt nanoparticles were used at room temperature. Due to the 0.4-0.5 eV activation barriers previously observed for CO-induced reconstruction of Pt{100} single crystal surface, the CO-induced reconstruction of Pt nanoparticle surfaces at room temperature during short time exposure is expected to be minimal.⁷ This was validated by similar IR spectra of CO adsorbed on Pt catalysts were shown to be similar at 148 K and 298 K. Thus, quantitative measurements of the WC and UC site concentrations found on bare Pt nanoparticle surfaces can be inferred from IR measurements made at saturation CO coverage and room temperature, where the surfaces are kinetically trapped from reconstruction.

Pt/Al₂O₃ catalysts used in the IR spectroscopy experiments were synthesized via incipient wetness impregnation of H₂PtCl₆ (37.50% Pt, Sigma Aldrich) onto α -Al₂O₃ support (>99.98%, Alfa Aesar). Details are described in previous publication.²⁷ The α -Al₂O₃ support was chosen to mimic the weakly interacting C support used in the *in-situ* STEM experiments, and maximize signal quality in the IR measurements. The catalysts were loaded into a high temperature reaction chamber equipped with ZnSe windows (Harrick Scientific). The reactor cell was placed inside of a Praying Manis diffuse reflectance adapter (Harrick Scientific), which was attached to a Thermo Scientific Nicolet iS10 FTIR spectrometer equipped with a liquid nitrogen cooled HgCdTe (MCT) detector. All spectra were obtained in Kubelka-Munk units (KM) units by using a reduced catalyst at 298K and 363K as a background for room temperature and elevated temperature spectral

measurements, respectively. Spectra were performed while purging the instrument and diffuse reflectance optical accessory with dry N₂ with an average of 128 scans with 4 cm⁻¹ resolution. In addition, a careful temperature calibration was performed using an optical pyrometer to calibrate the known difference between the catalyst surface and the reactor thermocouple. All temperatures reported for the IR spectroscopy experiments in this report represent the temperature of the catalyst surface.

In each experiment, the reactor chamber was loaded with ~80 mg of inert α -Al₂O₃ support, followed by approximately 25 mg of catalyst. The Al₂O₃ was used simply to conserve the amount of catalyst used in each experiment and to maintain the height of the catalyst bed to be flush with the top of the heated cup. Each catalyst was reduced at 500K in H₂ (99.999%, Airgas) for 1 hour, followed by flushing the reactor for 30-60 minutes with He (99.999%, Airgas) at 417K. After obtaining background spectra at 363K and 298K, each catalyst was exposed to a gas stream of 1% CO/He at 298K (total flow rate was held constant at 100 sccm) for 10 minutes, when the spectra became stable. After 10 minutes of exposure to CO at 298K, the reactor was heated to 363K (heating time took approximately 30-60 seconds), and spectra were taken for 30 minutes.

6.3.7. Quantitative Site Fraction Analysis based on DRIFT measurements

Quantitative analysis of relative site fractions of UC and WC Pt surface atoms were performed using DRIFT measurements, as described in previous publications.^{27,29} Gaussian profiles with fixed width and positions were assigned to the peaks associated with linearly bound CO on UC Pt (2060-2078 cm⁻¹) and on WC Pt (2085-2098 cm⁻¹). Peak areas

corresponding to each adsorption site were obtained and normalized by site specific attenuation coefficients as shown in equation 6.4.

$$X_i = \frac{A_i / \varepsilon_i}{\sum_{i=1}^2 [A_i / \varepsilon_i]} \quad (6.3)$$

In equation 6.4, X_i is the fraction of total adsorbed CO molecules bound to UC or WC Pt atoms, A_i is the peak area of each fitted and integrated peak for each site type and ε_i is the relative attenuation coefficient for CO adsorbed on UC and WC Pt sites. It has been shown in independent reports of CO adsorption on Pt single crystals that the attenuation coefficient of CO adsorbed on UC Pt sites is 2.7 times greater than on WC sites.^{30,31} Through this analysis, and assuming complete saturation CO coverage of all catalysts, the fraction of CO bound to UC and WC Pt sites can be quantified. The saturation coverage was ensured by utilizing a stream of 1% CO/He, which previously exhibited saturation coverages up to 525K.²⁷

6.3.8. Geometric Site Fraction Model

A geometric model of the expected change of UC and WC site fraction with particle size for cuboctahedron and icosahedron geometries was utilized from our previous work.²⁷ Small differences observed between the geometric model and measured site fractions from quantitative IR are likely due to broad particle size distributions and non-linearity of the site fraction change with particle size. Within these expected errors, the ambient quantitative IR measurements provide a reasonable prediction of the surface structure of clean catalysts.

6.4. Results and Discussions

The DFT calculated surface energies of adsorbate-free Pt surface terminations, listed in Table 6.1, show that the two most stable facets in vacuum are Pt{111} and Pt{100}. Thus, the DFT predicted Wulff constructions of bare Pt particles are found to form truncated octahedrons mainly composed of these two facets, as shown in Figure 6.4a for a 3 nm bare Pt particle viewed along zone axis $\langle 110 \rangle$. Figure 6.4b shows a typical HAADF-STEM image of a Pt nanoparticle of similar size along the zone axis $\langle 110 \rangle$ at 423 K and 500 Torr of N_2 . The STEM characterization also shows a truncated octahedral morphology for Pt nanoparticle with exposed Pt{111} and Pt{100} facets, which is in excellent agreement with the DFT-based Wulff construction predictions. In addition, the STEM image along the $\langle 110 \rangle$ zone axis directly reflects the fcc structure of the Pt nanoparticles where the lattice spacing of {200} and {111} planes are marked by the parallel lines.

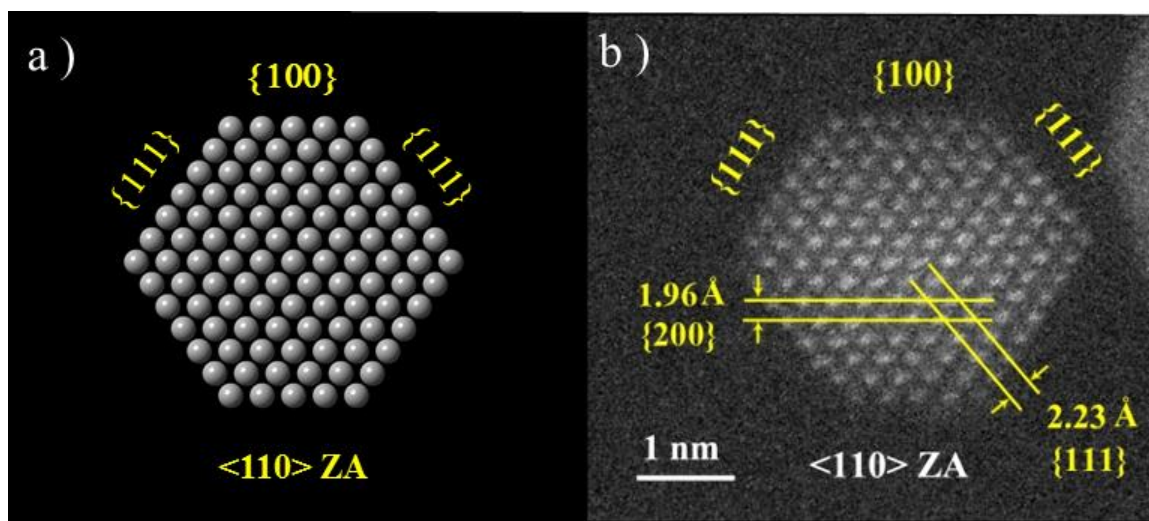


Figure 6.4. **a)** DFT based Wulff construction of a bare 3 nm Pt particle, viewed along the $\langle 110 \rangle$ zone axis **b)** HAADF-STEM image of a Pt nanoparticle at 423 K and 500 Torr of N_2 , viewed along the $\langle 110 \rangle$ zone axis, showing structural agreement between experiment and theory.

The comparison of DFT calculated surface energies of Pt facets (see Table 6.4 and Figure 6.2) show that Pt{111} facet is the most stable facet even under saturation CO coverage, indicating that these facets remain intact. However, the surface free energy of the second most stable bare facet, {100}, becomes comparable to the surface free energy of stepped vicinal surfaces, {210} and {310}, under saturation CO coverage, suggesting that there is a thermodynamic driving force for reconstruction of {100} facets at saturation CO coverage.^{26,32} Based on surface free energies of bare and CO saturated Pt surfaces, the Wulff construction method was used to predict nanoparticle shapes.^{21,22} Figure 6.5a shows the predicted particle shape of an adsorbate-free 7 nm Pt particle tilted slightly off the $\langle 110 \rangle$ zone axis. The particle is observed to undergo reconstruction at saturation CO coverage as seen in Figure 6.5b. These Wulff constructions clearly show, as predicted above, the {100} facets on bare Pt particles will reconstruct to vicinal stepped {210} and {310} surfaces at saturation CO coverage, whereas {111} facets remain intact and the overall particle shape remains largely unchanged, though with slightly “rounded” edges.^{2,3} The atoms highlighted with blue and green colors in Figure 6.5 represent the UC and WC surface sites respectively. The extent of the surface reconstruction or “rounding” of the particles can be characterized by increase in the concentration of UC surface atoms.

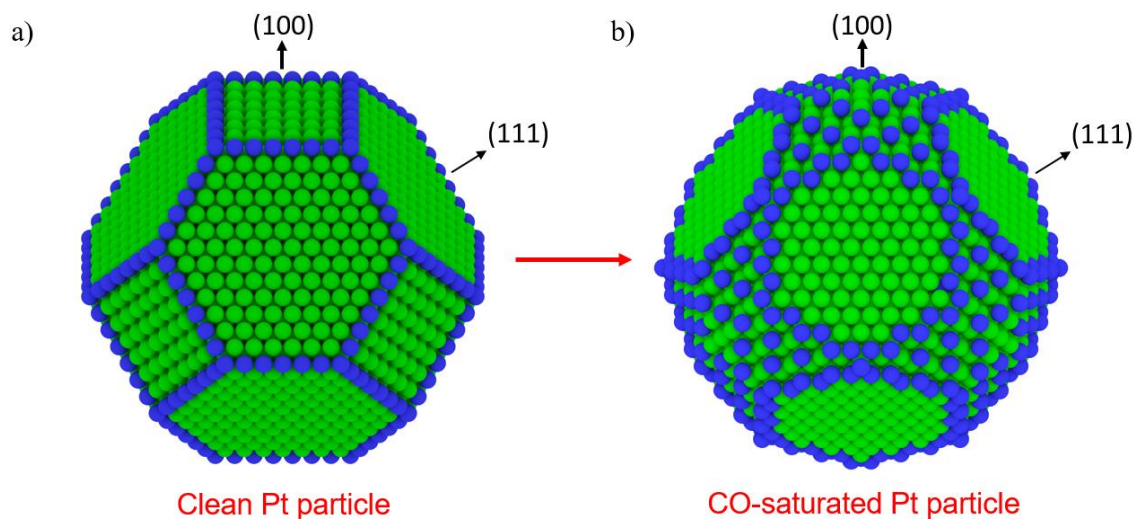


Figure 6.5. Wulff constructions of a 7 nm Pt particle based on DFT calculated surface free energies for **a)** bare surfaces, and **b)** CO saturated surfaces. Both images are tilted slightly off the $\langle 110 \rangle$ zone axis. The green atoms represent WC Pt atoms, and the blue atoms represent UC Pt edge and corner atoms.

Similar facet selective reconstruction on $\{100\}$ termination is observed in the Wulff construction of a 9.2 nm Pt particle shown in Figure 6.6a and b. The comparison of $\{100\}$ layers of the Wulff constructions at the two equilibrium conditions, bare (Figure 6.6a) and saturation CO coverage (Figure 6.6b), shows that an additional atomic layer (labeled layer 0) at the top of $\{100\}$ facet is created through migration of Pt atoms from lower $\{100\}$ layers (layers 1-3). The DFT predicted Wulff constructions for the 9.2 nm particle were compared with HAADF-STEM images of a similar size Pt particle, captured in *in-situ* STEM experiments under adsorbate-free (423 K and 500 Torr N_2 , Figure 6.6c) and high CO coverage (423 K, 500 Torr 5% CO, Figure 6.6d) conditions (see section 6.3.4). The HAADF-STEM image in Figure 6.6c also shows that the adsorbate-free Pt particle mainly consists of flat $\{111\}$ and $\{100\}$ facets, which were stable under N_2 environment at 423 K during an elapsed time of 30 minutes. The HAADF-STEM image of the same particle under saturation CO condition, after 10 minutes' exposure to CO, shows the formation of

a new atomic layer (marked as layer 0) on top of the originally exposed $\{100\}$ facet (marked as layer 1) which is in good agreement with the DFT predicted Wulff constructions shown in Figure 6.6a and b and the simulated HAADF-STEM images derived from the Wulff constructions, Figure 6.6e and f respectively.

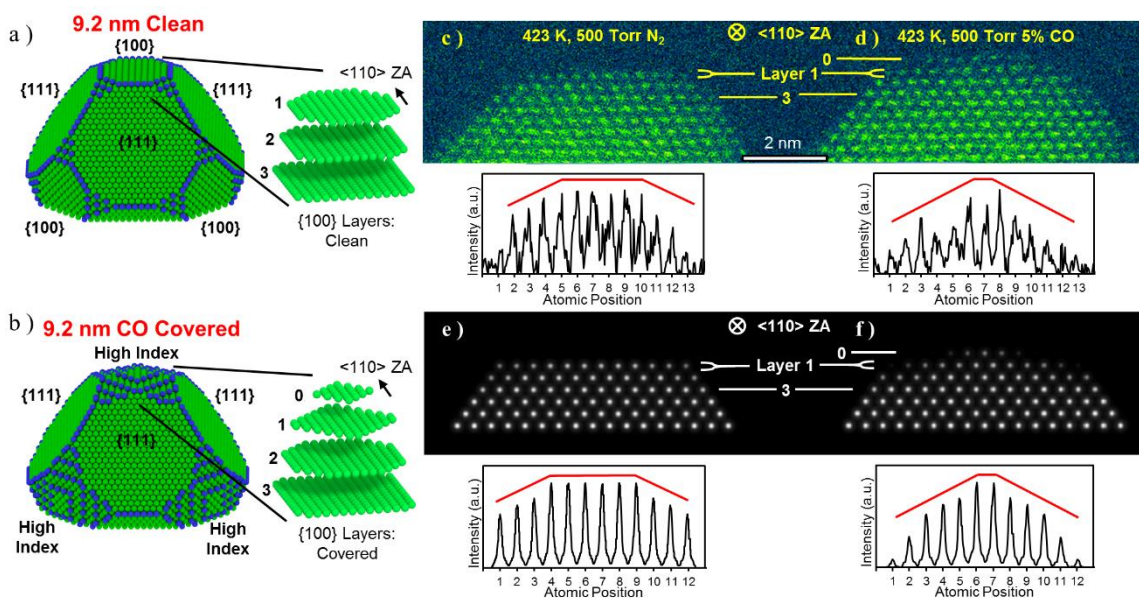


Figure 6.6. Visual comparison of DFT-calculated and *in-situ* STEM measurements of facet-specific CO induced Pt nanoparticle surface reconstruction. Wulff constructions of a 9.2 nm Pt particle based on DFT calculated surface free energies for **a)** bare surfaces, and **b)** CO saturated surfaces. Both images are tilted slightly off the $\langle 110 \rangle$ zone axis (ZA). The green atoms represent WC Pt atoms, and the blue atoms represent UC Pt edge and corner atoms. The layers to the right are the top 3-4 $\{100\}$ layers of the particle model, with the $\langle 110 \rangle$ zone axis going into the page. Aberration-corrected STEM images of a 9 nm Pt particle taken along the $\langle 110 \rangle$ zone axis **c)** at 423 K in 500 Torr N_2 , and **d)** at 423 K in 500 Torr of 5% CO in Ar (25 Torr CO). Layers 0 (for (D) only), 1, and 3 are labeled in each image for comparison. Below each image is the intensity analysis for layer 1 of each corresponding image. Each peak corresponds to an atomic column along the $\langle 110 \rangle$ zone axis. Simulated STEM-HAADF image based on layers 0-6 of the $\{100\}$ facets of the **e)** clean and **f)** CO saturated 9.2 nm Wulff constructions, along with the corresponding intensity analysis of layer 1 for each particle model. The red lines in each intensity analysis are used to guide the eye.

The results of spectral intensity analysis for the atomic columns in layer 1 of the sample ~ 9 nm particle are shown below each corresponding image (Figure 6.6a and d). It was observed that the relative intensity of atomic columns near the edges of layer 1 is decreased upon CO adsorption as the slope of the relative intensities moving away from the particle

center becomes sharper (highlighted with red lines). This suggests that layer 0 was formed through the migration of Pt atoms located near the edges of layer 1 in the adsorbate-free condition. Similar intensity analysis was performed using the simulated HAADF-STEM images in Figure 6.6e and f. The analysis of layer 1 in the simulated images of the bare and CO saturated Pt particle, shown below Figure 6.1e and f, exhibit the same loss of intensity near the edges of the layer upon CO adsorption as observed in the experimental images. A similar comparative analysis was performed on layer 0, shown in Figure 6.7, although both analysis showed there are more atoms near the center of the particles, however the results suggest that layer 0 in the experimental measurements is not structured identically to the Wulff construction model.

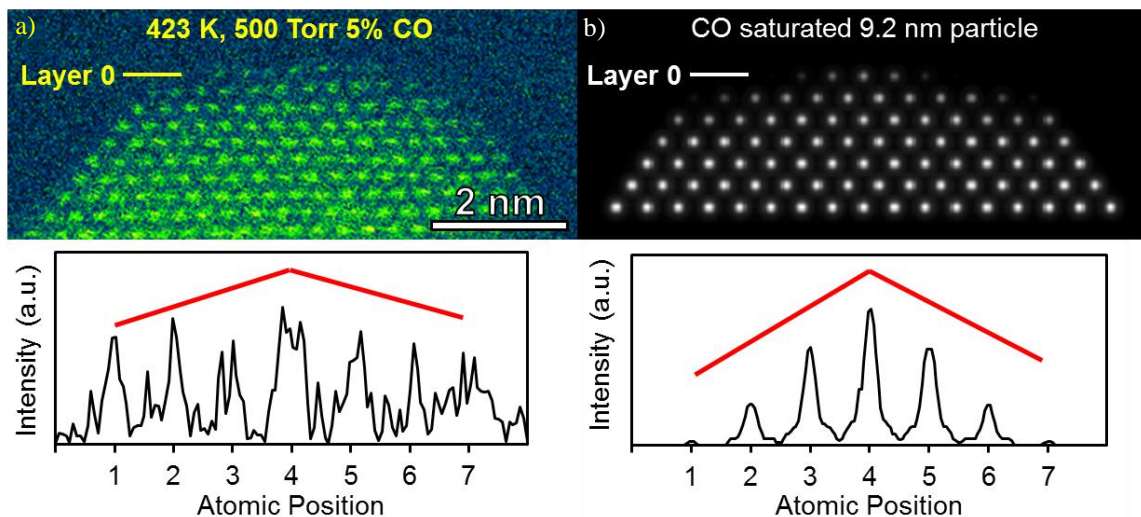


Figure 6.7. **a)** Aberration-corrected STEM image of a 9 nm particle at 423 K in an atmosphere of 500 Torr of 5% CO, viewed along the <110> zone axis (same as Figure 6.6c). Below the image is the line scan intensity analysis of layer 0. **b)** Simulated HAADF-STEM image based on a CO saturated 9.2 nm Pt particle, along with the intensity analysis of layer 0. Both images indicate more atoms in the atomic columns near the center of the particle. The red lines used in the intensity analysis are used to guide the eye.

It has been shown that CO-induced Pt surface reconstruction is a reversible process and it is expected that Pt nanoparticles will regain their original structures upon desorption of CO.^{3,27} To observe the reversibility of the reconstruction process in *in-situ* STEM experiments, the cell temperature was increased to 573 K in the CO environment which causes CO to desorb. The HAADF-STEM image of the 9 nm nanoparticle taken after 10 minutes at 573 K, shows that layer 0 has dissolved (Figure 6.8c) and the Pt particle is reverted to the original structure shown in Figure 6.8a (same as Figure 6.6c). The reversible, CO-induced facet selective {100} surface reconstruction was also observed for other Pt nanoparticle structures Figure 6.9. However, in this case multiple Pt particles were in close proximity (possibly touching) and the observed {100} facet selective reconstruction was more complex due to interference.

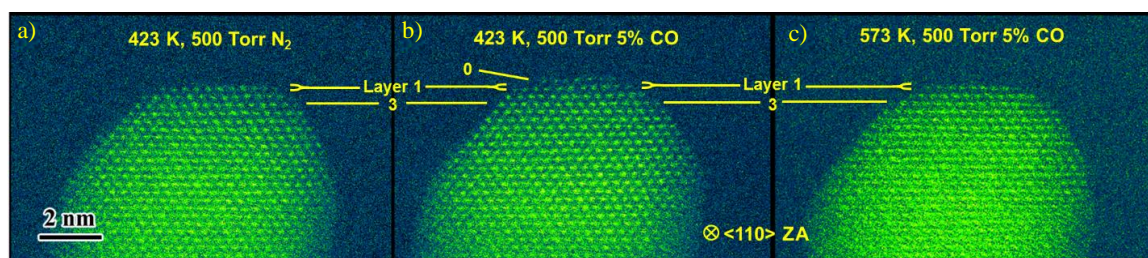


Figure 6.8. Comparison of STEM images of a 9 nm Pt particle under **a)** 423 K and 500 Torr N₂ environment (same particle as Figure 6.6c), **b)** 423 K and 500 Torr 5% CO environment (same particle as Figure 6.6d), and **c)** 573 K and 500 Torr 5% CO environment. All images are viewed along the <110> zone axis. a and c do not display any atoms in layer 0.

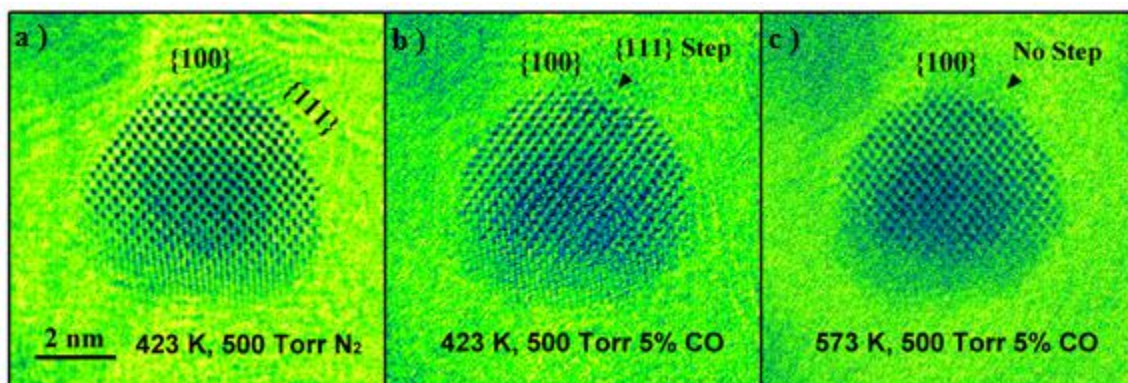


Figure 6.9. **a)**, **b)** and **c)** STEM image of a ~6 nm Pt nanoparticle under identical conditions as Figure 6.8a, b and c, showing reversible reconstruction. In this example, interference from nearby particles results in a more complicated reconstruction

Although the in-situ HAADF-STEM images provide a direct and atomic scale observation of the CO-induced surface reconstruction of Pt nanoparticles, which are in excellent agreement with our theoretical predictions based on DFT calculations, these experiments have limited spatial resolution and represent an extremely small sample size. To investigate if the proposed CO-induced reconstruction behavior is prevalent in the entire catalyst sample, we applied a quantitative IR spectroscopy approach that was recently shown to provide a realistic account of sample-averaged information regarding surface active site distribution.²⁷

Figure 6.10a shows the IR spectra obtained for reduced Pt/ α -Al₂O₃ catalysts with varied average Pt particle diameter (1.8 ± 0.3 nm, 8.1 ± 6.2 nm and 17 ± 9 nm) in an *in-situ* IR cell at 298 K and atmospheric pressure, which results in saturation CO coverage with minimal surface reconstruction (for details see section 6.3.6). The observed stretch at 2085-2098 cm⁻¹ was assigned to the collective vibration of linearly bound CO adsorbed on WC Pt sites, and the stretch at 2060-2078 cm⁻¹ was assigned to the collective vibration of linearly bound CO adsorbed on UC Pt sites (Figure 6.10a inset).^{33,34} The fractions of WC

and UC surface Pt atoms at room temperature, representing the unreconstructed bare Pt nanoparticles, were calculated using the normalized peak areas of each site type in Figure 6.10a. The results provided in Figure 6.11a, are in good agreement with predicted site fractions from DFT based Wulff construction models of bare Pt particles of the same size (Figure 6.11b) and expected fractions from TEM inferred particle sizes coupled with geometric models (Figure 6.11c). This agreement verifies that the quantitative information obtained through our approach is a realistic representation of surface structure of bare Pt particles.

To activate the surface reconstruction of Pt catalysts, the sample was heated up to 363 K in CO environment (see section 6.3.6). upon heating, the peak corresponding with CO adsorbed on UC Pt sites becomes more defined and grows in intensity as a function of time, ultimately reaching steady state after 10-20 minutes (Figure 6.10a). The increase in UC site concentration at higher temperature is direct evidence of CO-induced Pt surface reconstruction. Thus, the difference in the fraction of WC and UC Pt sites from quantitative IR measurements at 298 and 363 K provides a measure of the amount of reconstruction induced by saturation CO coverage. The change in the fraction of UC Pt atoms were calculated for different particle size samples using IR measurements. The results are compared to the predictions from the adsorbate-free and CO covered DFT-based Wulff construction models as a function of particle size in Figure 6.10b. As seen in Figure 6.10b, the amount of Pt surface reconstruction calculated based on IR measurements and predicted with Wulff construction models are in quantitative agreements and show an increasing

amount of reconstruction as a function of particles size, from ~2% for 2 nm particles, to ~10% for ~15 nm Pt particles.

The excellent agreement between sample-averaged quantitative IR measurements, DFT-based Wulff construction models, and the *in-situ* STEM measurements, is strong evidence that adsorption of CO at saturation coverage on Pt nanoparticle catalysts induces a facet selective reconstruction of {100} facets into higher index stepped facets and that this behavior is representative of the entire catalyst sample.

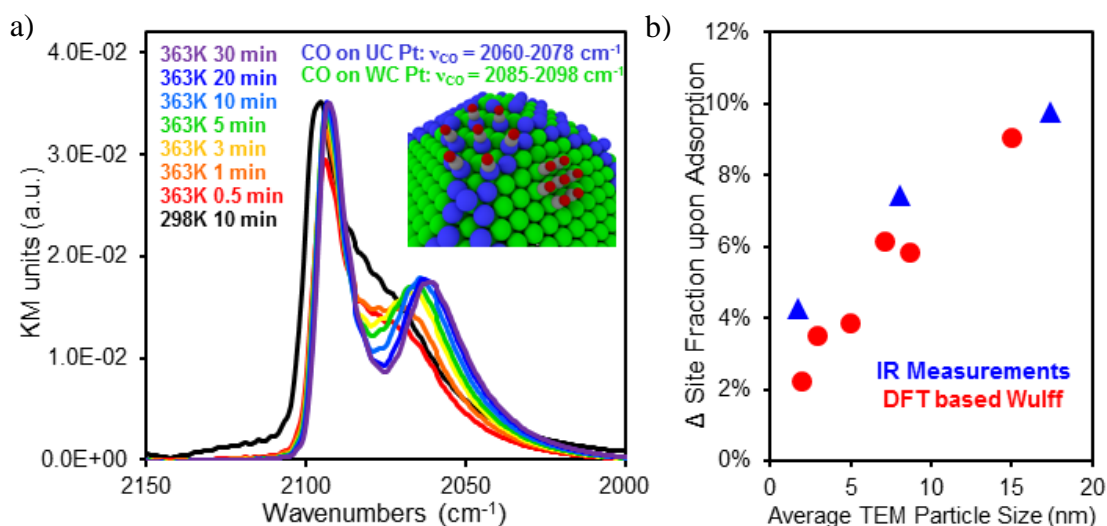


Figure 6.10. Quantitative correlation between IR measurements and DFT predictions of CO-induced Pt nanoparticle surface reconstruction. **a)** IR spectra from a pre-reduced 17 ± 9 nm Pt catalyst in a stream of 1% CO/He at room temperature (black), and held at 363K as a function of time. All spectra are presented in Kubelka Munk (KM) units. The inset shows example linear adsorption geometries of CO on a Pt nanoparticle on WC (green) and UC (blue) atoms, and the assigned vibrational frequencies (ν_{CO}). Additional CO molecules are excluded in this illustration for clarity. **b)** The change (Δ) in fraction of Pt surface atoms existing as UC Pt atoms, caused by CO induced reconstruction, as a function of particle size calculated from the DFT based Wulff construction models, and measured by IR for the three considered catalysts.

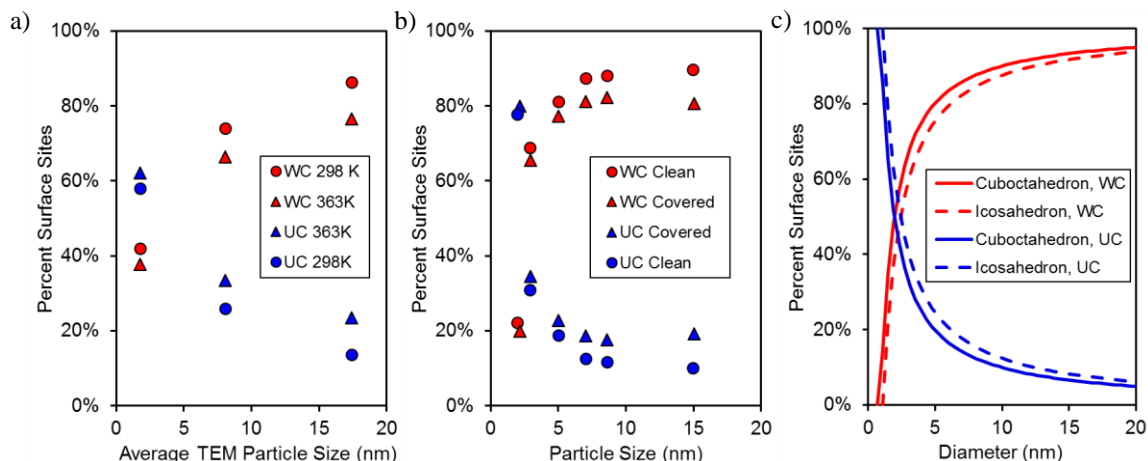


Figure 6.11. **a)** Results of *in-situ* quantitative IR analysis of UC (blue) and WC (red) site fractions on 1.8 ± 0.3 nm, 8.1 ± 6.2 nm, and 17 ± 9 nm Pt/Al₂O₃ catalysts measured at 298 K (circles) and 363K (triangles). **b)** Quantitative analysis of clean and CO saturated DFT calculated Wulff constructions of various sizes. **c)** Geometric model of the change in UC and WC site fractions with particle diameter for cuboctahedron and icosahedron particle geometries.

6.5. Conclusions

CO induced surface reconstruction of Pt nanoparticles were investigated by correlating atom-resolved direct imaging via *in-situ* STEM, with a sample-averaged surface structure analysis based on *in-situ* IR spectroscopy approach and DFT based Wulff-constructions. It was demonstrated that at high CO coverage, Pt nanoparticles undergo a reversible, facet-selective reconstruction where {100} facets reconstruct to stepped vicinal surfaces, while {111} facets are stable. This is the first example of an atomic scale and quantitative view of adsorbate induced metal nanoparticle surface reconstruction at realistic conditions and the approach introduced here is expected to be useful for identifying the exposed surface structure on various supported metal catalysts under reaction conditions.

6.6. References

1. Hansen, P. L. *et al.* Atom-Resolved Imaging of Dynamic Shape Changes in Supported Copper Nanocrystals. *Science* **295**, 2053–2055 (2002).
2. Yoshida, H. *et al.* Visualizing Gas Molecules Interacting with Supported Nanoparticulate Catalysts at Reaction Conditions. *Science* **335**, 317–319 (2012).
3. Vendelbo, S. B. *et al.* Visualization of oscillatory behaviour of Pt nanoparticles catalysing CO oxidation. *Nat. Mater.* **13**, 884–890 (2014).
4. Tao, F. & Crozier, P. A. Atomic-Scale Observations of Catalyst Structures under Reaction Conditions and during Catalysis. *Chem. Rev.* **116**, 3487–3539 (2016).
5. Jinschek, J. R. Advances in the environmental transmission electron microscope (ETEM) for nanoscale in situ studies of gas–solid interactions. *Chem. Commun.* **50**, 2696–2706 (2014).
6. Tao, F. *et al.* Restructuring of hex-Pt(100) under CO gas environments: Formation of 2-D nanoclusters. *Nano Lett.* **9**, 2167–2171 (2009).
7. van Beurden, P., Bunnik, B. S., Kramer, G. J. & Borg, A. Mechanism and dynamics of the CO-induced lifting of the Pt(100) surface reconstruction. *Phys. Rev. Lett.* **90**, 066106 1-4 (2003).
8. Thostrup, P. *et al.* Adsorption-Induced Step Formation. *Phys. Rev. Lett.* **87**, 126102 1-4 (2001).
9. Tao, F. *et al.* Break-up of stepped platinum catalyst surfaces by high CO coverage. *Science* **327**, 850–853 (2010).
10. Kim, J., Noh, M. C., Doh, W. H. & Park, J. Y. Thermal Evolution and Instability of CO-Induced Platinum Clusters on the Pt(557) Surface at Ambient Pressure. *J. Am. Chem. Soc.* **138**, 1110–1113 (2016).
11. Enkovaara, J. *et al.* Electronic structure calculations with GPAW: a real-space implementation of the projector augmented-wave method. *J. Phys. Condens. Matter* **22**, 253202 (2010).
12. Hammer, B., Hansen, L. B. & Nørskov, J. K. Improved adsorption energetics within density-functional theory using revised Perdew-Burke-Ernzerhof functionals. *Phys. Rev. B* **59**, 7413–7421 (1999).
13. Li, L. *et al.* Investigation of Catalytic Finite-Size-Effects of Platinum Metal Clusters. *J. Phys. Chem. Lett.* **4**, 222–226 (2013).
14. Monkhorst, H. J. & Pack, J. D. Special points for Brillouin-zone integrations. *Phys. Rev. B* **13**, 5188–5192 (1976).
15. Singh-Miller, N. E. & Marzari, N. Surface energies, work functions, and surface

- relaxations of low index metallic surfaces from first-principles. *Phys. Rev. B* **80**, 235407 1-9 (2009).
16. Vitos, L., Ruban, A. V., Skriver, H. L. & Kollár, J. The surface energy of metals. *Surf. Sci.* **411**, 186–202 (1998).
 17. Wen, Y.-N. & Zhang, J.-M. Surface energy calculation of the fcc metals by using the MAEAM. *Solid State Commun.* **144**, 163–167 (2007).
 18. Allian, A. D. *et al.* Chemisorption of CO and mechanism of CO oxidation on supported platinum nanoclusters. *J. Am. Chem. Soc.* **133**, 4498–4517 (2011).
 19. Yeo, Y. Y., Vattuone, L. & King, D. A. Calorimetric heats for CO and oxygen adsorption and for the catalytic CO oxidation reaction on Pt{111}. *J. Chem. Phys.* **106**, 392–401 (1997).
 20. Mason, S. E., Grinberg, I. & Rappe, A. M. Adsorbate–Adsorbate Interactions and Chemisorption at Different Coverages Studied by Accurate ab initio Calculations: CO on Transition Metal Surfaces†. *J. Phys. Chem. B* **110**, 3816–3822 (2006).
 21. Barmparis, G. D. & Remediakis, I. N. Dependence on CO adsorption of the shapes of multifaceted gold nanoparticles: A density functional theory. *Phys. Rev. B* **86**, 085457 1-7 (2012).
 22. Wulff, G. On the Question of Speed of Growth and Dissolution of Crystal Surfaces. *Zeitschrift für Krist.* **34**, 449–530 (1901).
 23. Bahn, S. R. & Jacobsen, K. W. An object-oriented scripting interface to a legacy electronic structure code. *Comput. Sci. Eng.* **4**, 56–66 (2002).
 24. Zhang, S. *et al.* Dynamical Observation and Detailed Description of Catalysts under Strong Metal–Support Interaction. (2016).
 25. Matsubu, J. C. *et al.* Adsorbate-Mediated Strong Metal-Support Interactions in Oxide Supported Rh Catalysts. *Nat. Chem.* **In Press**, (2016).
 26. Bourane, A. & Bianchi, D. Heats of adsorption of the linear CO species on Pt/Al₂O₃ using infrared spectroscopy: Impact of the Pt dispersion. *J. Catal.* **218**, 447–452 (2003).
 27. Kale, M. J. & Christopher, P. Utilizing quantitative in-situ FTIR spectroscopy to identify well-coordinated Pt atoms as the active site for CO oxidation on Al₂O₃ supported Pt catalysts. *ACS Catal.* **6**, 5599–5609 (2016).
 28. Koch, C. T. Determination of core structure periodicity and point defect density along dislocations. (Arizona State University, 2002).
 29. Matsubu, J. C., Yang, V. N. & Christopher, P. Isolated Metal Active Site Concentration and Stability Control Catalytic CO₂ Reduction Selectivity. *J. Am. Chem. Soc.* **137**, 3076–3084 (2015).

30. Yoshinobu, J., Tsukahara, N., Yasui, F., Mukai, K. & Yamashita, Y. Lateral displacement by transient mobility in chemisorption of CO on Pt(997). *Phys. Rev. Lett.* **90**, 248301 1-4 (2003).
31. Hayden, B. E., Kretzschmar, K., Bradshaw, A. M. & Greenler, R. G. An infrared study of the adsorption of CO on a stepped platinum surface. *Surf. Sci.* **149**, 394–406 (1985).
32. Longwitz, S. R. *et al.* High-coverage structures of carbon monoxide adsorbed on Pt(111) studied by high-pressure scanning tunneling microscopy. *J. Phys. Chem. B* **108**, 14497–14502 (2004).
33. Greenler, R. G. & Brandt, R. K. The origins of multiple bands in the infrared spectra of carbon monoxide adsorbed on metal surfaces. *Colloids Surfaces A* **105**, 19–26 (1995).
34. Xu, J. & Yates, J. T. J. Terrace width effect on adsorbate vibrations: a comparison of Pt(335) and Pt(112) for chemisorption of CO. *Surf. Sci.* **327**, 193–201 (1995).

Chapter 7

Conclusions and Future Outlook

7.1. Summary

The overall objective of this dissertation has been to employ fundamental mechanistic insights gained through a combination of computational and analytical methods to predict macroscopic observables associated with catalytic and photocatalytic processes on transition metal surfaces. We were able to identify performance controlling characteristics of transition metals for CO₂ reduction by H₂ through a detailed mechanistic study and developed an analytical approach to systematically identify the performance controlling steps for reactions on transition metals. In a separate study, we developed a novel approach that accurately predicted previously measured wavelength-dependent photocatalytic rates on metals and suggested approaches to control selectivity in photon-driven reactions on metal surfaces. In addition, by combining DFT calculations and in situ characterization methods, we provided a quantitative atomic-scale view of adsorbate induced metal

nanoparticle surface reconstruction at realistic conditions. In this chapter we summarize the main conclusions of the research presented in this dissertation and outline future research directions.

7.2. General Conclusions

In this dissertation quantum chemistry calculations were coupled with numerical and analytical models to obtain fundamental insights into mechanisms of catalytic and photocatalytic processes on transition metal surfaces. We developed models based on DFT calculated parameters to predict (photo)catalytic rates and selectivity trends among transition metals. The predicted catalytic performances were all validated based on experimental measurements. The theoretical models developed here provide atomic scale insights into the mechanisms of (photo)catalytic processes and suggest areas for future research in the design of novel catalysts. The main conclusions derived in this study are explained below.

Based on a thorough mechanistic study of CO₂ reduction by H₂ over Ru(0001), using DFT calculations and mean field microkinetic modeling, we addressed the important unresolved questions associated with the mechanism of the reaction. Direct CO₂ dissociation followed by hydrogenation of CO* to CHO* was identified as the prominent pathway for CH₄ production. The microkinetic model successfully predicted experimentally observed trends of surface coverage variations with temperature and reactant partial pressures, as well as CH₄ selectivity and rate dependence on feed composition. It was demonstrated through sensitivity analysis that CHO*→CH*+O* is the RLS in CH₄ formation, whereas CO* desorption is the RLS for CO production via rWGS.

CHO* dissociation and CO* desorption steps were identified as the selectivity controlling steps.

By further examining the energetics of reaction intermediates associated with the selectivity controlling steps, CHO* dissociation and CO* desorption, we found that variations of binding energies of these intermediates among late transition metal catalysts does not explain experimentally observed differences in selectivity. On the other hand, the tendency of the late transition metals for CH₄ formation was found to correlate well with the affinity of the metals for O* binding. It was shown that depth of catalytic CO₂ reduction by H₂ on late transition metal catalysts is directly related to the catalysts' oxygen adsorption strength, where weaker oxygen binding metals can only reduce CO₂ mildly to CO, whereas stronger oxygen binding metals reduce CO₂ more deeply to CH₄.

By including intrinsic parametric correlations of the late transition metals in the sensitivity analysis of CO₂ reduction system, we proposed a new analytical approach, called scaled degree of rate control (S-DoRC), to systematically identify the performance controlling steps that are relevant to transition metal catalysts. With S-DoRC approach we were able to analytically obtain identical conclusion to the qualitative conclusions derived above; it demonstrated that CHO* dissociation is much more important than CO* desorption for controlling differences in catalytic performance of different transition metals. With this approach, we are able to guide the sensitivity analysis in the specific direction that is relevant for transition metals and directly identify the parameters that are most influential and tunable across these surfaces.

In Chapter 5 we proposed a theoretical approach to investigate adsorbate specific behavior of substrate-mediated photochemistry processes on metal surfaces by coupling a first-principles based treatment of DIET mechanism with an extended version of the TTM. We specifically focused on three well-studied model reactions on Pt(111) surfaces, CO and NO desorption and O diffusion. The model calculations provided predictions of the time scales, wavelength dependent and temperature dependent behavior of photon induced reactions on metal surfaces in qualitatively good agreement with experimentally observed trends. The calculated probabilities of photo-induced reactions show significant dissimilarities in the efficiency of electron coupling with the resonant states of the three reaction systems, which is related to differences in the shape of unpopulated resonance states and PESs of the associated reactions. It was found that dissimilarities in the PES and resonance shapes of the three reaction systems caused unique temperature and wavelength dependent behavior in the systems, displaying significant adsorbate specificity. It is suggested that driving photocatalytic reactions on metal surfaces with a targeted wavelength and at an optimal temperature may provide increased control of reaction selectivity on metal catalyst surfaces.

In the last part of this dissertation we investigated the process of CO-induced reconstruction of Pt nanoparticle catalysts, with the use of extensive DFT calculations and Wulff construction modeling. By correlating atom-resolved imaging via *in-situ* scanning transmission electron microscopy (STEM), with *in-situ* quantitative, site-specific infrared (IR) spectroscopy and DFT based Wulff-constructions we demonstrated that at high CO coverage, Pt nanoparticles undergo a facet selective reconstruction where (100) facets

reconstruct to stepped vicinal surfaces, while (111) facets are stable. The quantitative understanding of the Pt surface reconstruction under high CO coverage is very important for the design of catalytic converters. Furthermore, we demonstrated the effectiveness of the combined characterization methods (in-site STEM and IR) with DFT calculations, by providing the first example of an atomic scale and quantitative view of adsorbate induced metal nanoparticle surface reconstruction at realistic conditions.

As a summary, we demonstrated the predictive power of first-principles based modeling with three distinct examples; We showed that DFT-based microkinetic models provide valuable insight into the mechanism of complex catalytic reactions which is crucial to the development of efficient catalytic materials. With a combination of DFT calculations and quantum mechanical approaches we were able to predict the adsorbate specific behavior of photocatalytic systems; which open up pathways to selectivity driving reactions on metal surfaces solar energy. Also, we demonstrated how DFT calculations can complement experimental methods to provide atomic scale, quantitative view of adsorbate-surface interactions under realistic reaction conditions, which is valuable information for the design of catalytic processes.

7.3. Outlook on Future Research

The main focus of this dissertation was to develop models that can accurately predict macroscopic observables associated with catalytic and photocatalytic processes from first-principles. A natural extension to this work would be to improve the accuracy of the developed models by incorporation of more sophisticated theoretical approaches and

realistic approximations. Here some future potential directions of for research in each study is discussed.

A major shortcoming of mean-field microkinetic models as employed in Chapter 3, is the exclusion of surface coverage effects in the calculation of reaction energies, which impacts the calculated surface coverage and consequently the predicted kinetic parameters of the reaction.¹ A rigorous study to include the correct coverage dependent surface kinetic would require kinetic Monte Carlo (kMC) simulations which involves numerous DFT calculations to account for various adsorbate configurations and is computationally expensive.² A more feasible approach that can be incorporated into our microkinetic model, is to derive correlations for calculating adsorption energies of reaction intermediates as a function of their surface coverage. These correlations can be derived by fitting adsorption energy data, calculated at different surface coverage of adsorbates, into a linear correlation.^{1,2}

The S-DoRC approach proposed in Chapter 4, was validated by demonstrating its application to a relatively simple reaction system, CO₂ reduction by H₂, where only two of the involved elementary steps had shown significant impact on the reaction rates and selectivity. We expect that this analysis will have a more significant influence on more complex reactions where multiple elementary steps control the kinetics. An important and necessary extension to this study is to demonstrate the application of the methodology to multiple more complex reaction systems.

In Chapter 5, an approached was developed to model substrate-mediated photocatalytic processes on metals. The model predicts wavelength dependent trends of QYs that agree

reasonably well with the experimental data for CO and NO desorption and O diffusion on Pt(111) surfaces. However, quantitative comparison of the results with the experimental data shows an overestimation of QY dependence on wavelength, specifically at lower wavelength photon excitations for CO desorption system which is attributed to an overestimation of primary electron distribution at higher energy levels that are in resonance with CO adsorbate unpopulated state. There are a few of possible routes to improve the electron thermalization model as described below:

(i) In our approach to model the dynamic electronic structure in the metal we assume direct conversion of primary excitations into thermalized FD electronic distribution. In reality, multiple new excitations typically occur during this conversion process, which will result in a redistribution of excited electrons to lower energy levels. In addition, the electron-electron scattering relaxation channel is not taken into consideration for FD thermalized electrons. These can be included more rigorously in our model by utilizing a more sophisticated thermalization model for the temporally evolving metal electronic structure where the entire thermalization process (rather than immediate conversion of primary excitations into an FD distribution) is considered. We plan to use Boltzman Transport equation which has been shown to describe the kinetics of charge carrier excitation and energy redistribution accurately.³ In this approach thermalized electron distribution is not separated from the primary excitations and a single electron distribution is followed temporally.

(ii) Although Fermi-Liquid theory captures the basic features of hot-electron lifetimes, for real metals the more complex band structure is expected to have a decisive influence.

First-principles based computational approaches such as DFT band-structure calculations and G_0W_0 approximation, allow accurate calculation of characteristic lifetimes for different materials, which are computationally expensive and time consuming.^{4,5} We propose simple approaches to incorporate metal specific corrections into our model which we expect to diminish the deviations of calculated wavelength dependencies from the experimentally observed trends. For example, Pt exhibits DOS near ϵ_F that is not flat (as considered here) and also exhibits time dependent electron cooling behavior that deviates from Fermi-Liquid theory.⁴ The real DOS of metals can easily be included in our modeling approach. This will alter the probabilities of photo-induced electronic transitions which we will incorporate in the calculation of initial distribution of primary excited charge carriers. An easy approach to include metal specific electron cooling behavior into our model is to use existing data from G_0W_0 calculations and numerical interpolation methods to define metal specific functions for electron scattering relaxation time.

(iii) The effect of nanometer size confinement of the Pt metal on the photo-induced processes is only included in our model through the assumption of a spatially homogenous charge carrier distribution in the system and the spatial isolation of photon absorption events. However, it has been demonstrated that the particle size reduction enhances the electron-electron interaction and scattering rates.³ These effects can be incorporated into the model by use of size dependent characteristic times of electron-electron and electron-phonon scattering processes and would be expected to impact intricacies of the resulting wavelength dependent QY's and potentially reaction time scales.

In Chapter 6 we demonstrated the DFT calculations combined with *in-situ* STEM and *in-situ* IR are powerful set of characterization tools that can provide detailed quantitative information reconstruction of supported metal catalysts that are driven by reaction conditions. An obvious and promising extension to this study is to use these characterization tools to investigate other important catalytic processes involving metal nanoparticles such as CO_x-induced reconstruction of Cu and Ru based catalysts which are involved in many important industrial processes (for example Water gas shift, Fischer Tropsch and methanol synthesis). In addition, these techniques can be used to gain understanding of metal-support interaction and the role this interaction play in the reconstruction of catalytic surfaces. The detailed knowledge catalyst surface structures and how they change under reaction conditions will guide the design of better catalysts for these processes.

7.4. References

1. Lausche, A. C. *et al.* On the effect of coverage-dependent adsorbate–adsorbate interactions for CO methanation on transition metal surfaces. *J. Catal.* **307**, 275–282 (2013).
2. Grabow, L. C., Hvolbæk, B. & Nørskov, J. K. Understanding Trends in Catalytic Activity: The Effect of Adsorbate–Adsorbate Interactions for CO Oxidation Over Transition Metals. *Top. Catal.* **53**, 298–310 (2010).
3. Voisin, C. *et al.* Ultrafast electron-electron scattering and energy exchanges in noble-metal nanoparticles. *Phys. Rev. B* **69**, 195416 (2004).
4. Ladstädter, F., Hohenester, U., Puschnig, P. & Ambrosch-Draxl, C. First-principles calculation of hot-electron scattering in metals. *Phys. Rev. B* **70**, 235125 (2004).
5. Bernardi, M., Vigil-Fowler, D., Lischner, J., Neaton, J. B. & Louie, S. G. *Ab Initio* Study of Hot Carriers in the First Picosecond after Sunlight Absorption in Silicon. *Phys. Rev. Lett.* **112**, 257402 (2014).